ABSTRACT

| | |
|---|---|
| Title of Document: | SILICON-GERMANIUM PHOTODETECTORS FOR OPTICAL TELECOMMUNICATIONS |
| | Dyan Ali, Doctor of Philosophy, 2012 |
| Directed By: | Professor Julius Goldhar, Department of Electrical and Computer Engineering<br>Dr. Christopher J. K. Richardson, Laboratory for Physical Sciences |

This thesis investigates the design and growth of silicon-germanium p-i-n photodetectors for optical telecommunications applications. Two types of heterostructures are considered: strained silicon-germanium layers grown directly on silicon substrates, and strain-balanced silicon-germanium/silicon superlattice grown on relaxed buffer layers. The heterostructures are designed using existing band structure models and are grown using solid source molecular beam epitaxy (SS-MBE). To facilitate these growths, an atomic absorption spectroscopy- based flux monitor for the silicon source is developed and calibrated. In addition, the development of a substrate preparation procedure for relaxed buffer layers that is compatible with SS-MBE is developed and allows the growth of epitaxial films with low defect densities. P-i-n diodes processed from these films are shown to have low

reverse leakage currents densities compared to other competing devices. Photocurrent spectroscopy is used to characterize these structures. A clear reduction in the bandgap of the heterostructures over that of the constituent alloys due to exploitation of the Type-II band offsets in the silicon-germanium material system is demonstrated in both, the strained and strain-balanced photodetectors. Finally, the low leakage current densities are exploited to fabricate devices with noise equivalent powers comparable to or better than competing approaches based on the growth of germanium on silicon substrates.

# SILICON-GERMANIUM PHOTODETECTORS FOR OPTICAL TELECOMMUNICATIONS

By
Dyan Ali

Dissertation submitted to the Faculty of the Graduate School of the
University of Maryland, College Park, in partial fulfillment
of the requirements for the degree of
Doctor of Philosophy
2012

Advisory Committee:
Professor Julius Goldhar, Chair
Dr. Christopher J.K. Richardson
Professor Thomas E. Murphy
Professor Neil Goldsman
Professor Lourdes G. Salamanca-Riba

# Dedication

To my family, as it's grown over the years

# Acknowledgements

The road that's led to this point has been long, and the journey's been facilitated by a lot of people along the way, and I would like to take this opportunity to thank them. First and foremost, I would like to thank Dr. Christopher Richardson, my research advisor, for the invaluable support, encouragement and advice that he has provided over the course of my study here at the University of Maryland. In addition to introducing me to MBE, and introducing me to new experimental techniques, he has helped me become a better researcher by emphasizing rigor and more detailed analysis to better understand the results of any experiment. His support and patience in the face of significant challenges has proven to be invaluable. I would like to thank Professor Julius Goldhar, my academic advisor for all the assistance over the years, for taking me under his wing when I first started graduate school, and for introducing me to Dr. Richardson.

I would like to thank the present and former members of the MBE group at at the Laboratory for Physical Sciences, Joseph Di Pasquale III, Dr. Justin Hackley, Dr. Subramaniam Kanakaraju and Dr. Lei He for all the significant assistance provided in training and assisting me in the seemingly innumerable maintenance cycles that are go with a silicon MBE reactor. I would also like to thank the present and past members of the Systems Maintenance Group and the R22 group at LPS, specifically Toby Olver, Steve Brown, Lisa Lucas, Dan Hinkel, Scott Horst and Warren Berk for training and assistance with microfabrication and analysis techniques that were

needed to fabricate the devices described in this thesis. I would also like to give thanks to Victor Yun for the immense engineering assistance he provided, and for enabling some of the rendered drawings in this thesis.

I would like to thank Prof. Thomas Murphy, Prof. Neil Goldsman, and Prof. Lourdes Salamanca-Riba for agreeing to serve on my committee and for helpful discussions we have had.

The technical discussions I've had with other group members have helped immensely, and I would like to give special thanks to Dr. Yongzhang Leng, Dr. Paveen Apiratikul, Dr. Shuo-Yen Tseng, Nathan Siwak, Arun Mampazhy, Ricardo Pizarro, Charlie Camp and Laura Clinger.

I would like to thank my friends who helped College Park feel like home, and to Elizabeth for making this *home*. You have been a source of love, support and comfort, and I thank you. Aoife, you have made the past eight months a lot more fun and rewarding.

Finally, I would like to thank my mother Myrtle and my father Mushtaqh for their love and support in encouraging me to pursue my own interests, helping me build the fortitude to deal with the setbacks I've had to deal with, and for instilling in me the importance of hard work.. My sister Ruhi, thank you for your love and friendship, and I hope your experience with graduate school is as rewarding as mine.

# Table of Contents

# List of Abbreviations

AAS – Atomic Absorption Spectroscopy

AFM – Atomic Force Microscopy

BEP – Beam Equivalent Pressure

BFM – Beam Flux Monitor

DLTS – Deep Level Transient Spectroscopy

EIES – Electron Impact Emission Spectroscopy

FCA – Free Carrier Absorption

HCL – Hollow Cathode Lamp

HH – Heavy Hole

LH – Light Hole

MBE – Molecular Beam Epitaxy

ML – Monolayer

MMWG – Multimode Waveguide

NEP – Noise Equivalent Power

NIR – Near Infrared

NRL – Naval Research Lab

pBN – Pyrolytic Boron Nitride

pG – Pyrolytic Graphite

PICTS – Photoinduced Current Transient Spectroscopy

QCM – Quartz Crystal Monitor

RBL – Relaxed Buffer Layer

RGA – Residual Gas Analyzer

RHEED – Reflection High Energy Electron Diffraction

SBSL – Strain-Balanced Superlattice

SEM – Scanning Electron Microscopy

SLS – Strained Layer Superlattice

SMWG – Single Mode Waveguide

SSMBE – Solid Source Molecular Beam Epitaxy

STM – Scanning Tunneling Microscopy

UHV – Ultra-High Vacuum

UPS – Ultraviolet Photoelectron Spectroscopy

XPS – X-ray Photoelectron Spectroscopy

XRD – X-ray Diffractometry

# Chapter 1 : Introduction

## *1.1 General introduction*

Since their inception about thirty years ago, fiber-optic communication systems have grown rapidly. Integral to this growth is the tremendous improvement in photodetector technology over the years. Simply put, photodetectors convert optical signals into an electrical signal that is a quantitative measure of the signal strength. These devices find use in several fields such as imaging systems, spectroscopy and optical telecommunications. Innovations in design and significant improvements in material growth and device fabrication technology have allowed for detectors capable of operating at 160 GHz [1] while ensuring high device yield, reliability and lifetime. All of these factors – high speed, high yields and high reliability – have facilitated the explosion in long-haul optical communication. In this thesis, a silicon-based photodetector for optical telecommunications will be presented.

## *1.2 Motivation*

The recent years have seen a dramatic increase in the bandwidth requirements of communication systems. In addition, the trend of miniaturization has facilitated the integration of as many components as possible on a single chip. This situation presents a conundrum for the integration of optical components on conventional microprocessors in long-haul communication systems. These systems have typically

operated in a close to 1.3 μm and 1.55 μm. The Original, or O- band from 1.26 - 1.36μm was originally favored due to the near-zero dispersion in silica optical fiber. This minimized dispersion-induced broadening of the optical pulses. More recently, the Conventional, or C-band, and the Long wavelength, or L-band, corresponding to 1.53 - 1.565 μm (C-band) and 1.565 - 1.625 μm, have been prefered due to the availability of more efficient optical amplifiers. Typically, C-band amplifiers are based on gain in Erbium-doped optical fibers, while the L-band amplifiers are based on gain in semiconductor media. The challenge is that semiconductor photodetectors in these O- C- and L-bands are typically based on the III-V semicondcutors (InP, InGaAs) that are incompatible with Si-based heteroepitaxy. While systems designed entirely on III-V semiconductors exist, they are not cost-effective as InP epitaxy is about twenty times as expensive as SiGe epitaxy and as much as ten thousand times as expensive as CMOS technology [2]. In addition, a silicon-compatible photodetector at these wavelengths is essential for implementing optical interconnects for multi-core processors. This clearly highlights the need for a silicon-based photodetector in the O, C and L bands.

Theoretically, several techniques could be used to achieve this end. Epitaxial films that absorb the bands we are interested in can be grown directly on silicon. This would require the growth of InGaAs directly on silicon. A second alternative is the growth of strained or unstrained silicon-germanium alloys on silicon substrates. Finally, conventional InGaAs detectors can be wafer-bonded onto the silicon substrate.

In practice, the first approach has proven to be difficult as III-V

semiconductors that are lattice matched to silicon do not grow as single crystals on a silicon substrate [3]. Recently, there have been reports on the growth of GaAs on thick germanium films grown on silicon substrates. [4] Direct growth remains a challenge. Thus, it is necessary to grow strained silicon-germanium films and this brings with it a slew of other issues that need to be taken into consideration during material design and material fabrication. This is not always a drawback – in the case of $Si_{1-x}Ge_x$, strained layers have higher electron and hole mobilities and this fact has already been exploited. This increased mobility is caused by strain-induced split in the degeneracy of the conduction and valence bands, resulting in states that have higher carrier mobilities [5]. In 2005, IBM demonstrated a SiGe HBT based on strained SiGe layers operating at 210 GHz. The third approach, that of wafer-bonding InGaAs detectors on silicon. This approach has led to novel silicon heterointerface photodetectors[6] that combine the high near-IR absorption of InGaAs with the high electron to hole impact ionization coefficient of silicon to fabricate avalanche photodiode with gain-bandwidth products as high as 300 GHz. However, wafer-bonding technology is still in the research phase and it has not been successfully demonstrated on wafers larger than 2 inch [7], much less than the current industry standard of 12 inch and even 15 inch wafers. Furthermore, the high cost of InGaAs epitaxy is still a challenge. All these factors lead to the conclusion that silicon-based photodetector is needed and this is the motivation for this thesis.

## *1.3 Literature overview*

In this section, an overview of available photodetectors for telecommunications in the O, C and L bands will be presented. In particular, p-i-n photodetectors and existing SiGe photodetectors will be considered. Performance criteria and figures of merit used to describe photodetectors will be presented.

### 1.3.1 Photodetector theory

The semiconductor photodetector considered in this thesis is of the interband type in which an incident photon of energy greater than the bandgap energy is absorbed in the active region resulting in the formation of an electron-hole pair that contributes to a current $I_p$. This current is a quantitative measure of the incident power $P_{in}$ and is given by

$$I_p = RP_{in} \tag{1.1}$$

where R is the responsivity and has units A/W. This parameter is defined in terms of the fundamental material property, quantum efficiency $\eta_i$ as [8]

$$R = \frac{\eta_i e}{h\nu}. \tag{1.2}$$

Here, e is the electron charge, h, Planck's constant and ν, the frequency of the incident photon. $\eta_i$ is defined as the ratio of the electron generation rate to the total incident photon rate. Assuming there is a one-to-one correspondence between the number of absorbed photons and generated electron-hole pairs, this $\eta_i$ can be written as the ratio of the absorbed power to incident power. Further, when photons are incident normal to a slab of width W, the quantum efficiency is given by

$$\eta_i = \frac{P_{abs}}{P_{in}} \cong 1 - \exp(\alpha W)(1-\rho), \quad \textbf{(1.3)}$$

where α is the material wavelength-dependent optical absorption coefficient and ρ is the Fresnel reflection coefficent. Thus, for αW>>1, it is possible to achieve near unity quantum efficiencies provided the photogenerated charges do not undergo recombination during transport to the contact layer. Typical semiconductors have large values of α (>$10^4$ $cm^{-1}$) for photons of energy larger than the bandgap and for W~10 μm, η ~0.99. The responsivity R is usually specified as a metric to compare photodetector performance.

Another important metric to compare photodetectors is the specific detectivity [11] or D-star, $D^*$.It is the noise equivalent power (NEP) normalized to unit area and unit bandwidth and has units $mHz^{1/2}/W$

$$D^* = \frac{\sqrt{A\Delta f}}{NEP}, \quad \textbf{(1.4)}$$

where A is the area of the photosensitive region of the detector and Δf is the effective noise bandwidth. NEP is defined as the signal strength that results in a signal-to-noise ratio of unity.

Before an attempt is made to design a SiGe photodetector, it is important to survey the existing options and design approaches used in current photodetector technology. Classifications can be made based on a number of criteria such as heterostructure design, device geometry or the material used.

**Classification Based on Device Geometry**

Different device geometries based on the above mentioned heterostructures can be used. For materials with very high absorption coefficients, a mesa-type architecture can be used. However, using thick absorption regions (~10-30 μm) results in devices with high carrier transit times which limit the bandwidth. In this case, it is common to use an edge-coupled waveguide architecture with a thinner active regions to reduce the carrier transit time while ensuring sufficient photon absorption. Further improvements in bandwidth can be achieved by adopting an electrode structure that supports traveling electric waves. This electrode structure is impedance matched to the external circuit so that the optical and electrical modes propagate with the same group velocity. This reduces the bandwidth-reducing reflections of the electrical wave. This structure is called a traveling wave photodetector and devices with bandwidths as high as 370 GHz have been reported [10]. In this thesis, only mesa- and waveguide photodetectors are considered.

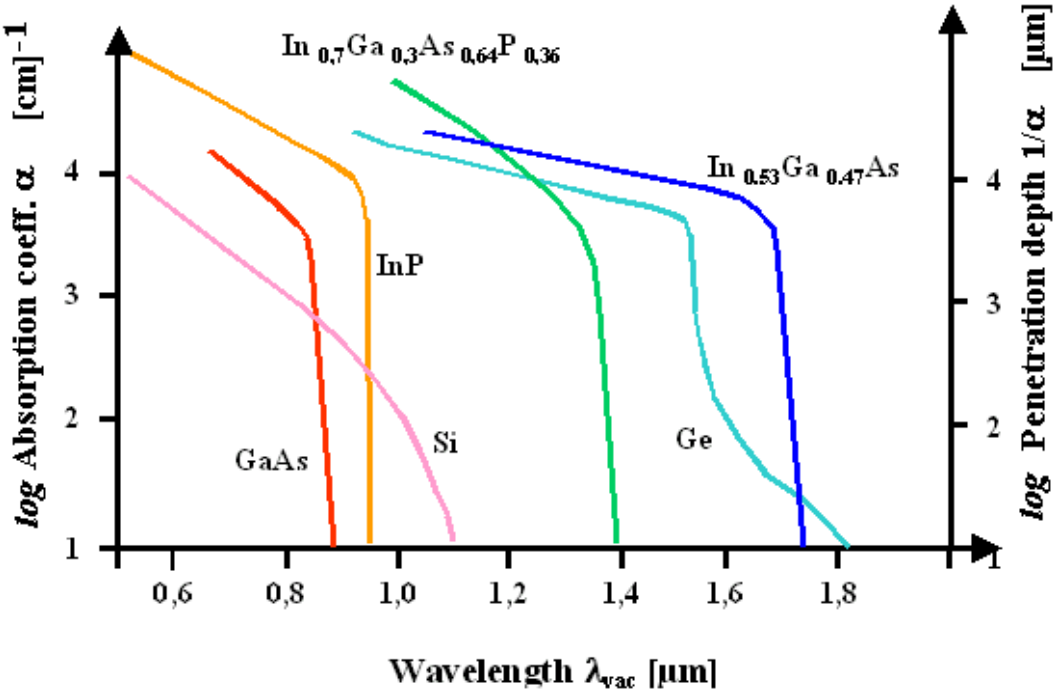


**Figure 1-1:** Variation of the absorption coefficient α with wavelength for various semiconductors [11]

### Classification Based on Active Region Material

Photodetectors for optical telecommunications can be fabricated out of different materials. Figure 1-1 shows the optical absorption coefficient and penetration depth for different semiconductors. For 1.3 µm detection, typical material choices are $In_{0.7}Ga_{0.3}As_{0.64}P_{0.36}$ and Ge. $In_{0.53}Ga_{0.47}As$ and Ge are commonly used for 1.55 µm detection. Figure 1-3 shows the variation of bandgap with composition for a variety of compound semiconductors. $Si_{1-x}Ge_x$ can also be used as the bulk bandgap spans the energy gap between 0.66 eV and 1.1 eV and will be the material of choice in this thesis.

### 1.3.2 p-i-n Photodetectors

The structure band diagram of a homojunction p-i-n photodetector under reverse bias is shown in Figure 1-2. The different components of the photocurrent – the diffusion and the drift components are also shown. The i-region and the depletion region are the source of the drift component, while electron-hole pair generation in the doped regions gives rise to the slow diffusion component. To completely eliminate the diffusion component, a heterostructure can be employed using a substrate that is transparent to the wavelength of the signal being detected. In the case of $Si_{1-x}Ge_x$ detectors for 1.3 μm and 1.55 μm, this is easily achieved using a silicon substrate.

The electron-hole generation rate G(x) at co-ordinate x is given by the number of photons incident multiplied by the absorption coefficient [8]

$$G(x) = \frac{(1-\rho)P_{in}}{Ah\nu}\alpha \exp(-\alpha x). \tag{1.5}$$

The drift component of the current density in a detector of area A is given by the integral of G(x) over the intrinsic region

$$\begin{aligned} J_{dr} &= -e\int_0^W \frac{(1-\rho)P_{in}}{Ah\nu}\alpha \exp(-\alpha x)dx \\ &= \frac{(1-\rho)P_{in}}{Ah\nu}(1-\exp(-\alpha W)) = \frac{e\eta P_{in}}{Ah\nu} \end{aligned} \tag{1.6}$$

The transit time $t_r$ is given by

$$t_r = \frac{W}{v_d} \tag{1.7}$$

where $v_d$ is the drift velocity of the charge carriers. The 3dB-cutoff for a modulated

signal incident on such a p-i-n diode is given by

$$f_{3dB} = \frac{2.4}{2\pi t_{tr}} \tag{1.8}$$

Using this relation for a silicon detector with $v_s \sim 10^5$ m/s and W~50 µm, we get $f_{3dB}$~0.8 GHz [8]. In contrast, an InGaAs detector which, as seen in Figure 1-1, has a higher optical absorption coefficient, allowing for smaller W (~5-10µm) and $f_{3dB}$~10 GHz with $v_s \sim 2x10^5$ m/s. These calculations do not take into account the degradation in bandwidth due to capacitance effects of the p-i-n junction.

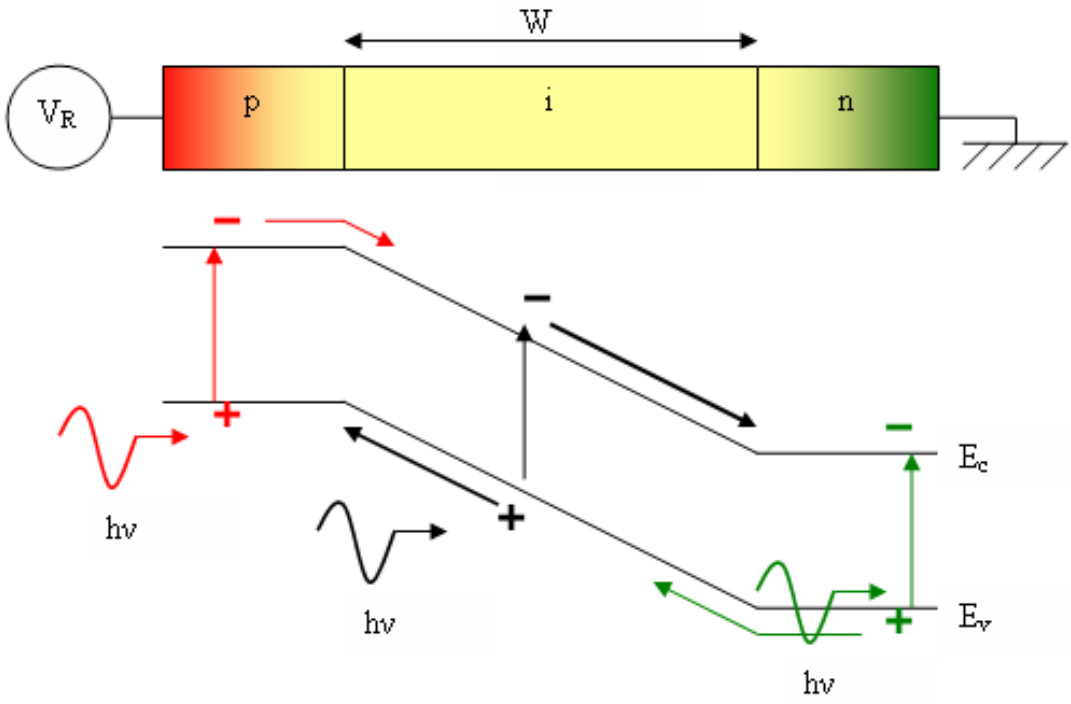


**Figure 1-2**: Structure (top) and band diagram (bottom) of a reverse-biased p-i-n diode. Absorption in the intrinsic region is indicated by black electrons(-) and holes (+) and constitute the drift current. The red and green carriers signify the absorbed carriers in the p-and n-doped regions and constitute the electron and hole diffusion currents respectively.

### 1.3.3 SiGe growth

Figure 1-3 shows the lattice parameter of different elemental and compound semiconductors and their bandgap for different compositions. Also shown is the lattice mismatch to Silicon. Based on the data in the figure, it is expected that epitaxial growth of GaP and AlP on silicon substrates would be the easiest. However, this approach is not suitable as the bandgap wavelength is in the visible portion of the spectrum. In addition, epitaxial growth has proven to be difficult [3]. The other III-V semiconductors have similar problems to GaP and AlP. The fact that the common Group V elements (P,Sb and As) are dopant atoms make diffusion difficult to avoid at the elevated growth temperatures. These drawbacks necessitate a suitable silicon-based compound semiconductor that spans the 1.3 μm to 1.55 μm range. The only real option for epitaxial growth is silicon-germanium. There is, however, a lattice mismatch of 4.3% for germanium grown on silicon. This introduces a significant concern for SiGe epitaxy, strain. Specifically, strain limits the thickness of the epitaxial film – for thicknesses larger than the critical thickness, defects and dislocations nucleate in the film to relieve the excess strain energy. In addition, strain also affects the bandgap of the film. Both these issues will be discussed in detail in Chapter 4.

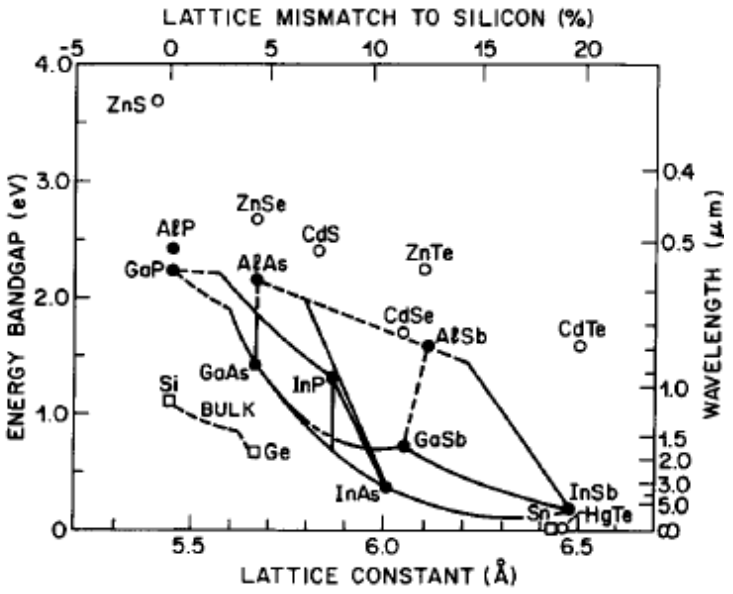


**Figure 1-3:** Lattice constant and bandgap energy and wavelength of different semiconductors. The top axis shows the lattice mismatch of the semiconductor to silicon. [3]

The most common techniques used to grown device-quality Silicon-Germanium heterostructures are Molecular Beam Epitaxy (MBE) and Chemical Vapor Deposition (CVD) and their variants such as Gas Source MBE, and Remote Plasma-enhanced CVD. Both techniques are carried out in an ultra high vacuum (UHV) environment and system base pressures are typically lower than $10^{-9}$ mBar. MBE is the most accurate epitaxial growth technique as it involves direct control of a beam flux by means of a mechanical shutter, enabling precise control of layer thickness, thus allowing monolayer control of the film. Metallo-organic CVD (MOCVD) involves a reduction reaction of the precursor molecules at the substrate resulting in the formation of neutral atom species that migrate on the surface to the most energetically favorable location to bond with the substrate atom. Typical

industrial production lines are based on CVD, especially for large wafers (8" and greater) [4] while MBE is more common in an R&D environment. It is to be noted, however, that GaN devices are commercially grown using MBE.

### ***1.4 Existing silicon: germanium photodetectors***

Over the years, several attempts have been made at realizing SiGe-based photodetectors. One of the earliest successful attempts [12] was a p-i-n waveguide photodetector with a 0.65μm thick strained superlattice (SLS) active region. The SLS consisted of 20 periods of 60 Å thick $Si_{0.6}Ge_{0.4}$ wells separated by 290 Å thick Si barriers and is designed for detection at 1.3 μm. The devices were found to have low dark current densities (71 $\mu Amm^{-2}$ at -10 V bias) which were found to decrease with a decrease in the well germanium composition. When butt coupled with a single mode fiber, the detector has an external quantum efficiency of 10.2% when biased at 10 V and 6% at 5 V. Devices with different well compositions were fabricated and the spectral response is shown in Figure 1-4.

Further improvements on the SLS-based design were made [13] by modifying the structure to incorporate an avalanche multiplication region. In addition, the composition of the SLS was optimized to maximize the absorption of the optical field while ensuring the constraints of disclocation-free growth were satisfied, yielding a 0.25-μm-thick SLS consisting of 33-Å-thick $Si_{0.6}Ge_{0.4}$ wells and 290-Å-thick Si barriers. A p-doped Si avalanche region is incorporated as shown in Figure 1-5. Waveguide detectors 250 μm in length and with large numerical apertures (~0.5)

were found to have an external sensitivity of 1.1 $AW^{-1}$ with a measured gain of 10.

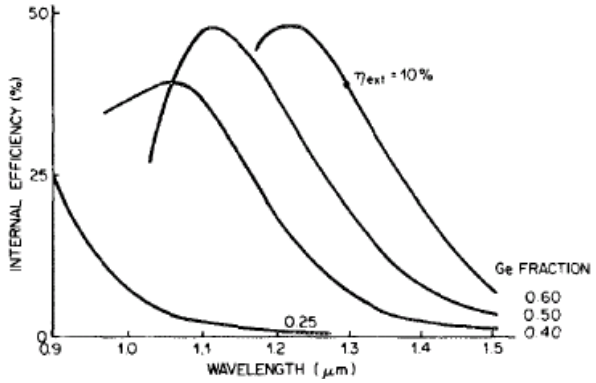


**Figure 1-4:** The internal quantum efficiency as a function of wavelength for different SiGe SLS waveguide photodetectors[12]

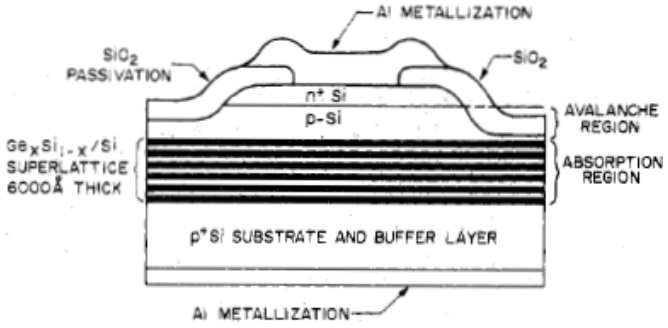


**Figure 1-5:** The cross-section of a SiGe SLS with an avalanche region incorporated [13]

Schuppert et al. [14] demonstrated a waveguide-MQW p-i-n detector with an active region consisting of 20 periods of 300 Å Si and 50 Å $Si_{0.55}Ge_{0.45}$. A 2 mm long detector when butt-coupled with a 1.3 μm laser had a measured external quantum efficiency of 11% which, when corrected for coupling inefficiencies, corresponds to an internal quantum efficiency of 40%. A 7 mm long device using a 2.2 μm thick MQW section was also fabricated and measured to have an internal quantum efficiency of 56%. Colace et al. [15] reported CVD-grown MSM Ge-on-Si

photodetectors with a measurable photoresponse beyond 1.55 μm with a responsivity of 0.24 $AW^{-1}$ at 1.32 μm when reverse biased to 1 V. This structure consists of a relaxed Ge-film on Si.

More recently, Geis et al. [16] reported on efficient near infrared photodetection in $Si^{2+}$ implanted silicon waveguides with responsivities up to 0.8 $AW^{-1}$ at 1.55 μm at a bias of -20 V. It is believed that oxygen-stabilized divacancies nucleated during the high energy implantation (which occurs at 190 keV) are involved in photodetection.

Another approach has been the growth of germanium in small regions of silicon wafers, a technique called selective-area-growth. This approach has yielded devices with responsivities similar to those of germanium detectors (~0.7 $AW^{-1}$ at 1.55 μm). [17]

Finally, Chaisakul et al. have reported on the use of strain-balanced germanium quantum wells grown on $Si_{0.1}Ge_{0.9}$ buffers with responsivities of ~ 0.05 $AW^{-1}$ in the NIR. [18] Both these devices, however, have large reverse leakage currents, which are known to be detrimental to detecting low signal levels.

## ***1.5 Thesis objectives and organization***

In this thesis, I shall present details on the design, growth, characterization and testing of silicon-germanium p-i-n photodectors. I shall demonstrate that it is possible to exploit the type-II band offsets of the silicon germanium material system to extend the bandedge of detection into the near infrared. Specifically, I shall:

1. Present the results on the performance of a conventional quantum-well based $Si_{1-x}Ge_x$ p-i-n photodetector grown on silicon for 1.3 μm detection
2. Present details on the design, growth and testing of a new photodetector heterostructure based on silicon-germanium heteroepitaxy grown on silicon for detection at 1.3 μm. This structure will be optimized and have a significant reduction in strain energy compared to the preliminary structure. The effect of each layer in the heterostructure on optical absorption will be presented
3. Present details on the design, growth and testing of silicon-germanium heteroepitaxy grown on silicon-germanium virtual substrates. This structure will be strain-balanced i.e. it will have zero net strain, thereby allowing for thick absorption regions and implementation of normal incidence photodiodes.

The devices detailed in this thesis are grown using solid-source molecular beam epitaxy. A discussion on the technique and the details on the MBE reactor used to grow these devices are presented in Chapter 2. Techniques used to analyze grown films are also presented.

Chapter 3 describes solutions to the specific challenges I faced with silicon MBE and the contributions made to the field. I will discuss the design, implementation and commissioning of an atomic absorption spectroscopy based controller for the silicon electron beam source. In addition, I will discuss the problem of crucible selection for boron doping applications in Si MBE. The development and analysis of a thermal deoxidation procedure for silicon-germanium surface in relation to that of pure silicon and germanium surfaces is also discussed.

In Chapter 4, I discuss the models used to describe the band structure of bulk and strained silicon germanium layers of arbitrary composition on an arbitrary silicon germanium substrate. All pertinent band parameters – bandgap, band alignment, band offsets and effective masses – are discussed. The critical thickness limitations mentioned in this chapter will be also be discussed. In addition, the mathematical techniques used to model the heterostructures is also presented.

Chapter 5 presents details on strained SiGe heterostructures for near infrared photodetection. Here, I discuss the design approach, epitaxial growth, post-growth characterization of the epitaxial layers, device design and fabrication techniques followed by experimental details on how these devices are tested and their performance is analyzed.

In Chapter 6, I present the motivation for strain-balanced silicon germanium heterostructures, and then present a similar progression to the realization and testing of these devices as detailed as in Chapter 5.

I conclude in Chapter 7, summarizing the contributions to the fields of MBE and silicon-germanium heterostructure design that I have made, and identify future avenues for exploration.

# Chapter 2 : Material Growth

## *2.1 Introduction*

The heterostructure devices detailed in this thesis were grown using solid-source molecular beam epitaxy (SSMBE). This technique enables the growth of a variety of crystals, including but not restricted to semiconductor homojunctions, heterojunctions, superconductors, rare earth oxides, magnetic materials and single crystal metal films for a number of applications. [19-24] In this chapter, a brief introduction to the technique is provided, along with the specific details about the MBE reactor used. Details will also be provided about the calibration of the system.

## *2.2 Theoretical description of MBE*

### 2.2.1 The physics of MBE

In simple terms, the physics of MBE can be understood with a combination of three processes that occur in an ultra-high vacuum (UHV) environment. First, clean atomic fluxes are generated by suitable evaporation cells. These fluxes are then incident on a clean substrate on which crystal growth is desired where a fraction is adsorbed. The ratio of the number of adsorbed species to the number of incident species is called the sticking coefficient α. In general, this sticking coefficient is temperature-dependent and typically decreases with an increase in substrate temperature. Now, if this substrate is held at a high enough temperature, the thermally-activated surface diffusion time of these adsorbed species (referred to as adatoms) is smaller than the arrival rate of atoms. This then enables the formation a

chemical bond that minimizes the free energy of the substrate – epitaxial film system. It is essential that the flux rate and hence, the growth rate be chosen such that this condition is met. For this reason, MBE is typically referred to be a kinetically-limited epitaxial technique in that the surface mobility of the adatoms fundamentally determines film crystallinity. This is in contrast with, for example, CVD reactors where the thermal activation of the chemical reaction of the precursor gases determines the film crystallinity. The typical growth rate is on the order of 1 atomic layer of coverage of a flat surface per second; also referred to as 1 monolayer (ML). These processes are shown schematically in Figure 2-1. When these three criteria are simultaneously met, a high quality crystal with a low defect density can be grown on the chosen substrate. Also shown are some competing processes that can occur such as desorption of the adsorbed species, incorporation of impurity atoms from the chamber, and desorption of the constituent atoms of the substrate.

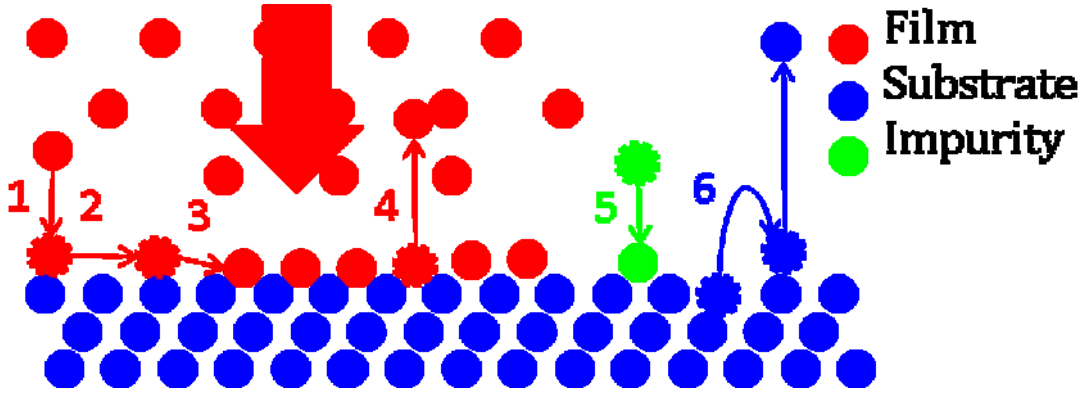


**Figure 2-1:** A schematic of some surface processes that occur during MBE. The atoms comprising the film (shown in red) are incident on the substrate (atoms shown in blue) and are adsorbed (process 1), migrate on the surface (process 2) and are incorporated into the crystal lattice, forming a bond (process 3). Also shown are competing processes of adatom desorption (4), impurity incorporation (5) and substrate decomposition (6). Intermediate states are shown in lighter colors with dotted borders.

For the simple case of atomic silicon and germanium beams incident on a substrate, the rate equations are given by

$$\frac{d\theta_{Si}}{dt} = F_{Si}\alpha_{Si} - \frac{\theta_{Si}}{\tau_{Si}}$$
$$\frac{d\theta_{Ge}}{dt} = F_{Ge}\alpha_{Ge} - \frac{\theta_{Ge}}{\tau_{Ge}}$$
$$\theta_{Ge} + \theta_{Si} = 1 \qquad \textbf{(2.1)}$$

Here the subscripts Si and Ge refer to the Si and Ge beams, θ is the fraction of the surface covered, F is the flux (in atoms/sec) of the species, α is the sticking coefficient and τ is the desorption time for that species. As mentioned earlier in this section, α and τ depend on the substrate temperature according to the Arrhenius equation. It should be noted that this simple model does not include the effect of other possible processes that can occur, some of which are listed below.

i. The incorporation of the background species in the vacuum chamber into the growing films is not explicitly included. If their concentration, sticking coefficients and desorption times are known, a similar equation can be written for their incorporation.

ii. The arrival of multi-atomic clusters which can adsorb, dissociate into individual atoms and which then desorb or are incorporated into the growing crystal

iii. During the growth of SiGe layer on Si substrates, the initial layers (< 1nm) are known to be Ge-rich due to segregation of germanium at the interface. [25] This effect is not included in the equations above, and can be minimized by maintaining substrate temperatures to 450 ºC or below during growth. The

reduced segregation is a consequence of the reduced rate of the thermally-activated segregation process.

iv. Chemical reactions involving the incident species occurring at the surface.

A detailed description of the growth kinetics is outside the purview of this thesis and can be found in [26, 27].

### 2.2.2 System requirements

As mentioned in the previous section, MBE requires a UHV environment. This is needed if crystal purity is to be maintained. This requirement can be understood by a study of the behavior of gases as a function of pressure. This allows the study of relationship between gas pressure P, molecular density n, and the monolayer formation time τ. Assuming a sticking coefficient of 1, these are given at temperature T for a gas molecule of mass M by

$$\begin{aligned} P &= nk_B T \\ \bar{c} &= \sqrt{\frac{3k_B T}{M}} \\ \tau &= \frac{4a}{n\bar{c}} \end{aligned} \qquad \textbf{(2.2)}$$

where $k_B$ is the Boltzmann constant, $\bar{c}$ is the rms velocity of the gas molecules, and a, the number of available sites per unit area for adsorption. Shown in Figure 2-2 is the gas density and monolayer formation time at different pressures for atomic oxygen at room temperature. From this figure, it is seen that at a background pressure of $10^{-11}$ mbar, the time taken to form one monolayer is $10^6$ s. This implies a possible

contamination level of 1 ppm if the sticking coefficient is unity with a film growth rate of 1 $MLs^{-1}$. This is typically impermissible for semiconductor applications, where foreign atoms that result in either shallow, dopant-like states or deep trap states are required to be below 1 ppb. Fortunately, most common residual gases in the UHV environment – $H_2$, $N_2$ – have sticking coefficients of much less than unity, allowing high purity crystals to be grown, even at background pressures of $10^{-10}$ mbar. Species such as $O_2$ and $H_2O$, both of which contribute elemental oxygen, have higher sticking coefficients. In the SiGe material system, oxygen is a deep level trap (0.41 eV above the valence band edge for Si [28]) and its partial pressure must be maintained at levels below $10^{-14}$ mbar for high performance applications.

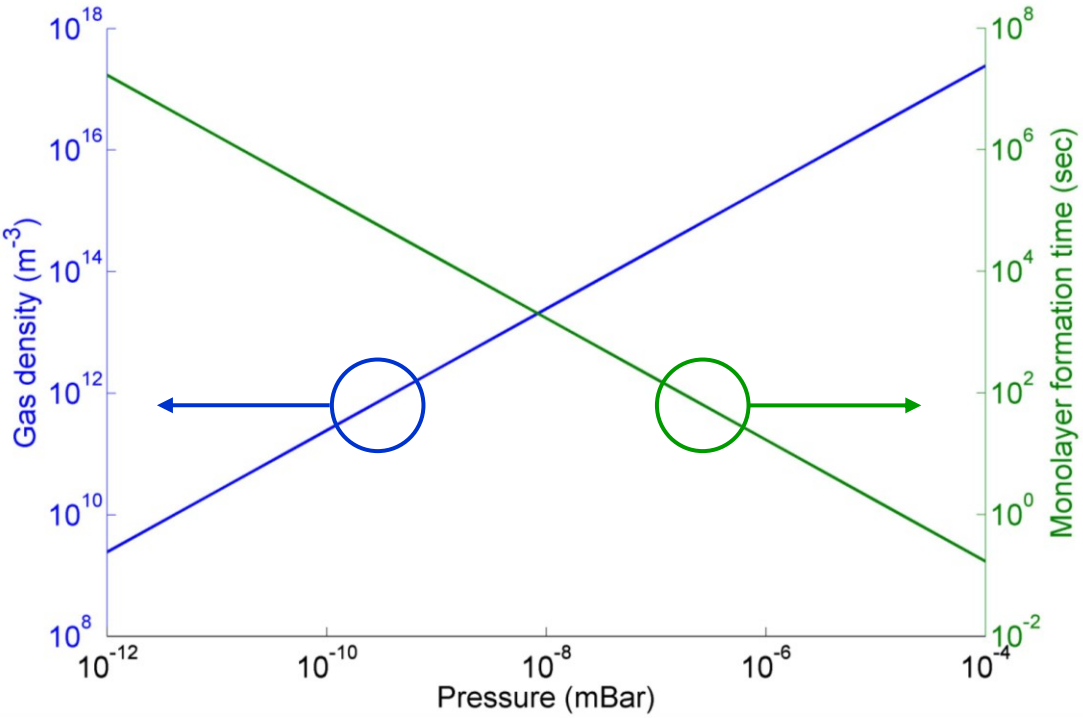


**Figure 2-2:** Gas density and monolayer formation time as a function of pressure at 300 K. For the purpose of this illustration, the gas was assumed to be oxygen and was assigned a sticking coefficient of 1.

This requirement of an UHV environment drives the specifications for all aspects of an MBE system, from materials for chamber construction to implementation of the source of the fluxes and choice of vacuum pumps. A historical overview of the evolution of MBE systems and detailed design concepts are presented in [26, 27]. The following section will discuss the design and operation of the MBE system that was used to grow the devices in this thesis.

## ***2.3 DepD – the MBE reactor at LPS***

### 2.3.1 Construction and vacuum pumping

The group-IV MBE system (designated as DepD) used is a modified EPI-930™ (now Veeco 930) research and development MBE system which accommodates one wafer up to 3 inches in diameter as a substrate for growth. The design is based on the EPI (Veeco) Gen-II system, a popular tool for epitaxial growth of III-V semiconductors. It consists of a growth chamber and a load-locked introduction chamber to enable the loading and unloading of wafers without necessitating venting of the growth chamber. This introduction chamber also allows for outgassing substrates prior to loading in the growth chamber. The growth chamber is equipped with nine ports for source cells, and each source port has a pneumatically operated shutter associated with it. This allows the user to select and control the composition of each grown layer. Perhaps the most significant modification is that the growth chamber was rotated about two axes such that one of the nine source ports is vertically oriented to allow for the use of an electron beam source for silicon. This

necessary to ensure that the silicon charge was horizontal at all times, as the molten silicon pool formed during normal operation cannot come in contact with other elements of the hearth due to contamination issues. This silicon source, which is housed in its own chamber called the mini chamber, will be described in the following section. Custom welded supports and a frame are used to ensure the stability of this arrangement. A photograph of this system is shown in Figure 2-3.

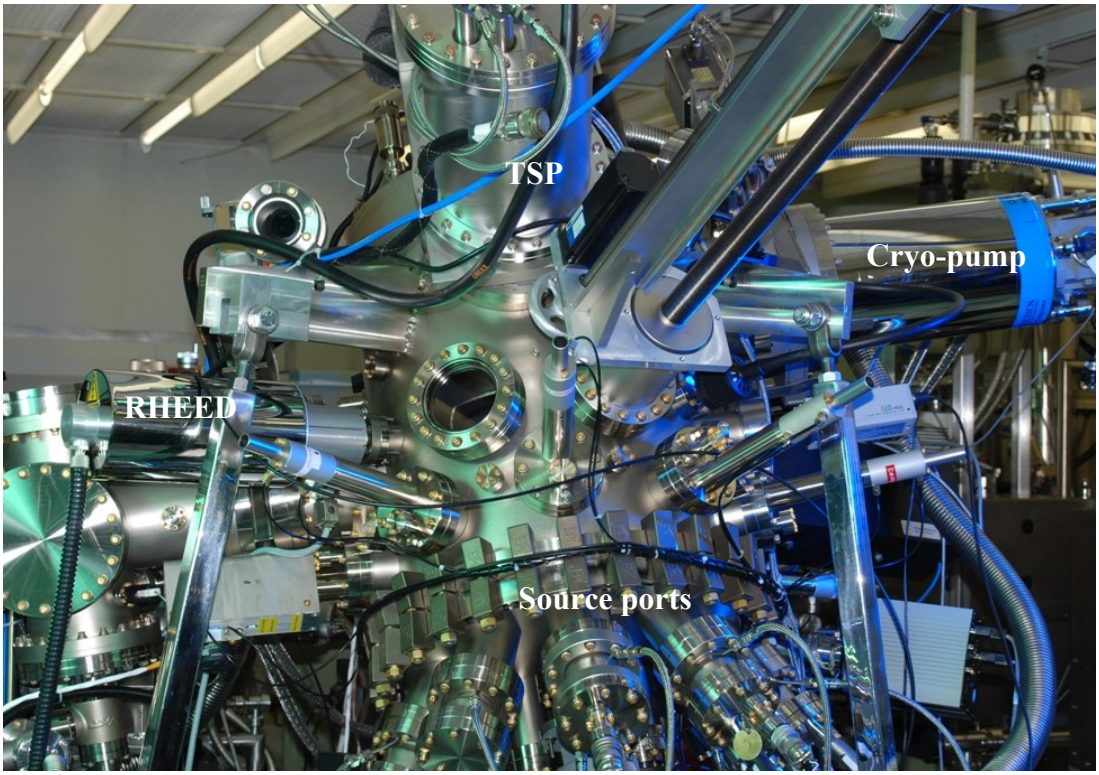


**Figure 2-3:** A photograph of the growth chamber of DepD. In this picture, the frame rotating the chamber can be seen, along with the crogenic pump, the titanium sublimation pump, the RHEED gun and five source ports. (Photo courtesy J. DiPasquale III)

The growth chamber is machined out of 316 grade low carbon stainless steel which facilitates high quality welds when required. Both, the growth and introduction

chambers (henceforth referred to as the intro chamber) are subsequently electropolished to reduce the vacuum surface area, which in turn results in a lower adsorption of gases and lower outgassing. A mechanical roughing pump and a turbomolecular pump are used to pump this system into high vacuum ($10^{-3}$-$10^{-6}$ mbar) before a combination of UHV pumps are used. For the intro chamber, an Oxford Instruments CTI-8 cryopump is used. This pump is highly effective for pumping and trapping water and air (nitrogen and oxygen), though it has a reduced capacity for hydrogen, it is capable of pumping the intro chamber to a pressure in the $10^{-9}$ mbar range. The growth chamber uses a combination of pumps. An identical CTI-8 is used as a primary pump, with a Perkin Elmer 400 $\ell s^{-1}$ triode pump. This ion pump is used as it is highly effective at pumping hydrogen. The silicon e-beam source has an additional Varian 60 $\ell s^{-1}$ ion pump. A titanium sublimation pump is also used to getter water and provides additional pumping for reactive gases such as oxygen and carbon monoxide. Finally, two liquid nitrogen cryopanels are present in the growth chamber with one welded onto the growth chamber, and the other, onto the source flange. This combination of pumps allows the growth chamber to be maintained at a pressure of $2x10^{-10}$ mbar in the idle state. With the help of a residual gas analyzer (RGA), the typical background concentrations of the residual gases are measured as listed in Table 2-1. Nude Bayard-Alpert ion gauges are installed in each, the growth chamber, the intro chamber and the mini chamber, enabling the monitoring of the system pressure.

| Species | Partial pressure ($\times 10^{-11}$ mBar) |
|---|---|
| $H_2$ | 14.8 |
| $H_2O$ | 0.88 |
| $N_2$ | 2.1 |
| $O_2$ | 0.78 |
| $CO_2$ | 1.4 |

**Table 2-1:** Typical background partial pressures of various contaminants in DepD

### 2.3. 2 Sources

DepD is a dedicated group-IV MBE system and has two germanium sources, one silicon source and one carbon source. The use of two germanium cells allows for the easy growth of double heterostructures. In addition, it also has boron and antimony as dopant sources. Each of these elements has different evaporation characteristics, and hence, each requires different cell designs. The choice of the cell used is driven by the vapor pressure of the element as a function of temperature. For these elements, this is shown in Figure 2-4.

Anitmony and germanium use standard thermal effusion cells. These cells comprise of a pyrolytic boron nitride (pBN) crucible filled with the high purity elemental charge that is radiatively heated by a tungsten filament. A carefully positioned thermocouple is used to monitor the temperature of the hot zone. This heater and crucible assembly are surrounded by tantalum heat shields to reduce the thermal load on the chamber. Since the vapor pressure of the evaporant is directly related to the evaporation rate (i.e. atomic flux), temperature control of these cells can be used as a means to control the individual fluxes. The upper temperature limit of

these cells is governed by the decomposition of the pBN crucible, which occurs at close to 1400ºC. [31] Above this temperature, incorporation of nitrogen and boron into the film can be expected and this lead to unintentional doping of the semiconductor. This is not a concern for the antimony cell, which is operated at temperatures below 500ºC, but is a concern for the germanium cells, which are used at temperatures up to 1400ºC.

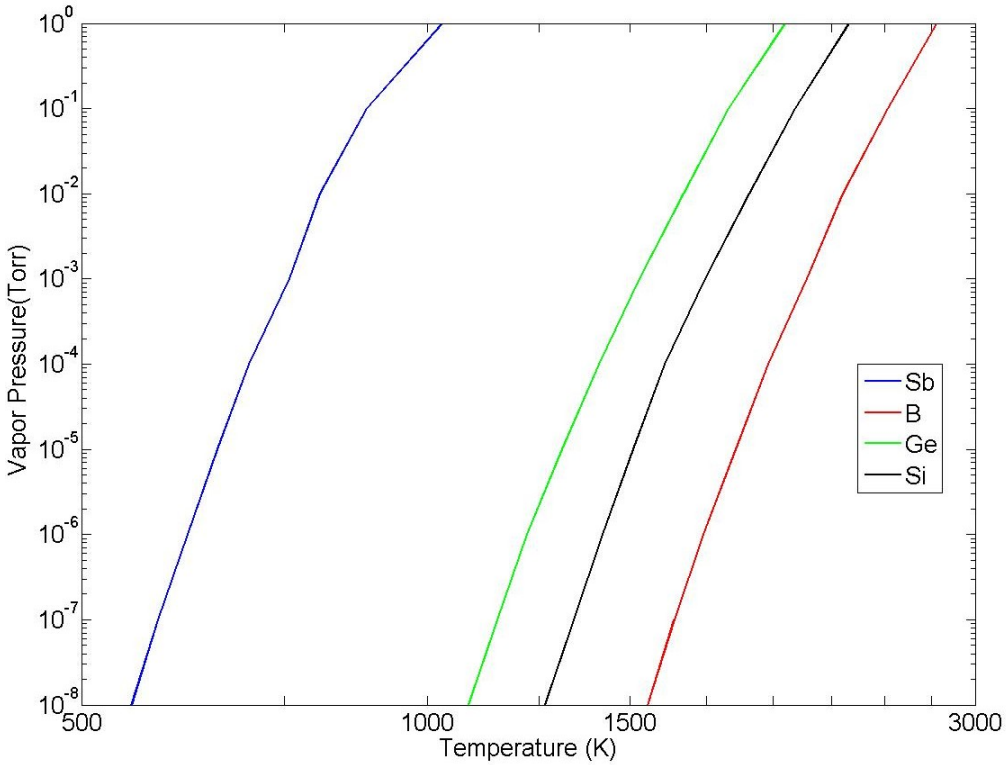


**Figure 2-4:** Vapor pressure as a function of temperature for the elements used in DepD (adapted from [29])

Boron has a much lower vapor pressure than both, antimony and germanium, and this requires a different cell design. This cell uses only refractory metals in the hot zone, allowing it to be used up to 2000ºC. As with the conventional effusion cell,

a thermocouple is used to monitor the temperature of the crucible, allowing for repeatable and reproducible use of this cell as a dopant cell. For the application of a boron dopant source, a tungsten crucible and a pyrolytic graphite crucible liner are used.

Conventional effusion cells cannot be used to evaporate silicon as a matrix element. As shown in Figure 2-4, silicon has a lower vapor pressure than germanium, and hence, a conventional effusion cell with a pBN crucible cannot be used if silicon is to be used as a matrix element. In addition, molten silicon is extremely reactive [26] and this precludes the use of a high temperature effusion cell similar to the one used for the evaporation of boron. This high reactivity necessitates that any molten silicon be self-contained i.e. the crucible for the silicon melt needs to be made of silicon. This can be implemented in an electron beam evaporator, where high energy electrons are focused on a silicon ingot source much larger than the spot size. Where incident, these electrons locally melt the silicon while the part of the source that is not exposed to an electron flux remains solid. This ingot is placed in a water-cooled copper hearth, which also houses the source of the electron beam. A drawing of the electron beam source is shown in Figure 2-5. To minimize direct heating by either the direct electron beam due to incorrect beam steering or the reflected electron beam, the exposed copper on the top face is covered with a silicon shield that is laser machined to provide maximum coverage. Controlling the electron beam source is a challenge and is discussed later.

The source material used in the cells is typically chosen to be of the highest purity available. In DepD, the boron used is 99.9999+% (6N+) pure, the antimony is

7N and the germanium, 6N. The silicon, machined out of a (111)-oriented float zone ingot of resistivity 10-20 kΩ-cm and carbon and oxygen levels $<10^{16}cm^{-3}$.

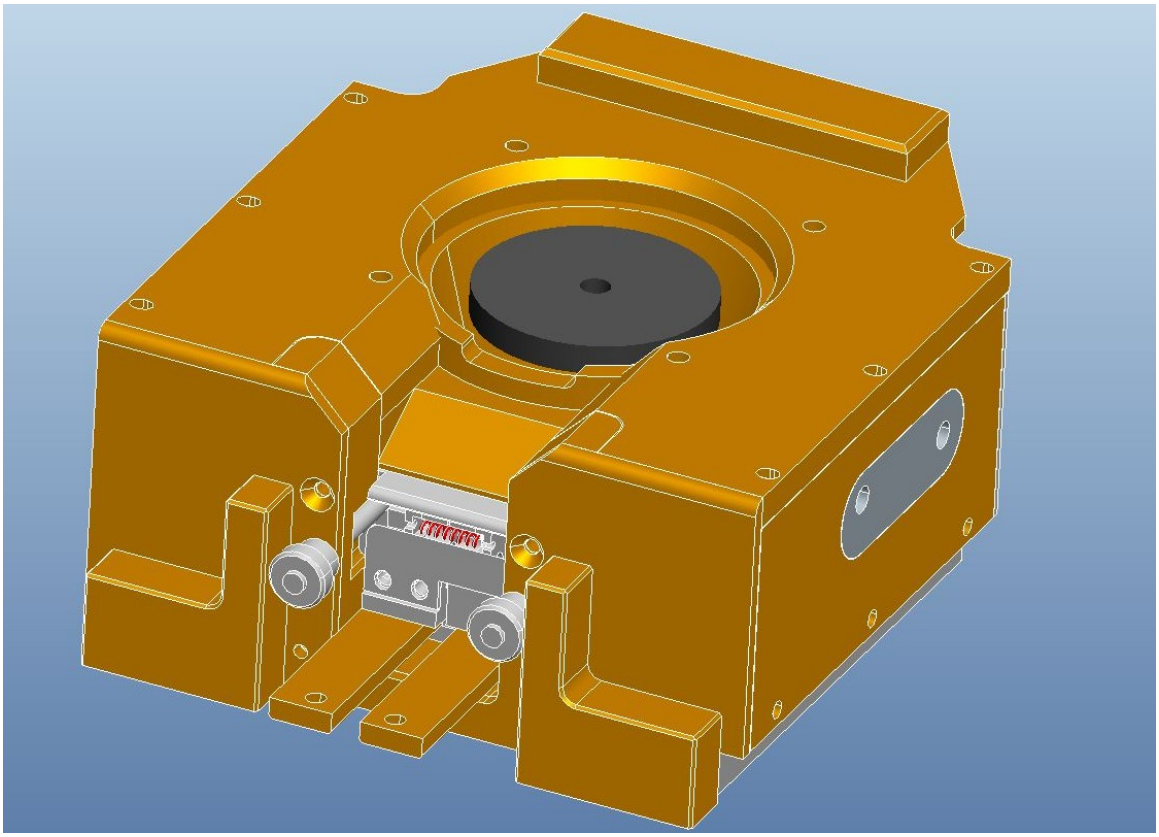

**Figure 2-5:** A rendered drawing of the electron beam hearth used as a silicon source in DepD. The silicon slug used is shown in black, and the electron beam source, including the protruding high voltage leads and the filament (in red) are also seen. The beam steering coils are mounted in two panels on the side of the source, one of which can be seen. (Image courtesy V. Yun)

### 2.3.3 Substrate assembly

As mentioned in the section 2.2.1, the process of epitaxial growth intimately depends on the temperature of the substrate. Ensuring temperature uniformity across the entire wafer is important, especially when the growing layers where the

constituent atoms have temperature-dependent sticking coefficients that vary differently from one another. By using a specially designed heater, the temperature across the substrate can be maintained to within ±5ºC [30]. To ensure uniform coverage of the substrate across the entire 3" wafer, it is rotated during growth, typically at 30 – 60 RPM.

Monitoring the temperature of the substrate is achieved in two ways. As with an effusion cell, a thermocouple is placed in the hot zone to monitor the temperature in the vicinity of the substrate. While this is used to as the primary process variable, this temperature is not necessarily an accurate representation of the actual substrate temperature. In such a radiatively heated system, where there is no conductive or convection heating, the actual temperature of the substrate depends on how effectively the emission spectrum of the heater at the chosen temperature overlaps with the absorption spectrum of the substrate. For example, highly doped substrates are more absorptive of thermal radiation, and for this reason, at a given temperature of the substrate heater, the true wafer temperature is higher than it would be for an undoped substrate. A true measure of the substrate temperature can be made through the technique of optical pyrometry. In this technique, the emission from the substrate $I(\lambda,T)$ in a particular spectral range (0.91μm-0.97μm in our case) is monitored and is compared to that of a black body $I'(\lambda,T)$.

$$\begin{aligned}\varepsilon_\lambda &= \frac{I(\lambda,T)}{I'(\lambda,T)} \\ &= 1 - R_\lambda - T_\lambda\end{aligned} \qquad \textbf{(2.3)}$$

where $R_\lambda$ and $T_\lambda$ are the reflection and tansmission of the substrate at the wavelength

λ, and the black body radiation I′(λ,T) is given by Planck's Law as

$$I'(\lambda,T)=\frac{2hc^2}{\lambda^5}\frac{1}{\exp\left(\frac{hc}{\lambda kT}\right)-1} \qquad \textbf{(2.4)}$$

If the emissivity $\varepsilon_\lambda$ is known, then the true substrate temperature can be calculated. A comparative measurement of the two, the pyrometer temperature at a given thermocouple temperature for an intrinsic and highly doped substrate, is shown in Figure 2-6.

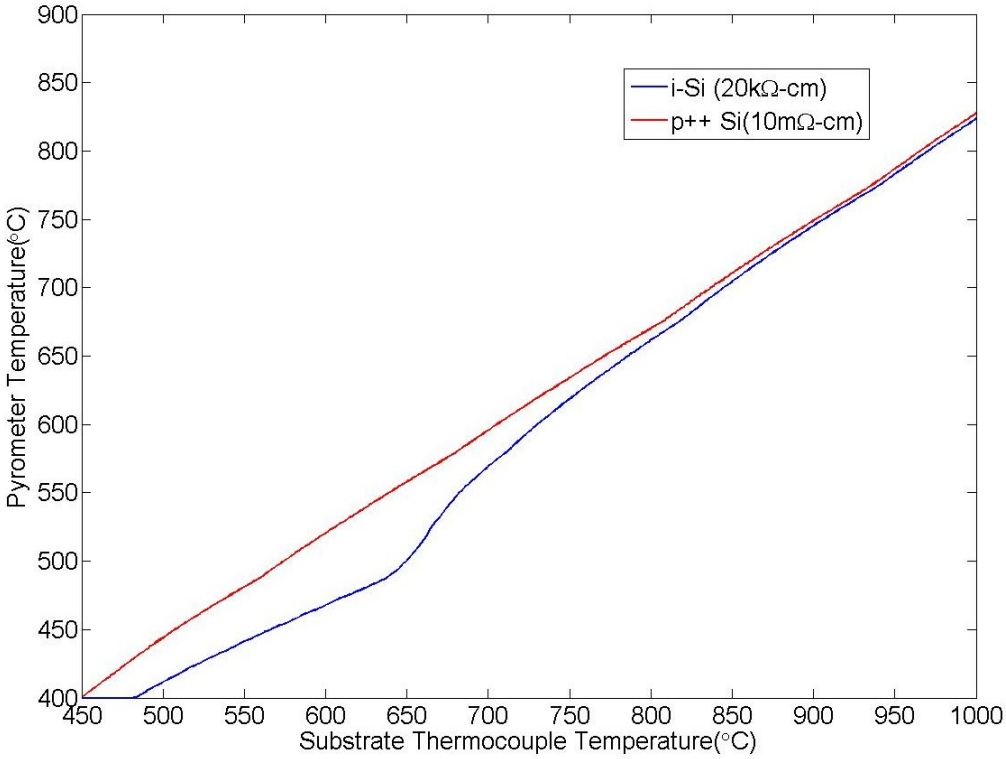


**Figure 2-6:** The difference between the temperature of the wafer as indicated by the substrate thermocouple and the true temperature measured by the pyrometer for an intrinsic and highly doped silicon wafers.

In addition, DepD has a retractable ion gauge that can be positioned to be

right below the substrate. This assembly is called the beam flux monitor (BFM), and allows the measurement of the pressure of an incident beam of atoms (called the beam equivalent pressure, or BEP for short) from a source cell on the substrate. This assembly assists in calibration of the system.

### 2.3.4 Analytical capabilities

The growth of an epitaxial layer is a process that intimately involves the surface of the growing layer. This surface typically consists of atoms that have unbonded electrons, and this often results in neighboring atoms forming a bond to reduce the free energy of the surface layer. This process is called surface reconstruction, and conveys information about the nature of the surface. One technique to study this surface is reflection high energy electron diffraction (RHEED). In this technique, a narrow, low divergence (spot size <100 μm, divergence <0.2 mrad) beam of high energy electrons (10-35 kV) is incident on the substrate at a glancing angle (0.5-2.5º). A schematic of the setup is shown in Figure 2-7. The penetration of the beam into the surface is low, and is restricted to the outermost atomic layers [31]. As a result, RHEED provides information about *only* the surface of the growing layer and not the bulk.

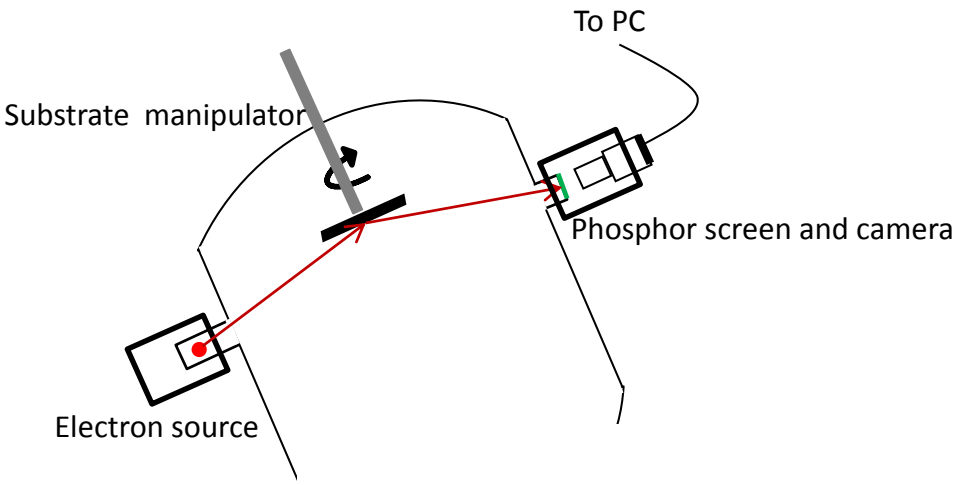


**Figure 2-7:** The geometry of a typical RHEED system, showing the relative position of the electron beam source, the rotating substrate and the phosphor screen.

The de Broglie wavelength of electrons accelerated through a potential V is given by

$$\lambda = \frac{h}{\sqrt{2m_o eV\left(1 + eV/m_o c^2\right)}} \tag{2.5}$$

This formula takes into account relativistic corrections for the high energy electrons, which is calculated to be 3.5% for a 35 keV electron. For a typical RHEED operating voltage of 30 kV, this wavelength is 0.069 Å. The RHEED pattern can be derived from first principles and is discussed briefly below.

Consider a bare (001)-oriented silicon surface. This surface consists of a

periodic lattice with one atom at each lattice point. The basis vectors for this lattice are

$$\overline{a_1} = \frac{a_s}{2}(110)$$
$$\overline{a_2} = \frac{a_s}{2}(\bar{1}10) \quad \textbf{(2.6)}$$

where $a_s$ is the lattice parameter for the substrate. In reciprocal space, the corresponding basis vectors are obtained from the relation $\overline{a_i^*} = 2\pi \overline{a_j} \times \hat{n} / (\overline{a_i} \cdot \overline{a_j} \times \hat{n})$, where $\hat{n}$ is (001), the unit vector corresponding to the surface normal

$$\overline{a_1^*} = \frac{2\pi}{a_s}(110)$$
$$\overline{a_2^*} = \frac{2\pi}{a_s}(\bar{1}10) \quad \textbf{(2.7)}$$

These basis vectors span the reciprocal lattice in the plane of the film according to

$$\overline{G} = n_1 \overline{a_1^*} + n_2 \overline{a_2^*} \quad \textbf{(2.8)}$$

where $n_1$ and $n_2$ are integers. In the direction perpendicular $\hat{n}$ to the surface, the reciprocal space consists of rods originating at these lattice points. This is because the chosen basis vectors for the surface have no explicit periodicity information in this direction. This is a direct consequence of the limited penetration of the electron beam into the bulk, as mentioned earlier in this section. As a result, the reciprocal space also has no periodicity in this direction. Thus, Equation 2.8 gives rise to reciprocal lattice rods in the direction of the surface normal. This reciprocal lattice net is shown in Figure 2-8, along with the incident and scattered electron wave vectors.

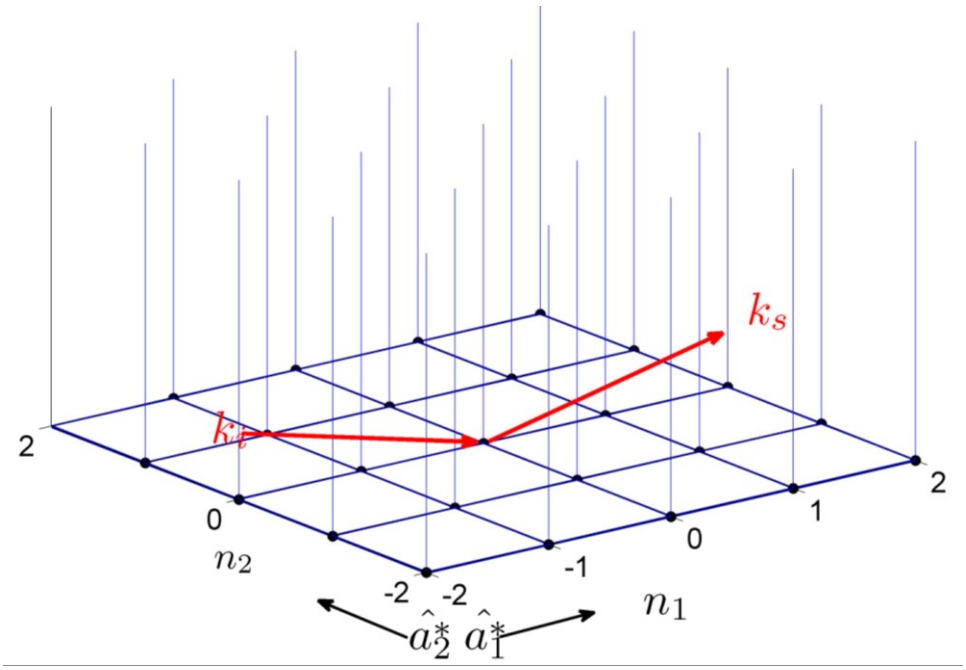


**Figure 2-8:** The reciprocal lattice net for the surface of the crystal showing the lattice points in the plane of the surface, the rods perpendicular to this surface, and the incident and scattered electron beams at the 00 point.

The high-energy electrons with wave vector $\overline{k_i} = \frac{2\pi}{\lambda}\hat{k}_i$ are incident on this reciprocal lattice net, and elastically scatter with final wave vector $\overline{k_s}$ of same magnitude $k_i$ but in a different direction as shown in Figure 2-8. Using the Laue condition for diffraction, we have a diffraction maximum when

$$\overline{k_i} - \overline{k_s} = \overline{G} \tag{2.9}$$

In three dimensions, this equation gives the locus of points on a sphere of radius $k_i$ ($=k_s=2\pi/\lambda$) that intersect the reciprocal lattice net. This sphere, called the Ewald sphere, can be sketched as a means to identify these diffraction maxima. A two-

dimensional elevation view is shown in Figure 2-9 for an incident electron beam along the $\hat{a}_1^*$ direction.

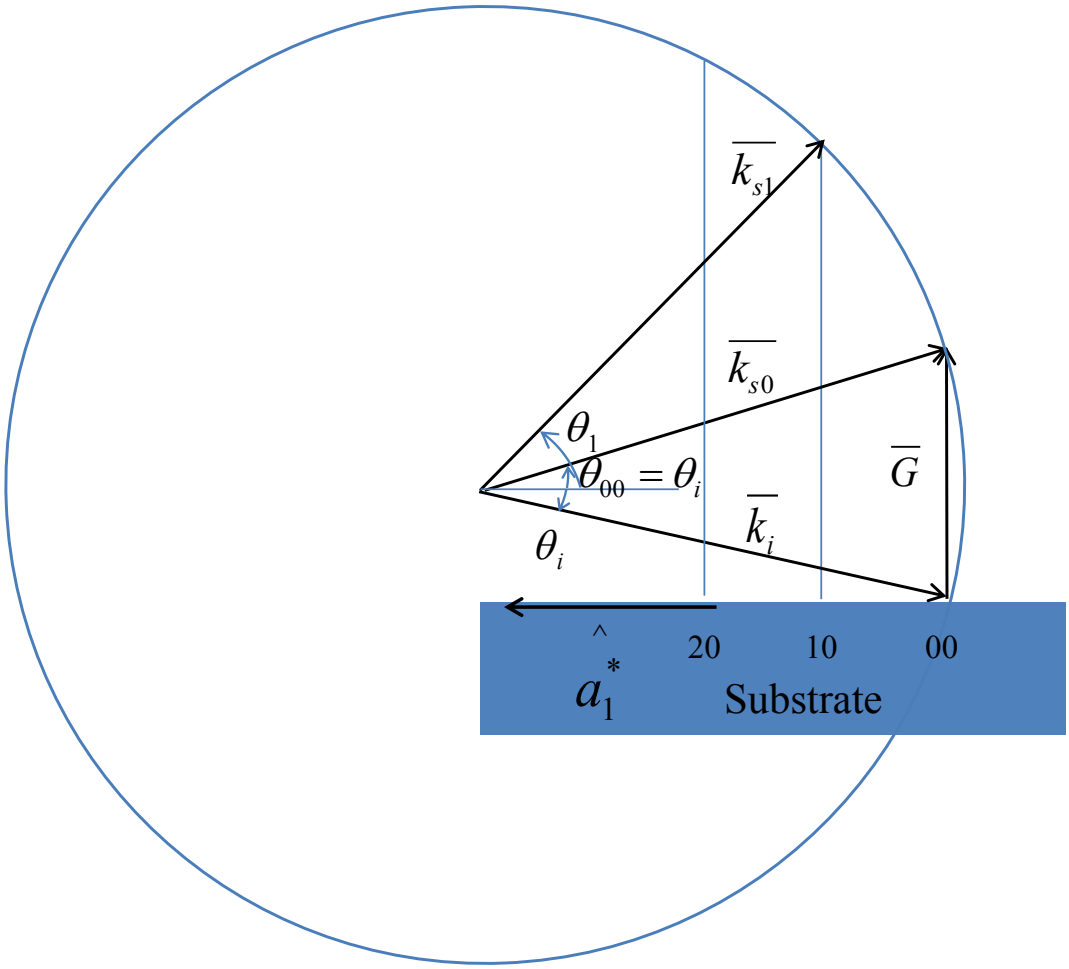


**Figure 2-9:** A section of the Ewald sphere (not to scale) for RHEED showing the Laue condition and the relative orientation of the substrate and the incident electron beam. The labels 00, 10 etc. correspond to $n_1$ and $n_2$ in Equation 2.8.

This construction gives us the spacing in real space between the diffraction orders corresponding to the 00, 10, 20… n0 etc orders as

$$k_i \cos\theta_i = k_s \cos\theta_n + n a_1^* \qquad \textbf{(2.10)}$$

or

$$\cos\theta_n = \cos\theta_n - \frac{na_1^*}{k_i} = \cos\theta_i - \frac{n\sqrt{2}\lambda}{a_s} \tag{2.11}$$

These n correspond to the n Laue zones. It should be noted that while the electron beam is not incident on the origin of reciprocal space as shown, it can be translated in to the 00 point without loss of generality.

This equation gives the locations of the n0 diffraction maxima. To calculate the spacing in the orthogonal direction, we look at the plan view of the Ewald sphere shown in Figure 2-9.

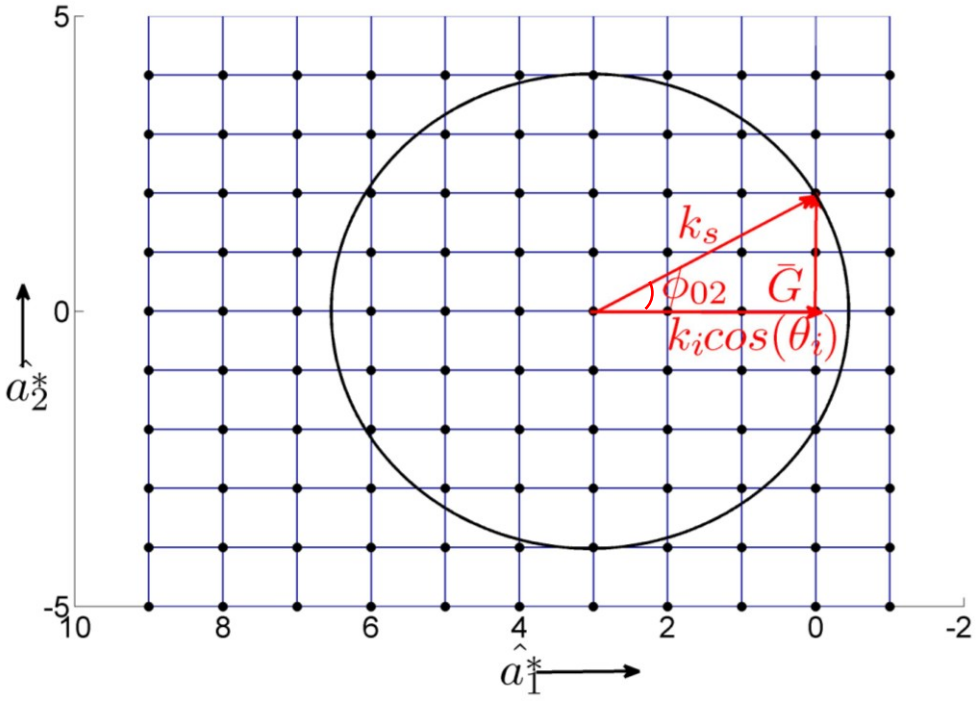


**Figure 2-10:** A plan view of the section of the Ewald sphere showing an electron beam incident on the 00 point and scattering to the 02 point in reciprocal space

The figure shows an electron beam incident at an angle θi on a substrate and

scattering to the 02 point in reciprocal space. We can write, for general n,

$$\tan\phi_{0n}\left(\approx \phi_{0n}\right) = \frac{na_2^*}{k_i \cos\theta_i} \tag{2.12}$$

For typical values of $a_s$ and λ, we have $a_2^*$=1.63 Å$^{-1}$ and $k_i$ =91.1 Å$^{-1}$ and the approximation tan(ϕ)≈ ϕ holds. If the distance L from the substrate to the RHEED screen is known, this relation gives the spacing of the spots in a particular Laue zone:

$$t = \frac{La_a^*}{k_i \cos\theta_i} \tag{2.13}$$

This general framework has been extended to reconstructed surfaces and for electron beams incident along any arbitrary direction. A MatLab script to calculate the same is in Appendix A. The calculated position of spots in the diffraction pattern for a 30 keV electron beam incident at 2.5º to the horizontal along the (110) direction of (1×1) reconstructed silicon surface is shown in Figure 2-11. The distance from the substrate to the screen used is the specified value for DepD, 10.3". The actual pattern will be different as the intensity of each spot, which hasn't been calculated, requires full dynamical calculations

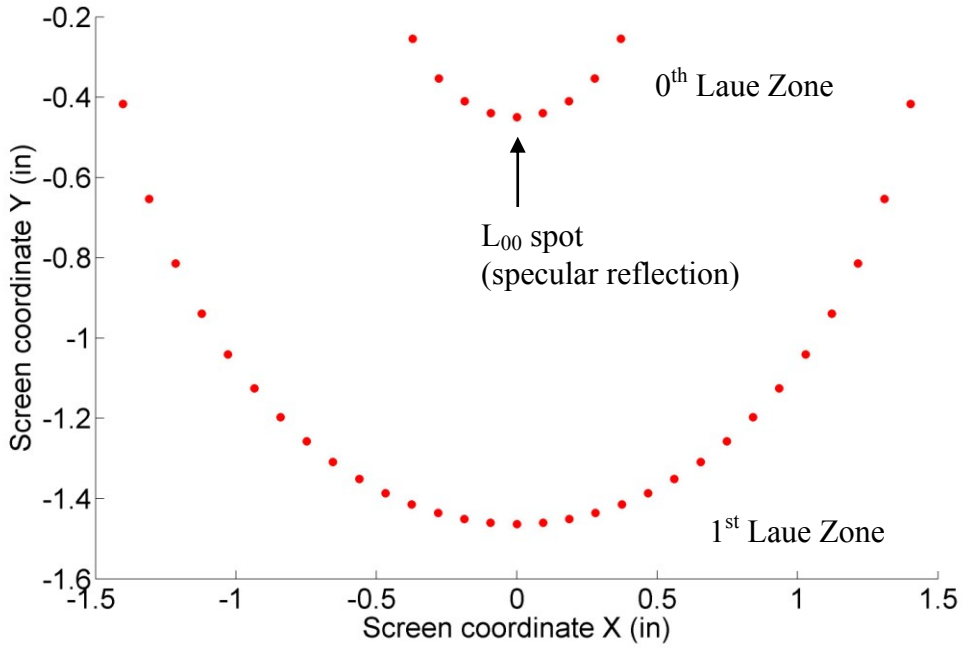


**Figure 2-11:** The expected position of diffraction maxima from a (1×1) reconstructed (001) silicon surface with the electron beam incident along the (110) direction.

## *2.4 System calibration*

### 2.4.1 Source cells

To be able to grow a film of arbitrary composition and thickness, the constituent cells need to be calibrated. The typical calibration procedure for MBE typically involves two steps. The first step is the measurement of the BEP of the cells as a function of temperature using the BFM. The BEP is fit to temperature in K as

$$\log(BEP) = \frac{m}{T} + C \qquad \textbf{(2.14)}$$

To relate the BEP to growth rate (J) of two different cells loaded with a source with atomic mass M and atomic number Z operating at different temperatures T, one can use the relation [26]

$$\frac{J_A}{J_B} = \frac{BEP_A}{BEP_B}\frac{\eta_B}{\eta_A}\sqrt{\frac{T_A M_B}{T_B M_A}}$$
$$\eta = 0.4 + \frac{0.6Z}{14} \qquad \textbf{(2.15)}$$

Here, η is called the atomic efficiency and is a calibration factor for the ion gauge. Thus, it is seen that for the same cell operated at two different temperatures, the ratio of the growth rates is

$$\frac{J_1}{J_2} = \frac{BEP_1}{BEP_2}\sqrt{\frac{T_1}{T_2}} \qquad \textbf{(2.16)}$$

In principle, it is possible to calculate the incident atomic flux from the pressure readout of this gauge, though this is difficult in practice as the reading of the BEP ion gauge depends on a combination of geometric factors and the calibration of the ion gauge controller. The geometric factors in play here are the surface areas of the molten charge, which is different in different cell ports, the relative orientation of the source port with the BEP gauge, and the portion of atomic flux that is directly sampled by the BEP gauge. In addition, ion gauge controllers cannot be used with electron beam sources because the atomic flux from these sources contains ionized species which interfere with the measurement mechanism of the ion gauge.

The second step in source cell calibration is correlating a particular BEP with a growth rate. This is done in one of two ways. First, individual cells can be calibrated using the technique of RHEED oscillations. This involves observation of the intensity of diffraction peaks during crystal growth. The initial surface on which the epilayer is grown is typically smooth, and this results in strong diffraction. As the substrate is exposed to the atomic flux, the surface is roughened on the atomic scale

as the coverage of the surface increases to ½ ML. This results in a reduction of the strength of the diffraction peak from the maximum. As the surface coverage increases, it grows smoother and results in stronger diffraction up until the coverage increases to 1 monolayer. At this point, the cycle is repeated, resulting in a variation of the intensity of the chosen diffraction order that has a period of the time required to grow 1 monolayer of the epilayer. This is entire process is shown schematically in Figure 2-12.

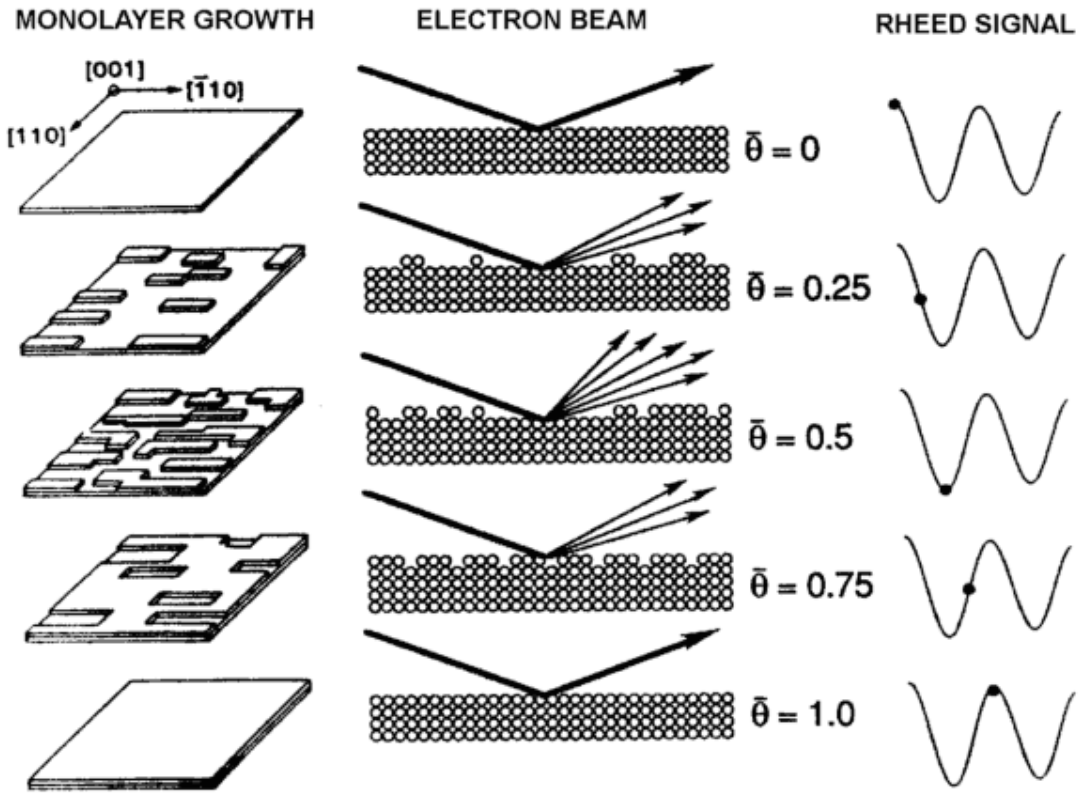


**Figure 2-12:** The evolution of the surface of a crystal with growth, and its effect on the intensity of a particular RHEED maximum [32].

This technique of calibrating cells is both, quick and easy. In particular, the

growth rate at different BEPs can be determined in the same run, reducing the amount of time needed to calibrate the cell. However, inaccuracies in determining true peak and valley positions results in errors in calibration. In addition, analysis of the growth of compound semiconductors is not easy as the relative growth rates, and hence, the composition of the grown layer, cannot be determined unless the growth rate of one of the elements in the matrix is known. Other pertinent crystal information such as layer relaxation cannot be obtained easily. Such information can be obtained by X-ray diffraction analysis. This technique probes the spacing of the crystal planes in a material. These experiments are conducted ex-situ in a commercially available x-ray diffractometer. The geometry of the system is shown in Figure 2-13.

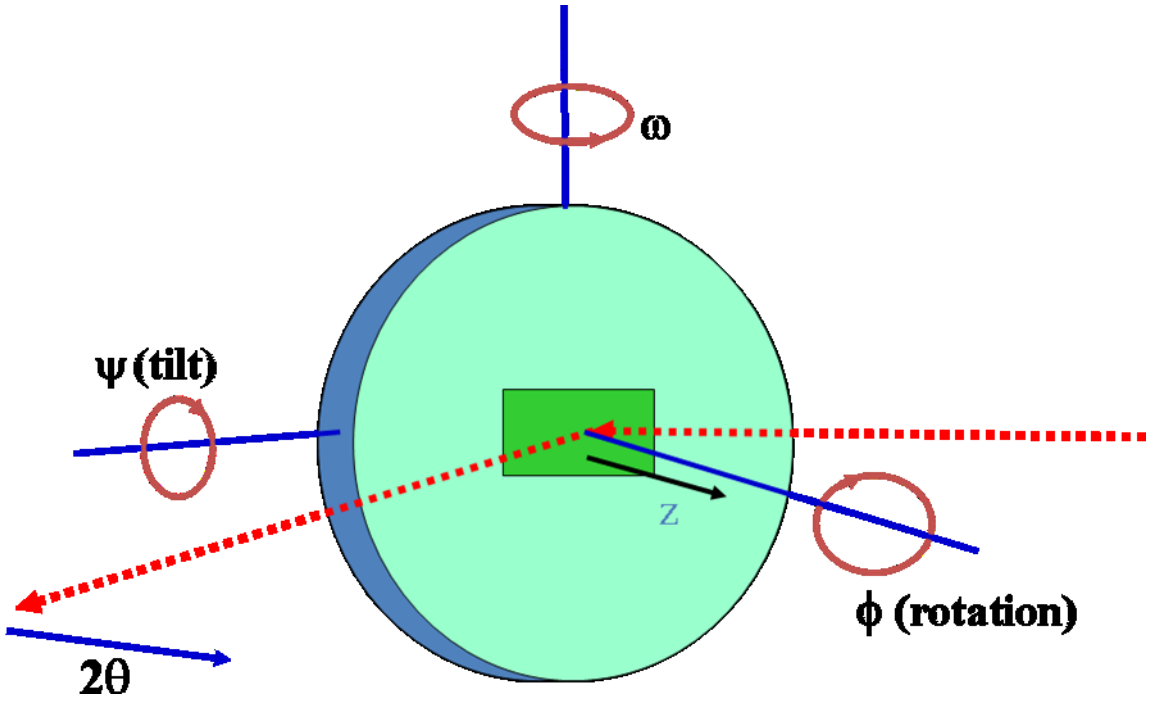


**Figure 2-13:** Geometry and angles in a standard high resolution x-ray diffractometer.

The scattering of the X-rays off the crystal is shown in Figure 2-14. Of two scenarios the symmetric scan (ω=2θ) is shown. Diffraction maxima in both cases can be expected at angles that satisfy the Bragg condition

$$2d\sin\theta = n\lambda \qquad \textbf{(2.17)}$$

In this case of a symmetric scan with $\theta_i = \theta_d$, the lattice parameter being probed is the spacing between the planes in the direction of epitaxial growth. This does not allow a direct measurement of the lattice spacing in the plane of growth, and hence, layer relaxation cannot be measured. By probing the sample asymmetrically, the in-plane lattice constant and the layer relaxation can be determined.

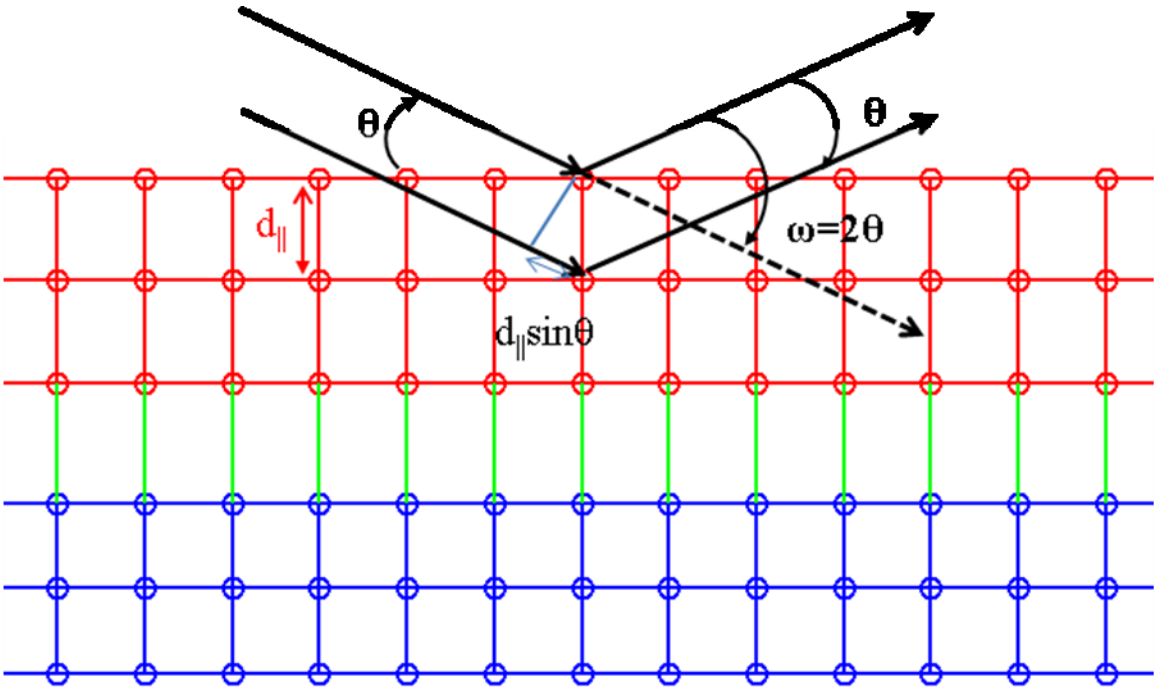


**Figure 2-14:** The Bragg condition for X-ray diffraction, showing the path difference between the two beams.

The collected data is studied using the accompanying software which implements a dynamical model for x-ray diffraction to fit both, the peak positions and peak heights. As with RHEED, the peak positions are easily identified by a repeated application of the Laue condition. A complete description of the technique is beyond the scope of this thesis and the reader is referred to [35] for a thorough discussion. By growing a typical short period superlattice and analyzing the so-called $\omega$-$2\theta$ scan, the absolute growth rate of a particular cell at a particular temperature can be calculated.

### 2.4.2 Dopant cells

Calibration of dopant cells differs significantly from that of matrix source cells. This is because the standard technique of measuring the BEP cannot be applied as the fluxes involved are very low. For example, in a semiconductor doped to $10^{17}$ $cm^{-3}$, this corresponds to a dopant to source flux ratio of approximately $10^{-6}$, which in turn corresponds to a BEP of $\sim 10^{-12}$ mbar. This is below the measurement range of ion gauges ($10^{-11}$ mbar). A BEP measurement would not convey information about electrical activation of the dopant species in the semiconductor. Finally, unlike boron, the sticking coefficient of antimony on silicon depends strongly on substrate temperature [34], necessitating a direct electrical characterization of the grown film instead of solely measuring the BEP. To that end, the dopant cells in DepD are calibrated using a standard Lakeshore 7504 Hall measurement setup. First, doped Si films are grown on intrinsic (100) Si substrates at a fixed growth rate $R_{Si}$, with the dopant cell maintained at a constant temperature. From the vapor pressure chart of

Figure 2-4, the dopant density at a particular temperature can be estimated to within an order of magnitude, assisting the estimation of the cell temperature. In this thesis, all n-doped films are grown at a substrate temperature of 450ºC, p-Si films are grown at 550ºC, and p-SiGe films are grown at 450ºC. Once this sample is grown, pieces 4mm x 4mm are cleaved and mounted in a van der Pauw geometry as shown in Figure 2-15.

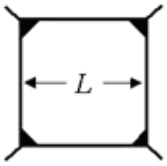


**Figure 2-15:** Van der Pauw geometry used to make electrical contact to the Hall samples. Typically, L=4 mm and for accuracy, $L/t > 15$ , where t is the thickness of the doped layer

The sample is then probed electrically while being placed in a constant magnetic field that is normal to its surface. By measuring the resistances across different pairs of contacts as a function of applied magnetic field (typically 1-5 Tesla) at a constant drive current, the Hall coefficient $R_H$ and magnetoresitivity $\rho_{av}$ can measured. This can be converted to a carrier mobility $\mu_H$ using

$$\mu_H = \frac{|R_H|}{\rho_{av}} \tag{2.18}$$

Using the mobility and the resistivity, the carrier concentration N can be extracted as

$$N = \frac{\rho_{av}}{\mu_H e t} \tag{2.19}$$

This measurement technique is accurate to within ±10% provided the film thickness t

is significantly larger than the depletion layer thickness for the structure grown. The extent of the depletion region into the doped layer is given by

$$W_d = \frac{n_i}{n_i + N}\sqrt{\frac{2\varepsilon_{Si}}{eN}\frac{kT}{e}\ln\left(\frac{N}{n_i}\right)} \tag{2.20}$$

This depletion region width is typically very small and is calculated to be 6pm for a carrier concentration of $10^{15}$ $cm^{-3}$. As a result, this effect can typically be ignored. However, this can be a concern while growing films with higher intrinsic carrier concentrations, such as germanium.

By growing doped films at three different cell temperatures T (in units of K), the dopant density at any cell temperature at this growth rate is given by the fit

$$\log(N) = \frac{m}{T} + c \tag{2.21}$$

If a growth necessitates a different growth rate $R_2$, the required temperature $T_2$ to achieve a dopant density N can be determined by solving

$$\log\left(\frac{R_2 N}{R_{Si}}\right) = \frac{m}{T_2} + c \tag{2.22}$$

### 2.4.3 Pyrometer calibration

Of the elements used in DepD, only the sticking coefficient of antimony is a strong function of temperature. As a result , an accurate substrate temperature monitor is essential to be able to grow n-doped films in a repeatable and reproducible manner. [34] In this thesis, the pyrometer was calibrated using the eutectic point off aluminum in silicon. It is widely known that aluminum dissolves in silicon at precisely 577ºC.

[35] This is seen clearly in the binary alloy phase diagram of the Al-Si material system, shown in Figure 2-16. At this temperature, the aluminum dissolves into the silicon, causing the smooth, highly reflective aluminum to turn rough and textured.

The procedure is as follows. [36] First, a silicon wafer is cleaned in hydrofluoric acid and loaded into a metal evaporator with a metal shadow mask. Next, 3000 Å of aluminum is evaporated. Upon unloading from the evaporator, it is immediately loaded in the intro chamber of DepD and after a standard overnight bake at 150ºC, it is transferred into the growth chamber. Next, the substrate heated at a slow ramp rate of 1ºC/min. The substrate through one of the quartz viewports, and when the aluminum spots begin to turn rough, the ramp is stopped and the emissivity is adjusted so that the pyrometer reads 577 ºC with a typical value of 0.48.

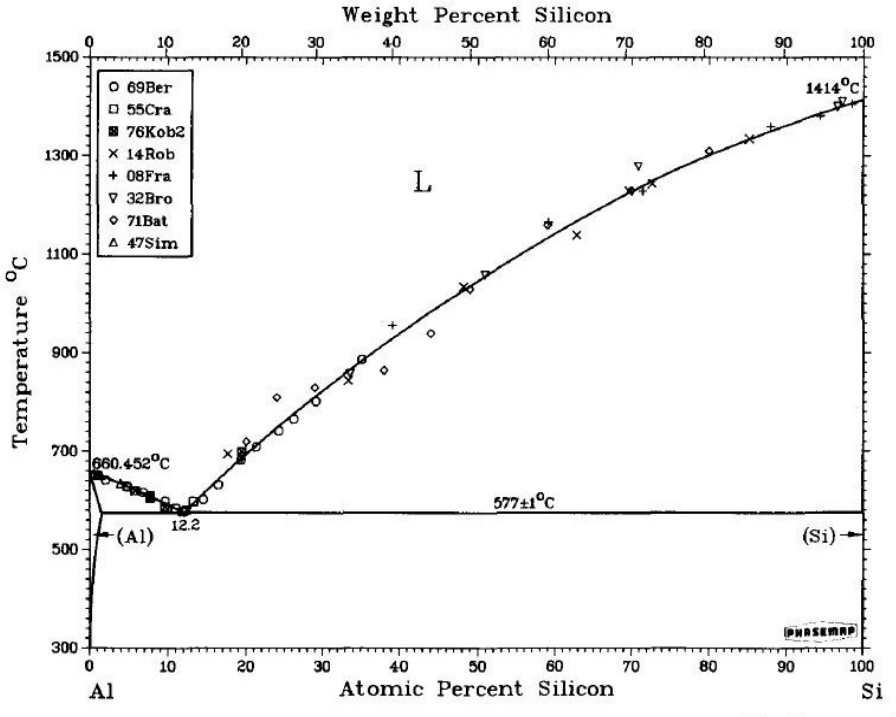


**Figure 2-16:** The binary alloy phase diagram for aluminum and silicon, showing the eutectic point at 577 ºC [37]

# Chapter 3 : Improvements to Silicon MBE

## *3. 1 Introduction*

The biggest difficulty faced was the realization of an accurate rate controller for the silicon electron beam. Solving this problem necessitated the design, assembly and calibration of an atomic absorption spectroscopy-based rate controller. This is detailed in Section 3.2. The other challenges faced were identifying a suitable crucible and liner for the high-temperature boron cell (Section 3.3) and identifying the optimal substrate cleaning and thermal treatment for growth on silicon and silicon-germanium virtual substrates (Section 3.4)

## *3.2 Rate control of the silicon electron beam source*

### 3.2.1 Challenges and preliminary solutions

As mentioned in the previous chapter, the use of solid source MBE as a growth technique for silicon necessitates the use of an electron beam source for silicon. This presents its own unique challenges. First, the conventional method of calibrating a cell by measuring its BEP cannot be used. This is because the silicon flux from the e-beam source contains charged particles that interfere with the operation of the ion gauge. This is shown in Figure 3-1 where the BEP is measured with the cell shutter opened and closed. Also shown for comparison is the same measurement but with a germanium cell. For the silicon cell, the decrease in BEP with the shutter open suggests that the increased number of positively charged silicon atoms is neutralized by the electrons emitted from the ion gauge. This precludes the

use of the BEP gauge to calibrate the cell at a particular emission current. In addition, there is no direct measure of cell temperature, further hampering the ability to control the flux.

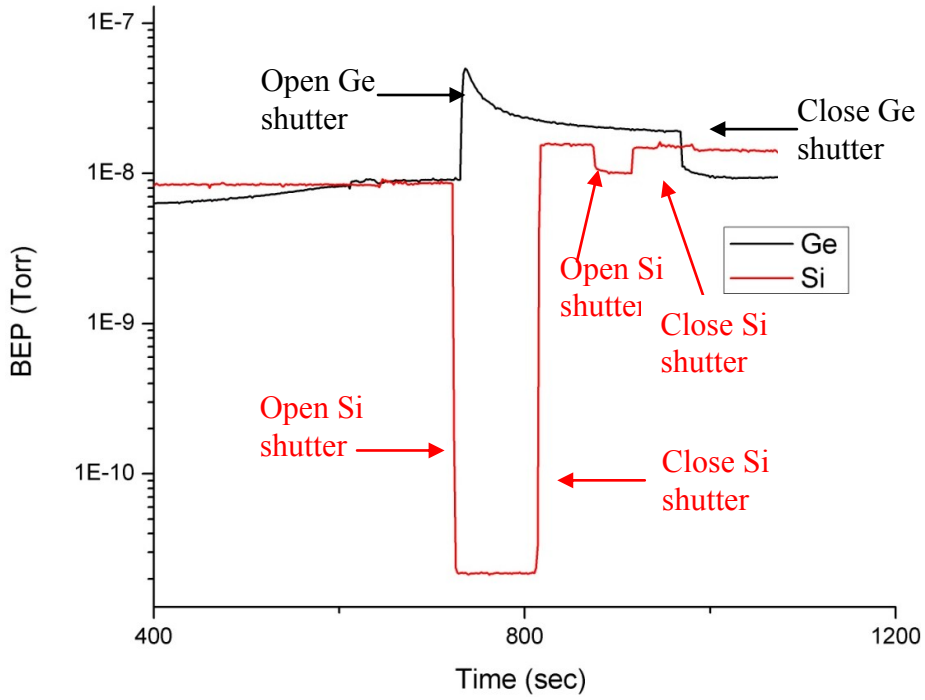


**Figure 3-1:** The BEPs (collected separately) of the silicon cell at an electron beam emission current of 75 mA and for a germanium cell at 1300ºC. In each case, the shutter was opened at approximately 750 seconds. On exposure to the charged silicon flux, the pressure read by the BEP gauge is artificially low. The Ge cell does not demonstrate this problem, and a BEP measurement can be made.

Another problem with calibrating the growth rate against emission current is that this is variable. The origin of this variation is two-fold. First, from geometric conditions, the flux that passes through the aperture on the cooling roof and the water cooled jacket on the source flange depends on the location of the melt with respect to

these apertures. This is understood by studying the cutaway diagram in Figure 3-2. Moving the melt across the entire source is necessary to maximize the usage of available material.

Second, as the source is consumed, the thickness of the ingot charge is reduced. This reduces the thermal resistance of the charge, which in turn reduces the source temperature at the same emission current. This causes the cell to drift out of calibration. The solution to these problems is to directly measure the silicon flux while the epitaxial layers are being grown. One way this can be achieved is by using a quartz crystal monitor (QCM). The silicon e-beam source used is outfitted with a QCM and its location with respect to the source and filament is shown in Figure 3-3.

While this approach was found to be usable, it did not allow for a stable measurement. This is again from geometrical concerns. As seen in the figure, the QCM does not sample the flux that is directed towards the substrate, but a portion of it. This results in the same problem as before – drifting calibration with consumption of the source material. While it is possible to correct for this by recalibrating the QCM during the growth, this is not an attractive option. In addition, the QCM presents two significant challenges. One, the crystal is observed to fail frequently, approximately once every five epitaxial growths. This necessitates a full system shutdown and venting the chamber to atmosphere. This is highly undesirable from an operation standpoint as it involves a two-week downtime.

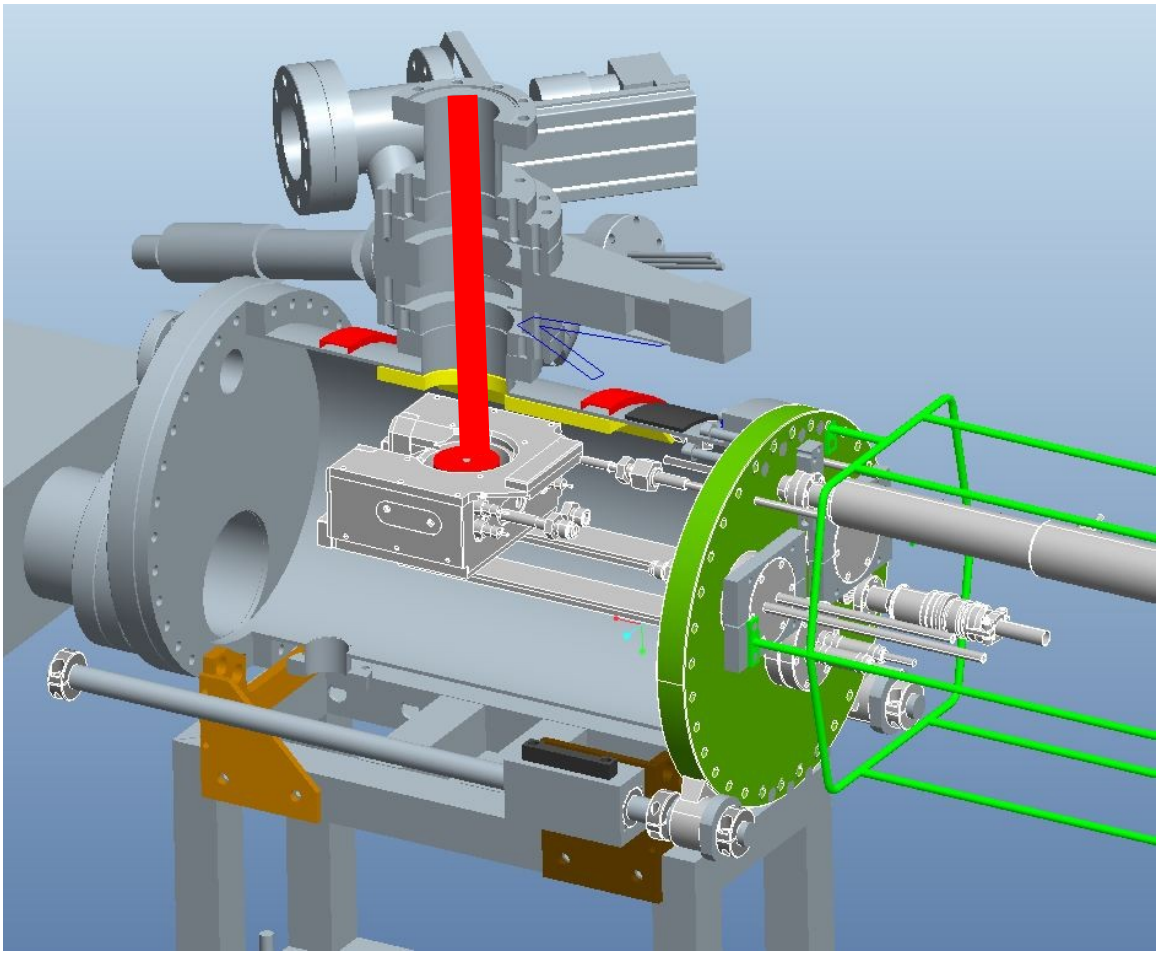

**Figure 3-2 :** A cutaway view of the silicon source, highlighting the apertures of the cooling roof (in yellow) and the multiple flange adapters and the gate valve. Any drift in the position of the melt results in a change in the direction of the atomic beam, and hence, the flux incident on the substrate. (Image courtesy V.Yun)

A second, more subtle challenge is that the controller used (an Inficon XTC/2) has a resolution of 0.1 Å/s. With a typical growth rate of 0.8-1.0 Å/s, this corresponds to a potential variation of up to 12.5%, which is unacceptably large for MBE applications. In addition, QCMs are sensitive to changes in temperature and stress, both of which reduce the usability of the technique. [26]

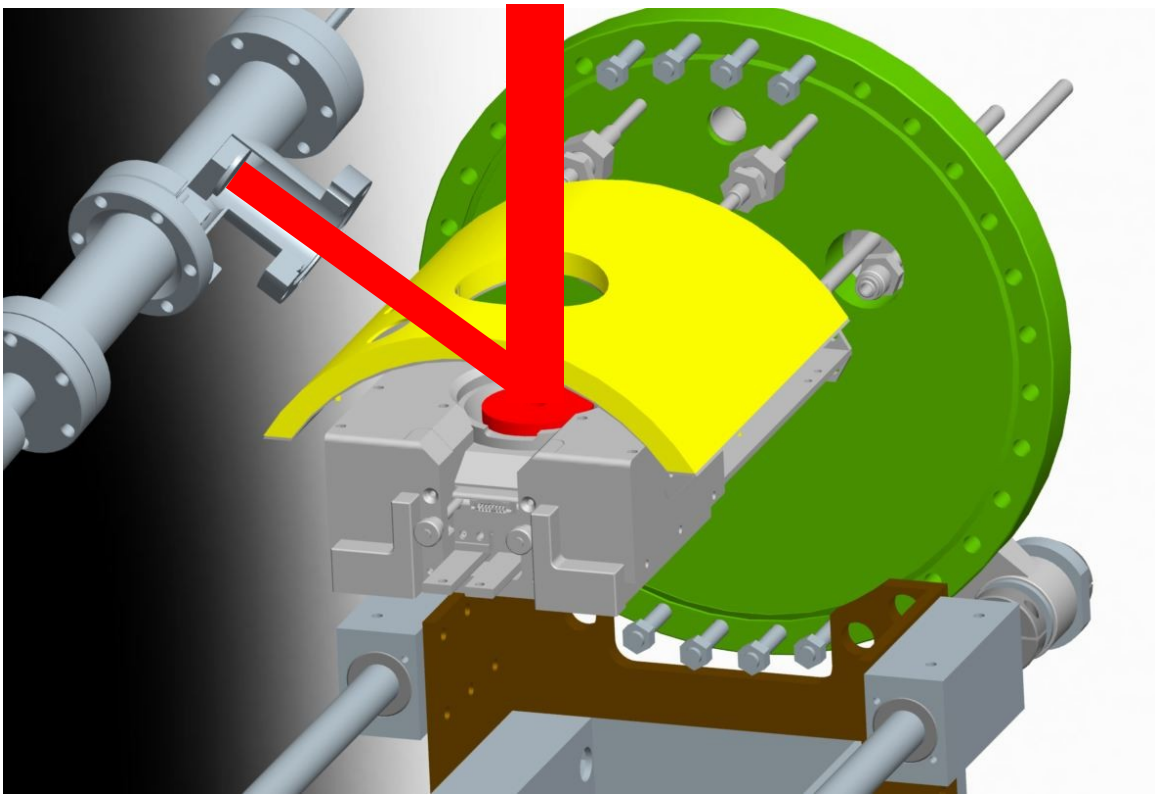

**Figure 3-3** : The location of the QCM in relation to the source and the path of the atom flux to the substrate. In such a configuration, it is to be expected that a drift in position of the melt would cause a change in the flux incident on the QCM. (Image courtesy V.Yun)

### 3.2.2 Direct monitoring of the atomic flux

The solution to the problems listed is to actively measure the flux that is incident on the substrate. In addition, if this measurement is performed between the source and the shutter, it will allow for a controlled ramp to the desired silicon growth rate. Two common methods of implementing such a flux monitor are the techniques of atomic absorption spectroscopy (AAS) [37, 38] and electron-impact emission spectroscopy (EIES) [39]. Both techniques involve actively probing the atomic flux.

Atomic absorption spectroscopy is a highly sensitive and selective technique that is used to accurately determine the concentration of an atomic species in the vapor phase. It is based on the selective absorption of photons resonant with an atomic line of free atoms. A block diagram illustrating the operating principle of a typical AAS flux monitor is shown in Figure 3-4. In this setup, a light source with strong output intensity $I_0$ at one of the strong resonance lines of the species being evaporated is coupled through the vacuum system. As these resonant photons pass through the atomic flux, some are absorbed, transferring the neutral atoms to an excited state. The instantaneous absorption coefficient of the flux cloud α is determined by the number of atoms according to

$$\alpha = N\sigma \tag{3.1}$$

where N is the number of atoms in the atomic beam that interacting with the optical beam and σ is the absorption cross-section of each atom. This absorption results in a decrease in the throughput intensity at this resonant line according to Beer-Lambert's law

$$I = I_0 \exp(-\alpha l) \tag{3.2}$$

where l is the geometrically described interaction length of the optical beam and the atomic flux and is shown in the figure. This can be monitored instantaneously using a suitable photodetector, allowing a direct measurement of the atomic flux, which in turn allows control of the source.

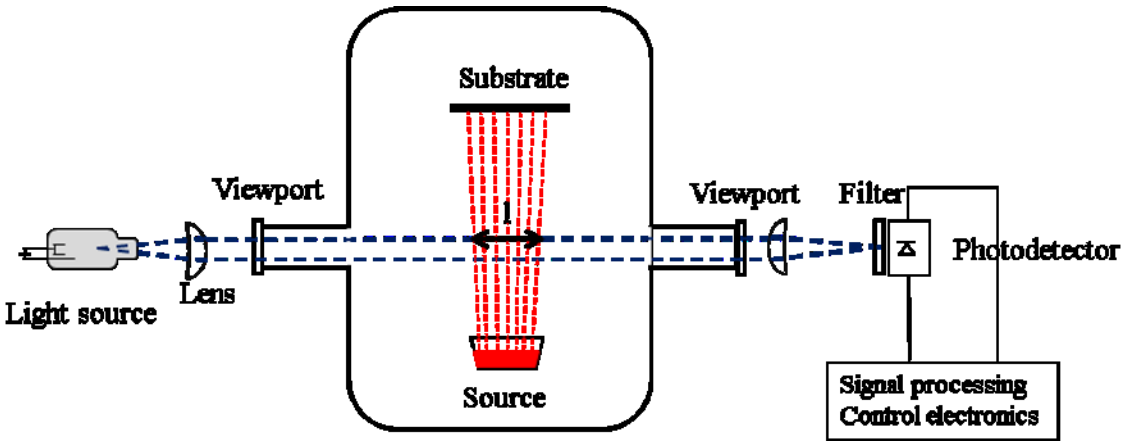


**Figure 3-4:** A basic schematic of an AAS flux monitor as described in the text. Also indicated is the geometric extent of interaction between the optical beam and the flux.

Electron impact emission spectroscopy is an analogous technique where optical emission at the same resonant line is monitored. In this technique, thermionic electrons from a filament driven at a specific current excite the atoms to a specific excited state. When these atoms relax to their ground state, they emit a photon at a characteristic wavelength. The intensity at this emission line is a direct measure of the atomic flux, and is monitored by a suitable photodector as in the case of an AAS system. This measure of atomic flux allows control of the e-beam source. A detailed description of the design and operation of an EIES flux monitor is presented in [39]. For the purpose of this thesis, an AAS flux monitor is chosen for the following reasons:

i. An AAS monitor has no in-vacuum parts. This means that any service to the flux monitor can be done without venting the MBE system, even during a growth. An EIES system, on the other hand, requires a filament in vacuum. Replacement of this filament would require that the growth be aborted, and

the system be vented.

ii. An AAS monitor can be designed to sample the entirety of the atomic flux beam, while an EIES monitor samples only a part of the beam that interacts with the electrons emitted by the EIES filament.

The rest of this section will provide details on the design of an AAS flux monitor and it's commissioning.

### 3.2. 3 Design of an AAS flux monitor

As seen in Figure 3-4, the main components of an AAS flux monitor are the light source with strong emission at the resonant line with the atom, the wavelength selection element to only select photons close to this resonant line, and a photodetector. For silicon, the conventional analytical absorption (and hence, emission) line is the $3p4s\ ^3P_2 \rightarrow 3p^2\ ^3P_2$ line at 251.6nm. Conventional incandescent lamps which have very low output in the UV range cannot be used. Instead, a specialized lamp (Cathodeon HC-3QNY/Si) with strong output at the desired UV line, called a hollow cathode lamp (HCL), is used. The construction of such a lamp is shown in Figure 3-5.

This discharge lamp consists of a hollow, cup-shaped cathode made of the element of interest and an anode, and is filled with a low pressure inert gas such as neon or argon. When the applied voltage is sufficiently high, a plasma is created which then sputters neutral silicon atoms from the cathode. These silicon atoms that are now in the vapor phase are then excited by the electrons, and when they relax to

the ground state, optical emission at the characteristic analytical lines are observed. This light is collected and focused by the lens at the output window of the lamp. It is important to note that the output will contain the spectral lines of both, the fill gas and silicon, the cathode element.

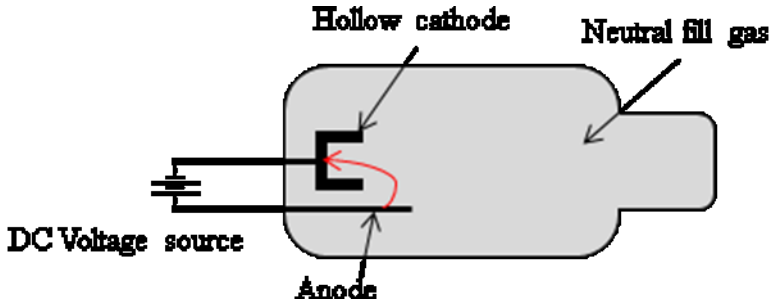


**Figure 3-5:** The internal structure of a hollow cathode lamp. At a sufficiently high drive voltage, a fill-gas plasma is created electrons from the anode sputter atoms from the cathode. Interaction between the neutral atoms and the electrons cause excitations that generate light.

This light is then mechanically chopped to enable a lock-in detection scheme to maximize sensitivity and is then suitably coupled into the vacuum chamber. In our case, this is achieved using UV-transmissive multimode fiber (1mm core diameter) and a custom modified water cooling jacket shown in Figure 3-6. The chopped HCL output is coupled in and out of the vacuum system through UV-fused silica viewports mounted on the 1.33" diameter conflat flanges. To minimize deposition of silicon on the viewports, the tube to they are mounted are 3.5" long. This jacket is mounted on the source flange of the growth chamber, below the source shutter. This location for the flux monitor is chosen to best represent the flux incident on the substrate – it is above the apertures of the cooling roof shown in Figure 3-2, and that of the flange

that attaches the mini chamber to the growth chamber.

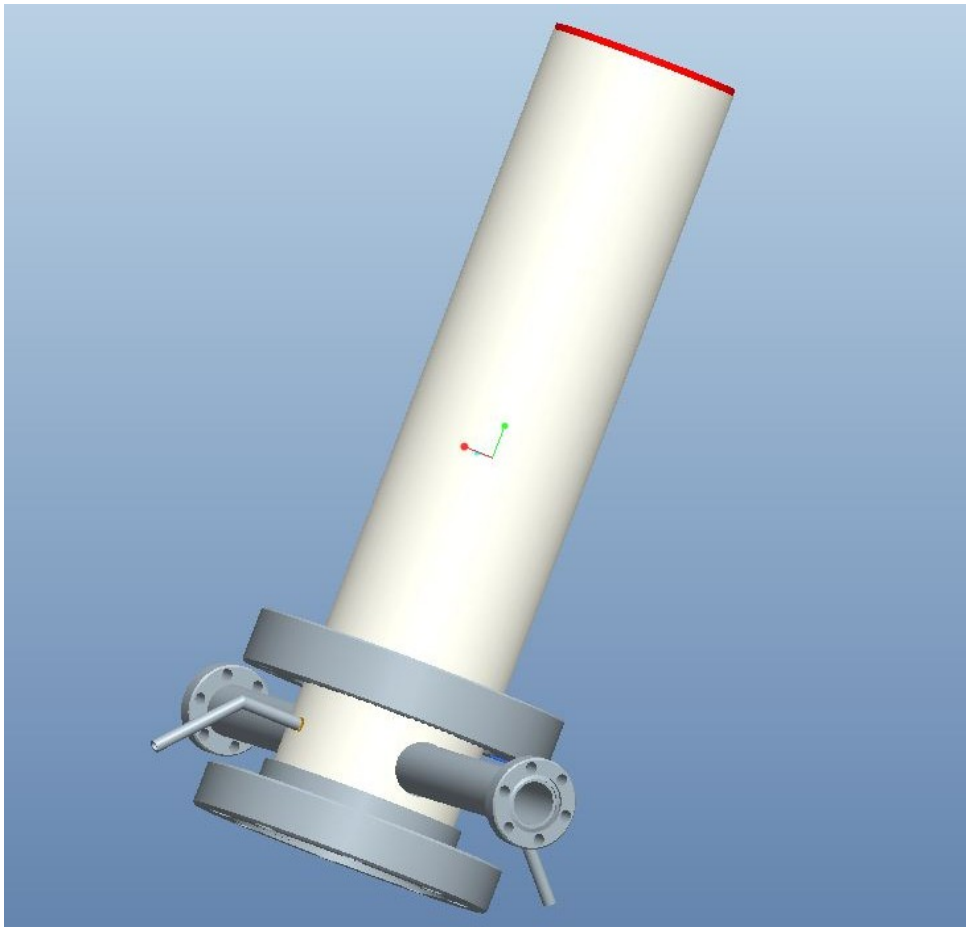

**Figure 3-6:** The custom water cooling jacket (with 1.33" UVFS viewports removed) that allows coupling of the HCL into the vacuum chamber. This jacket is attached to the topmost flange shown in Figure 3-2. (Image courtesy of V. Yun)

To maximize coupling in and out of the vacuum system, this cross is outfitted with fused silica (UVFS) viewports that transmit 92% of the light at 250 nm. At the output viewport, a custom housing is used to attach a focusing lens, a UV bandpass interference filter and a photomultiplier tube. The interference filter used has a central wavelength of 253 nm and a passband of 10 nm and a peak transmission of 12%. This

filter is needed to block the spectral lines of the fill gas in the HCL, as well as radiation from the hot silicon source. It is to be noted that the analytical line, like any atomic line, is extremely narrow (~10 pm), and a narrower filter would improve the signal-to-noise (SNR) of the measurement scheme. Using a monochromator in place of the chosen filter will allow a reduction of the passband to ~1 nm, and with increased peak transmission due to the fact that UV gratings can achieve efficiencies >60%. However, geometric concerns preclude the use of a monochromator in our system, and a filter is used instead. It should be noted that in addition to the fundamental transition of interest, there are other competing transitions within the bandwidth of the filter that result in an increased background. A compact photomultiplier tube (PMT) module (Hamamatsu H7732-01), which consists of a PMT and the necessary drive electronics, is used to measure the optical power transmitted through the atomic flux. Use of a PMT is vital for the implementation of an AAS flux monitor as conventional UV-enhanced silicon photodiodes have a prohibitively high noise floor. This is shown in Figure 3-7, which compares the normalized outputs of a photodiode and a PMT. This comparison is obtained by separately focusing the output of the HCL on the filter-photodiode and the filter-PMT combinations. As can be seen, the PMT is able to resolve variation in the beam intensity, while the photodiode could not.

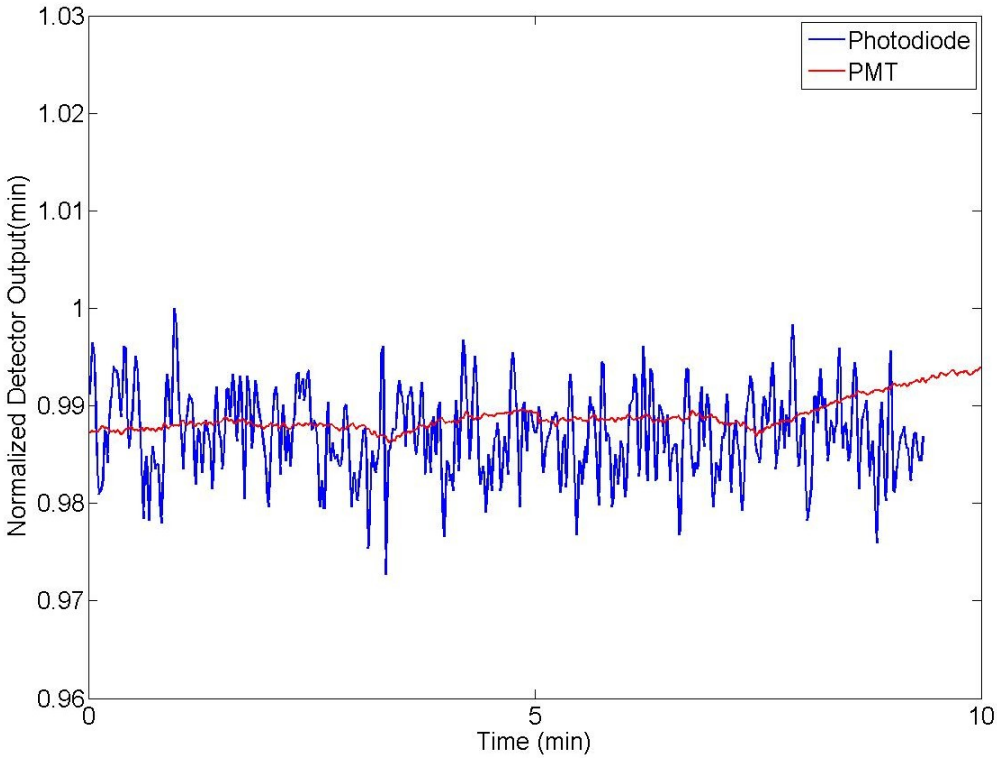


**Figure 3-7:** The normalized HCL output as measured by a PMT and a UV-enhanced silicon photodiode. The noise level of the PMT is sufficiently low enough to allow a measurement of the drift of the HCL output, while the photodiode cannot.

With this choice of detector, a preliminary attempt at using this setup was made. This revealed that drift in the lamp was larger than the specified 0.05%, and was measured to be 0.35% over a period of 1 hour. To compensate for drift in the lamp, a reference arm is included. This dual beam dual detector implementation is shown schematically in Figure 3-8. The reference signal was obtained by using the Fresnel reflection from a 1" diameter UVFS beam sampler. This reflected beam is then focused onto a second filter-PMT combination. This setup requires two separate lock-in amplifiers (Signal Recovery 7265). This combination is found to significantly

reduce the short term drift in the setup. This is shown in Figure 3-9 where drift of ~1% in both the signal and reference arms is observed, but the ratio of the signal to ratio is effectively constant (<0.1% drift), allowing a true measure of the transmission through the atomic flux.

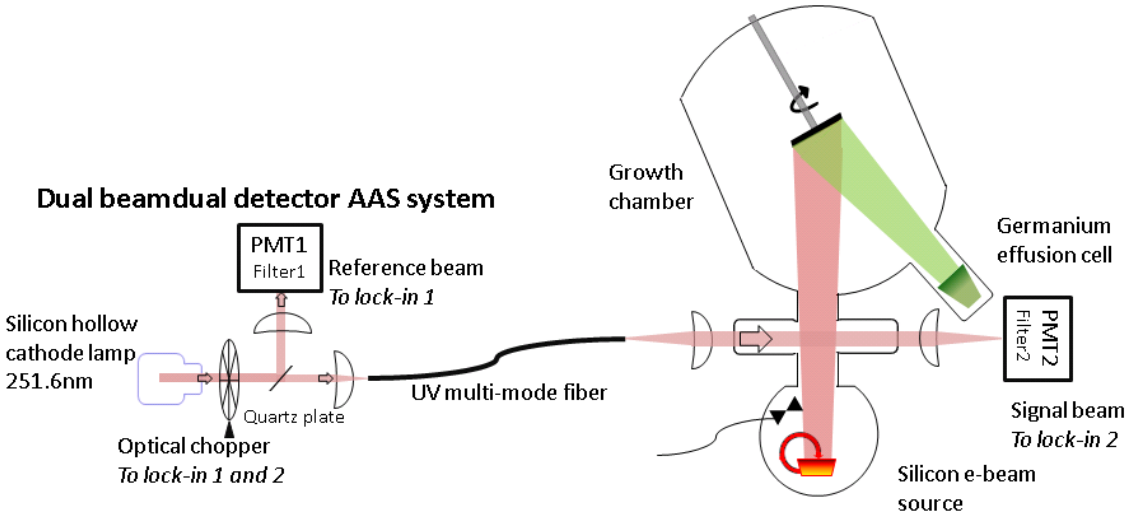


**Figure 3-8:** The implementation of a dual beam, dual detector AAS flux monitor.

It is important to note that the reference signal must be generated by the analytical line being used and not the variation in the fill gas background. It was found that the drift in the optical output outside at two different wavelengths, that of the silicon and of the neon fill gas, were uncorrelated. This is seen in Figure 3-10, where a simultaneous measurement at the 251.6 nm line using the PMT is compared with the fill gas spectrum as measured by a photodiode.

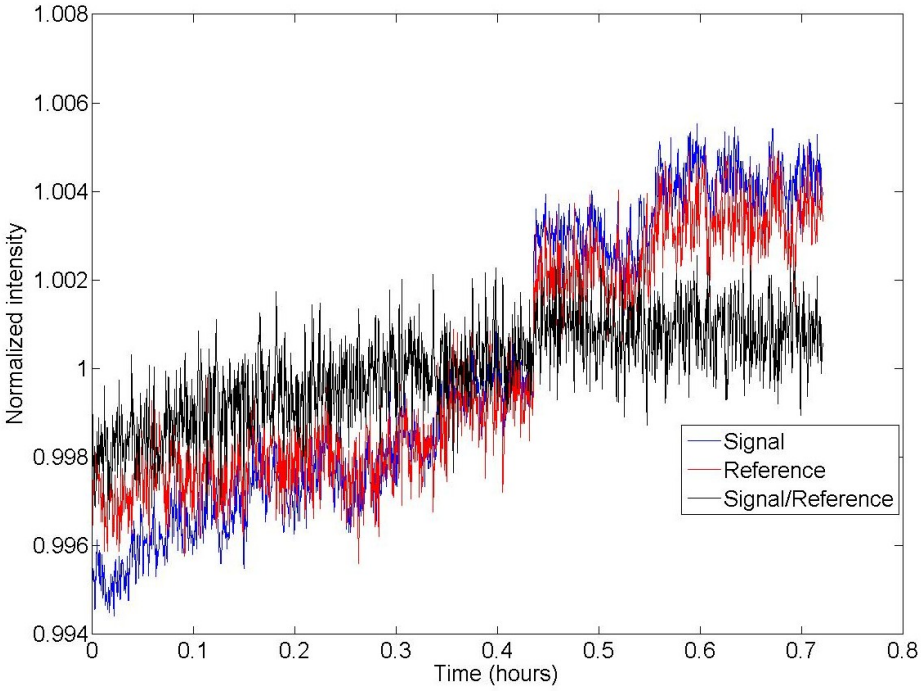


**Figure 3-9:** The measured intensities of the signal and reference channels, and the ratio of the two, highlighting the advantage of using a dual beam scheme.

While Figure 3-9 demonstrates the significant improvement in the short term stability of the optical circuit engendered by the implementation of the dual beam setup, it does not address long term instability that is observed. It is observed that the transmission through the system varies gradually over a period of 1 hour in the absence of a silicon flux. This long term drift causes significant errors in the calibration of the system, reducing the viability of the AAS system to accurately control the flux.

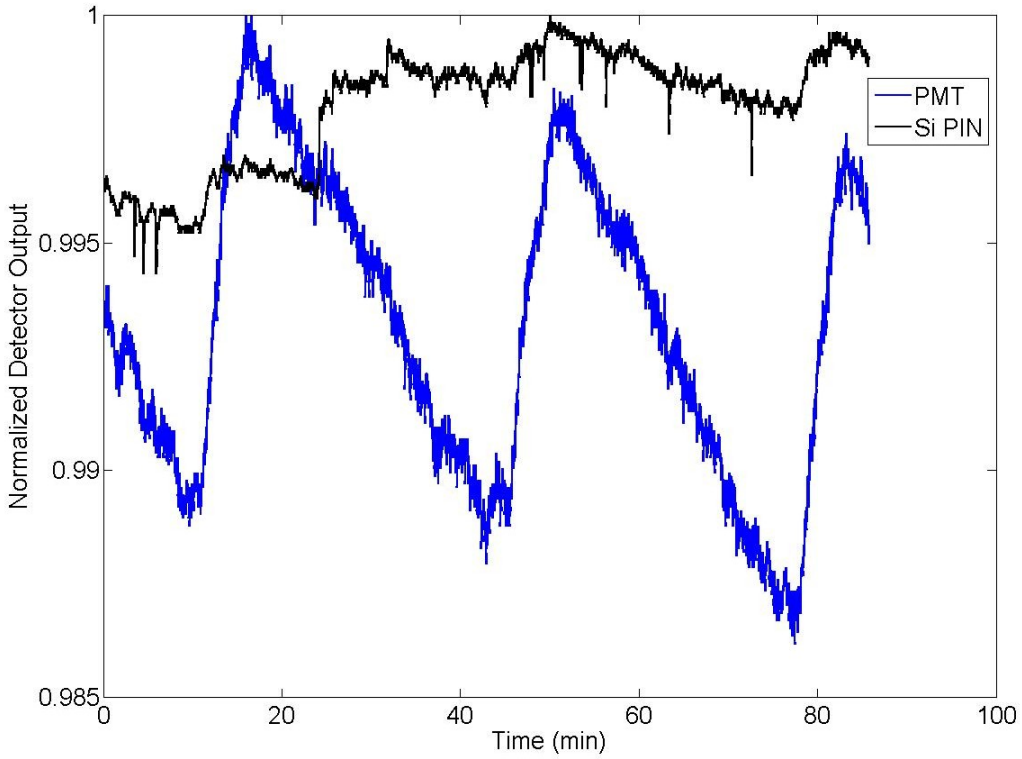


**Figure 3-10:** The measured lamp intensities at the analytical line (251.6nm) measured using a PMT, and that of the unfiltered fill gas spectrum, measured using a photodiode. The lack of correlation between the two highlights the unsuitability of this method.

This drift has two sources:

i. The two filters used aren't identical and have differing transmission characteristics. In the setup shown, the filter used on the reference arm has a center wavelength of 256.35 nm, a FWHM bandwidth of 10.02 nm and a peak transmission of 15.44%. This is in contrast with the filter on the signal arm, which is centered at 254.87 nm with a bandwidth of 9.87 nm and a peak transmission of 16.08%. When the background around the analytical line changes slightly, the light passing through each of these filters is slightly

different due to the differing transmission characteristics, which in turn results in non-identical changes in the light incident on the PMT.

ii. The two PMTs have photocathodes with different emission characteristics. This is an additional source of non-correspondence of the outputs of the signal and reference arms.

The combination of these two factors can be expressed mathematically as

$$\frac{I_S(t)}{I_R(t)} = \frac{\int_{\lambda_{1S}}^{\lambda_{2S}} T_S(\lambda) G \eta_S(\lambda) \alpha_S P_{HCL}(\lambda, t) d\lambda}{\int_{\lambda_{1R}}^{\lambda_{2R}} T_R(\lambda) G \eta_R(\lambda) \alpha_R P_{HCL}(\lambda, t) d\lambda} \neq \frac{\alpha_S}{\alpha_R} \tag{3.3}$$

Here, the subscripts S and R refer to the signal (S) or reference (R) beam. I is the PMT current at time t, $\lambda_1$ and $\lambda_2$ are the cut on and cut-off wavelengths of the filter, $T(\lambda)$ is the transmission of the filter, $\alpha$ is a constant that accounts for the differing coupling and propagation losses in the signal and reference arms, as well as the Fresnel reflection and factors $\eta(\lambda)$ is the spectral efficiency of the photocathode of the PMT. G is the PMT gain and $P_{HCL}(\lambda,t)$ is the time-varying spectral power density of the HCL.

As can be seen, the ratio of the signal to reference beam in such a case is not exclusively a measure of the absolute drift of the analytical line, but includes other factors. While correcting for this is possible if all four transfer functions are known, this is computationally intensive and not feasible. A simpler and more elegant solution is to use a single filter and a single PMT to measure both, the signal and reference beams. Absent a flux, this can be expressed mathematically as

$$\frac{I_S(t)}{I_R(t)} = \frac{\int_{\lambda_1}^{\lambda_2} T(\lambda) G \eta(\lambda) \alpha_S P_{HCL}(\lambda, t) d\lambda}{\int_{\lambda_1}^{\lambda_2} T(\lambda) G \eta(\lambda) \alpha_R P_{HCL}(\lambda, t) d\lambda} = \frac{\alpha_S}{\alpha_R} = SR \tag{3.4}$$

and is time-invariant with value SR.

While such an experiment would typically require two lock-in amplifiers, it can be carried out with one, if the dual reference mode of the SR7265 is used. This gives us the final version of the AAS flux monitor implementing a dual beam single detector scheme, shown in Figure 3-11. The long term stability of this implementation is shown in

Figure 3-12 highlighting the improvement over the dual beam dual detector scheme. For the measurement period shown (7 hours), the rms drift in the single detector implementation was only 0.06%, in comparison to the 0.2% variation in the dual detector implementation.

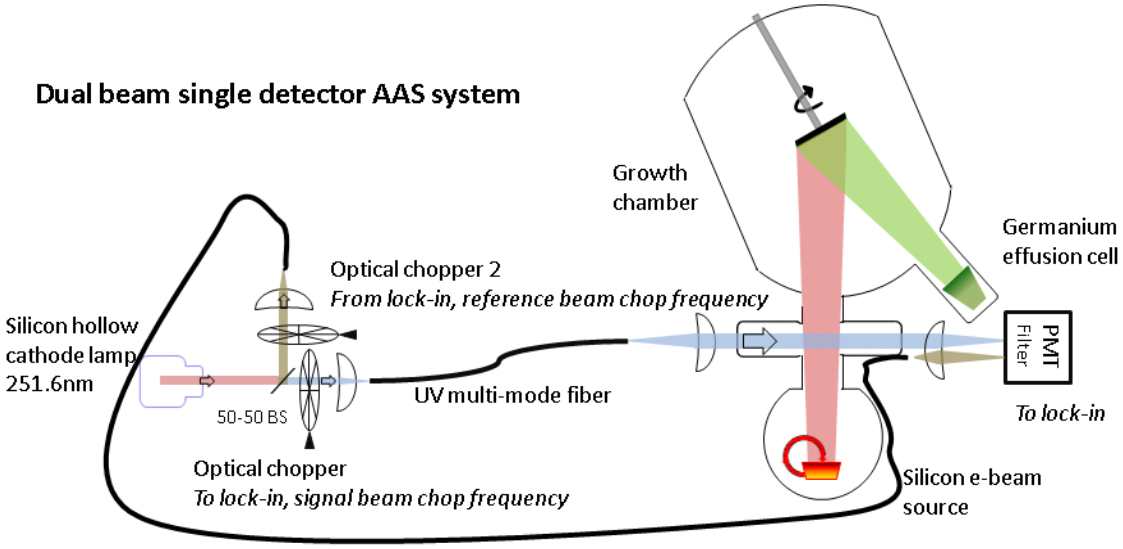


**Figure 3-11:** The schematic of the implemented dual-beam single-detector AAS flux monitor

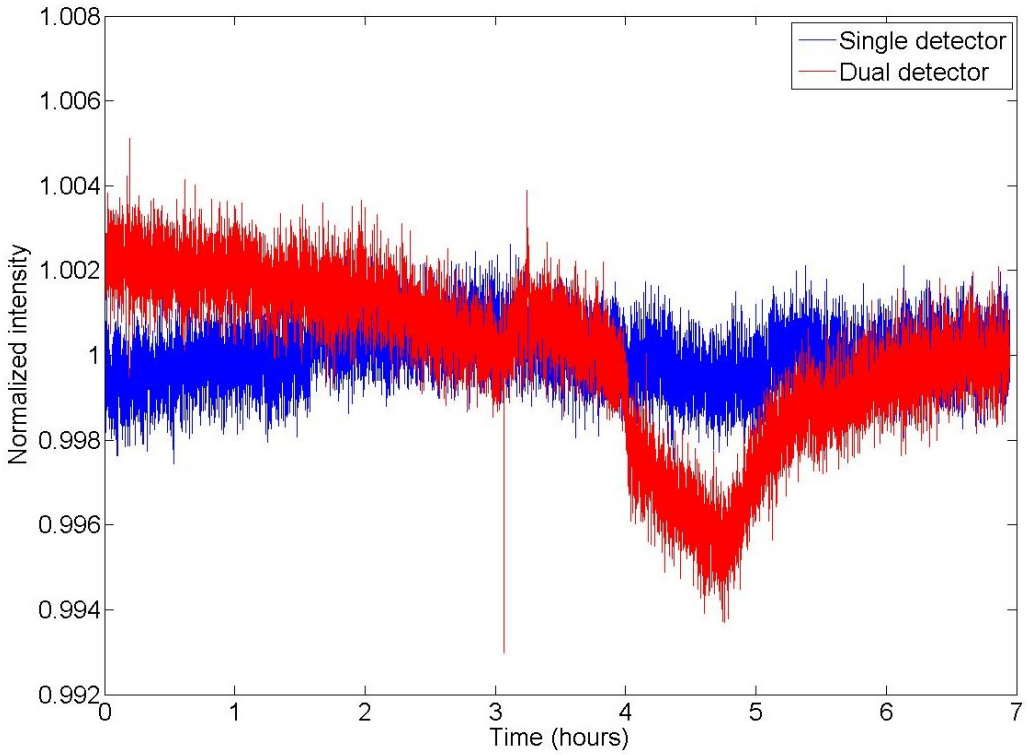


**Figure 3-12:** The drift in the transmission in the single and dual detector schemes. The single detector scheme is observed to be significantly more stable.

### 3.2.4 Calibration

As with standard effusion cells, the silicon cell with the AAS flux monitor can be calibrated either using the technique of RHEED oscillations or by growing strained-layer superlattices and analyzing the fringe spacing using X-ray diffractometry (detailed in section 2.4.1). It was found that excellent calibration could be obtained by measuring the RHEED oscillations of a growing, unstrained silicon layer on a (111) oriented silicon substrate. The calibration was performed as follows. First, the HCL was turned on and set at a constant emission current, typically 10mA and allowed to stabilize for an hour. After this period, the intensity of the signal and

reference beams was recorded to obtain the relative strengths of the signal and reference in the absence of any silicon flux. This allows recording of the value of SR in equation (3.2). The data is recorded using a MatLab GUI that interfaces with the SR7265 via a GPIB connection. This value is retained for the rest of the experiment. At this point, the transmission T and absorption A through the system can be expressed as

$$T(t) = 1\frac{I_S(t)}{I_R(t)SR}$$
$$A(t) = 1 - T(t) \quad \textbf{(3.5)}$$

Next, the silicon cell was ramped up slowly to a number of emission set points. At each location, where possible, the absorption was measured as a function of the silicon growth rate as measured from the RHEED oscillations. This is shown in Figure 3-13 and allows for the calibration of the system as

$$GrowthRate(\text{Å}/s) = {}^{A(t)}\!/_{0.0454} \quad \textbf{(3.6)}$$

As seen in the figure, absorption varies linearly with growth rate, enhancing ease of control of the silicon electron beam source. This AAS flux monitor facilitated the growth of heterostructures detailed in this thesis.

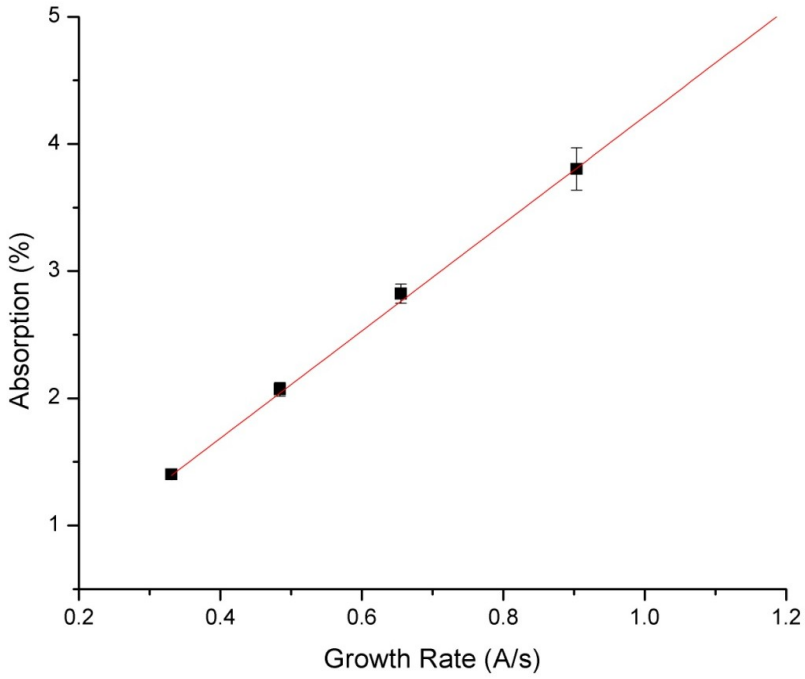


**Figure 3-13:** The calibration curve for the implemented AAS flux monitor, showing linear operation.

## *3. 3 Selection of liner for boron dopant cell*

As mentioned in Chapter 2, boron is a low vapor pressure element, requiring the use of a high-temperature effusion cell. This cell uses only refractory metals in the hot zone, allowing it to be used up to 2000ºC. This high temperature precludes the use of a standard pBN crucible, which is not recommended for use above 1400ºC. Instead, refractory materials such as tungsten, tantalum and alumina are used. In this case, a 10cc tungsten crucible is used. To avoid contamination of the source material by metal, a liner is used to prevent physical contact between the source and the metal crucible. Alumina, beryllium oxide, pyrolytic graphite (pG) and zirconium oxide are all liner materials specified by the manufacturer as compatible choices, with beryllium oxide being the original liner used. It is found that this configuration could

be used to grow epitaxial films with the required carrier concentrations. However, it is found that this configuration is not suitable for MBE applications, as there is evidence of the films being of poor quality. Covington and Meeks have reported that BeO is unsuitable material for use in substrate heaters in GaAs MBE systems due to an increased n-type carrier concentration in the grown films. [40] These contaminants were not identified, and were ascribed to occurring in the porous BeO matrix. It has been hypothesized that these might be beryllium or oxygen, but no proof was provided. [28] In this section, a comparison of samples grown using pG and BeO liners is made.

As mentioned in the previous chapter, RHEED can be used to study the evolution of the surface during crystal growth. In the case of boron-doped silicon films grown with this configuration, the evolution of the RHEED pattern suggests that there is possible contamination of the film.

Figure 3-14 shows the reconstructed silicon surface before and after the growth of a film that was measured to have a carrier concentration of $10^{18}cm^{-3}$. It is well known that boron is a well-behaved dopant in silicon MBE with excellent film quality for dopant densities up to $10^{20}cm^{-3}$. [41] In particular, the (2×1) reconstruction of the silicon surface is expected to be preserved during the course of the growth, and is not observed here.

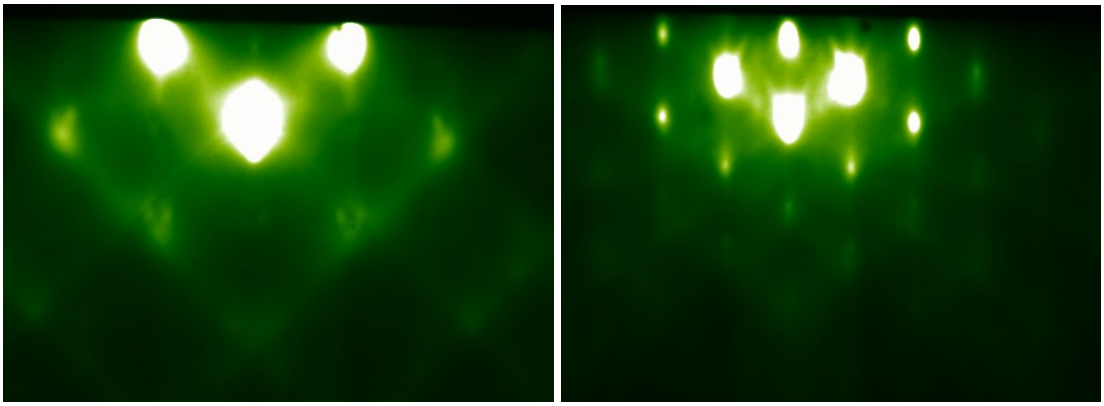

**Figure 3-14:** The RHEED images obtained from the boron-doped Si sample ($p = 10^{18}$ $cm^{-3}$) with a 15 kV electrons incident along the [100] (left) and [110] azimuths. The highly spotty nature of the image indicates poor film quality and poor long range order. For this operating condition, only the $0^{th}$ Laue zone is imaged.

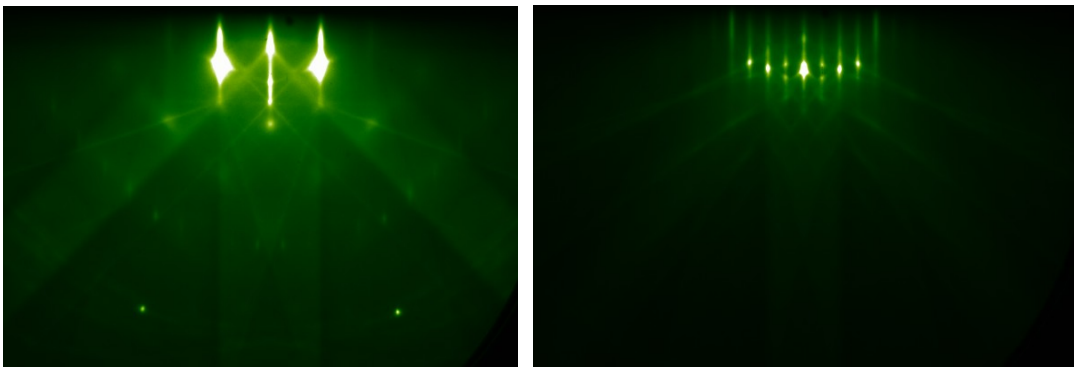

**Figure 3-15:** The RHEED images obtained from the boron-doped Si sample ($p=4x10^{18}$ $cm^{-3}$) with a 30 kV electrons incident along the [100] (left) and [110] azimuths. In both cases, the $1^{st}$ Laue zone is seen, though in the [110] image, it is extremely faint. The smooth, streaky patterns in the $0^{th}$ zone indicate quality material.

In contrast, the film grown with the pG liner does not show similar degradation. Figure 3-15 shows the post-growth RHEED patterns of a sample doped to $4x10^{18}cm^{-3}$. Strong streaks are observed, indicating smooth films.

Further evidence of poor material quality is obtained by comparing the surfaces of the films using tapping-mode atomic force microscopy (AFM). Figure 3-16 shows a scan of a 4 μm x 4 μm area of a typical film grown with a BeO liner. This surface is highly textured and is measured to have a root mean squared (rms) roughness of 1.9 nm. This is equivalent to almost 14 monolayers, which is strongly indicative of poor film quality. In contrast, the films grown using the pG liner are significantly smoother. Figure 3-17 shows an AFM image of a representative 4 μm x 4 μm area with an rms roughness of 0.1 nm.

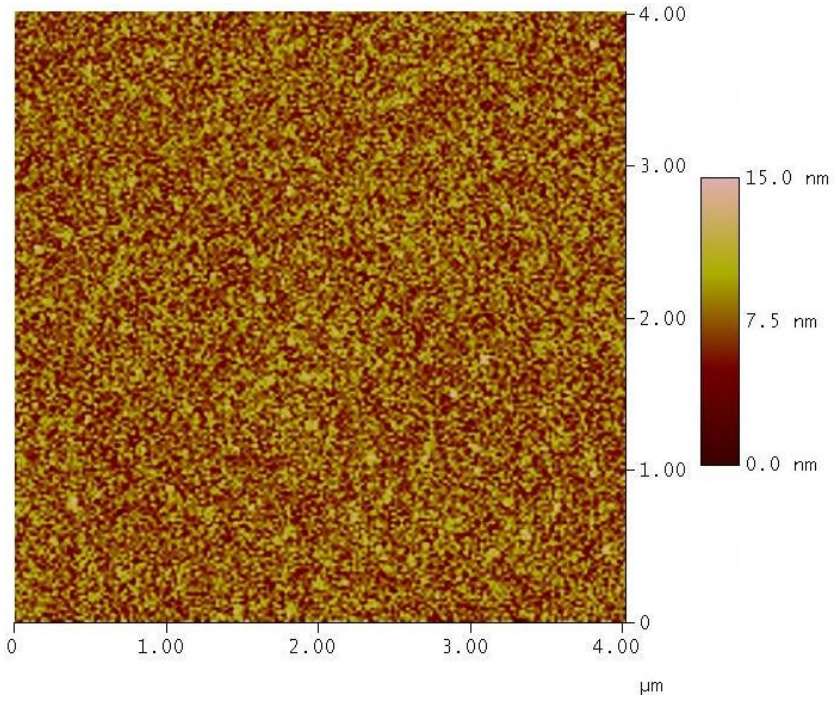


**Figure 3-16:** The observed surface morphology using AFM of the boron-doped sample grown with a beryllium oxide liner as described.

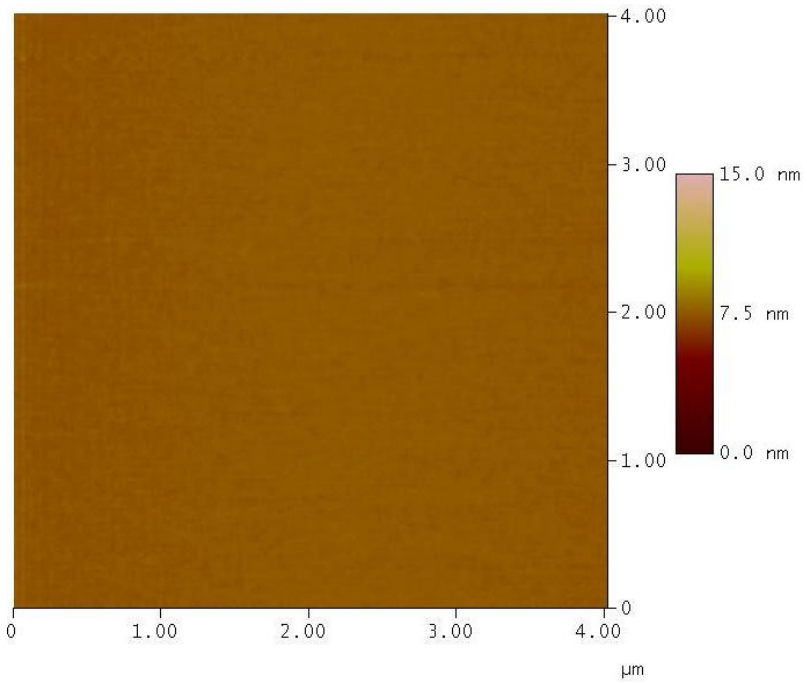


**Figure 3-17:** An AFM image of the surface morphology of the structure grown with a pG liner in the boron cell. While point defects are observed, the sample is smoother.

XRD was used to study of the crystallinity of these films. It is known that doping silicon with boron causes a contraction of the lattice and introduces tensile strain in the films. [41] Evidence of this strain can be observed in films of high-quality as thickness fringes in the ω-2θ XRD scan. Shown in Figure 3-18 is this comparison for two films with measured dopant densities of $4x10^{18}$ $cm^{-3}$ grown with each liner type. The film grown with the pG liner shows fringes corresponding to a strained film that is 480 nm ± 30 nm thick. In contrast, the film grown with the BeO liner shows a broadening of the silicon peak without thickness fringes, indicating lower crystal quality.

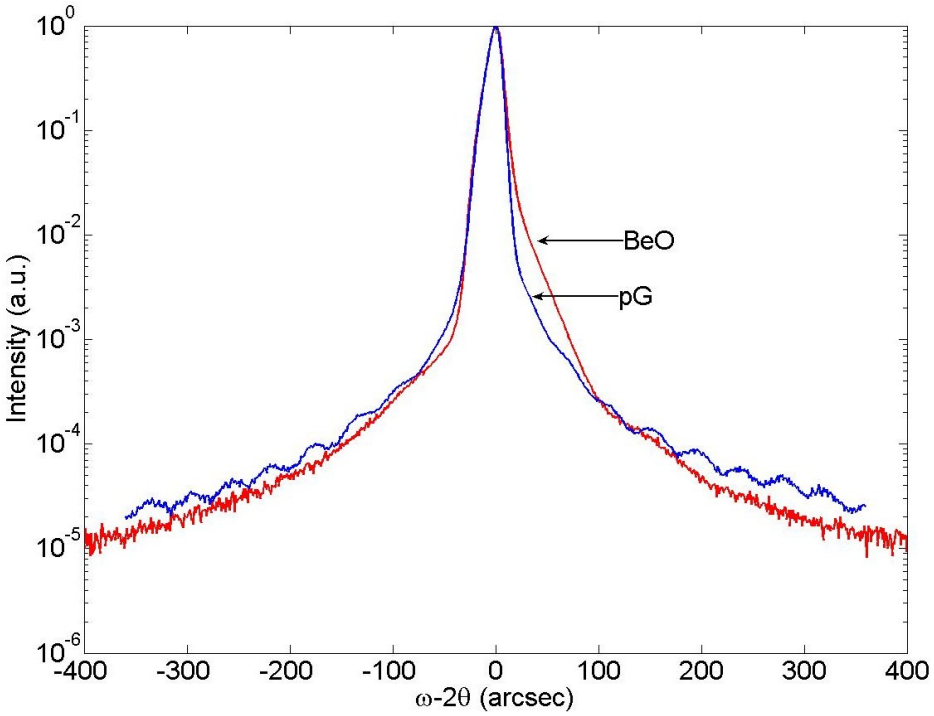


**Figure 3-18:** XRD scans of p-doped silicon films grown with a BeO and pG liners.

Verification that the source of contamination was the BeO liner and not another unknown cell was obtained by destructive analysis of a carefully designed sample using secondary ion mass spectroscopy (SIMS). The schematic of this sample is shown in Figure 3-19. The results of this SIMS analysis are shown in Figure 3-20, highlighting the step-like increases in the boron concentration with a corresponding increase in both, the beryllium and oxygen concentration. Furthermore, at high cell temperatures, the carbon level is found to increase significantly above the background level of $10^{17}$ $cm^{-3}$. The concentrations of Be, B and O as a function of cell temperature for the sample grown with the BeO liner are plotted in Figure 3-21. Because beryllium is an acceptor in silicon, [30] the majority of carriers observed during Hall analysis are associated with the beryllium from the

decomposing liner and not the boron charge. As shown in Figure 3-21, the temperature dependent concentrations are fit to an Arrhenius model, $c \sim \exp\left(-E_a / k_B T\right)$, yielding a characteristic energy of 4.65 eV ± 0.3 eV for beryllium and 4.89 eV ± 0.06 eV for oxygen. This is close to 4.66 eV ± 0.23 eV, the experimentally determined bond dissociation energy of BeO. [42] The proximity of these values to the bond dissociation energy of BeO further suggests that the decomposition is not catalyzed by the boron charge. It should be noted that the concentrations of beryllium and oxygen exceed their solubility limits in silicon, which explains the mechanism that causes the surface roughness and XRD peak broadening. [43, 44]

| |
|---|
| 0.1µm p-Si layer (p>1E20 cm-3) ($T_B$=1650ºC) |
| 0.1µm i-Si spacer |
| 0.3µm p-Si layer (p~1E19 cm-3) ($T_B$=1500ºC) |
| 0.1µm i-Si spacer |
| 0.3µm p-Si layer (p~1E18 cm-3) ($T_B$=1350ºC) |
| 0.1µm i-Si spacer |
| 0.3µm p-Si layer (p~1E17 cm-3) ($T_B$=1200ºC) |
| 0.4µm i-Si buffer |
| p-B (100) Si substrate |

**Figure 3-19:** Layer structure of the sample designed to demonstrate the unsuitability of the use of a BeO liner.

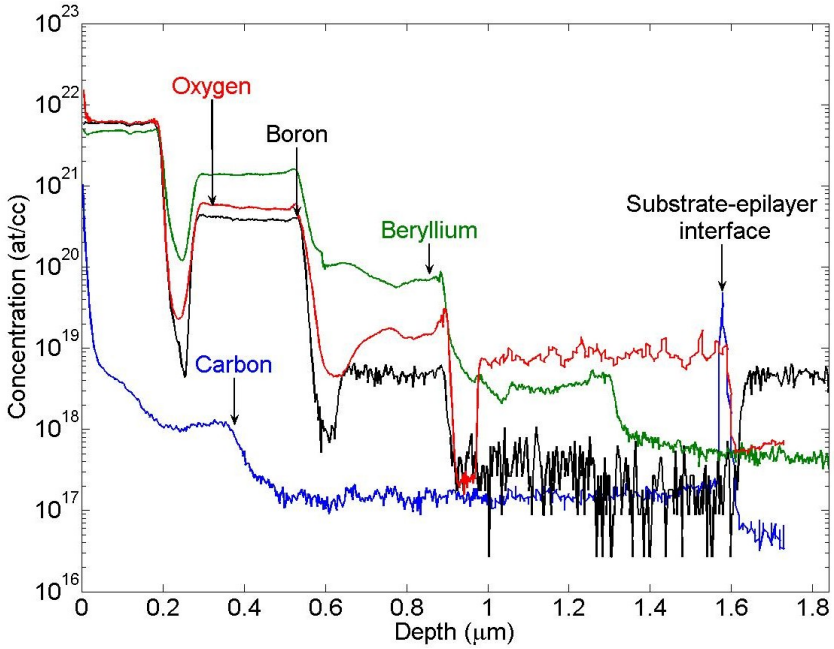


**Figure 3-20:** SIMS analysis of the sample shown in Figure 3-19, showing significant beryllium and oxygen contamination.

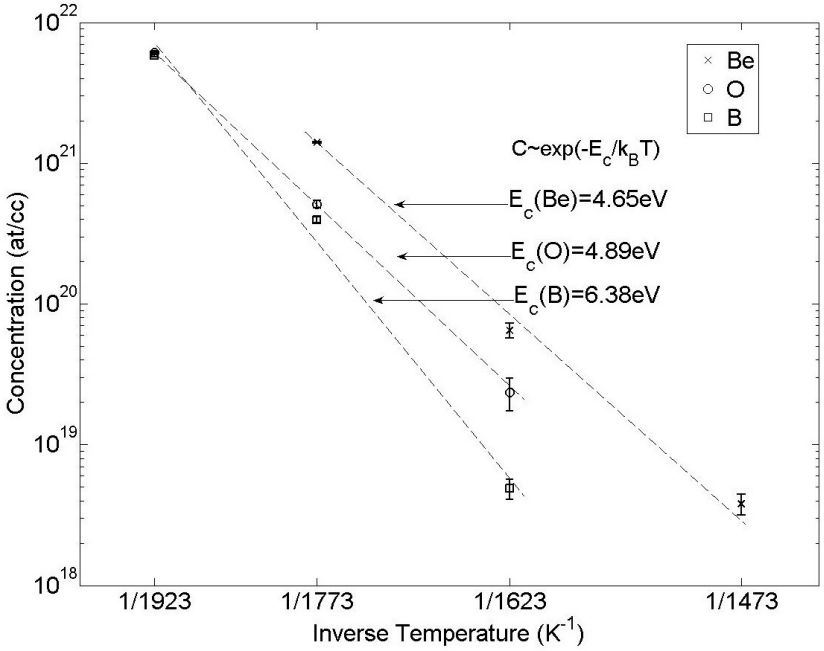


**Figure 3-21:** Concentrations of Be, O and B in the sample grown with the BeO liner as a function of the boron cell temperature as measured by SIMS.

SIMS analysis of a layer structure similar to the sample shown in Figure 3-19 revealed that there was no similar step-like increase in beryllium and oxygen and that the carbon background is not significantly affected either. This structure and SIMS analysis are shown in Figure 3-22 and Figure 3-23 respectively. Carbon is measured to be at a constant background level, suggesting the stability of the pG liner. In fact, this concentration is almost identical to the carbon background of the sample grown with the BeO liner ($1.5x10^{17}$ $cm^{-3}$), suggesting that the carbon source is not the pG liner but could result from the vacuum chamber, possibly from the carbon cell. The Be concentration is below the detection limit of this analysis. Oxygen is at a constant background value of $1.3x10^{19}$ $cm^{-3}$ and is related to a leak in the chamber that has since been fixed.

| |
|---|
| 0.13µm p-Si layer (p>1E20 cm-3) ($T_B$=1700ºC) |
| 0.13µm i-Si spacer |
| 0.27µm p-Si layer (p~1E19 cm-3) ($T_B$=1584ºC) |
| 0.13µm i-Si spacer |
| 0.27µm p-Si layer (p~1E18 cm-3) ($T_B$=1488ºC) |
| 0.13µm i-Si spacer |
| 0.27µm p-Si layer (p~1E17 cm-3) ($T_B$=1390C) |
| 0.18µm i-Si buffer |
| Intrinsic (100) Si substrate |

**Figure 3-22:** The layer structure of the sample designed to verify the suitability of the pG liner.

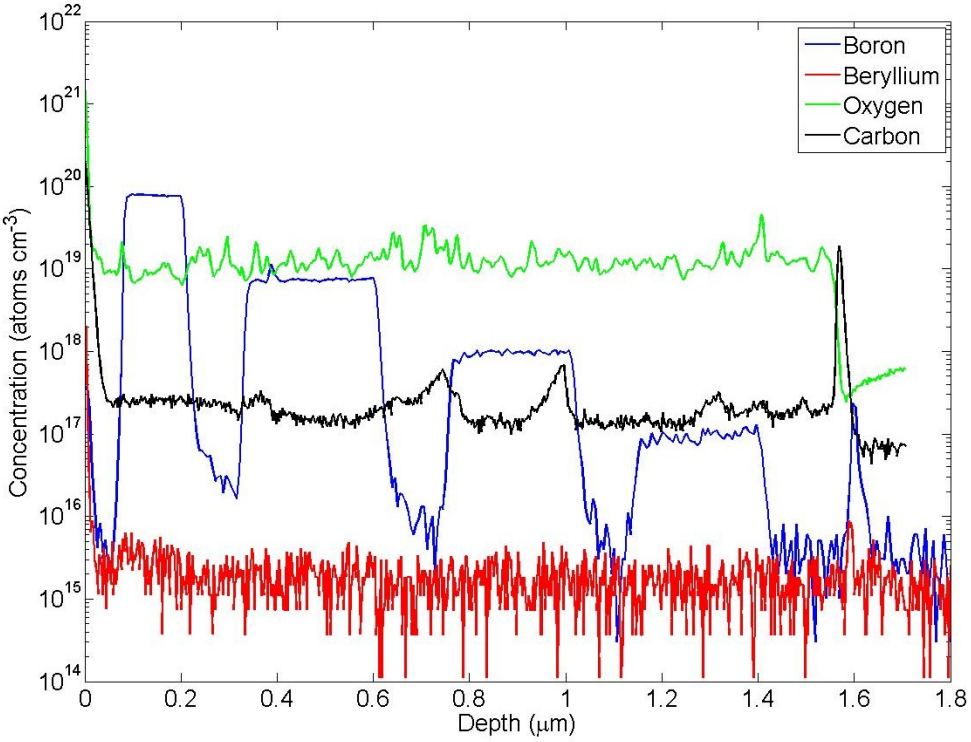


**Figure 3-23:** The SIMS analysis of the sample shown inFigure 3-22, showing the improvement over the previous cell configuration.

Fitting the measured carrier concentrations for the Hall samples grown with the BeO liner to an Arrhenius model yield a characteristic energy of 5.07 eV ± 0.37 eV. In contrast, a similar fit of the boron concentration as measured by SIMS gives a characteristic energy of 6.38 eV ± 0.57 eV. Alternatively, fitting the measured boron concentrations from Hall measurements of samples grown with the pG liner yields a characteristic energy of 6.29 eV ± 0.07 eV, which is close to 6.19 eV ± 0.06 eV that is obtained from SIMS analysis. In addition, the SIMS-measured boron concentration is within 10% of the Hall-measured carrier concentration. No similar comparison can be made for the samples grown with the BeO liner, where the expected concentrations

of boron as predicted from the analysis of the SIMS data differ by up to an order of magnitude. This disparity, along with the differing characteristic slopes of the Hall-measured carriers and SIMS analysis of boron, demonstrates that the beryllium and boron donors are partially compensated by oxygen for the sample grown with the BeO liner.

These results prove the superiority of the pG liner over the BeO liner. This allows growth of good quality p-doped layers, which is crucial for the growth of p-i-n diodes that this thesis sets out to accomplish.

### ***3.4 Substrate cleaning and thermal pre-treatment***

A clean substrate is a prerequisite for the growth of high-quality epitaxial films. Defects and impurities on the substrate can adversely affect the quality of the epitaxial layer. To that end, identifying an effective substrate preparation procedure is vital. This procedure consists of two parts – a wet chemical clean of an as-received substrate followed by thermal treatment immediately prior to growth. While the effectiveness of several wet chemical cleaning procedures, such as the RCA-1, RCA-2 and Piranha cleans have been reported [45, 46], the effect of the thermal treatment as it relates to epitaxial film quality and device performance isn't well documented. In this section, the process and evaluation of silicon substrates will be discussed in detail, with additional information for the preparation of silicon germanium virtual substrates

### 3.4. 1 Wet chemical cleaning and the need for thermal treatment

It is well known that silicon forms a stable oxide when exposed to ambient conditions. This oxide chemically passivates the surface. The precise thickness of oxide layer depends on the storage conditions, but typically is between 2 and 20Å. [47] If the initial substrate is clean, removing this oxide layer reveals this clean substrate layer underneath. This assumption of a clean, initial substrate is typically valid, especially if the wafers used are polished and clean and not exposed to a non-clean room environment. The oxide layer is easily removed in an aqueous medium containing hydrofluoric acid.

$SiO_2$ (s) + 4HF (l) → $SiF_4$ (l) + $2H_2O$ (l)

The $SiF_4$ salt formed is easily dissolved by water, leaving a clean silicon surface. Unlike the atoms in the bulk, the surface silicon atoms have two unbonded electrons. Such a configuration is highly reactive, and stability is achieved by forming a weak bond with hydrogen from the acidic environment.

Si + 2 H → H--Si--H

This hydrogen terminated surface is hydrophobic, effectively passivating the surface. This surface is stable in air for several minutes and for much longer in the absence of oxygen. [48]

In this thesis, a 5% solution of HF is used to remove this oxide layer, leaving behind a clean silicon surface. The substrate is then briefly rinsed in deionized water (DI) to remove any residual HF and dried with clean nitrogen. It is then loaded in the intro chamber and roughed out immediately. The typical time elapsed between when

the substrate is removed from HF and loaded in the intro chamber is between 1 and 2 minutes and it is expected the hydrophobic surface is retained. Approximately another 5 minutes are required to evacuate the intro chamber and crossover to ultrahigh vacuum.

Several authors have reported on more involved cleaning procedures. [49-52] However, it is found that the procedure detailed above when combined with a thermal treatment is sufficient.

The need for thermal treatment is two-fold and is carried out in a two-step process. One, the residual water from the final rinse needs to be removed before the substrate is introduced into the growth chamber. This is required to preserve the low water background pressure and maintain chamber cleanliness. This is accomplished by heating up the substrate to a temperature of 150ºC at a rate of 1-5ºC/min in the intro chamber. In this process, any water that is adsorbed on the substrate is thermally driven off and is captured by the cryo pump.

The second reason that a thermal treatment is required comes from recognizing the fact that the substrate is not yet ready for growth. At this point, the substrate is still hydrogen terminated. While epitaxial growth on a hydrogen-terminated silicon surface has been reported, these wafers have large dislocation densities ($10^4$-$10^5$ $cm^{-2}$) at the epilayer-substrate interface. [51] This is unacceptably large for device applications. The stability of this hydrogen-terminated Si-surface in clean water allows for the removal of large drops of HF without disturbing the clean surface. [48] However, XPS studies have shown that up to 0.08 monolayers (ML) of residual fluorine, along with oxygen and carbon are present on this surface. [49, 53]

In addition, there is potential for contamination from the loading procedure. This is because the entire intro chamber is exposed to ambient air, and the potential for adsorption of atmospheric contaminants and hydrocarbons exists. Further, the ion gauge that is used to monitor the pressure of the intro chamber can act as a hot zone to crack some of these hydrocarbons, resulting in a carbon-contaminated substrate. [51] While this can be partly avoided by not using the ion gauge, it would involve defeating safety interlocks and isn't the preferred approach. For these reasons, a second, higher temperature thermal soak to desorb the hydrogen and any other contaminants. This thermal treatment is performed in the growth chamber while using RHEED to monitor the evolution of the surface. This is particularly important for silicon-germanium virtual substrates/relaxed buffer layers, where the thermal budget is limited. Specifically, diffusion of germanium from a silicon-germanium relaxed buffer layer into the silicon substrate is observed when annealed at temperatures higher than 850ºC and this condition is to be avoided. [54]

This section is organized as follows. First, the thermal evolution of the RHEED pattern of several different wafers (001)-oriented Si and Ge wafers is described and defines the temperature window for study. Changes in the surface reconstruction with temperature are identified and explained using the desorption or incorporation into the interface of known residual contaminants from the cleaning procedures used. Included in this discussion is the evolution of $Si_{0.83}Ge_{0.17}$ relaxed buffer layers (RBL) capped with a 175-Å-thick tensile-strained Si layer. Next, the RHEED progression of commercially available $Si_{0.83}Ge_{0.17}$ and $Si_{07}Ge_{0.3}$ RBLs is presented. The effect of incomplete oxide desorption on epitaxial Si/SiGe film quality

is then demonstrated by comparing defect densities of films grown oxygen-contaminated and oxygen-free Si and SiGe surfaces using etch pit density measurements and cross-section transmission electron microscopy. Finally, the thermal evolution of these surfaces is explained in terms of known surface contaminants and reconstructions imaged using STM.

### 3.4. 2 Evolution of the silicon surface

As mentioned earlier, the as-loaded substrate is hydrogen terminated. This can be visualized as seen in Figure 3-24, where the diamond lattice is shown. All atoms not on the surface are bonded to 4 other silicon atoms. The atoms on the surface, however, are bonded to two hydrogen atoms each as shown. When evaluated using RHEED, the surface shows an unreconstructed surface. Figure 3-25 shows the RHEED images obtained with the incident electron beam along the [110] and [100] direction.

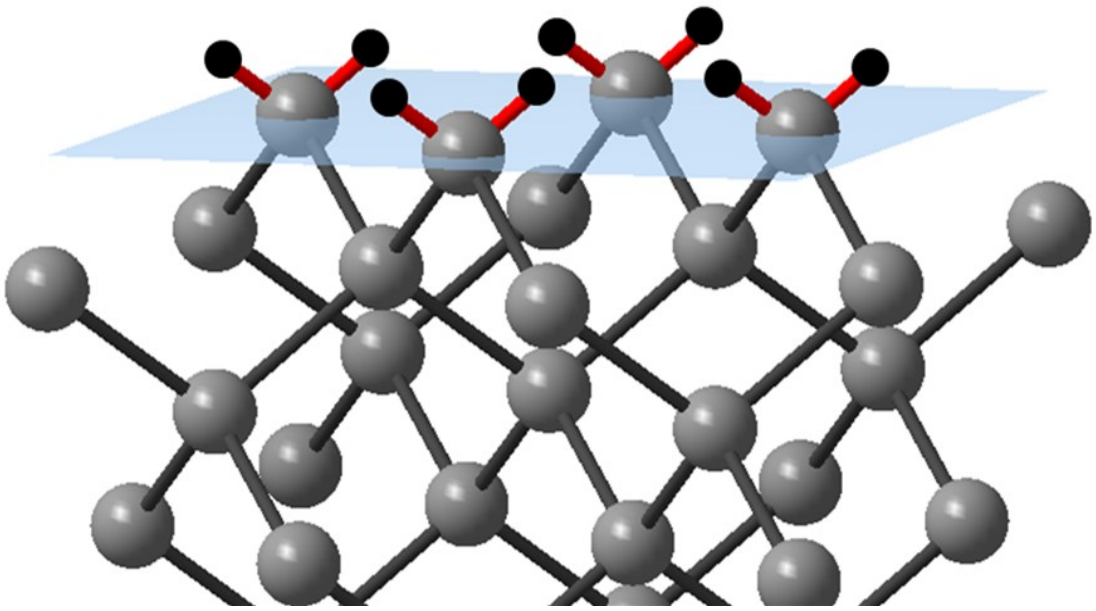

**Figure 3-24:** The hydrogen-terminated (001) Si surface. The blue plane is the (001) plane and separates the surface atoms from the bulk atoms below, with the large grey balls representing silicon atoms. The edges of the plane as shown are along the <100> directions. Each surface atom has two unbonded electrons which pair with atomic hydrogen, passivating the surface.

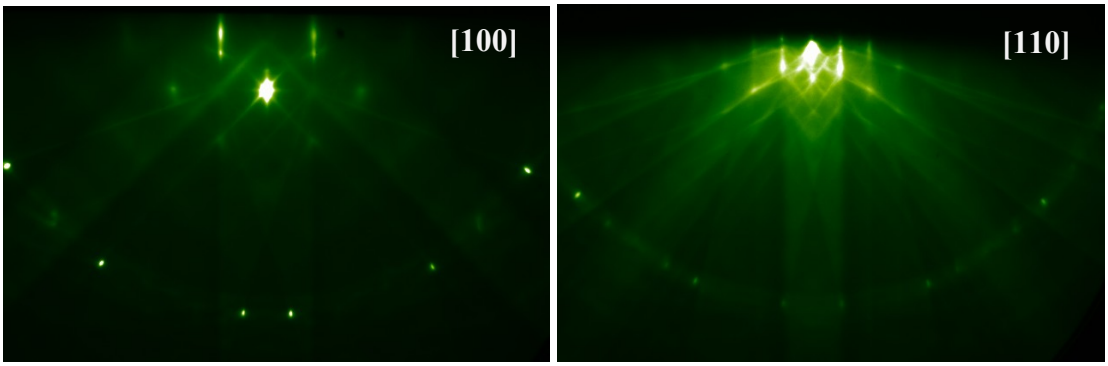


**Figure 3-25:** The RHEED images of the (1×1) H-terminated silicon surface with 30kV electrons incident along the [100] (left) and [110] (right) azimuths.

When loaded into the growth chamber, the substrate temperature is 200ºC. Upon heating to a temperature of approximately 440ºC, the hydrogen desorbs, resulting in the formation of the (2×1) reconstruction and results in the reconstruction of the surface to a (2×1)-like structure as seen in Figure 3-26.

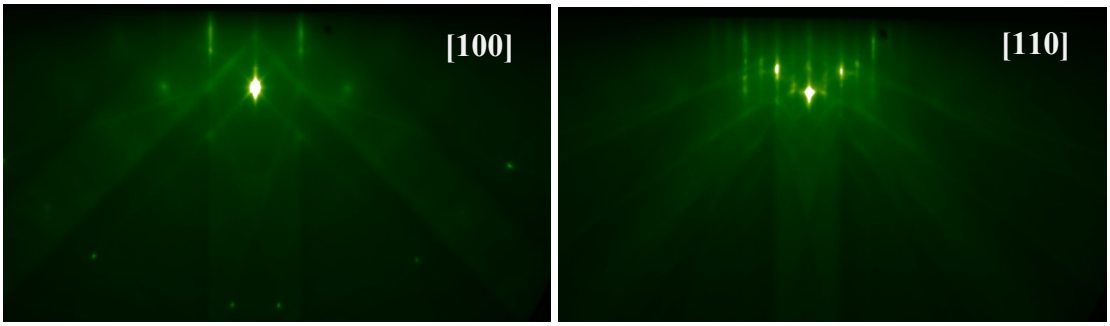


**Figure 3-26** The RHEED images of the (2×1) silicon surface immediately after hydrogen desorption with 30kV electrons incident along the [100] (left) and [110] (right) azimuths. The clean, streaky nature of the spots in the $0^{th}$ Laue zone suggests a clean surface, but this is not the case.

This desorption is accompanied by a brief increase in the hydrogen background from $1.3x10^{-14}$ mBar to $6x10^{-14}$ mBar in the vacuum chamber as measured using a residual gas analyzer. No change in the reconstruction is observed at the highest desorption temperature of fluorine associated with $SiF_2$ near 530ºC.[55] Further heating to 630ºC does result in changes of the surface to a *c*(4×4) structure shown in Figure 3-27. It is to be noted that this reconstruction is along the (100) directions, instead of the (110) directions of a clean silicon surface. As a result, when investigated along the principal (110) directions, the surface appears to be clean. However, with the incident electron beam along the (100) direction, a clear four-fold

symmetry is observed.

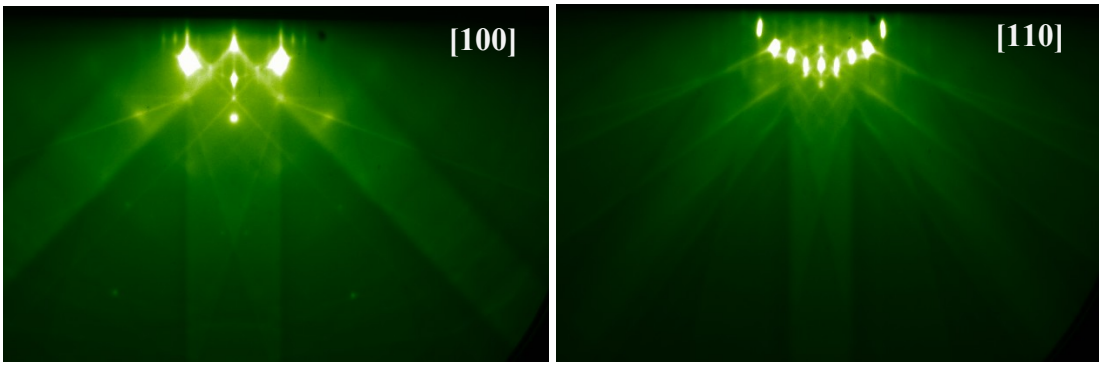


**Figure 3-27:** The RHEED images of the c(4×4) silicon surface immediately after hydrogen desorption with 30kV electrons incident along the [100] (left) and [110] (right) azimuths. The fractional (1/4) orders are clearly seen in the $0^{th}$ Laue zone of the left image, with the 0, ±1/4, ±1/2, ±3/4, ±1, ±5/4 and ±6/4 streaks observed.

At approximately 720ºC, the strength of this pattern decreases, and as seen in Figure 3-28. This temperature is observed to change from growth to growth and is typically between 760ºC and 785ºC. The substrate is then held at a temperature 15ºC higher for a period to 10 minutes to ensure a clean surface and then cooled down to the growth temperature.

To verify that the c(4×4) reconstruction is associated with contaminants on the surface that are desorbed, and not a reconstruction of a clean silicon surface, the substrate is cooled down to 450ºC and then heated up to 700ºC again. This thermal cycling does not affect the (2×1) reconstruction of the surface, indicating that it is stable and clean. This clean (2×1) surface is shown in real space in Figure 3-28 and as imaged using RHEED in Figure 3-29. This reconstruction is stable up to 820ºC which is the maximum temperature achievable in our system. This surface appears to be

stable, in that subsequent cooling to 150ºC and reheating the sample to 820ºC does not result in any changes to this (2×1) reconstruction.

It is found that the RHEED evolution for both, Si wafers and Si-capped $Si_{0.83}Ge_{0.17}$ relaxed buffer layers (RBLs) follow a similar progression. For the Si-capped RBLs, the *c* (4×4) appeared at a reduced temperature of 570ºC, weakened near 730ºC and disappeared at a higher temperature close to 750ºC. The temperature at which the *c* (4×4) reconstruction is observed on tensile-strained Si is consistently lower than the unstrained Si surfaces. This observation is consistent with theoretical [56] and experimental [57] studies of the effect of tensile strain on the mobility of dimers on (001) oriented silicon surfaces. Theoretical calculations [56] predict a 9% decrease in the energy barrier to surface diffusion for 1% tensile strain. Applying this result to the case of stained-Si on $Si_{0.83}Ge_{0.17}$ with 0.69% strain yields a reduction of 6.1% in the activation energy for dimer mobility. This corresponds well with our observation of a 6.2% decrease in the temperature where the *c* (4×4) reconstruction is first observed, suggesting that the observed discrepancy in temperature is, in fact, associated with the contribution of strain to dimer mobility.

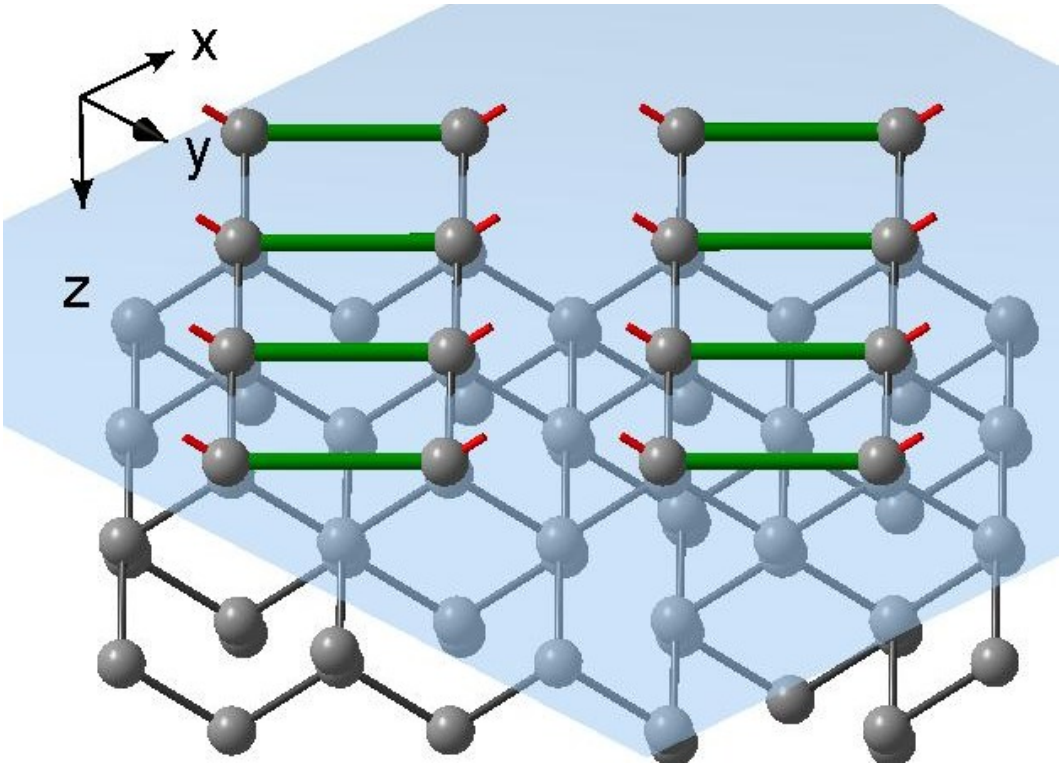


**Figure 3-28:** The (2×1) reconstructed (001) silicon surface, showing the bond direction (along the [110] direction in this case) and reduction in total number of unpaired electrons from 2 per atom to 1 per atom.

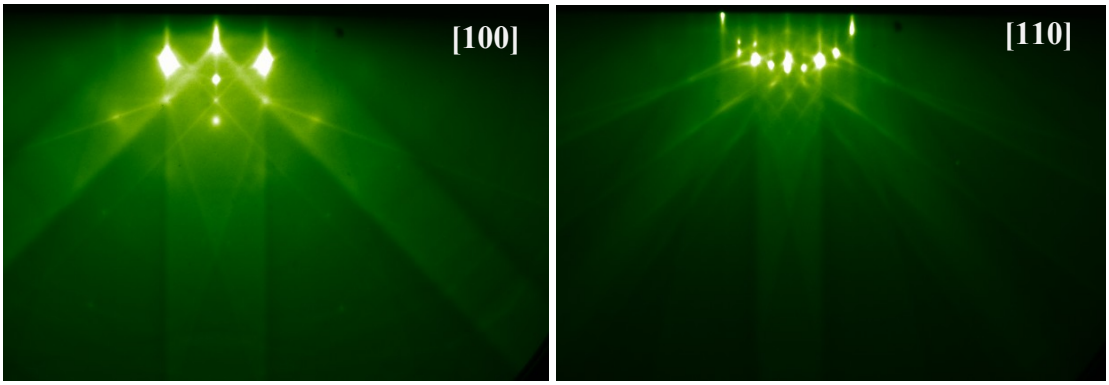


**Figure 3-29:** The clean (2×1) reconstructed silicon surface as imaged using RHEED with 30keV electrons along the [100] (left) and [110] (right) directions.

### 3.4.3 Evolution of the Ge surface

Ge substrates were cleaned using a sequential oxidation in $NH_4OH$ and deoxidation in aqueous HCl with a final DI rinse to remove HCl. [58] Unlike the HF-based process for Si and SiGe wafers, the surface of the clean Ge wafer is not hydrophobic, necessitating a longer DI rinse (30 sec) and longer drying time with nitrogen (2 min). As with the Si wafers, the Ge wafers were outgassed at 150ºC in the UHV introduction chamber.

The evolution of the RHEED pattern of a chemically cleaned Ge wafer was found to be different from that of Si surfaces. Cleaned, as-loaded wafers exhibited a (1×1) reconstruction as shown in Figure 3-30. Upon heating the substrate, a (2×1) reconstruction shown in Figure 3-31 was observed once these residual suboxides were desorbed. Since the temperature at which the transition was observed is outside the usable range of the pyrometer, it was necessary to estimate the wafer temperature by extrapolating the pyrometer temperature from the linear relationship between the pyrometer and thermocouple temperatures observed at higher temperatures. The reconstruction change from the (1×1) to (2×1) occurred at the extrapolated wafer temperature of 395ºC. This is close to the desorption temperature for GeO which is reported to be 400ºC. [59] This observation is also consistent with XPS and ultraviolet photoelectron spectroscopy (UPS) studies of water-rinsed germanium oxides, where the water was found to remove $GeO_2$ but not GeO.[60] Further increasing the wafer temperature to 670ºC did not result in any change in the surface reconstruction. It is expected that some carbon contamination from the wet chemical

treatment is present.[61] However, we do not observe any evidence of GeC formation in the reconstruction pattern, based on the lack of diffraction peaks corresponding to the theoretical lattice constant of 4.52 Å. [62] This observation is consistent with the prediction that bulk germanium carbide is not stable [61], we expect that the residual carbon is incorporated in the germanium and does not contribute extended defects in the homomorphic overgrowth. [63, 64]

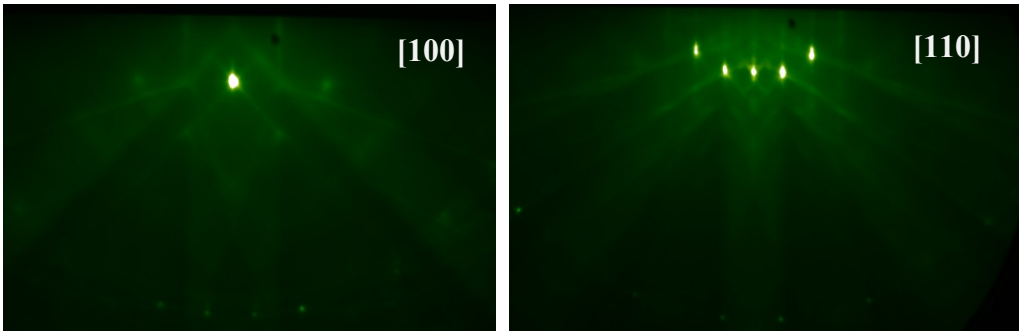


**Figure 3-30:** RHEED patterns of germanium surfaces imaged along the [100] and [110] directions showing the (1×1) reconstruction of the as-loaded Ge wafer

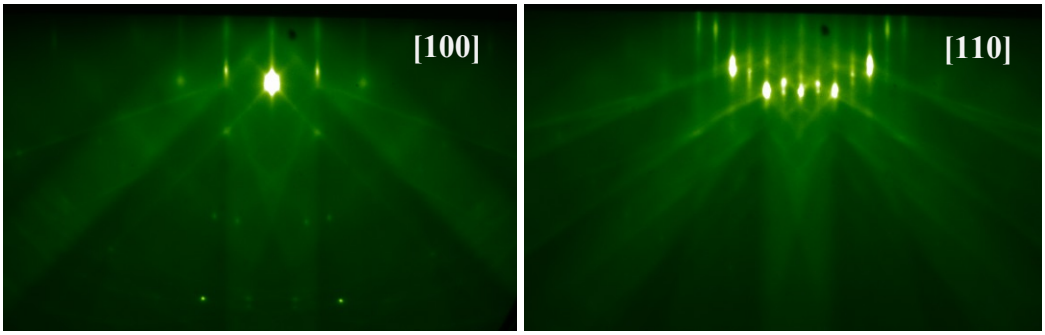


**Figure 3-31:** The (2×1) reconstruction of clean germanium

### 3.4.4 Evolution of the SiGe surface

The evolution of the RHEED pattern from $Si_{0.83}Ge_{0.17}$ and $Si_{0.7}Ge_{0.3}$ surfaces was found to contain characteristics similar to that of germanium and silicon. The wafer preparation for the un-capped SiGe RBL wafers is the same HF etch, rinse, and dry process that was used for bare silicon wafers. The as-cleaned SiGe RBL wafers displayed the (1×1) reconstruction when loaded into the growth chamber as shown in Figure 3-32 (a) and (b), consistent with a hydrogen-terminated silicon phase and an unreconstructed oxide-contaminated germanium phase. Upon heating, this reconstruction was found to be stable until 430ºC, beyond which the (2×1) reconstruction shown in Figure 3-32 (c) and (d) was observed. This reconstruction change matches the hydrogen desorption temperature of silicon, indicated that the oxygen desorption from germanium that occurs at lower temperature is obscured by the existence of hydrogen on the sample surface. As with silicon surfaces, no transition was observed at the $SiF_2$ desorption temperature. However, unlike silicon, further heating did not result in the c (4×4) reconstruction. Instead, the RHEED pattern, shown in Figure 3-32 (e) developed spots near 690ºC for the $Si_{0.83}Ge_{0.17}$ and close to 650ºC for $Si_{0.7}Ge_{0.3}$ surfaces. These spots are adjacent to the 1st order streaks in the 0th Laue zone.

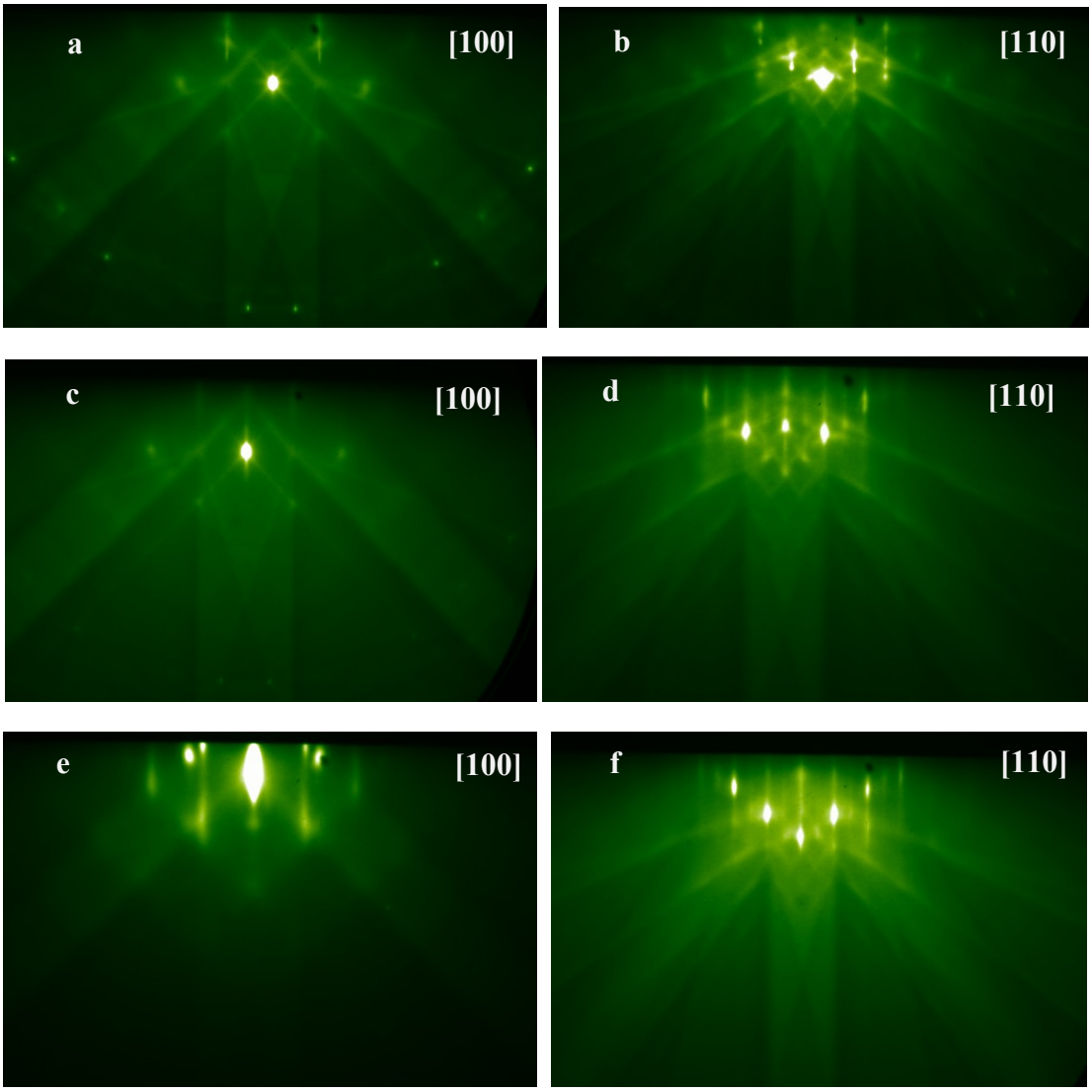


**Figure 3-32:** RHEED patterns of $Si_{0.7}Ge_{0.3}$ surfaces imaged along the [100] (a,c,e) and [110] (b,d,f) azimuths. (a) and (b) show the (1×1) reconstruction of the as-loaded $Si_{0.7}Ge_{0.3}$ RBL. (b) and (d) show the (2×1) reconstruction at 610ºC observed after hydrogen desorption. As the sample is heated, (2×1) reconstruction is preserved (e,f, at 800ºC), with the β-SiC transmission pattern observed when imaged along the [100] direction(f) This pattern was preserved when the temperature was reduced to 450ºC.

Analysis of the positions of these spots yielded a lattice parameter of 4.37 Å ± 0.01 Å, which is consistent with β-SiC particulates of lattice parameter 4.36 Å

oriented along the <100> directions. [65, 66] In addition, the correspondence between the RHEED-measured lattice constant of the β-SiC spot and the expected value suggest that germanium is not incorporated into the carbide precipitates. Reducing the angle of incidence of the electron beam from ~2.5º to ~0.5º enhanced the visibility of this pattern. For the $Si_{0.7}Ge_{0.3}$ surface, the intensity of this spot increased with temperature and was found to be stable beyond 700ºC and up to 820ºC. Cooling to the growth temperature of 450ºC was found to have no effect on either the β-SiC pattern, or the (2×1) surface reconstruction.

### 3.4.5 Effect of oxide desorption on epitaxial film quality

While RHEED allows study of the surface of the crystal, it provides no information on the quality of the crystal, either in terms of crystallographic defects or electrically active defects. The effect of the nature of the surface on the quality of the crystal is determined by growing several epitaxial layers, both on silicon wafers and on silicon germanium relaxed buffer layers.

1. Sample 1: 0.5µm-thick silicon on silicon with thermal treatment prior to growth at a thermal desorption temperature $T_D$ of 770ºC.
2. Sample 2: Strain-balanced silicon germanium p-i-n diode grown on a $Si_{0.83}Ge_{0.17}$ relaxed buffer layer (RBL) with $T_D$=670ºC i.e. on a c(4×4) surface
3. Sample 3: The same structure as sample 2 but with $T_D$=785ºC i.e. on a (2×1) surface
4. Sample 4: A $Si_{0.7}Ge_{0.3}$ layer on a $Si_{0.7}Ge_{0.3}$ RBL with $T_D$=586ºC

5. Sample 5: A structure similar to sample 4 but with $T_D$=795ºC

These samples were subsequently analyzed for relaxation using XRD as mentioned in Chapter 2. The defect density in these films was then determined using a defect-selective etching technique. While several etches exist for this purpose [67-70], the Secco etch [67], is used. As with all defect-selective etchants in the silicon germanium material system, this etch is a two-step process. First, an oxidizing agent strong enough to react with atoms near a dislocation core, but too weak to react with atoms outside this area is causes local oxidation near this dislocation core. Next, the oxidized silicon near this dislocation core is dissolved in a suitable etchant. The Secco etch uses a 1:2 mixture of 0.15 M $K_2Cr_2O_7$ and 49%HF. This etch is carried out in an ultrasonic bath to enhance delineation of defects. The etch rate for silicon in this solution is typically 0.5 μm/min, and higher for silicon germanium, up to approximately 1 μm/min. Extended etching will reveal defects present in the entire film, including the substrate-epilayer interface, while shorter etch times will only reveal defects in the film. Thus, the etching time is determined by whether the defect density in the film or at the interface is required. The number of defects is determined by counting the number of pits using an optical microscope at an appropriate magnification over 5 different randomly chosen areas. The efficacy of this method at delineating defects is verified by etching a sample with a known etch pit density (EPD) and verifying that the measured EPD is close to the specified value. In this analysis, the standard used is the $Si_{0.83}Ge_{0.17}$ RBL, which is specified by the manufacturer to have an EPD < $2x10^5$ $cm^{-2}$. When this RBL is etched for 30 seconds

to a depth of 0.4 μm, the measured EPD is (2.8±1.1) $\times 10^5$ $cm^{-2}$, which is within the specified value, demonstrating the suitability of this process. The results for the rest of the samples are discussed below.

*Sample 1*

This structure was an n-dopant calibration structure with 0.5-μm-thick antimony-doped silicon ($n=9x10^{18}$ $cm^{-3}$) layer grown on an intrinsic silicon substrate. Since this sample has no misfit strain associated with it, no misfit defects are expected. The sample was then etched as described above for 10 seconds to reveal defects in the epitaxial film. A micrograph of the etched layer is shown in Figure 3-33. The defect density of 60 $cm^{-2}$ was measured. All defects identified were isolated point defects, as seen in the figure.

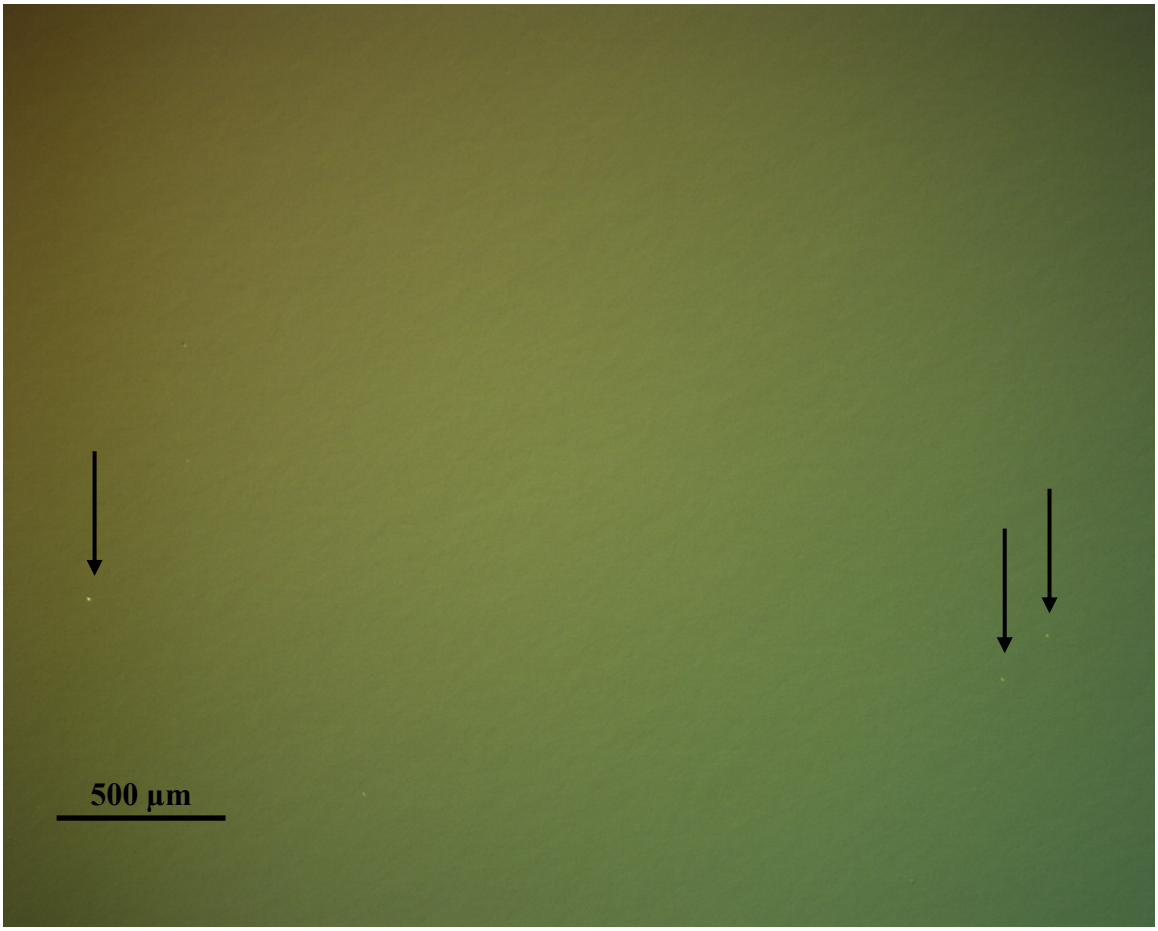


**Figure 3-33:** A 50x optical micrograph with a field of view (FOV) of 9.3 $mm^2$ of an etched silicon epilayer, highlighting etch pits, highlighted with arrows to aid visibility, corresponding to defects.

*Sample 2*

This structure was a strain-balanced 1.4 µm thick p-i-n diode with a 50 period 70 Å Si/27 Å $Si_{0.45}Ge_{0.55}$ active layer as the central undoped layer. This structure was grown on a commercially available relaxed buffer layer (described in detail later in this thesis). For this sample, a $T_D$ of 680ºC was chosen and the *c* (4×4) reconstruction was observed immediately prior to growth. While this structure is strain-balanced as designed, the final structure grown was measured to have a residual strain of 0.08%

using XRD. In addition, XRD measurements also revealed that there is no relaxation of the strain in the film in this sample. As a result, no misfit dislocations associated with the growth are expected. The sample is then etched for 20 seconds to reveal defects in the top 0.3 μm contact layer. The EPD for this sample was found to be $6x10^4$ $cm^{-2}$, as seen in Figure 3-34. In addition to isolated defects, linear defect features are also observed as shown. These features are oriented exclusively along the <110> directions. Such features are consistent with two different types of crystallographic defects – misfit dislocations and stacking faults. However, there are two reasons to doubt that these are misfit dislocations:

i. XRD measurements revealed no layer relaxation in the film, and hence, no misfit segments are expected
ii. Misfit segments are confined to the substrate-strained epilayer interface. In this case, these linear features are found 1μm above this interface, making it unlikely that these features are misfit dislocations.

The areal density of these stacking faults is $2.6x10^4$ $cm^{-2}$. With an average length of 3.7 μm, the linear density of these defects is 9.5 $cm^{-1}$.

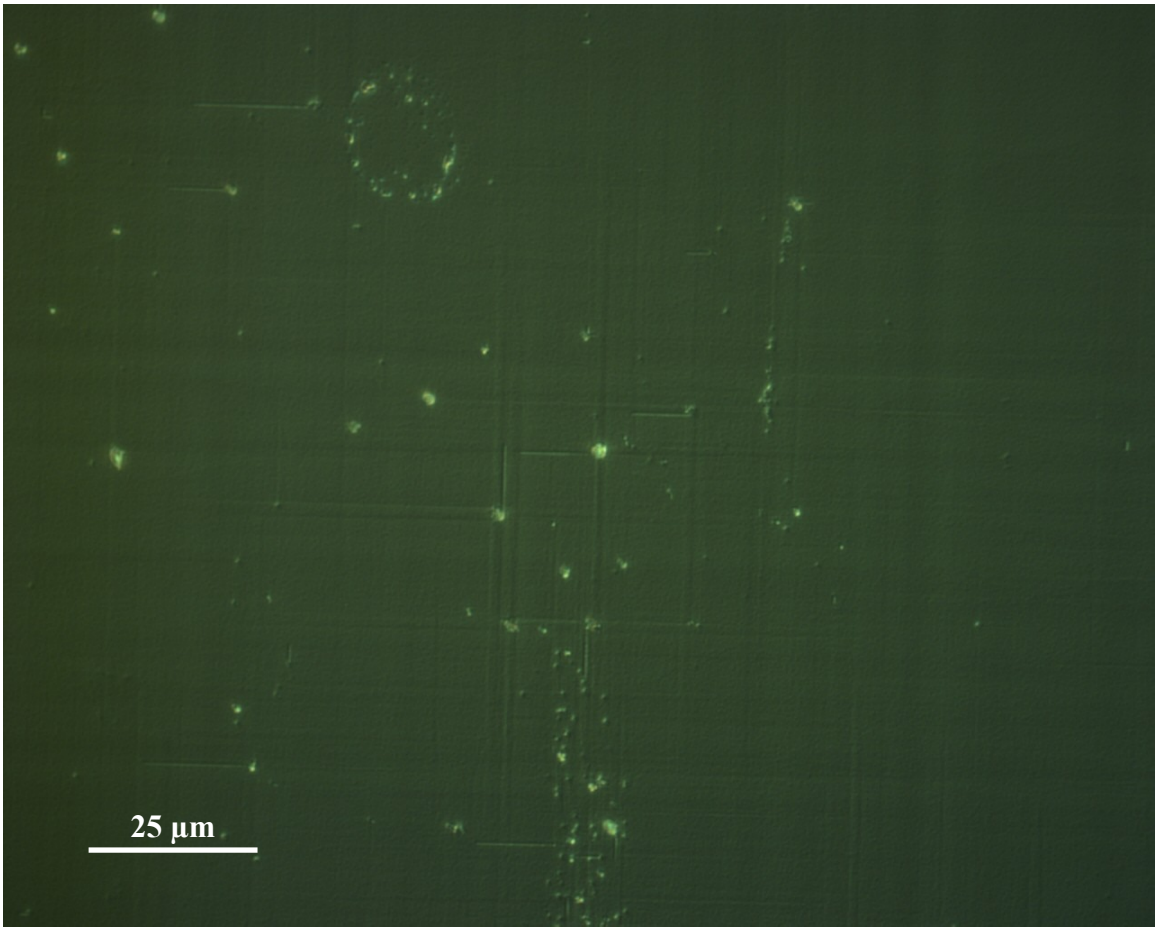


**Figure 3-34:** A 1000x optical micrograph with an FOV of $2.2x10^{-2}$ $mm^2$ of an etched silicon germanium epilayer, highlighting etch pits. Also seen are several linear features corresponding to stacking faults

*Sample 3*

This structure is identical to the one described above, with the only difference being that the $T_D$ chosen for this sample was 785ºC. As with sample 2, based on XRD measurements, there is no relaxation in the film. This sample was etched for 10 seconds, revealing an EPD of $1.2x10^5 cm^{-2}$ which is higher than that of sample 2. However, no stacking faults are observed.

The effect of these stacking faults on device performance was determined by fabricating mesa p-i-n diodes with passivated sidewalls and testing them electrically. Fabrication details are discussed in depth later in this thesis in Chapter 5. V-I characteristics for these two samples are obtained using a HP4156B semiconductor parameter analyzer and are shown in Figure 3-35. It is found that the diodes fabricated from sample 2 are poor with very high reverse leakage currents and poor turn-on characteristics. Such a high reverse leakage current precludes the use of this sample for use as photodetector applications where low dark currents are required.

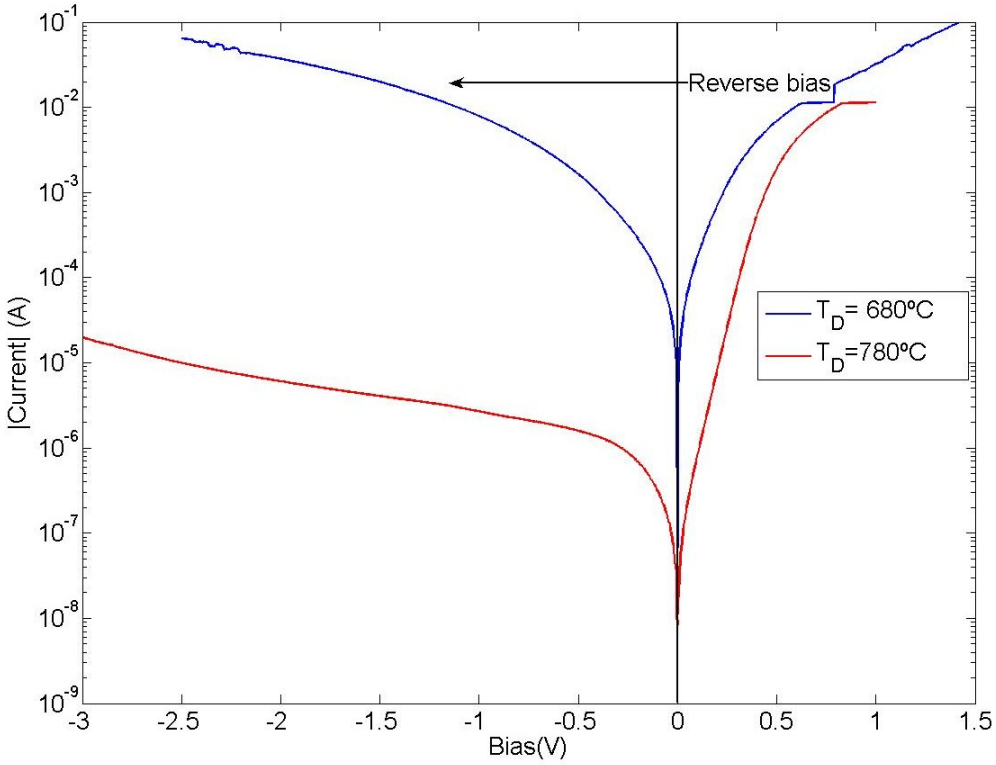


**Figure 3-35:** V-I characteristics of diodes fabricated from samples 2 and 3. Samples grown with lower $T_D$s have poorer characteristics, with extremely high dark currents, making them unsuitable for device applications.

*Sample 4*

This sample consisted of a 0.625 μm thick $Si_{0.7}Ge_{0.3}$ layer with an 180-Å-thick Si layer 75nm below the top. This layer structure was grown on a $Si_{0.7}Ge_{0.3}$ RBL with $T_D$ =590ºC. As with sample 2, it is expected that the substrate-epilayer interface is contaminated. This sample was etched for 10 seconds, revealing a high defect density of $5x10^5$ $cm^{-2}$ as shown in Figure 3-36. In addition, a very high areal stacking fault density of $8.8x10^6$ $cm^{-2}$ is measured. The average length of these stacking faults is 6.2 μm, yielding a linear density of 5460 $cm^{-1}$. Further evidence that these defects are stacking faults and not misfit segments is obtained from cross-section transmission electron microscopy imaging (TEM). This is also seen in Figure 3-37, where a high-resolution TEM image of the cross-section clearly shows dark lines originating at the substrate-epilayer interface, continuing through the silicon layer and to the surface. From this image, these defects are measured to lie on the {111} planes. This is unlike the behavior of misfit defects, which are confined to the interface and whose threading arms are not confined to any particular crystal plane. Counting the number of stacking faults over several images spanning 6.1 μm of the substrate-epilayer interface, a stacking fault density of 5500 $cm^{-1}$ is obtained, which almost identical to the value obtained from the Secco etch.

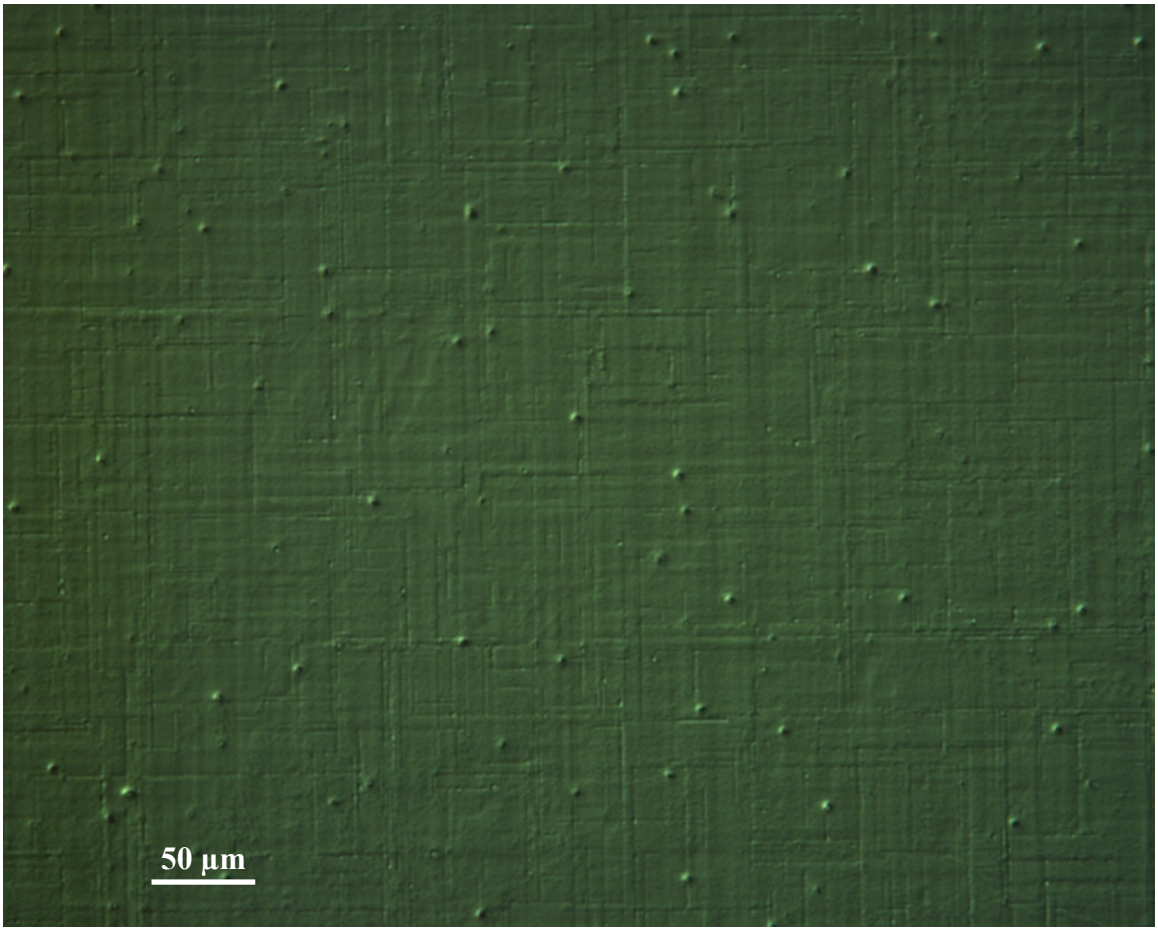


**Figure 3-36:** A 1500x optical micrograph with an FOV of $9.9x10^{-3}$ $mm^2$ of an etched silicon germanium epilayer, highlighting etch pits. For this sample, grown with $T_D$=586ºC, the stacking fault density is exceedingly high

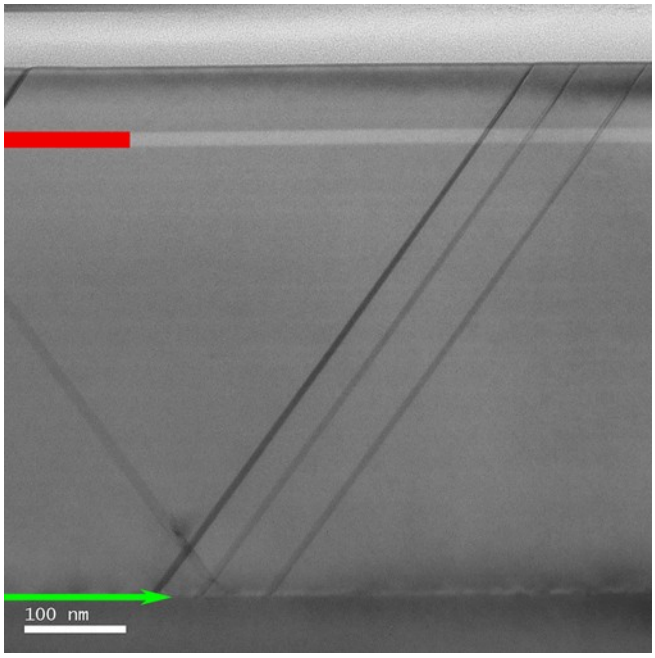


**Figure 3-37:** A bright field high resolution cross-section TEM image of sample 4 taken with the incident beam along the [220] direction. In the FOV, 5 stacking faults are visible, the origin of 4 of which is seen at the interface. The substrate-epilayer interface located at the green line, with the arrow pointing toward the <110> direction. The thin silicon layer is marked by the red box.

*Sample 5*

This sample is identical to sample 4 except the silicon layer thickness, which is reduced to 120 Å. To ensure a clean surface, a thermal desorption temperature of 795ºC is used. As expected, when this sample was etched to a depth of 0.3 μm in 10 seconds, no stacking faults were found. The EPD for this sample was found to be $1.9 \times 10^5$ $cm^{-2}$, which is typical for a RBL [71].

The results for these 5 samples are summarized in Table 3-1, clearly showing the correlation between an insufficient thermal desorption process and a poor epitaxial film. In addition, the extremely detrimental effect of even a moderate

stacking fault density on device electrical performance has been demonstrated. This knowledge allows for the optimum choice of thermal desorption temperature, ensuring high crystalline quality.

| Sample # | Thermal desorption temperature $T_D$ (ºC) | Etch pit density ($cm^{-2}$) | Stacking fault density ($cm^{-1}$) |
|---|---|---|---|
| 1 | 770 | 60 | 0 |
| 2 | 680 | $2.6x10^4$ | 9.5 |
| 3 | 785 | $1.2x10^5$ | 0 |
| 4 | 586 | $5x10^5$ | 5460 |
| 5 | 795 | $1.9x10^5$ | 0 |

**Table 3-1**: A summary of the effect of $T_D$ on the stacking fault density

### 3.4.6 Understanding the evolution of the surface

The *c* (4×4) reconstruction on silicon has been attributed to a combination of missing dimers, and parallel and mixed ad-dimers on the surface. It has been shown that exposing clean silicon to high levels of hydrogen [72] and oxygen [73] in UHV can facilitate the *c* (4×4) reconstruction. Hydrogen is an unlikely participant in the surfaces studied here, because the required high hydrogen surface density is not present at 630ºC, when the *c* (4×4) occurs, as the chemisorbed hydrogen from the HF dip is desorbed at a lower temperature.

It is also unlikely that the observed reconstruction is due to carbon. It has been reported that the (2×1) reconstruction is stable with up to approximately 0.03

monolayers of carbon coverage, with a two-phase surface of the (2×1) and *c* (4×4) up to about 0.08 ML of carbon coverage. [74] Secondary ion mass spectroscopy (SIMS) analysis of typical Si films grown in this chamber reveal an interfacial carbon concentration of $1.97 \times 10^{13}$ at-cm$^{-2}$ for Si surfaces, equivalent to 0.03 monolayers, which is at the edge of the single-phase (2×1) surface. Furthermore, the expected spots in the RHEED pattern associated with the formation of β-SiC particulates at higher temperatures for the surfaces that show the carbon-associated *c* (4×4) is not observed. [75]

While high doses of oxygen at room temperature (~$10^{-5}$ Torr-s) [73] were required to form the *c* (4×4) reconstruction, it is noted that for molecular oxygen on (001) Si, the sticking coefficient is low (0.01-0.005). As a result, only 0.03-0.06 ML is adsorbed for every $10^{-5}$ Torr-s dose, yielding a surface with oxygen concentration that is comparable to the typical residual oxygen concentration for the cleaning procedure used, which has been measured by other groups to be ~0.1 ML by SIMS [49] and XPS [53]. The *c* (4×4) reconstruction was observed and ascribed to periodic missing Si dimers created during the desorption of SiO for this level of oxygen contamination. [73, 75] It is important to note, however, that the reconstruction is not that of adsorbed oxygen atoms. This is because there is no periodicity to the adsorption sites for oxygen on the (001) Si surface [76] and the activation energy for surface diffusion of oxygen on silicon (2.4 eV) is larger than that of silicon atoms (0.65 eV) and Si dimers (1.3 eV) [77], making rearrangement of surface oxygen atoms significantly less likely than that of silicon atoms and dimers. a*b initio* total energy and electronic structure calculations [72] reveal that the energy of surfaces

with this reconstruction are higher than that of the (2×1) reconstructed Si surface. This energy difference explains the irreversibility of the *c* (4×4) to (2×1) transition near 750ºC upon subsequent temperature cycling.

The metastable *c* (4×4) reconstruction on Si requires the existence of dimer vacancies and ad-dimers at specific lattice sites corresponding to the *c* (4×4) structure. On a SiGe surface, the Si and Ge atoms are distributed randomly due to the complete miscibility of Ge in Si [78]. To our knowledge, *ab initio* calculations comparing the energies of *c* (4×4)-reconstructed and (2×1)-reconstructed random SiGe surfaces have not been reported. These experiments suggest that the *c* (4×4) reconstruction on SiGe is unstable, though a combination of more sensitive surface analysis techniques, such as STM, and *ab initio* calculations are necessary to prove this.

The results from all the epitaxial samples detailed here suggest that the residual oxide on a SiGe surface is a two-phase mixture. The implication of this finding is that to obtain an oxide-free SiGe surface conducive to defect-free epitaxial film growth, it is necessary to heat the wafer up to the temperature where a clean silicon surface is obtained. This observation is consistent with XPS studies of ultraviolet ozone-prepared SiGe oxides which were found to be a two-phase mixture of $SiO_2$ and $GeO_2$.and their suboxides, SiO and GeO. [79] Figure 3-38 summarizes the results of this RHEED study, showing a schematic form of the reconstruction and expected contaminants on the surface of the wafers as a function of temperature.

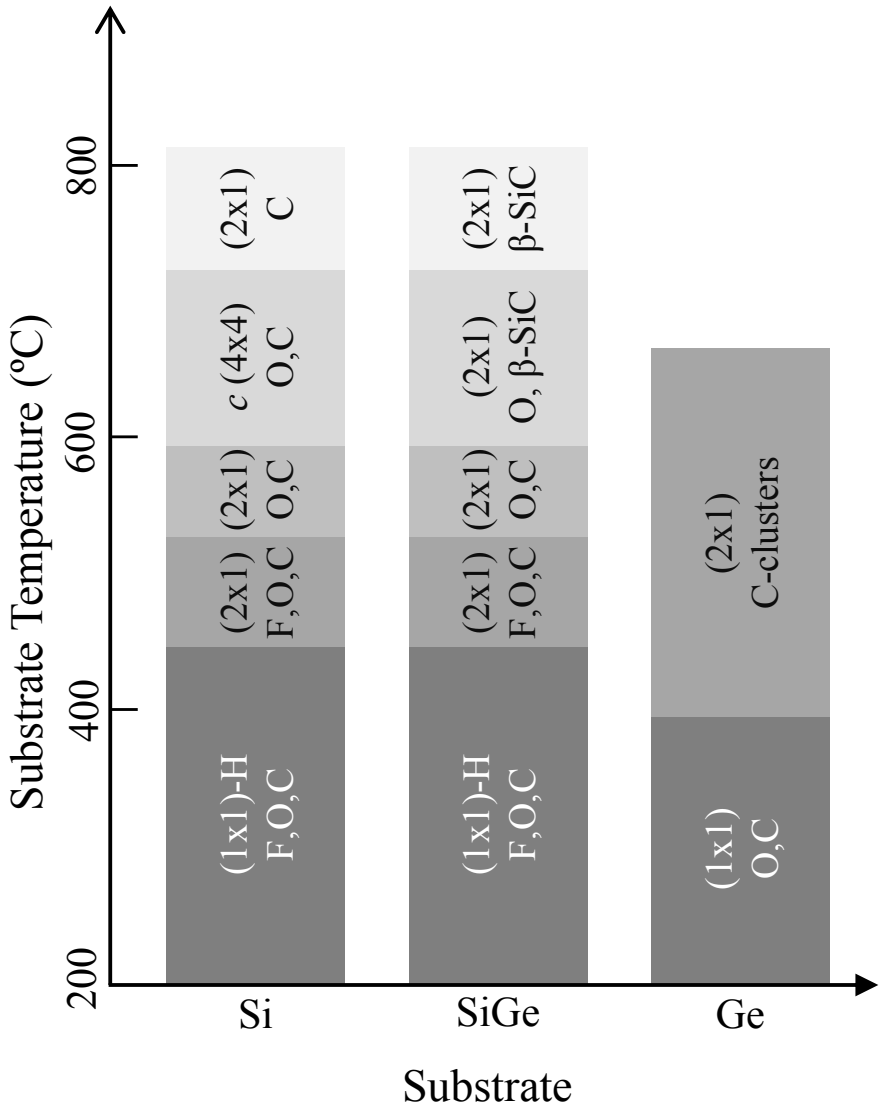


**Figure 3-38:** A schematic summarizing the surface state of (001)-oriented unstrained Si, SiGe and Ge surfaces as a function of temperature.

# Chapter 4 : Material Modeling

## *4. 1 Introduction*

The design of a semiconductor heterostructure for optical applications requires knowledge of both, the electronic and optical properties of all layers involved. The material bandgaps determine the threshold for optical absorption while band offsets determine the potential depth of a quantum well and whether the electrons and holes are localized in the same layer or adjacent layers. The effective masses of the carriers determine both, transport properties and the energy levels of confined states. From an epitaxial standpoint, the critical thickness puts an upper bound on the ultimate thickness of a strained layer that can be grown without relaxation in the film. The variation of the impact ionization coefficients for holes and electrons with both, electric field and composition enables the design of avalanche multiplication regions and calculation of expected performance characteristics. Knowledge of the refractive index allows the design, where possible, of optical waveguides as well as calculation of reflection losses from bare semiconductor material.

In this chapter, the different models used to determine these properties will be detailed. In addition, the mathematical techniques used to solve Schrödinger's equation for the carriers in different structures are also presented. The specific design concepts of this thesis – exploring the limits of critical thickness and the utilization of the band offsets – will also be discussed in detail.

## *4.2 Critical thickness*

The lattice constant of silicon is 4.2% smaller than that of germanium. As a result, any epitaxial SiGe layer grown on a silicon substrate is compressively strained. Similarly, a SiGe film grown on a germanium substrate is in tension. The more general case of a $Si_{1-x}Ge_x$ films grown on $Si_{1-y}Ge_y$ substrates ($0 \leq x, y \leq 1$) yields film either in tension ($x > y$) or compression ($x < y$). This strain is accommodated by a tetragonal distortion of the cubic lattice, as can be seen in the lower panel in Figure 4-1. With an increase in thickness of the epitaxially grown layer, the strain energy in the film increases and beyond a certain thickness, called the critical thickness $h_c$, it is energetically favorable for the strain to be relieved plastically through either partial or complete relaxation of the film. This involves breaking of a bond in the lattice, and results in a grown layer with a lattice constant that is different from that of the substrate with a so-called misfit dislocation at the substrate-layer interface. This is also shown in the lower panel of Figure 4-1.This misfit dislocation can be visualized as an extra half plane (in the case of compressive strain) or a missing half plane (in the case of tensile strain) of atoms threading the substrate-epilayer interface in the crystal. As will be seen in the following sections, relaxation in the film causes a dramatic change in the electronic properties of the material. In addition, threading dislocations are generated with rise through the epitaxial layer, creating a number of electronically active defect states throughout the epitaxial layer. It has been widely reported [80] that misfit defects in an active layer are linked with poorer device performance and increased reverse leakage currents. With layer relaxation, the optical and thermal properties also change. To this end, it is important to be able to calculate

the expected value of the critical thickness of a $Si_{1-x}Ge_x$ film grown on a $Si_{1-y}Ge_y$ substrate.

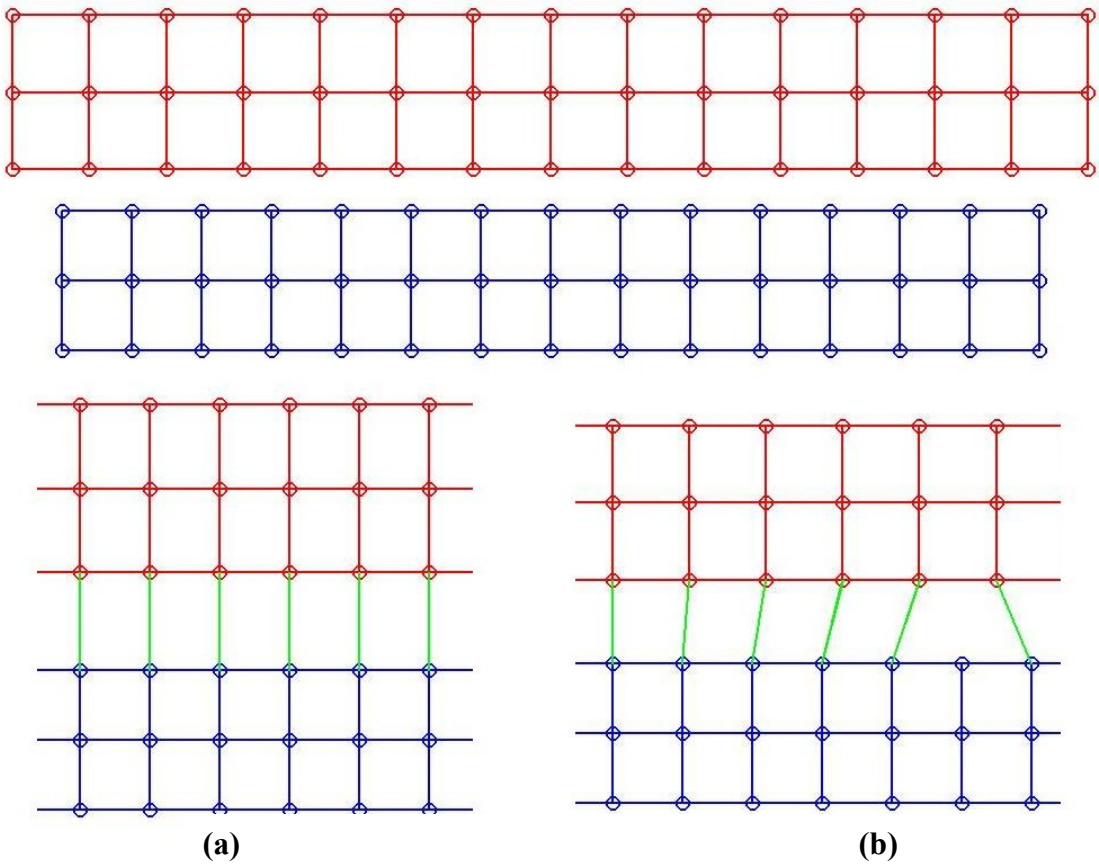


**Figure 4-1:** A schematic of the substrate (blue) – epilayer (red) interface of a lattice-mismatched film. (a) shows the accommodation of strain through tetragonal distortion of the crystal lattice, while (b) shows relaxation of the grown layer, resulting in a dangling bond at the interface.

The theoretical framework for the calculation of the critical thickness of strained epilayers is described by Matthews and Blakeslee [81]. It should be noted, however, that experimentally, defect-free layers thicker than calculated by equilibrium theories such as the Matthews-Blakeslee formalism have been grown by

different groups [82] due to the existence of kinetic barriers to the nucleation of misfit dislocations. The ultimate limit is that of the Matthews-Blakeslee formalism, and it is instructive to understand it first. This approach involves balancing the force exerted by the elastic misfit strain and the tension in the dislocation line. At the onset of relaxation, these two forces are in balance, and the critical thickness is given by

$$h_c \approx \frac{b}{4\pi f}\frac{1}{(1+\nu)}\left[\ln\left(\frac{h_c}{b}\right)+1\right] \qquad \textbf{(4.1)}$$

Here b is the magnitude of the Burgers vector of the dislocation,

$f = a_{film}/a_{substrate} - 1$ is the misfit, ν is Poisson's ratio,.

In the SiGe material system, the misfit defects are neither pure edge nor screw dislocations [83], but are a mixture of the two, and are called the a/2 <110> 60º dislocations. The magnitude of the Burgers vector for these is $a_{substrate}/\sqrt{2}$ and the angles θ and λ are equal to 60º. With the experimentally determined value of ν, the critical thickness can be calculated. Figure 4-2 shows the critical thickness as a function of composition for strained layers grown on a Si substrate (shown in blue) and a $Si_{0.83}Ge_{0.17}$ substrate (shown in red). The plot shows that the critical thickness rapidly decreases to less than 10 nm for composition mismatches that are larger than 10%.

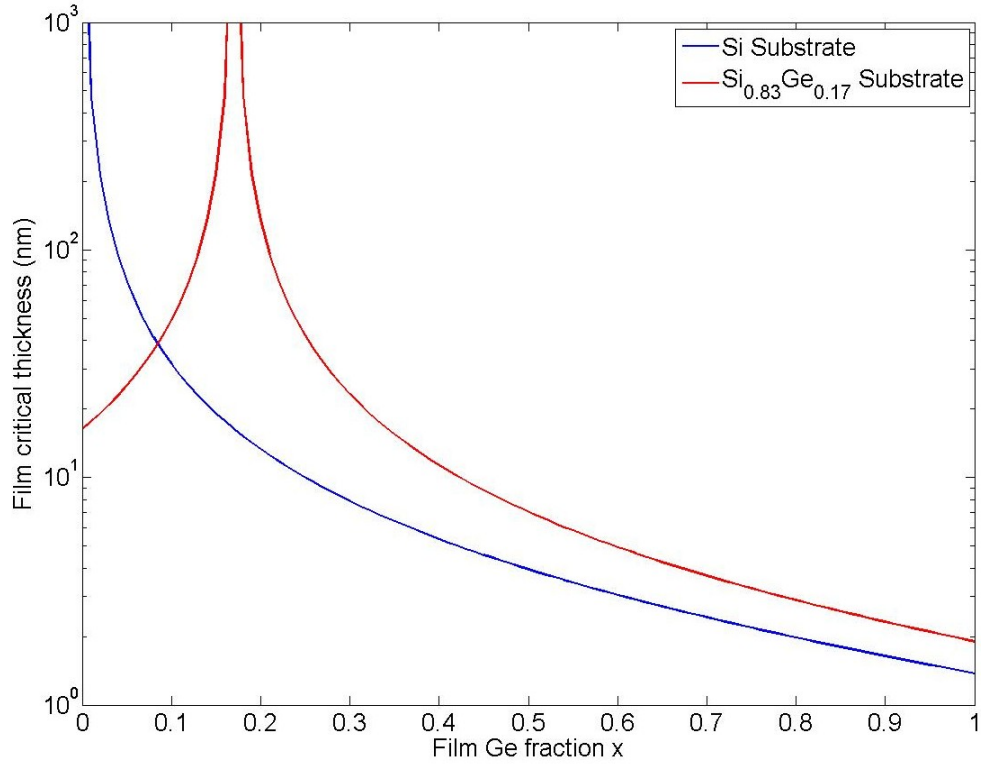


**Figure 4-2:** Equilibrium critical thickness of strained layers grown on Si and $Si_{0.83}Ge_{0.17}$ substrate.

As mentioned earlier in this section, it is possible to grow films of thickness larger than the Matthews-Blakeslee critical thickness. This is because there is a kinetic barrier to the relaxation process that exists. Specifically, there are two distinct processes that occur during relaxation – the nucleation of a misfit dislocation and the extension of this through the process of dislocation glide – both of which cause the strain in the film to relax. These processes have been extensively studied as a function of temperature by Houghton [84], and this formulation is used here. First, the effective stress in GPa acting to extend a misfit dislocation is derived as

$$\tau_{eff}^{s} = f_{Ge-Si}\,\mu\cos\psi\left(\frac{1-\nu}{1+\nu}\right)\left(x-\frac{0.55}{h}\ln\frac{4h}{b}\right) \qquad \textbf{(4.2)}$$

where $f_{Ge\text{-}Si} = 0.0418$ is the lattice mismatch of Ge on Si, $\mu = 64$ GPA is the shear modulus of SiGe, $\psi$ is the angle between the strained interface normal and the slip plane (35º) and h is the film thickness. In this kinetic model, the film thickness h is related to the growth rate R(t) and elapsed time $t_e$ as $h(t) = \int_0^{t_e} R(t)dt$ .For the case of SiGe films on Si, the above values can be substituted into Equation 4.2 yielding a value of $\tau_{eff}$ in GPa as

$$\tau_{eff}^{s} = 3.88\left( x - \frac{0.55}{h} \ln 10h \right) \tag{4.3}$$

An increase in this strain causes an increase in both, the dislocation glide velocity V(t) and the dislocation nucleation rate N(t)/dt according to

$$\frac{dN}{dt} = BN_0 \left( \frac{\tau_{eff}^{s}}{\mu} \right)^{m} \exp\left( -\frac{Q_N}{kT} \right)$$
$$V(t) = V_0 \left( \frac{\tau_{eff}^{s}}{\mu} \right)^{n} \exp\left( -\frac{Q_V}{kT} \right) \tag{4.4}$$

where B, $V_0$, m and n are material constants obtained by fitting experimental data. Here, $N_0$ is the initial number of dislocations that act as nucleation sites, which are typically defects or contaminants at the substrate-epilayer interface. $Q_N$ and $Q_V$ are the kinetic barriers to dislocation nucleation dislocation glide respectively. The instantaneous rate of change of strain in the film is given as

$$\frac{d\varepsilon}{dt} = N(t)V(t)b\cos\lambda \tag{4.5}$$

Substituting the expressions for N(t) and V(t) from above and integrating gives the instantaneous change in strain in the film as

$$\Delta\varepsilon(t) = \frac{BV_0N_0b\cos\lambda}{2}t^2\left(\frac{\tau_{eff}^s}{\mu}\right)^{m+n}\exp\left(-\frac{Q_N+Q_V}{kT}\right) \quad \textbf{(4.6)}$$

Given the growth rate and growth temperature, the relaxation in a metastable film can be calculated by numerically integrating this equation. This metastable film thickness as a function of Ge mole fraction is plotted in Figure 4-3 for the typical growth rate of 1Å/s and growth temperatures of 450ºC and 550ºC. The rest of the parameters are taken from Houghton and are summarized in Table 4-1. From this plot, it is clear that lower growth temperatures are preferable for growth of films significantly thicker than the equilibrium critical thickness. This, however, could be detrimental to film crystallinity, as detailed in the previous chapter.

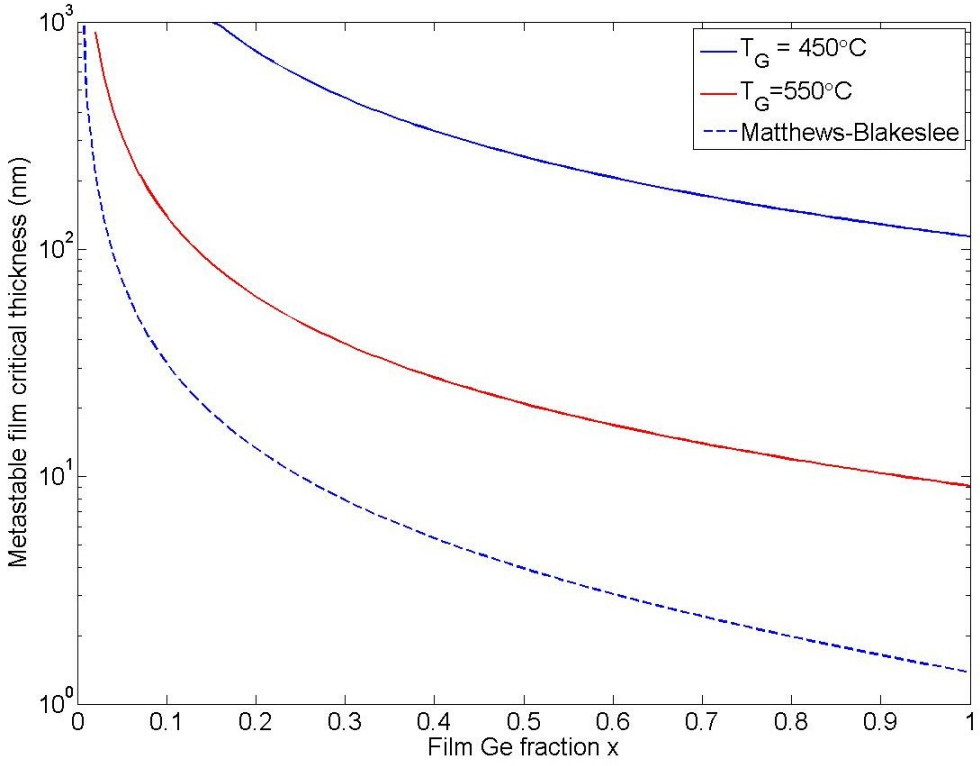


**Figure 4-3:** Metastable film critical thickness for growth on Si substrates at different growth temperatures.

Knowledge of the metastable film thickness is useful in when layers are designed to be grown on silicon substrates, but is less useful in the case of virtual substrates, where the existing number of dislocations is much higher. For example, the $Si_{0.83}Ge_{0.17}$ virtual substrate from IQE has a specified threading dislocation density of $\leq 2x10^5$ $cm^{-2}$. As a result, the metastable film thickness being closer to the critical thickness derived from Equation 4.1**,** especially at higher growth temperatures. This is shown in Figure 4-4, where the temperature-dependence of the metastable film critical thickness for a $Si_{0.5}Ge_{0.5}$ film grown on a $Si_{0.83}Ge_{0.17}$ substrate is plotted and is observed to asymptotically approach the Matthews-Blakeslee limit at high growth temperatures.

| **Substrate** | **B** ($s^{-1}$) | **$V_0$** ($mms^{-1}$) | **$N_0$** ($cm^{-3}$) | **λ** | **$Q_N$** (eV) | **$Q_V$** (eV) | **m** | **n** | **μ** (GPa) |
|---|---|---|---|---|---|---|---|---|---|
| Si | $10^{18}$ | $4x10^{14}$ | $10^3$ | 60º | 2.5 | 2.25 | 2 | 2.5 | 64 |
| $Si_{0.83}Ge_{0.17}$ | $10^{18}$ | $4x10^{14}$ | $10^5$ | 60º | 2.5 | 2.25 | 2 | 2.5 | 64 |

**Table 4-1**: Parameters for the calculation of metastable film critical thickness

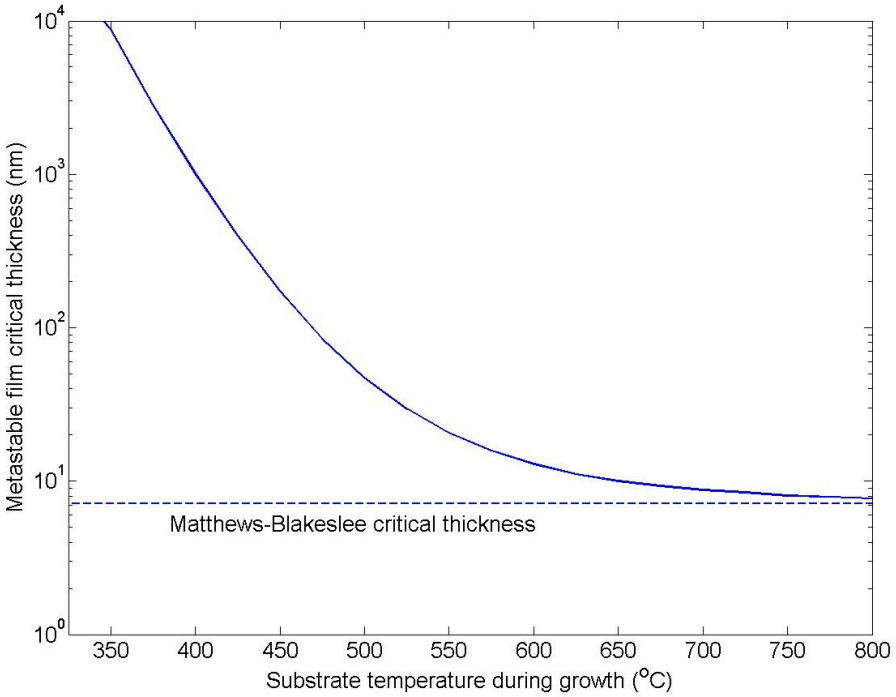


**Figure 4-4:** Metastable film critical thickness of a $Si_{0.5}Ge_{0.5}$ film grown on a $Si_{0.83}Ge_{0.17}$ virtual substrate as a function of substrate temperature during growth.

## ***4.3 Band structure calculations***

The $Si_{1-x}Ge_x$ alloy system is completely miscible for all compositions. This means that during epitaxial growth, the constituent atoms do not segregate and form a uniform alloy. Like Silicon, Silicon-Germanium is an indirect bandgap semiconductor. Of the two, Si has a higher bandgap of 1.12 eV at 300K while Ge has a bandgap of 0.661 eV at the same temperature [85]. The nature of this bandgap remains indirect for all SiGe films, either strained or relaxed. For such indirect bandgap materials, the radiative recombination rate is several orders of magnitude lower than the non-radiative recombination rate. As a consequence, a conventional LED or laser based on SiGe cannot be achieved. Of fundamental importance from the

point of view of photodetector design is the value of this bandgap. The $Si_{1-x}Ge_x$ bandgap has been a subject of study, both theoretically and experimentally. In this section, the method used to calculate the various parameters used in this proposal will be detailed. The band parameters are calculated as follows: First, the lattice constant of the film is computed. Next, the band profile for the strained film is computed. Finally, hydrostatic and hydrodynamic strain corrections for the band profile are calculated independently and applied, yielding the complete band structure including the band offsets

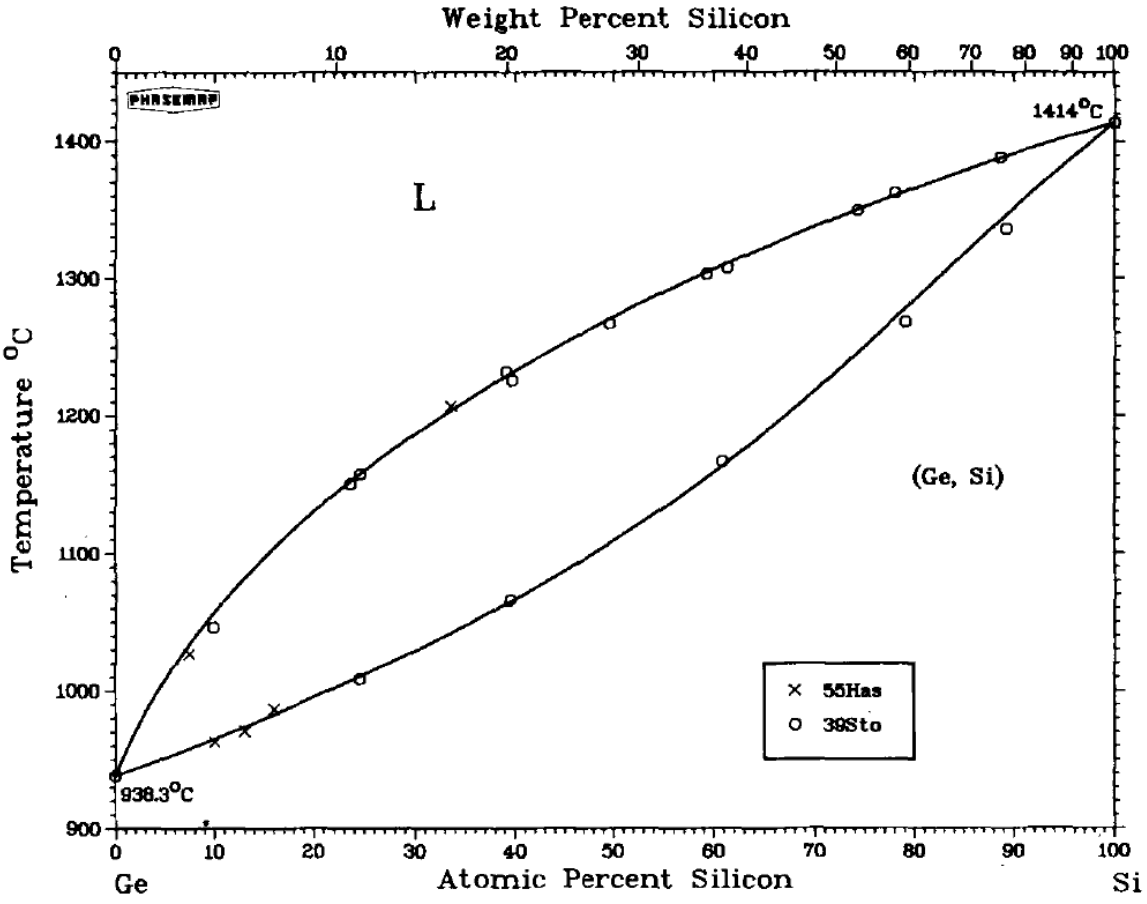


**Figure 4-5:** The binary phase diagram for the Ge-Si system, showing full miscibility in the solid and liquid phase for all compositions. [79]

### 4.3.1 Lattice constant and strain

Pure Si has a lattice constant $a_{Si}$ of 5.431 Å and pure Ge has a lattice parameter $a_{Ge}$of 5.658 Å (at 300K) i.e. a lattice mismatch of 4.3%. According to Dismukes et.al, [86], the variation at 300K is given by a quadratic relation

$$a(x) = \left(5.431 + 0.2x + .027\,x^2\right) \tag{4.7}$$

In this thesis, a linear interpolation scheme according to Vergard's Law [87] is used to compute the lattice constant of an arbitrary alloy $Si_{1-x}Ge_x$

$$a(x) = (1-x)a_{Si} + xa_{Ge} = \left(5.431 + 0.227\,x\right) \tag{4.8}$$

While this is not as accurate as the Dismuke's relationship, the maximum error associated with the linear fit is computed to be 0.12% and is offset by the flexibility of applying thermal corrections (if required) to the lattice parameter via the known coefficients of thermal expansion for Si and Ge where required.

The in-plane strain $\varepsilon_{\|}$ of a $Si_{1-x}Ge_x$ film grown on a $Si_{1-y}Ge_y$ substrate is determined from the lattice contstants of the two alloys

$$\varepsilon_{||} = \frac{a(x) - a(y)}{a(y)} \tag{4.9}$$

and the perpendicular strain $\varepsilon_{\perp}$ is given by

$$\begin{aligned} \varepsilon_{\perp} &= \frac{a_{\perp}(x)}{a(x)} - 1 \\ a_{\perp}(x) &= a(x)\left(1 - \frac{C_{12}(x)}{C_{11}(x)}\frac{a(y) - a(x)}{a(x)}\right) \end{aligned} \tag{4.10}$$

where $C_{12}(x)$ and $C_{11}(x)$ are the elastic constants of the film. When the native lattice constant of the grown film (given by Eq. 4.1) is larger than that of the substrate, the

film is under biaxial tensile strain in the plane of the film. Similarly, when this lattice constant is smaller than that of the substrate, the film is under biaxial compressive strain. In this thesis, a linear interpolation between the values of silicon and germanium is used to obtain the elastic constant for any arbitrary alloy [88].

### 4.3. 2 Bulk and strained bandgaps

The band diagrams for bulk Si and Ge are shown in Figure 4-6 a and b respectively. In this thesis, full band structure calculations are not performed. Instead, a minimal description of the energies of the participating bands at critical points is used. However, a brief description is illustrative.

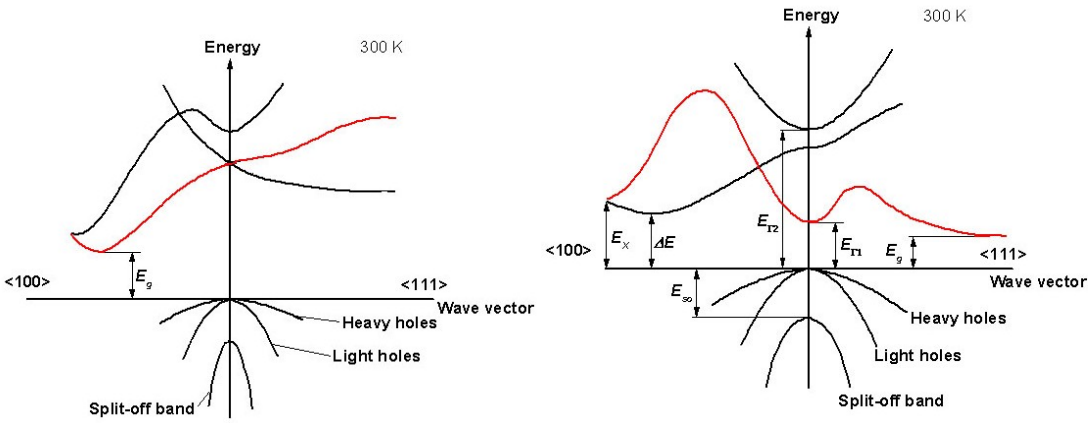


**Figure 4-6 (a)** Band structure of bulk silicon and **(b)** bulk germanium [28]

In both cases, the lowest energy gap is indirect, and the valence band minimum is doubly degenerate at the Γ point (the zone center) with a split-off band lower in energy. In Si, the lowest gap is governed by the energy difference between the conduction band consisting of 6 equivalent ellipsoids at 0.85x2π [001]/a (2π

[001]/a in the Brillouin zone is termed the X-point) points in the conduction band and the degenerate non-parabolic valence bands at the gamma point. In Ge, this fundamental gap is determined by the conduction band consisting of eight equivalent half-ellipsoids at the L-point ($2\pi$ [111]/a in the Brillouin zone) and the doubly degenerate valence bands at the $\Gamma$ point. In addition, it can be seen that for Ge, there is a direct gap 140meV above the L-point gap. From the point of modeling the band structure of SiGe alloys, these three bandgaps are of interest. The higher energy gaps are of particular interest in high-field transport, where carriers from multiple bands participate. With a change in composition, each of these bandgaps shifts relative to the other. In the case of bulk material, the fundamental gap at 10K is experimentally determined to be given by: [89]

$$E_g(x) = \begin{cases} 1.155 - 0.43x + 0.206x^2; x < 0.85 \\ 2.01 - 1.27x; x > 0.85 \end{cases} \quad \textbf{(4.11)}$$

This is shown in Figure 4-7. The change in the slope at x=0.85 is due to the fact that at this composition, the bandgap changes from being defined by the difference between Si-like conduction band minima at 0.85X and the valence band to the difference between the Ge-like conduction band minima at the L-point and the valence band. In all cases, the bandgap is indirect.

The next step toward the realization of a usable material model is the incorporation of strain. These calculations are carried out as detailed by Rieger and Vogl [90] using the empirical pseudopotential method.

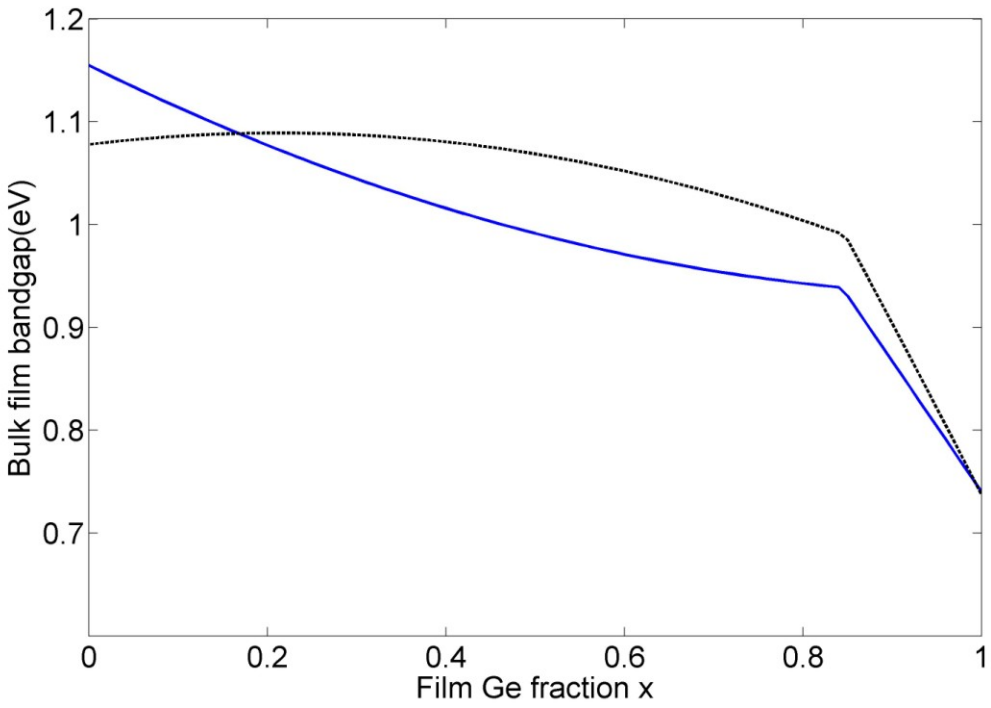


**Figure 4-7:** Bandgap of bulk $Si_{1-x}Ge_x$ as a function of Ge mole fraction x. The blue curve is from Eq 4.11, while the dashed black curve is the predicted bandgap from Eq. 4.12

The energy gap of a strained $Si_{1-x}Ge_x$ film grown on $Si_{1-y}Ge_y$ has been fit to a polynomial and can be calculated by

$$E_g(x,y) = \begin{bmatrix} 1 & (x-y) & (x-y)^2 \end{bmatrix} \overline{G} \cdot \begin{bmatrix} 1 \\ (x+y) \\ (x+y)^2 \end{bmatrix} \tag{4.12}$$

where $\overline{G}$ is a 3x3 matrix with each element given by

$$G_{ij} = G_{ij}^{<}\Theta(y-x) + G_{ij}^{>}\Theta(x-y)\,. \tag{4.13}$$

Here, Θ(x) is the unit step function i.e. Θ(x)=1 for x≥0 and Θ(x)=0 for x<0. $G_{ij}^{<}$ and $G_{ij}^{>}$ are matrices given in [90] and are reproduced in Appendix B. The $G_{ij}^{<}$ and

$G_{ij}^{>}$ matrices are different for the Δ and L-valleys, with separate matrices for the $\Delta_2$ and $\Delta_4$ valleys, which are described in the following section. This formulation is convenient as it allows simple determination of the strained bandgaps for all possible combinations of SiGe films on SiGe substrates. These bandgaps are plotted in Figure 4-8.

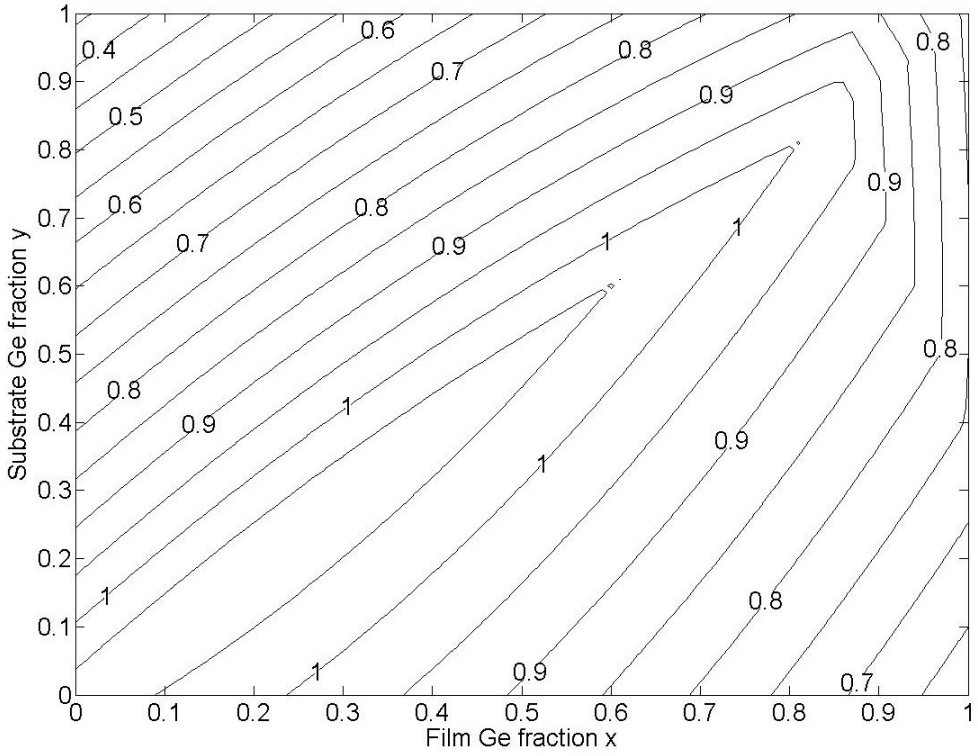


**Figure 4-8**: Contour plot of the bandgap of strained $Si_{1-x}Ge_x$ as grown on $Si_{1-y}Ge_y$ as calculated from empirical pseudopotential theory.

It is important to recognize the limitations of this model. As seen in Figure 4-7, this model does not accurately predict the bulk bandgap of $Si_{1-x}Ge_x$. In addition, this model predicts a bandgap of 0.95 eV for strained silicon on $Si_{0.83}Ge_{0.17}$, while the experimentally determined value is about 1 eV [89] This model does, however,

provide the necessary framework to fully explore the composition space of the SiGe material system, and for that reason, it is the chosen model for use in this thesis.

### 4.3. 3 Band alignments

To be able to use the previously described strained and unstrained bandgaps to design heterostructures, one also needs to know how the valence bands line up at the heterointerface. The band alignment across a heterostructure interface is an extremely important property, especially for optoelectronic devices. Mathematically, this can be expressed as

$$\Delta E(x,y) = E(x) - E(y) \qquad \textbf{(4.14)}$$

$\Delta E_c < 0 < \Delta E_v$ : Type-I Alignment

$\Delta E_c, \Delta E_v > 0$ : Type-II Alignment

where the conduction and valence band offsets $\Delta E_c$ and $\Delta E_v$ as measured as shown in Figure 4-9 Also shown is the difference between the two band-alignment types.

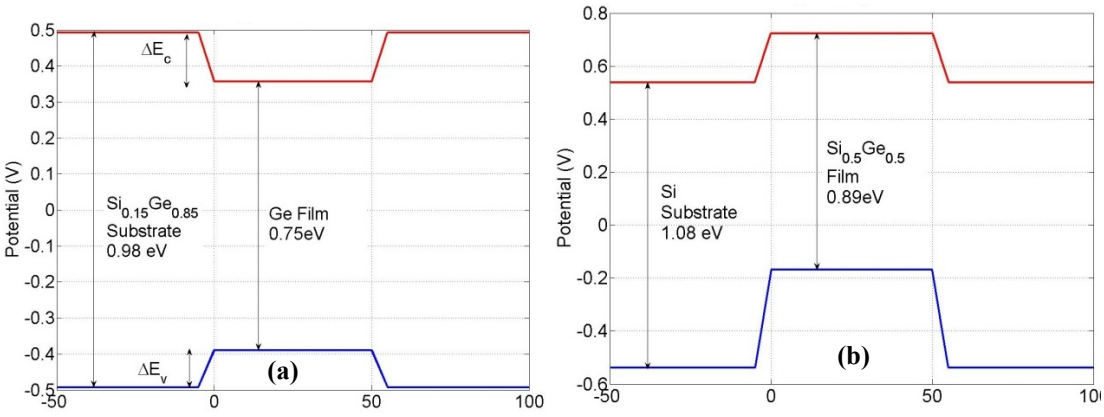


**Figure 4-9:(a)**Type-1 and **(b)** Type-II band offsets

In the SiGe material system, the band alignment is of Type-II. Here, electrons and holes are localized in spatially separate regions, resulting in a lower interaction between the two states. This has implications for the design procedure that will be detailed later in this chapter.

The effect of strain on the position of the doubly degenerate valence band is depicted in Figure 4-10

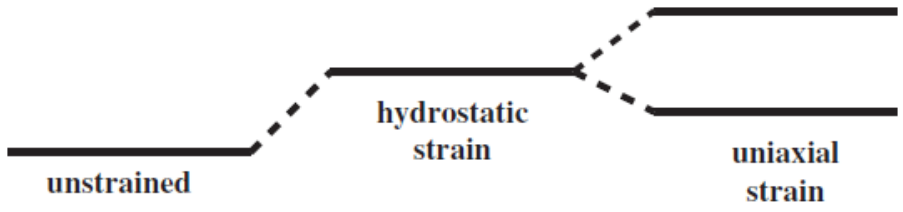


**Figure 4-10**: The effect of hydrostatic and uniaxial strains on the position of the band-edge [91]

Hydrostatic strain, which arises due to a change in the volume of the strained crystal, causes a shift in the position of the average band edge while shear strain causes a split in the band degeneracy. As described by Van de Walle et al.[92], the average energy of the three valence band maxima for a strained $Si_{1-x}Ge_x$ film grown on a relaxed $Si_{1-y}Ge_y$ substrate is given by

$$\Delta E_{v,av}(x,y) = (0.47 - 0.06y)(x - y)\,\text{eV} \qquad \textbf{(4.15)}$$

This includes the contribution of the bulk offset and hydrostatic strain shift. The effect of uniaxial shear strain on the light hole, heavy hole and split-off bands from this average position is modeled in terms of uniaxial deformation potentials as in equation 4.16.

$$\begin{aligned}
\Delta E_{LH} &= -\frac{1}{6}\Delta_0 + \frac{1}{4}\delta E + \frac{1}{2}\sqrt{\Delta_0{}^2 + \Delta_0\delta E + \frac{9}{4}\delta E^2} \\
\Delta E_{HH} &= \frac{1}{3}\Delta_0 - \frac{1}{2}\delta E \\
\Delta E_{SO} &= -\frac{1}{6}\Delta_0 - \frac{1}{4}\delta E + \frac{1}{2}\sqrt{\Delta_0{}^2 + \Delta_0\delta E + \frac{9}{4}\delta E^2} \\
\delta E &= 2b\left(\varepsilon_{\perp} - \varepsilon_{||}\right)
\end{aligned} \tag{4.16}$$

Here, b is the uniaxial deformation potential for tetragonal strain b, and $\Delta_0$ is the spin-orbit splitting. In this thesis, a liner interpolation scheme of the experimentally measured values of both these parameters is used to determine the value of these parameters for an arbitrary alloy [91]. With this information, the valence band offset for a strained $Si_{1-x}Ge_x$ film grown on a relaxed $Si_{1-y}Ge_y$ substrate can be calculated as

$$\Delta E_v(x,y) = \Delta E_{v,av} + \max(\Delta E_{LH}, \Delta E_{HH}, \Delta E_{SO}) \tag{4.17}$$

The separation of the split-off band from the top of the degenerate valence band $\Delta_0$ is given in eV by

$$\Delta_0(x) = 0.044 + 0.252x \tag{4.18}$$

Figure 4-11 is a contour plot showing the variation of the valence band offset as a function of both, film and substrate composition. It is noted that a tensile-strained SiGe film acts as a hole barrier and a compressively-strained SiGe layer is a hole well. In addition, it is important to note that in compressively-strained SiGe, the heavy hole band is the highest, and hence, is most energetically favored to participate in transitions near the band edge. This is not the case in tensile-strained SiGe where the light hole band is the highest. This distinction needs to be taken into account while calculating the transport properties and energy levels in structures where the

strain in the SiGe layers changes from tensile to compressive, such as in strain-balanced structures grown on SiGe virtual substrates.

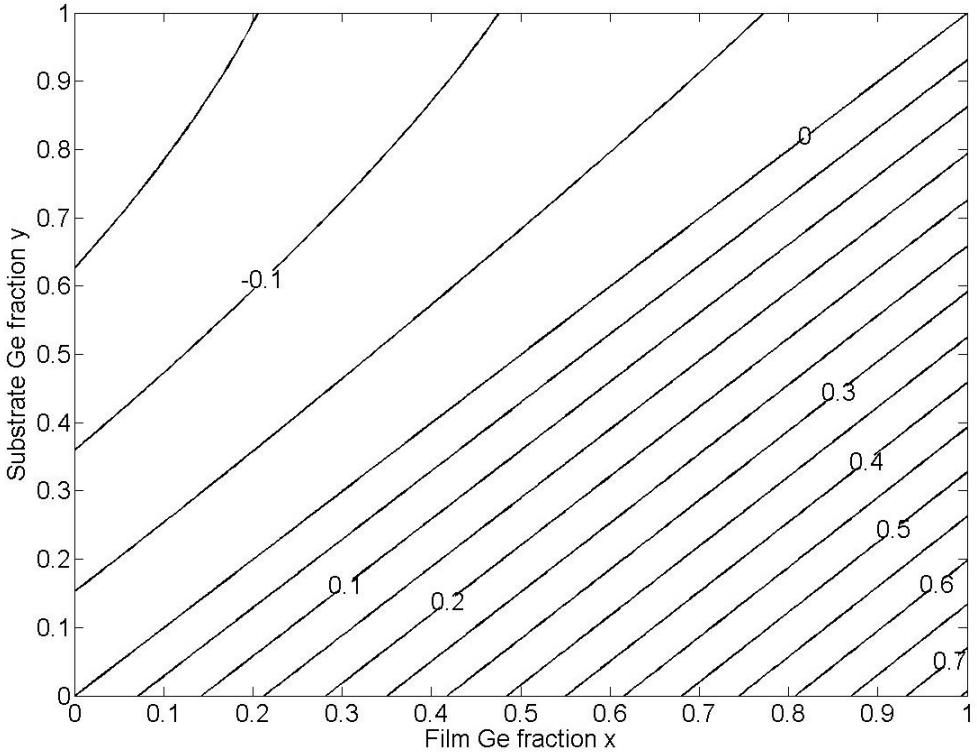


**Figure 4-11**: Valence band offset for strained $Si_{1-x}Ge_x$ grown on relaxed $Si_{1-y}Ge_y$.

A similar approach can be used to calculate the conduction band offsets, as is detailed in [91, 93]. As with the valence band, this approach involves the separate effects of the hydrostatic strain shift and the splitting of degeneracy due to uniaxial strain. However, since both, the bandgaps corresponding to the $\Delta_2$ and $\Delta_4$ conduction band valleys, and the valence band offsets are known, the conduction band offset can be calculated separately for the $\Delta_2$ and $\Delta_4$ valleys as

$$\Delta E_c(x,y) = E_g(x,y) - E_g(y,y) + \Delta E_v(x,y) \qquad \textbf{(4.20)}$$

In Figure 4-12, a contour plot of the variation of the conduction band offset as a function of substrate and strained film composition is shown.

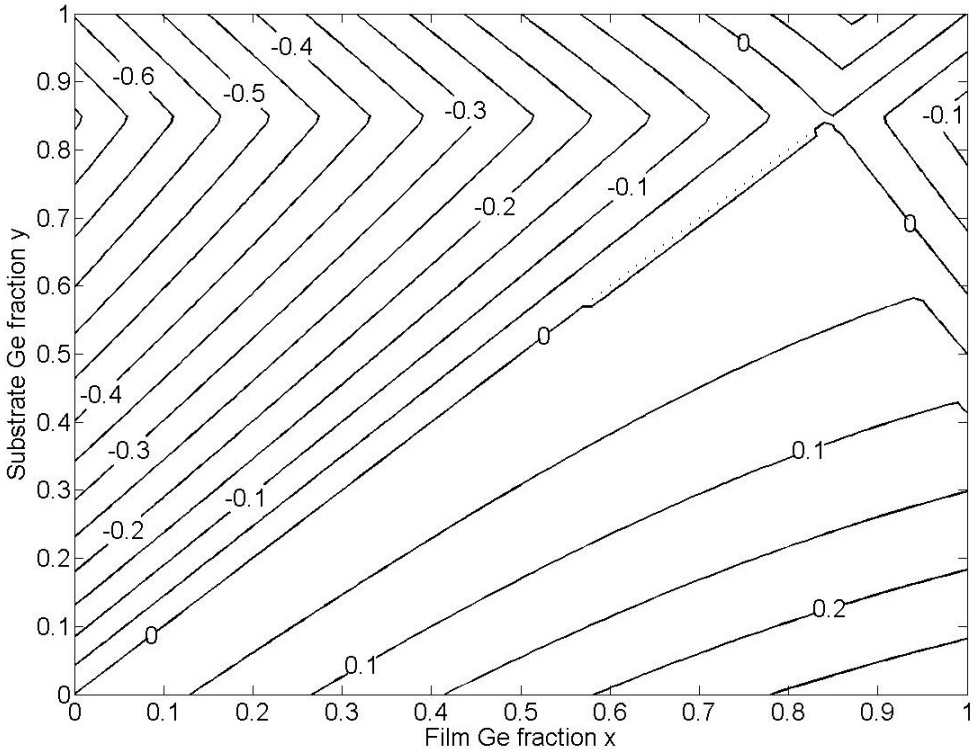


**Figure 4-12:** Conduction band offset for strained $Si_{1-x}Ge_x$ grown on relaxed $Si_{1-y}Ge_y$.

As with the valence band, strain breaks the valley degeneracy in the conduction band. However, unlike the case of the valence band, this isn't always the case. This can be understood as follows. Biaxial strain causes a tetragonal distortion of the crystal lattice. A carrier moving in the plane of the interface experiences a different potential as that experienced by a carrier moving normal to the interface. It is known from quantum mechanics that increasing the periodicity of a potential results in an increased ground state energy for the carrier, while a decrease in this periodicity results in a decreased ground state energy. This is analogous to how the

ground state energy in a thick quantum well is lower than that of the same carrier in a thinner quantum well. Now, in the case where the conduction band is Si-like (x,y<0.85) with minima in the (100) directions, electrons in the plane experience a different potential from those out of the plane. Thus when the film is under biaxial compressive strain (i.e. x<y), the carriers in the plane experience a increased periodicity, and hence, these four-fold degenerate band minima $\Delta_4$ move up the energy axis, while the doubly-degenerate minima $\Delta_2$ along [001] and $[00\bar{1}]$ experience a reduced periodicity, and hence become the energetically favorable lowest energy minima. Similarly, when the film is under biaxial tensile strain (x>y), the situation is reversed, and the $\Delta_2$ minima become less energetically favorable than minima the four $\Delta_4$ minima. This is schematically shown in Figure 4-13. In the case of Ge-like minima at the L-point, strain along the [001] direction does not break the symmetry of conduction band as all the (111) valleys are still equivalent in energy, as shown.

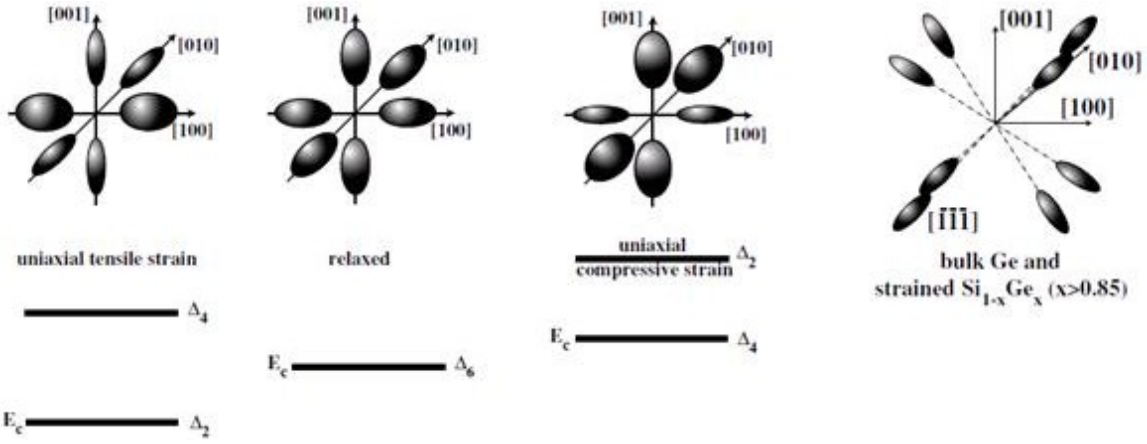


**Figure 4-13**:Effect of uniaxial tensile and compressive strains on the conduction band minima of Si-like and Ge-like constant energy surfaces. [91]

## *4. 4 Effective mass*

The effective mass of charge carriers has a strong impact on the electronic performance of heterostructure devices. Transport properties such as mobility are governed by the effective mass, having a direct impact on high speed performance of device performance. In addition, the carrier mass also determines the energy level and the wavefunction of a confined carrier, both of which are of importance in the design of active regions. In this section, the model used to calculate the effective masses of carriers is presented.

### 4.4.1 Electron effective masses

The conductivity effective mass for carriers in materials with ellipsoidal constant energy surfaces is given by

$$\frac{1}{m_c} = 3\left(\frac{1}{m_{t1}} + \frac{1}{m_{t2}} + \frac{1}{m_l}\right) \tag{4.21}$$

where $m_{t1}$, $m_{t2}$ and $m_l$ describe the ellipsoid. In the case of bulk Si and Ge, $m_{l1}$ and $m_{l2}$ are equal, but strain breaks this symmetry. In this thesis, the method derived Rieger and Vogl [90] is used. Each of these masses is parameterized at each conduction band minima of interest (at the 0.85X-point of Si-like conduction band minima, at the L-point of Ge-like minima and the fundamental direct gap)

$$m_i(x,y) = \begin{bmatrix} 1 & (x-y) & (x-y)^2 \end{bmatrix} W_{3\times 2} \begin{bmatrix} 1 \\ (x+y) \end{bmatrix}, i = t1, t2, l \tag{4.22}$$

through the 3x2 matrix W and the final value of $m_c$ is calculated. The value of effective mass chosen in calculations is determined by the band in which the carrier is

expected to reside, i.e. the near the X-point for Si-like bands and at the L-point for Ge-like bands. A contour plot of this effective mass is shown below in Figure 4-14.

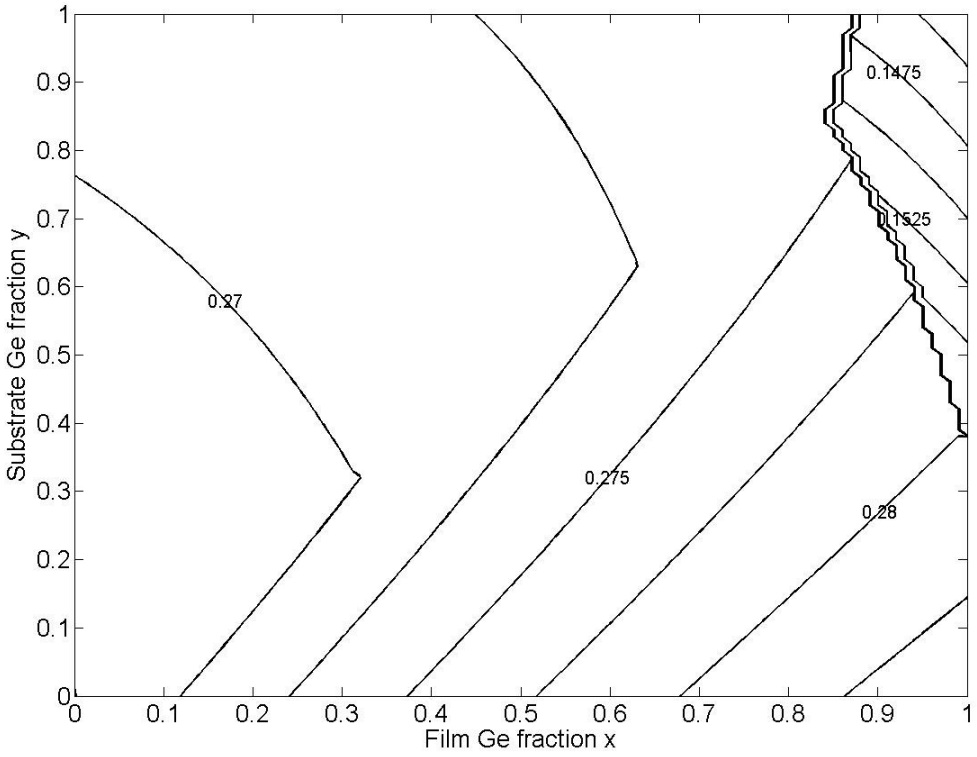


**Figure 4-14**: Effective mass of electrons in strained $Si_{1-x}Ge_x$ grown on relaxed $Si_{1-y}Ge_y$.

### 4.4. 2 Hole effective masses

The valence band structure of Si, Ge and their alloys differs significantly from typical III-V semiconductors such as GaAs in that the bands are non-quadratic. In both Si and Ge, the energy-wave vector (E-k) dispersion relations for the heavy holes (hh), light holes (lh) and the split-off (so) holes is of the form

$$E_{hh,lh}(\vec{k}) = E_v - \frac{0.5h^2k^2}{m_o}\left\{A \pm \left[B^2 + \frac{C^2}{k^4}\sum k_x{}^2 k_y{}^2\right]^{1/2}\right\}$$
$$E_{so}(\vec{k}) = E_v - \Delta - \frac{0.5h^2k^2}{m_o}A \qquad \textbf{(4.23)}$$

where A,B and C are material dependent and vary non-linearly with alloy composition in a way that has not been accurately determined. In this formulation, the effective mass depends on the location of the carrier in reciprocal space and offers no simple information for device design. In this thesis, an alternative formulation based on the Luttinger parameters $\gamma_1$, $\gamma_2$ and $\gamma_3$ [94] is used. This formulation allows the calculation of the effective mass for transport in the plane of the film as well perpendicular to this plane.

$$\frac{m_{hh}^z}{m_0} = \frac{1}{\gamma_1 - 2\gamma_2}; \frac{m_{hh}^t}{m_0} = \frac{1}{\gamma_1 + \gamma_2}$$
$$\frac{m_{lh}^z}{m_0} = \frac{1}{\gamma_1 + 2\gamma_2}; \frac{m_{lh}^t}{m_0} = \frac{1}{\gamma_1 - \gamma_2} \qquad \textbf{(4.24)}$$
$$\frac{m_{so}^z}{m_0} = \frac{1}{\gamma_1}; \frac{m_{so}^t}{m_0} = \frac{1}{\gamma_1}$$

In this framework, the effect of strain can be included according to Chuang as[94]

$$\frac{m_{hh}^z}{m_0} = \frac{1}{\gamma_1 - 2\gamma_2}; \frac{m_{hh}^t}{m_0} = \frac{1}{\gamma_1 + \gamma_2}$$
$$\frac{m_{lh}^z}{m_0} = \frac{1}{\gamma_1 + 2f_+\gamma_2}; \frac{m_{lh}^t}{m_0} = \frac{1}{\gamma_1 - f_+\gamma_2} \qquad \textbf{(4.25)}$$
$$\frac{m_{so}^z}{m_0} = \frac{1}{\gamma_1 + 2f_-\gamma_2}; \frac{m_{so}^t}{m_0} = \frac{1}{\gamma_1 - f_-\gamma_2}$$

where $f_\pm$ is a parameter determined by the uniaxial deformation potential b, the spin-orbit splitting $\Delta$ and the shear strain through

$$f_{\pm}(x) = \frac{2x\left[1+\frac{3}{2}\left(x-1\pm\sqrt{1+2x+9x^2}\right)\right]+6x^2}{\frac{3}{4}\left(x-1\pm\sqrt{1+2x+9x^2}\right)^2+\left(x-1\pm\sqrt{1+2x+9x^2}\right)-3x^2}$$

$$x = \frac{Q_\varepsilon}{\Delta} \qquad \textbf{(4.26)}$$

$$Q_\varepsilon = -\frac{b}{2}\left(\varepsilon_{xx}+\varepsilon_{yy}-2\varepsilon_{zz}\right)$$

In this thesis, a standard linear interpolation between the experimentally determined values of the uniaxial deformation potentials for Si and Ge is used to determine the value of b in Eq (4.17). In addition, the Luttinger parameters for SiGe alloys are also calculated by linearly interpolating between the theoretically calculated values for Si and Ge. Figure 4-15 and Figure 4-16 show the variation of the effective mass in the heavy hole and light hole bands respectively.

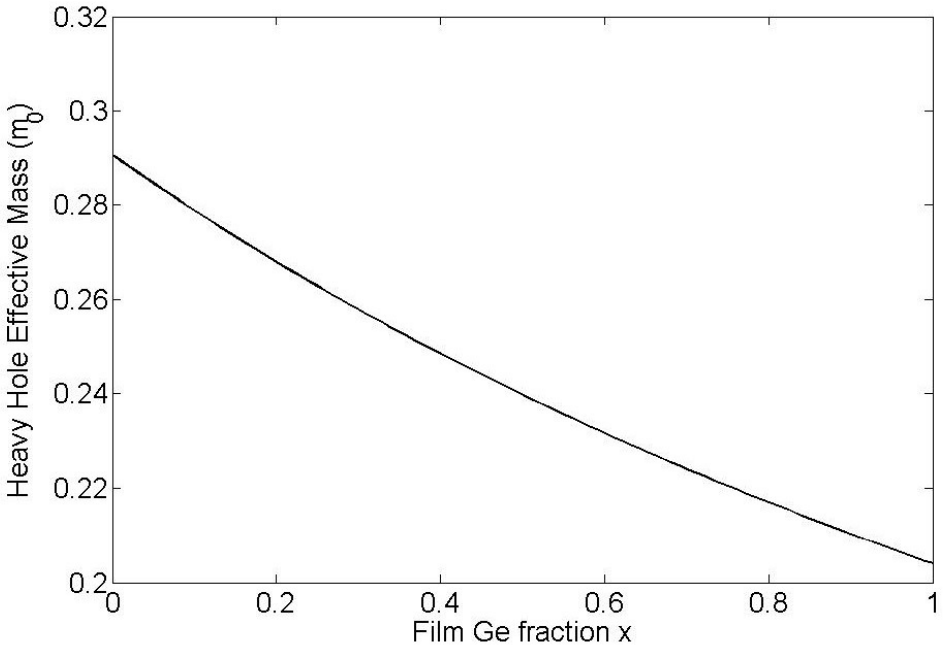


**Figure 4-15**: Heavy hole effective mass as a function of Ge mole fraction x

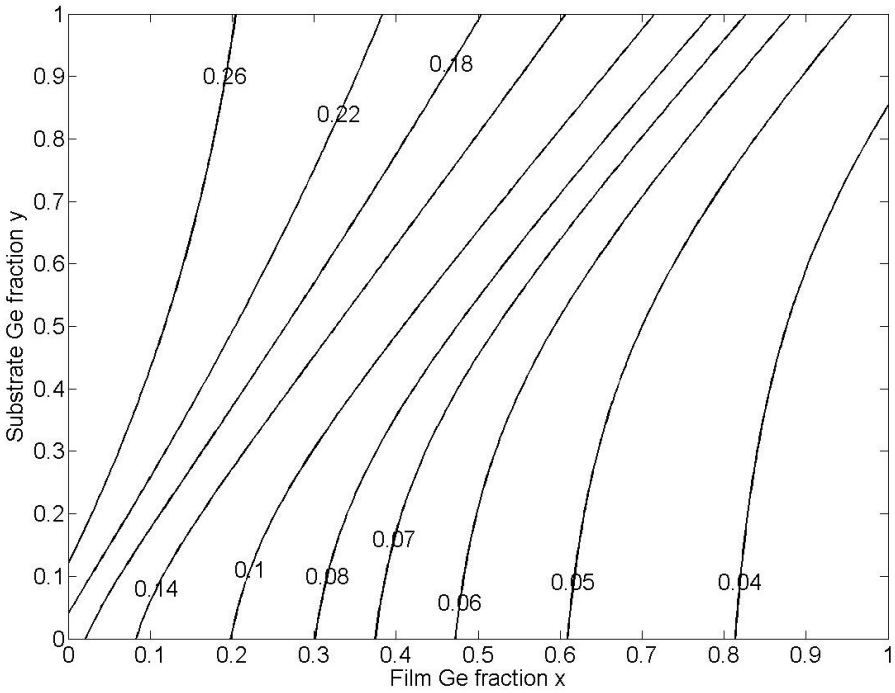


**Figure 4-16:** Light hole effective mass as a function of Ge mole fraction x in $Si_{1-x}Ge_x$

## ***4.5 Refractive index***

The refractive index of a heterostructure needs to be determined to ensure the choice of a suitable device architecture, especially in cases where the use of a waveguide device would be advantageous. It also allows for optimization of waveguide devices and accurate calculation of device capacitance via the dielectric constant. In this thesis, a standard linear interpolation is used to calculate the refractive index of $Si_{1-x}Ge_x$ as

$$n(x) = n_{Si}x + n_{Ge}(1-x) = 3.42 + 0.58x \qquad \textbf{(4.27)}$$

## *4.6 Mathematical techniques*

Two of the types of structures considered for active layers in this thesis are quantum wells and superlattices. To understand the behavior of carriers in such structures, it is important to be able to calculate both the energy levels and the wavefunctions of the confined states. In general, Schrödinger's equation for a carrier confined in an arbitrary potential profile $V_b(z)$ can be written as

$$-\frac{\hbar^2}{2}\frac{d}{dz}\left(\frac{1}{m^*(z)}\frac{d\psi}{dz}\right)-(E-V_b(z))\psi=0 \tag{4.28}$$

Both numerical and analytical techniques are used and both are briefly explained in this section. Analytical solutions are used when the potential profile is simple and step-like, as is the case of an infinite superlattice or a single quantum well, while numerical techniques are used in more complex profiles such as biased quantum wells.

### 4.6.1 Numerical solution

To solve Schrödinger's equation numerically, it is necessary to discretize Equation 4.19 above. In this thesis, a central difference scheme is used. The discretization step $\Delta z$ used is W/100, where W is the z-extent of the narrowest potential step in the problem space. This fine grid spacing is necessary to ensure that discretization errors are minimized. For typical potential profiles considered in this thesis, this corresponds to 2-5 steps $Å^{-1}$. The discretized form is obtained as [95]

$$\frac{\psi(z+\Delta z)}{m^*(z+\Delta z/2)} = \left\{\frac{2\Delta z^2}{\hbar^2}\left[V(z)-E\right]+\frac{1}{m^*(z+\Delta z/2)}+\frac{1}{m^*(z-\Delta z/2)}\right\}\psi(z)-\frac{\psi(z-\Delta z)}{m^*(z-\Delta z/2)} + O(\Delta z^2)$$

**(4.29)**

where

$$m^*(z\pm\frac{\Delta z}{2}) = \frac{m^*(z)\pm m^*(z+\Delta z)}{2}$$

**(4.30)**

Using the notation $F_n=F(n\Delta z)$ for variable/parameter F(z), the discretized equation is cast into the standard tri-diagonal form as

$$\frac{\hbar^2}{2\Delta^2}\begin{bmatrix} \frac{2\Delta^2}{\hbar^2}V_0+\frac{1}{m^*_{1/2}} & -\frac{1}{m^*_{1/2}} & 0 & \cdots & \cdots & 0 \\ -\frac{1}{m^*_{1/2}} & \frac{2\Delta^2}{\hbar^2}V_1+\frac{1}{m^*_{1/2}}+\frac{1}{m^*_{3/2}} & -\frac{1}{m^*_{3/2}} & \cdots & \cdots & 0 \\ 0 & -\frac{1}{m^*_{3/2}} & \ddots & \ddots & \vdots & \vdots \\ \vdots & 0 & \ddots & \ddots & \ddots & \vdots \\ \vdots & \vdots & \cdots & \ddots & \ddots & -\frac{1}{m^*_{n-1/2}} \\ 0 & 0 & \cdots & \cdots & -\frac{1}{m^*_{n-1/2}} & \frac{2\Delta^2}{\hbar^2}V_n+\frac{1}{m^*_{n-1/2}} \end{bmatrix}\begin{bmatrix}\psi_1\\ \psi_2\\ \psi_3\\ \vdots\\ \vdots\\ \psi_n\end{bmatrix} = E\begin{bmatrix}\psi_1\\ \psi_2\\ \psi_3\\ \vdots\\ \vdots\\ \psi_n\end{bmatrix}$$

**(4.31)**

This tri-diagonal matrix is numerically solved as an eigenvalue problem using the eigs() function in MatLab to obtain the electron and heavy-hole wavefunctions and

ground-state energies ($\Psi_e$, $E_e$) and ($\Psi_{hh}$, $E_{hh}$). These wavefuntions are normalized as

$$\|\Psi\| = \frac{\Psi}{\sqrt{<\Psi \mid \Psi>}}. \tag{4.32}$$

These normalized wavefunctions are then used where needed in the design process.

The accuracy of this numerical technique is studied by comparing the numerical and analytical solutions to Schrödinger's equation for multi-layer structures consisting of a double well formed by two 30-Å-thick Si layers with a 17.5-Å-thick fully-strained $Si_{0.61}Ge_{0.39}$ barrier. This double well is completed by two 750-Å-thick fully-strained $Si_{0.9}Ge_{0.1}$ layers. The potential diagram is shown in Figure 4-17. Also shown is the electron probability as a function of position. The numerical technique described here yields a ground state energy of 37.1354 meV, which is within 0.0037 meV of the analytical solution. This demonstrates the suitability of this numerical technique.

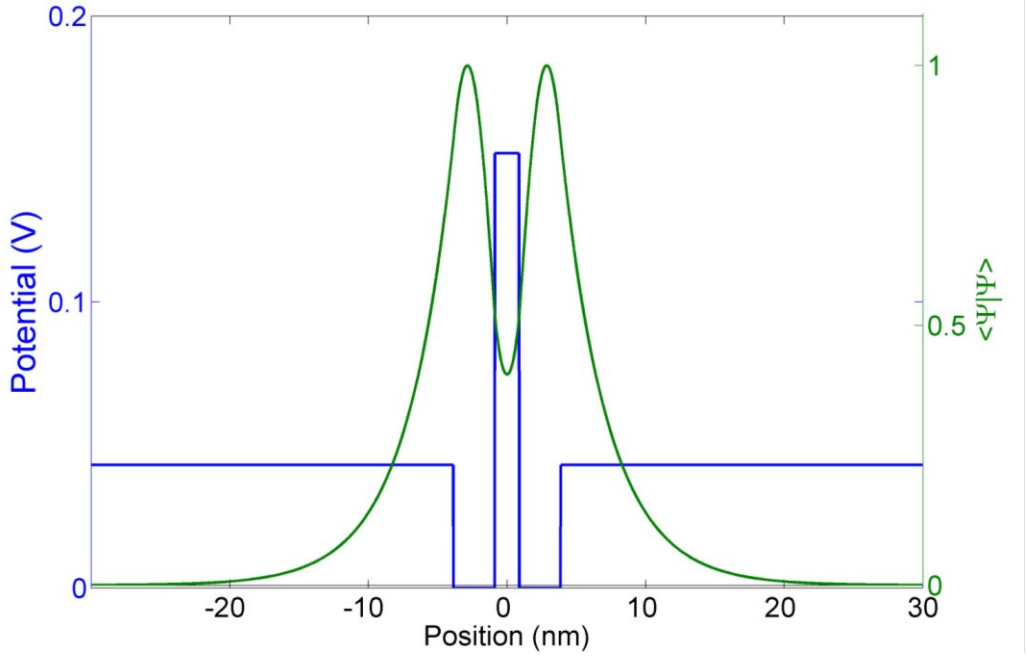


**Figure 4-17:** The potential well used to verify the numerical technique described in section 4.6.1

### 4.6.2 Analytical solutions

While numerical techniques are easy to implement, analytical solutions to Schrödinger's equation offer a form where the effect of varying parameters can be intuitively gleaned. In addition, for the case of an infinite (or even a very large) superlattice, analytical solutions for the energy levels are arrived at rapidly and efficiently. Consider the potential profile with N repeating units expressed as

$$V(z) = \begin{cases} 0; |z - nL| \le l_w \\ V_b; |z - nL| > l_b \end{cases}$$
$$L = l_w + l_b \qquad \textbf{(4.33)}$$

where n is an integer. This profile can be graphically represented as shown below in Figure 4-18 .

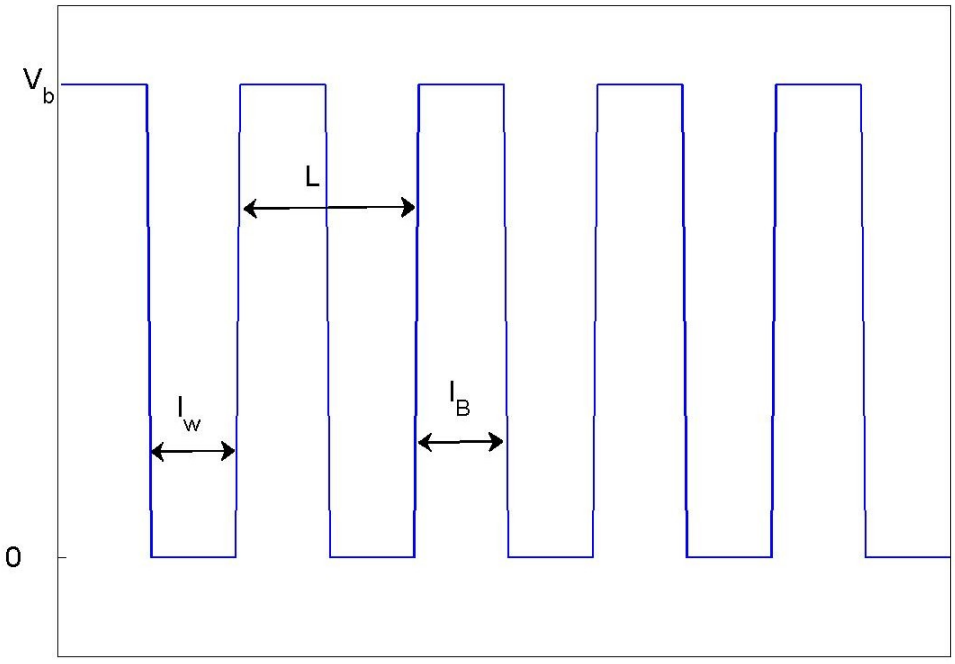


**Figure 4-18**: A schematic of a superlattice potential

The wavefunctions in the well (w) and barrier (b) acting regions can be written in terms of the energy level of the confined state E as

$$\begin{aligned}
&\psi_w(z) = A\exp\left(ik_w\left(z-nL\right)\right) + B\exp\left(-ik_w\left(z-nL\right)\right); \left|z-nL\right| \le l_w \\
&\psi_b(z) = C\exp\left(\kappa_b\left(z-nL\right)\right) + D\exp\left(-i\kappa_b\left(z-nL\right)\right); \left|z-nL\right| > l_b \\
&E = V_b - \frac{\hbar^2\kappa_b^2}{2m_b^*} = \frac{\hbar^2 k_w^2}{2m_w^*}
\end{aligned} \tag{4.34}$$

Solutions for E (and hence, the propagation constants) can be derived as the zeros of the equation

$$\begin{aligned}
&\cos\left(kL\right) = \cos\left(k_w l_w\right)\cosh\left(\kappa_b l_b\right) - \frac{1}{2}\left(\frac{m_b k_w}{m_w \kappa_b} - \frac{m_w \kappa_b}{m_b k_w}\right)\sin\left(k_w l_w\right)\sinh\left(\kappa_b l_b\right) \\
&k = \frac{2p\pi}{NL}
\end{aligned} \tag{4.35}$$

where p is an integer index denoting the $p^{th}$ superlattice band.

Now, the first superlattice band is bounded by $0<qd<2\pi$, the second band by $2\pi<qd<4\pi$ and so on. With this formulation, the band structure of a superlattice can be solved. Figure 4-19 shows the calculated electron band structure for a 30 Å Si/ 30 Å $Si_{0.66}Ge_{0.34}$ superlattice grown on a $Si_{0.83}Ge_{0.17}$ substrate. This superlattice has a potential depth $V_b$ of 0.24eV. Also shown for comparison is the energy level of the bound electron state in a single quantum well of same width and depth.

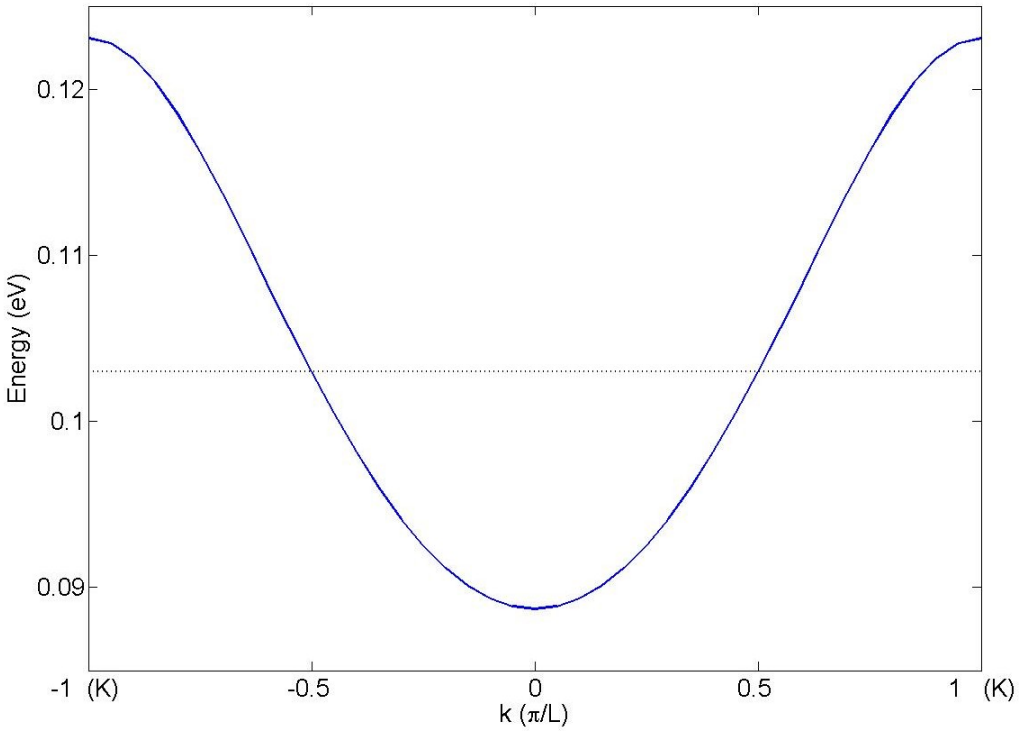


**Figure 4-19:** The superlattice band for the potential profile detailed in the text

Finally, a comparison between the wavefunctions of carriers in superlattices and in multiple quantum wells should be made. To study this, two different superlattices are considered – the 30 Å Si/ 30 Å $Si_{0.66}Ge_{0.34}$ superlattice grown on a $Si_{0.83}Ge_{0.17}$ substrate described above, and a 30 Å Si/ 300 Å $Si_{0.66}Ge_{0.34}$ superlattice on the same substrate. Due to the large separation between the electron wells in the second superlattice, and the large potential barrier between the wells, it is expected that this structure would behave like a multiple quantum well structure. This is seen in the solutions to the two potentials as shown in Figure 4-20 a and b. It is clearly seen that in the MQW-type structure, the probability of finding a carrier in the region between the wells becomes vanishingly small. In contrast, carriers in the superlattice

are observed to have a diminished but significantly larger inter-well presence, when compared to the MQW structure. The significance of this fact is explained in Section 4.7

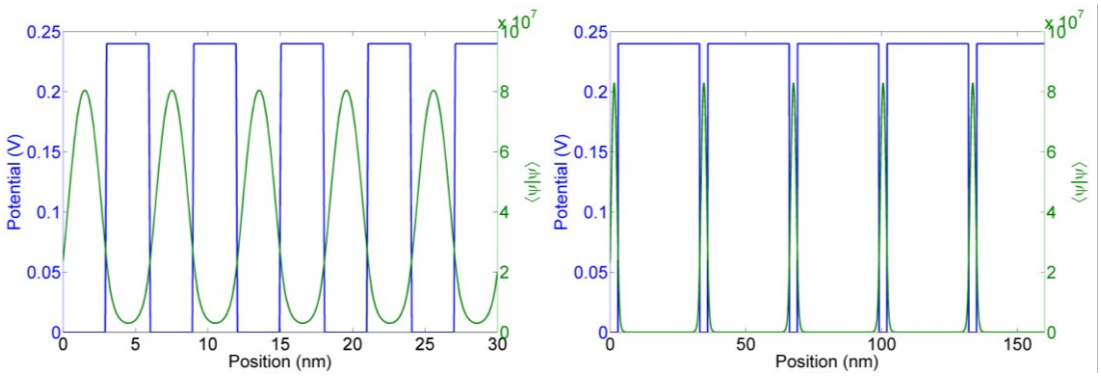


**(a)** **(b)**

**Figure 4-20:** The carrier probabilities in a **(a)** 30 Å Si/ 30 Å $Si_{0.66}Ge_{0.34}$ superlattice and **(b)** 30 Å Si/ 300 Å $Si_{0.66}Ge_{0.34}$ superlattice

### 4.6.3 Density of states

In addition to the energy levels, knowledge of the density of states is also necessary to better design heterostructures for optical transitions. The density of states for single and multiple quantum wells are well known as being stair-like with equal steps occurring at each confined energy level [96].

$$\rho(E) = \frac{m^*}{\pi\hbar^2}\sum_{i=1}^{n} U(E - E_i); E_i < V_b \tag{4.36}$$

Here U(x) is the unit step function.

For superlattices, however, the density of states shows a combination of smooth increases associated with unconfined carriers and discrete steps resulting from

the fact that the carriers are confined. To obtain the density of states, the following approach is used. First, the dispersion relation for the $i^{th}$ subband, which is approximated in the vicinity of the energy level of the isolated quantum well $E_i$ as

$$\begin{aligned} E_i(k) &= E_i(0) + s_i + 2t_i \cos(kL) \\ s_i &= -\frac{F(E_i)}{F'(E_i)}; t_i = \frac{1}{2F'(E_i)} \end{aligned} \tag{4.37}$$

where F(E) is the RHS of Equation 4.26 and ′ denotes the first derivative with respect to E and is a tight binding approximation is used for the different superlattice bands. Using this approximation, the density of states at energy E can be obtained as the sum of the density of states over all bands with energy less than E

$$\rho(E) = \sum_{i=1}^{n} \rho_i(E)$$

$$\rho_i(E) = \begin{cases} 0 & ;E < E_i + s_i - 2|t_i| \\ N\dfrac{m^*}{\pi\hbar^2}\dfrac{1}{\pi}\arccos\left(\dfrac{-E + E_i + s_i}{2|t_i|}\right) & ;|E - E_i - s_i| < 2|t_i| \\ N\dfrac{m^*}{\pi\hbar^2} & ;E > E_i + s_i + 2|t_i| \end{cases} \tag{4.38}$$

A comparative plot is shown in Figure 4-21. This figure clearly illustrates the 3-D-like density of states for a superlattice in sharp contrast with the 2-D density of states for the quantum well. This results in the absorption spectrum from a superlattice being smoother than that of a quantum well.

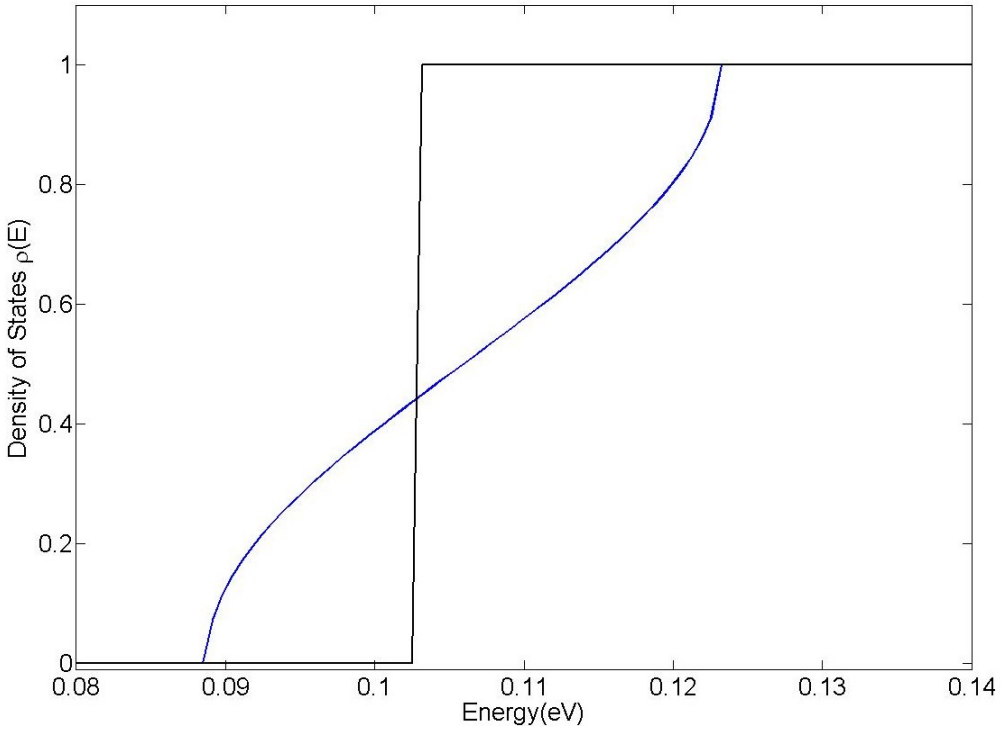


**Figure 4-21**: The superlattice density of states (blue curve) for the superlattice detailed in Section 4.7.2. For reference, the density of states of the isolated quantum well is also shown as the black line.

## *4.7 Design concepts*

In this thesis, two specific design concepts are explored. First, the limits of critical thickness are explored. This involves the design of a highly strained SiGe absorption layer. In this approach, the sole considerations are the bandgap of the heterostructure and the thickness of the layers. The second approach, which is explored in greater detail, involves utilizing the band offsets to create interacting confined states, either as quantum wells or superlattices, in addition to the concerns of the bandgap and the critical thickness.

As mentioned in section 4.3.3, the fact that the band offsets in the SiGe

material system are of Type-II has implications on the expected performance from these devices. For photodetector applications, these type-II offsets are typically detrimental to performance. This effect can be quantified by a study of how optical absorption occurs between two bound states. From an analysis of quantum wells [97], we get the transition rate per unit volume between two bound states 1 and 2 in units of $s^{-1}cm^{-3}$ with an incident photon of energy $\hbar\omega$ as

$$R_{21}(\omega) = \frac{2\pi}{\hbar}\left|H_{21}^{'}\right|^2 \rho_f(E_{21})\delta(E_{21} - \hbar\omega), \tag{4.39}$$

where $\rho_f(E_{21})$ is the density of the final states i.e. electron in the conduction band and holes in the valence band, $E_{21}$ is the energy of the transition from initial state 1 to final state 2,and the strength of an interaction of two subband levels is given by

$$\left|H_{21}^{'}\right|^2 = \left(\frac{q\mathsf{A}}{2m_0}\right)^2 \langle u_c \left|\hat{\mathbf{e}}.\mathbf{p}\right| u_v\rangle^2 \langle \psi_2 | \psi_1\rangle^2 . \tag{4.40}$$

The first inner product represents the interaction of the Bloch functions of the conduction and valence bands with the incident electric vector potential. $\vec{\mathsf{A}}$. Polarization dependence in transitions involving quantum wells arise from this term. The second product is a measure of the overlap of the electron and hole wavefunctions and is dependent on the dimensions of the wells in which these species are present, and it is this term that demonstrates the relative weakness of a transition involving a type-II structure when compared with that in a type-I structure. In the latter case, the electrons and holes are in the same spatial layer, and their overlap is maximized. In a type-I structure, however, this overlap is always less as it is now governed by extent of the electron and hole wavefunctions into their barrier layers as

shown in Figure 4-22. For this illustration, a simple potential consisting of a 0.2eV deep well, 30-Å-thick and a 0.3 eV high barrier that is 40-Å-thick is chosen for both holes and electrons. The holes are assigned a mass of 0.2 $m_0$ and the electrons, a mass of 0.1 $m_0$. In this case, the overlap of electron and hole wavefunctions is calculated to be 32%.This is in contrast with a type-II structure, shown in Figure 4-23, for the same electron and hole masses, but in a 30-Å-thick, 0.2 eV deep well. For this structure, the overlap is calculated to be 97%. This implies that for these structures, three repeating units of the type-II heterostructure will be needed to obtain an absorber that is as efficient as one unit of the type-I structure. This applies to both, quantum well-type devices and superlattices. The following chapters will present attempts to overcome this difficulty through careful design of the heterostructure.

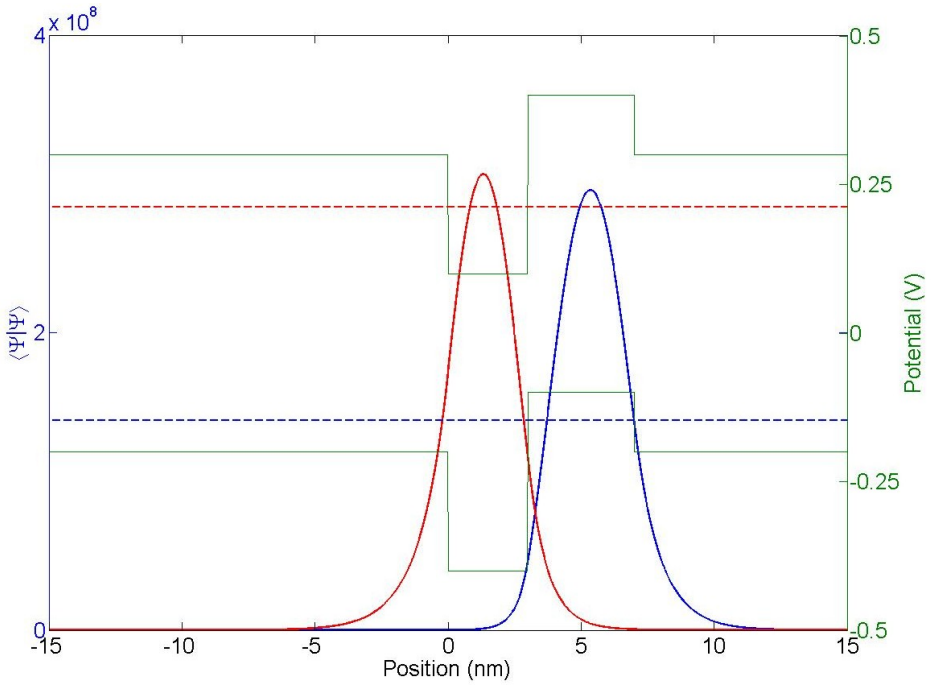


**Figure 4-22**: The solutions of the electron (red) and hole (blue) wavefunctions and energy levels for the type-II potential profile shown by the green line.

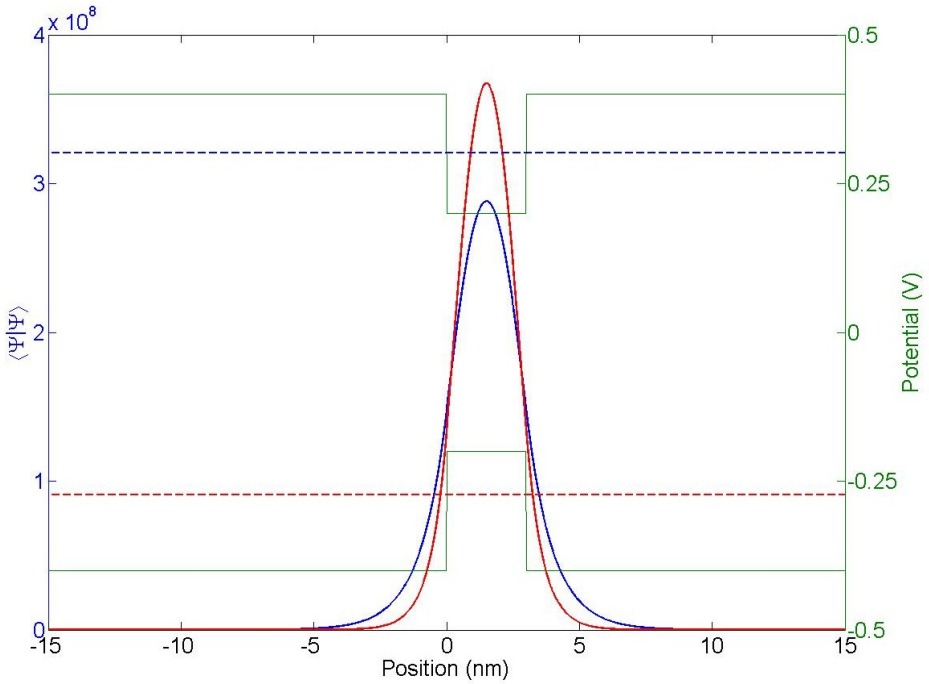


**Figure 4-23**: The solutions of the electron (red) and hole (blue) wavefunctions and energy levels for the type-I potential profile shown by the green line.

# Chapter 5 : Strained Silicon-Germanium Photodetectors

## *5.1 Introduction*

Silicon germanium heterostrucures grown on a silicon substrate free of misfit dislocations are necessarily compressively strained. As no tensile-strained layers can be grown on this substrate, the layer thicknesses are to be sufficiently thin to prevent the relaxation of misfit strain. This requirement necessitates the careful design of the optical absorber region.

In this chapter, two broad classes of optical absorber regions are considered. First, only the reduced bandgap of SiGe is used to create a quantum well absorber. The thickness of this absorber is limited by strain. The second type of optical absorber utilizes the type-II band offsets, as detailed in Chapter 4. This is done to increase the optical absorption coefficient of a SiGe heterostructure by using the band offsets in conjunction with bandgaps in order to create a heterostructure that exhibits a band-edge that is smaller than that of any individual layer in the system.

## *5.2 Design 1: Single quantum well*

### 5.2.1 Design and growth

A preliminary test structure based on a single quantum well absorber region was designed to study the effectiveness of a simple design that did not utilize the band offsets. In addition, this structure provided an understanding for the material system and helped establish fabrication processes. The structure detailed in this

section was grown by Dr. Phillip Thompson at Naval Research Laboratory, Washington DC. The MBE reactor used to grow this structure is detailed in [98]. It is different from the LPS SiGe MBE reactor in that both, silicon and germanium are evaporated from electron beam sources. Further, an EIES flux monitor is used to control the Si and Ge electron beam sources.

The central absorber region for this structure consists of a 10nm thick $Si_{0.6}Ge_{0.4}$ layer with bandgap 0.93 eV from Figure 4-8. This thickness is larger than the equilibrium critical thickness but less than the metastable critical thickness as detailed in Chapter 4. This absorber is sandwiched between two 75nm thick $Si_{0.9}Ge_{0.1}$ regions that act as optical confinement layers. This allows the fabrication of a waveguide detector with increased optical interaction volume. In this structure, photodetection involves bound to continuum transition. In addition, no optimization has been performed on this design as adjusting the well widths and Ge composition to maintain energy transitions. A 2-μm-thick n-doped silicon layer acts as a top cladding layer and a thin $n^{++}$ silicon layer is grown for low-resistance ohmic contacts. Boron was used as a p-dopant, while phosphorous is used as an n-dopant. The layer structure and the band edge diagram (neglecting the band bending caused by doping and applied bias) are shown in Figure 5-1and Figure 5-2 respectively.

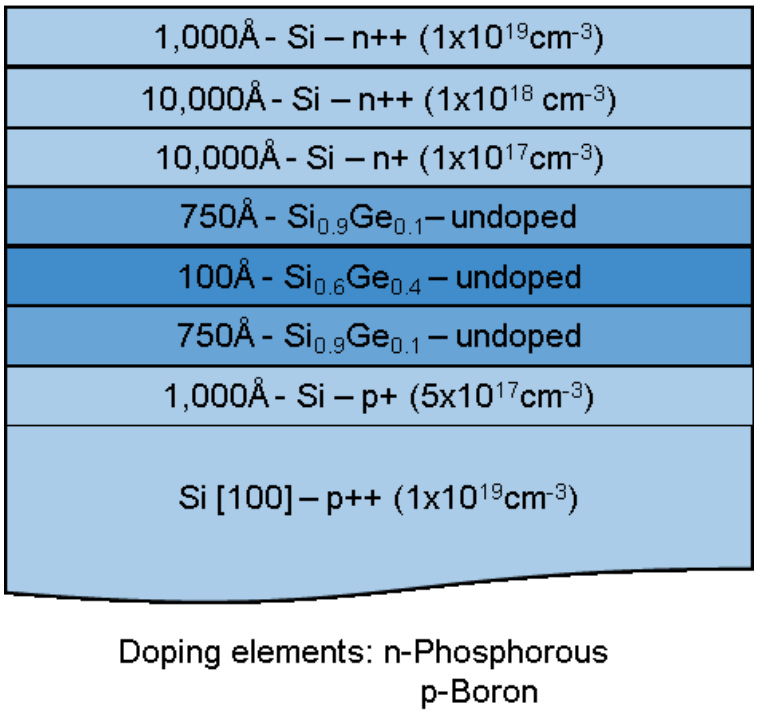


**Figure 5-1:** The layer structure of the single QW test structure

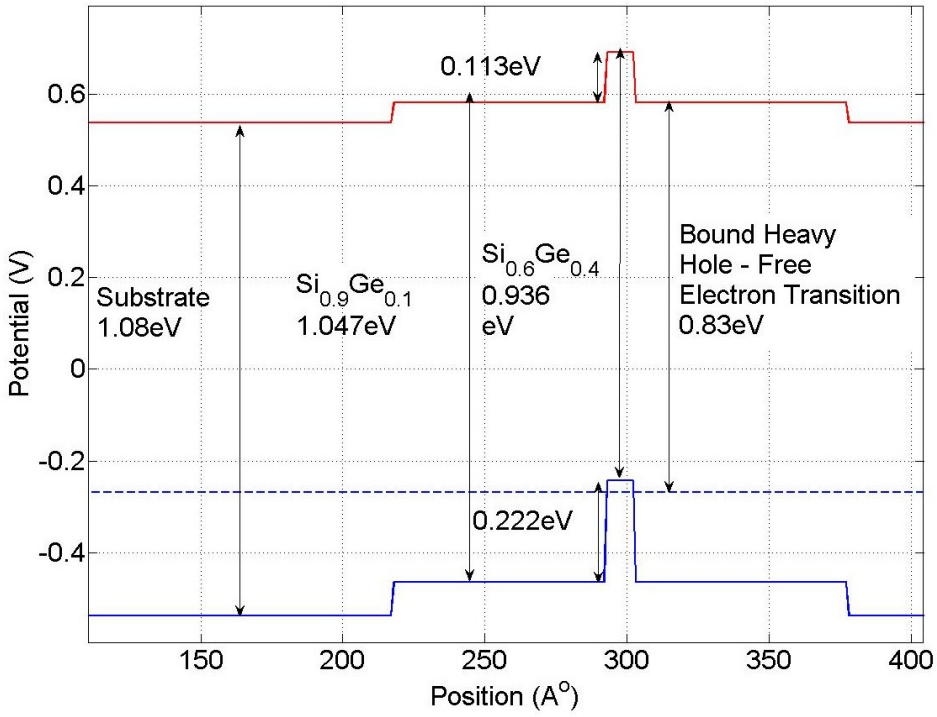


**Figure 5-2:** The computed band-edge profile of the preliminary single QW structure

It is important to note that this design is highly strained, so the active region consists of a single well. Another concern is that the narrow well resulting in an appreciable blue-shift in the absorption band-edge. Solving Schrödinger's equation for a heavy hole in a conduction band gives a blue shift of 6.58 meV, ensuring that that the absorption band-edge is still in the 1.3 μm window.

Another concern in material design is the refractive index profile of the heterostructure. To ensure confinement of the optical mode close to the active region, it is necessary for it to have a higher refractive index than the surrounding region. As predicted by Equation 4.18, this is the case and we expect strong confinement. Shown in Figure 5-3 are the refractive index profile of the structure and the fundamental mode for a 5μm wide and 6μm tall waveguide as calculated by BeamProp.

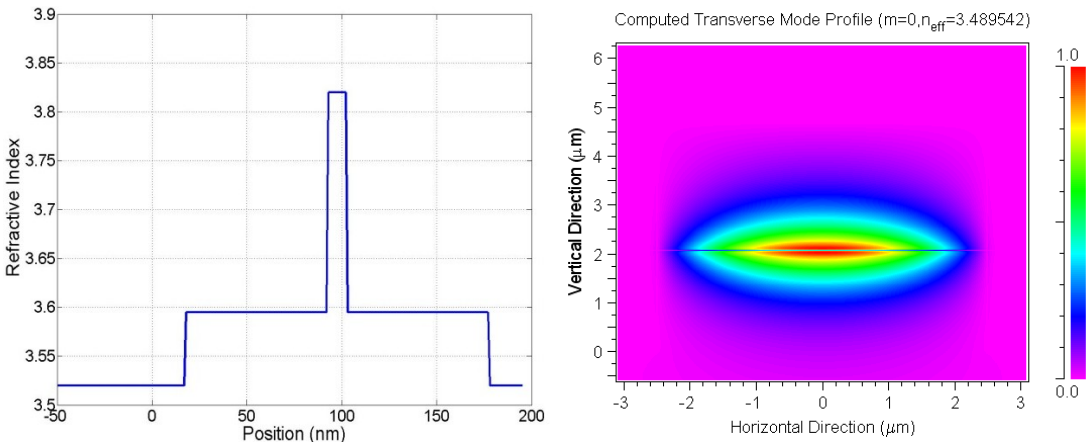


**Figure 5-3: (a)** Refractive index profile and **(b)** computed optical mode for the shown heterostructure implemented as a waveguide

The Secco etch described in Chapter 4 is used to determine whether defects have been nucleated in the active region as a result of the strain. First, a piece of the

sample is etched down to the $Si_{0.9}Ge_{0.1}$ layer in a 10% $NH_4OH$ bath at 60°C. This step is facilitated by the fact that $NH_4OH$ cannot etch through SiGe. [99] A Secco etch is then performed on this sample, revealing an average defect count of $2.07x10^7$ $cm^{-2}$ in the active region of the device, shown in the SEM image in Figure 5-4. This extremely high defect density is expected to result in devices with very high reverse leakage currents.

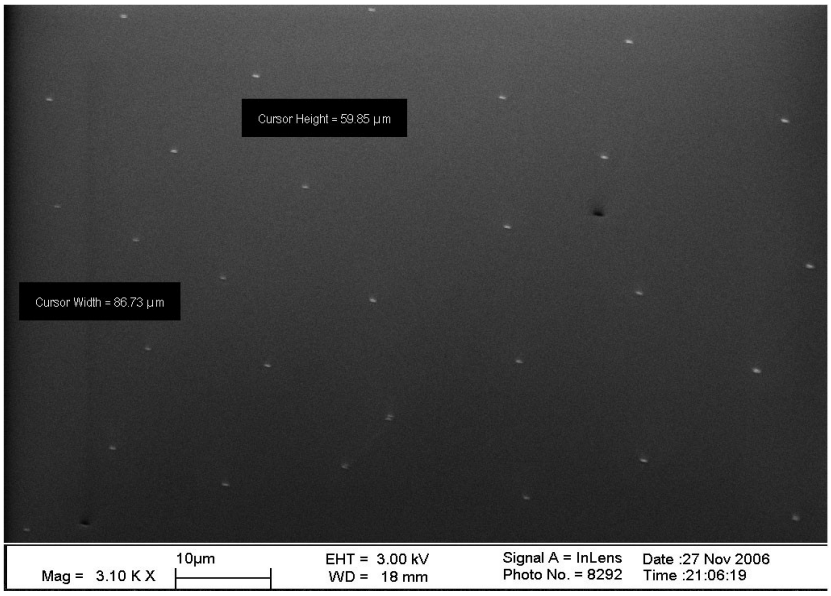


**Figure 5-4:** An SEM image of the Secco-etched single QW device. Each white dot corresponds to a defect. The FOV for this image is 86µm x 60µm

### 5.2.2 Device fabrication

To test this design, preliminary multimode waveguide (MMWG) devices 5 µm tall and 10, 20 and 40 µm wide were fabricated. Features were defined by UV-lithography using a contact aligner. The use of a stepper was not necessary as the features are large enough to make alignment of different layers relatively easy.

Fabrication involved four main steps. First, the waveguides were defined by KOH etching. The wet etch is necessary to obtain smooth sidewalls and the results are detailed in this section. Next, a $Si_3N_4$ dielectric window was defined. This step is necessary to allow for isolated top contacts. This step does not passivate the sidewalls of the waveguides. The third step was p-and n-type metallization with a Ti/Pt/Au layer stack, followed by die thinning and cleaving to define waveguide facets. Photomicrographs of the device at each of these three steps are shown in Figure 5-5

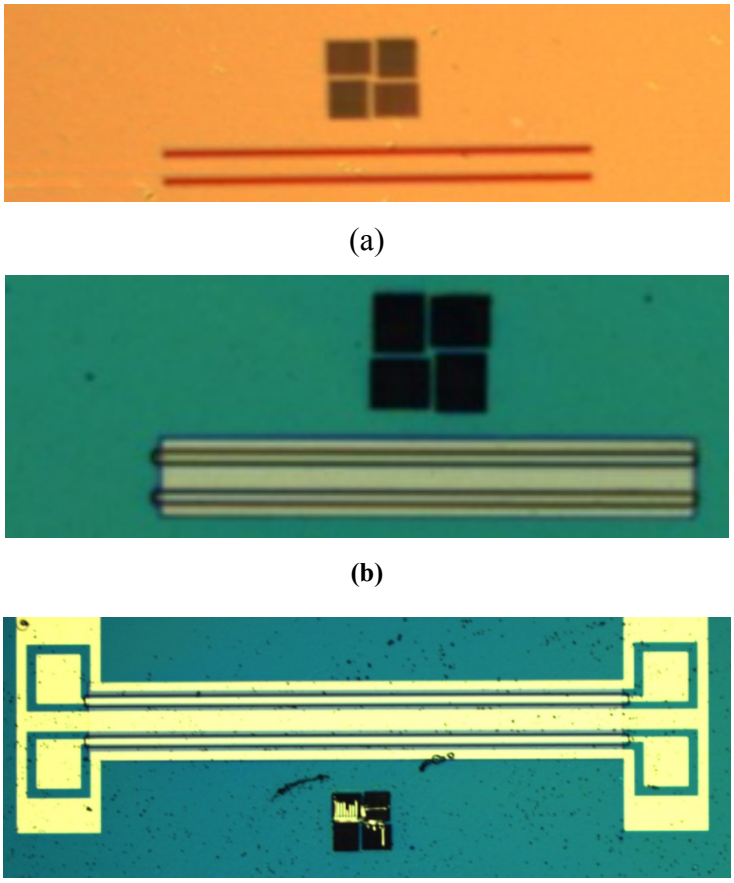

(a)

(b)

(c)

**Figure 5-5:** 50X micrographs of the device after each of three steps **(a)** KOH wet etch **(b)** definition of the dielectric window and **(c)** after metallization

The most critical step involved is the wet etch used to define the waveguide and sidewalls. To reduce optical scattering loses, especially in waveguide devices, sidewalls should have a maximum rms roughness of 130 nm (i.e. $\lambda/10$). Conventional dry etch processes using RIE are found to produce very rough sidewalls and hence, unsuitable and the need for a good anisotropic etch was established. Potassium hydroxide (KOH) and tertramethyl ammonium hydroxide (TMAH) are conventional anisotropic silicon wet-etchants. When used to define features, the sidewalls are defined by the <111> planes and are at an angle of 37° with the <100> planes. However, the use of KOH has found to result in pits and pyramids on the Silicon surface [38], increasing the surface roughness. These pits and pyramids are formed by micro-masking caused by $H_2$ and $H^+$ bubbles that attach to the surface of the etched Silicon surface. The fact is that etching in TMAH or KOH is anisotropic results in the formation of self-sustaining pyramids and pits even after the bubbles detach from the surface. Campbell et al. [100] found that the addition of isopropyl alcohol and saturating the reagent in gaseous oxygen inhibited the formation of these features. The addition of IPA to make the solution to 5% in IPA results in a three-fold decrease in surface tension, influencing the adhesion of the hydrogen to the silicon surface. IPA incorporation is also a common procedure in commercial etching baths for the production of regular surfaces. Oxygen-saturation ensures the rapid removal of the hydrogen adhered on the surface by the formation of water. This reduces the chance of surface micromasking and improves the surface finish. The etchant used is a 7.5 M KOH solution to which 20 ml IPA is added. The solution is heated to 80°C and stirred at 120 RPM. Ultra-high purity oxygen is bubbled through the solution to obtain an

oxygen-saturated etchant. Atomic Force Microscopy (AFM) was used to study the sidewall roughness and was found to be 8.8 nm rms with a maximum roughness of 75 nm for the sidewalls and 14.14 nm rms with a maximum roughness of 108 nm for the bottom <100> silicon surface. An AFM scan of the sidewall over a 2 μm × 2 μm area is shown in Figure 5-6

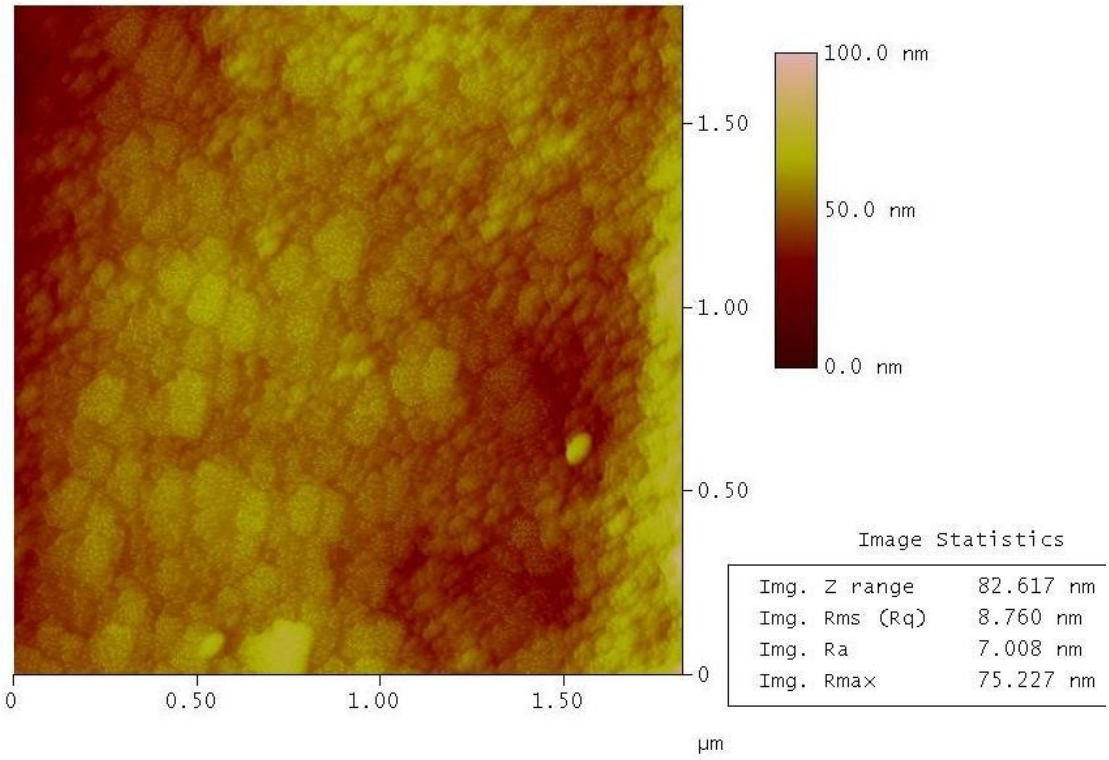


**Figure 5-6:** An AFM image of the sloped sidewalls defines by hot KOH etching.

### 5.2.3 Device testing

The first electrical test conducted was a standard V-I Characteristic on a 40 μm wide waveguide device. The device was connected to an Agilent 6611C voltage source and the voltage was varied linearly between -4V and +4V and the V-I plot is

shown in Figure 5-7. The dynamic resistance of the device is found to be 9.14 Ω in the forward-biased region of operation. We note the relatively large dark current of 53.9 mA at -4 V and this suggests that we will face difficulties in measuring very weak signals.

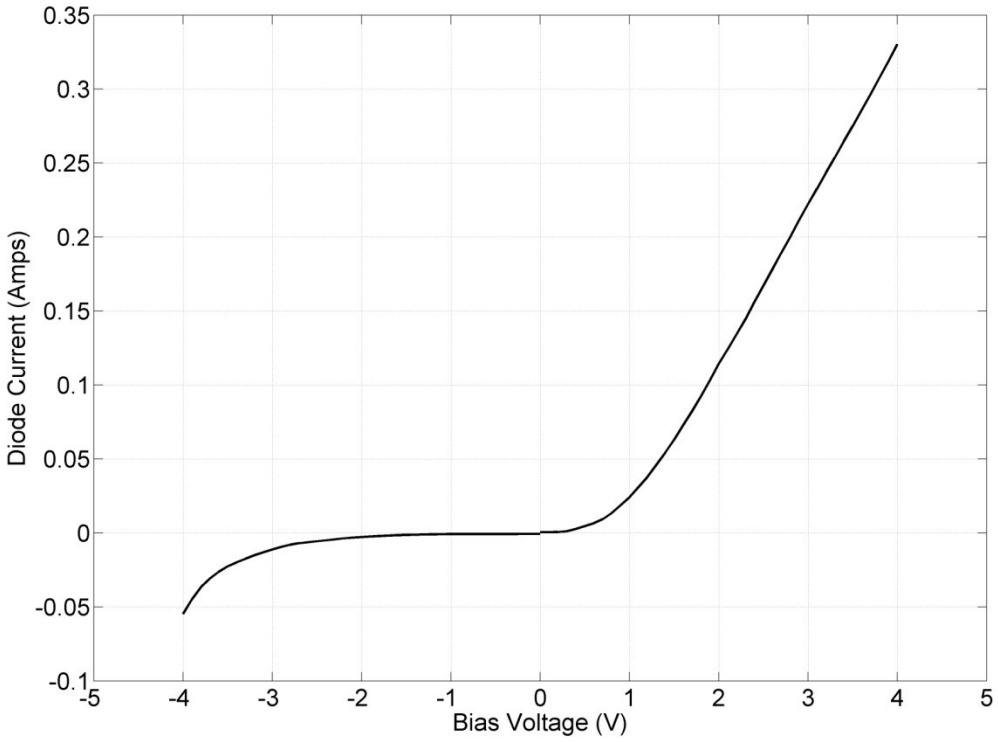


**Figure 5-7:** The V-I characteristics of a 40 μm (W) x 5 μm (H) x 1.9 μm (L) p-i-n waveguide

The next step is the quantifying the photoresponse in terms of a spectral response of the detector. This is performed using the technique of photocurrent spectroscopy. The setup is shown in Figure 5-8 and consisted of a 30 W tungsten halogen lamp coupled with a Spectral Products DK480 monochromator. A series of collimating and focusing lenses are used to focus the beam down to a spot of 300 μm

by 500 µm at the facet of 20-µm and 40-µm-wide waveguide. A beam-splitter and a CCD camera are used to estimate the spot size and optimize the location of the spot on the device facet. A lock-in detection scheme is used to improve the sensitivity of the measurement setup. An Agilent 6611C DC voltage source which is capable of high-precision measurement of low currents is used to operated and probe the device.

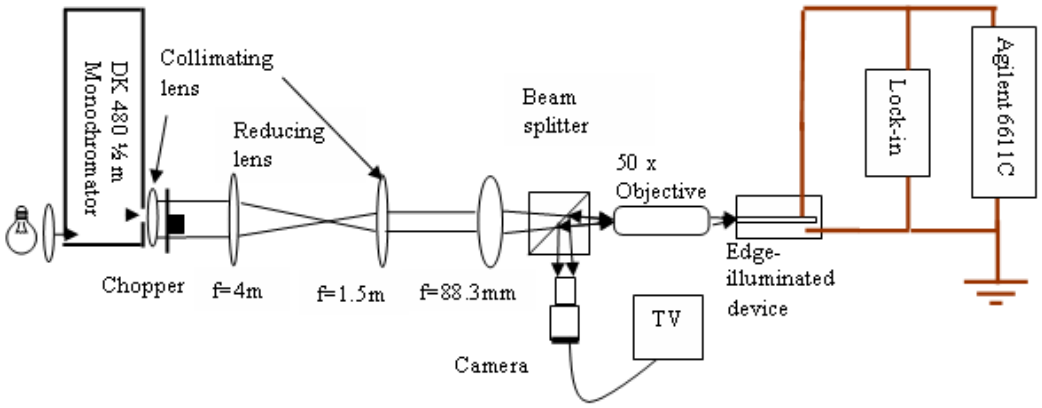


**Figure 5-8:** Measurement setup for spectral response measurement of the single quantum well device.

This setup did not yield any measurable spectral response as the dark current proved to be too large a background noise. To allow for the device to be characterized, a cryogenic setup is used to suppress the dark current, thereby decreasing the noise signal level. The setup consisted of an ARS Displex DE 202-S closed-cycle cryostat that is designed to cool down to 1.4 K. In addition, the 6611C Voltage source is replaced with an Agilent 4156B Semiconductor Parameter Analyzer. The V-I characteristics of a 20-µm-wide waveguide device at different temperatures are shown in Figure 5-9. It should be noted that it is the absolute value of the current that has been plotted on the y-axis. This is done to show structure in V-I

characteristic over several orders of magnitude of current. This method of plotting is especially useful in observing features in V-I characteristic in the region between diode turn-on and reverse breakdown. The typical reverse leakage current density at room temperature is 25 $mAmm^{-2}$. The reduction in dark current densityin these devices is small (~5X at -1V bias) and is several orders of magnitude larger than that of a commercially available silicon diodes (~ 100 $nA\text{-}mm^{-2}$).

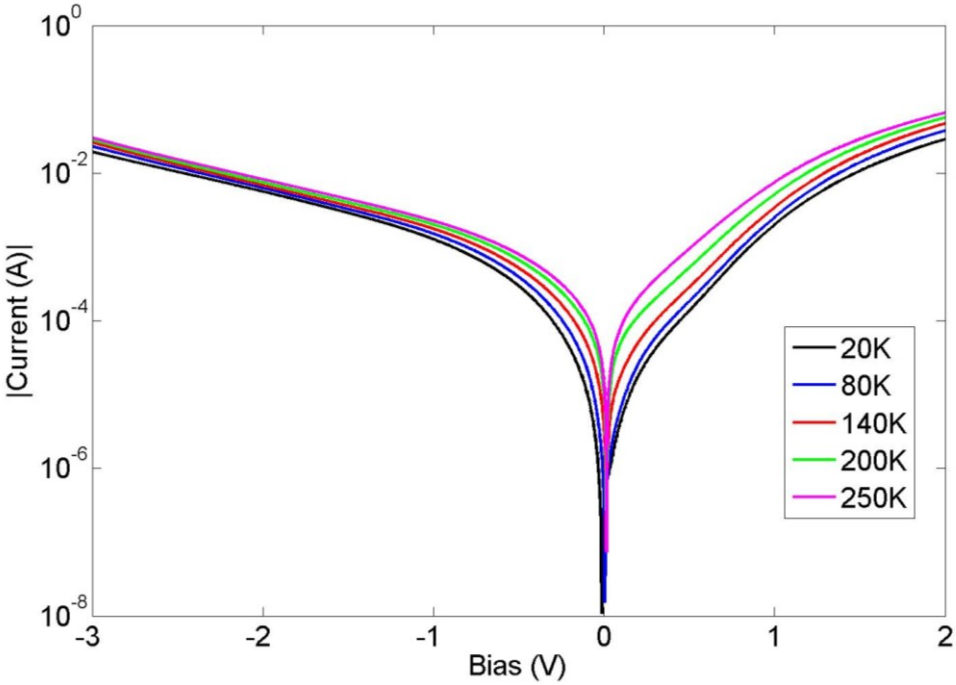


**Figure 5-9:** The V-I characteristics of a 20 μm wide waveguide device as a function of temperature

To optically characterize this material, it is tested with a solid-state laser at 1.319 μm with an output power of 188 mW. The beam profile is measured to be Gaussian and using a 10X microscope objective, the beam is focused down to spot 102μm in diameter. The responsivity of the waveguide detector is measured to be 18.2 $mAW^{-1}$ at a reverse bias of 4 V when cooled to 20 K. As a spectral

photoresponse cannot be obtained using a monochromatic source, the spectral responsivity and detectivity of the devices could not be measured. The poor responsivity and high dark currents make this approach to NIR photodection unpractical, and alternate designs are pursued.

## ***5. 3 Design 2: W-detectors***

### 5.3. 1 Heterostructure design

The second design is a W-Structure design with the type-II band alignment resulting in electron- and hole- wavefunctions concentrated in different layers. A similar approach has been used to fabricate interband lasers in gallium antimonide [101]. The advantage of such architectures is that the band offsets are used to reduce the required bandgaps of each individual layers. In the SiGe system, there is an added benefit that the layers can be designed such that the average strain energy in one active region is significantly less than that of a conventional p-i-n design.

W-Structures are called so because the conduction and valence bandedge profiles look like the letter "W". Figure 5-10 shows the bandedge diagram of a proposed W-Structure detector designed for 1.3 μm detection grown on a Silicon substrate. The various band offsets are calculated in MatLab using the relations detailed in Chapter 2. The active region consists of a W sandwiched by two 75-nm-thick $Si_{0.9}Ge_{0.1}$ optical confinement layers. The W consists of a 1.75-nm-thick $Si_{0.61}Ge_{0.39}$ electron-barrier layer in the middle of two 3-nm-thick silicon electron-well layers. The Si-well acts as the electron confinement region while the $Si_{0.61}Ge_{0.39}$

barrier acts as a hole confinement region.

Also shown in Figure 5-11 are the wavefunctions of the electron and heavy holes. Because the regions are so thin, there is a significant wavefunction overlap and this is the parameter that determines the detector efficiency. Unlike traditional quantum well detectors where detection usually involves a bound state-bound state transition in the same material, in this design, the bound states are in adjacent layers. The interband transition energy is governed by the difference between the ground state electron energy level in the conduction band and the ground state heavy hole energy level in the valence band. These energies are also shown in the figure. The heavy hole level is the most important from the design perspective as this is the highest level in the conduction band due to strain splitting of the degeneracy of the valence band. By virtue of their lighter mass, light- and spilt-off holes are more energetic and hence, not the preferred ground state.

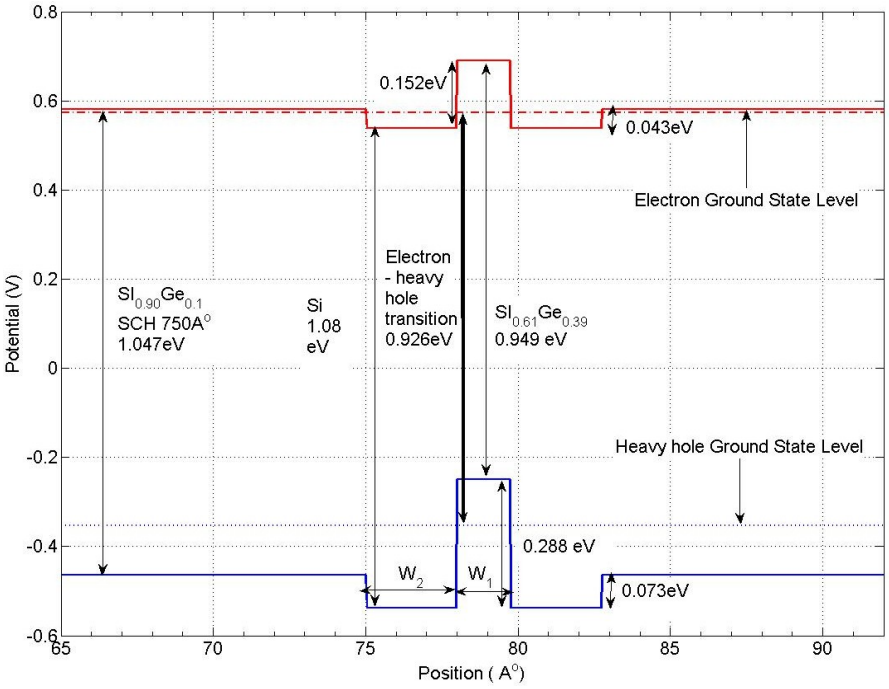


**Figure 5-10:** The band edge diagram of a W-structure, showing the ground state levels of the conduction band and the heavy hole band.

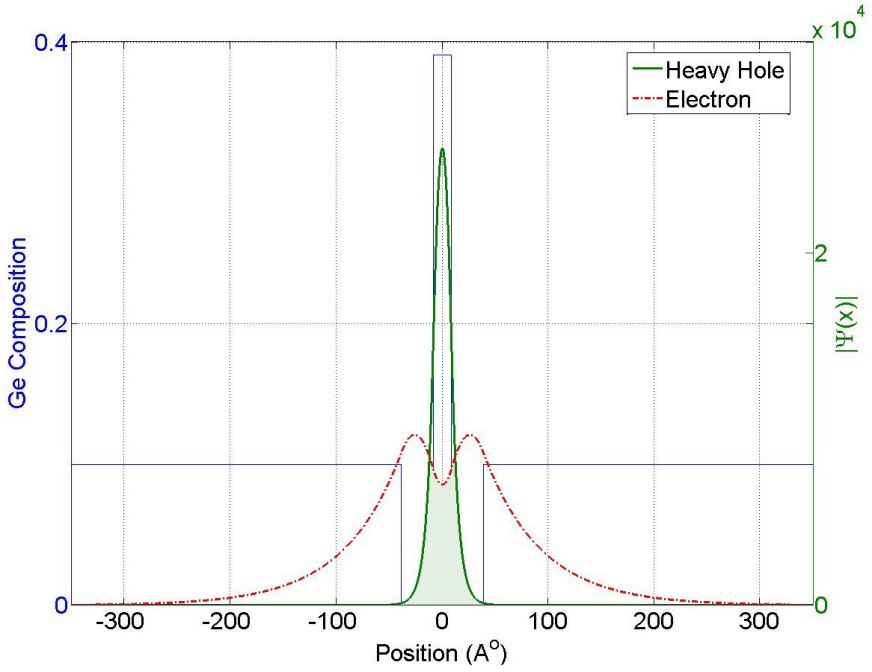


**Figure 5-11:** The electron and heavy hole wavefunctions as a function of position in the W-structure.

Given the qualitative explanation of W-structure photodetectors from the preceding section, it is important that a design algorithm be developed to arrive at optimized W-structure photodetectors on silicon and silicon-germanium virtual substrates. The chosen optimization parameter is the overlap of the ground-state electron and heavy hole wavefunctions. As detailed in the section on optical absorption, this is the suitable choice as the probability of electron-hole pair generation by photon absorption is directly related to this overlap.

As the design objective is a waveguide detector, a good optical confinement layer is required. As the active W-region is extremely thin, it cannot support an optical mode and this necessitates the use of a separate confinement hetereostructure (SCH) to ensure optical confinement. To ensure this, the two 75 nm $Si_{0.9}Ge_{0.1}$ regions are used as optical confinement layers. Regions with higher Ge-content will ensure better optical confinement as well as confine the electrons better. However, this will increase the strain and problems similar to those encountered in the preliminary design will be an issue. The next important step is the design and optimization of the absorption region. This involves the following steps. First, the composition x of the barrier layer is chosen. To ensure effective hole confinement in the valence band, x>0.1. If this design rule is not followed, the ground state of the hole will be in the optical confinement region. Next, using the methods detailed in Chapter 4, the band offsets and the energy profile $V_b(z)$ are determined. The fundamental gap of the semiconductor

$$E_g = E_{CB,Si} - E_{VB,Si_{1-x}Ge_x} \qquad \textbf{(5.1)}$$

is calculated where $E_{CB,Si}$ is the energy of the Si-well in the conduction band and $E_{VB,Si1-xGex}$ is the energy of the $Si_{1-x}Ge_x$ barrier in the valence band. These energy levels are determined by solving Equation 4.19**.** If $E_g$>0.95 eV, the chosen x will not result in a W-structure suitable for 1.3 μm detection and that composition is discarded. For compositions with $E_g$<0.95 eV, the widths of the barrier and wells $W_1$ and $W_2$ are chosen. To ensure significant overlap, it was found that these regions should be less than 4-nm-thick. The transition energy $E_{e\rightarrow hh}$ for the designed W-structure is then determined as the difference between the ground-state electron energy level in the conduction band and the ground-state heavy hole energy level in the valence band. This process is repeated for different $W_1$, $W_2$ and x to obtain the maximum overlap for $E_{e\rightarrow hh}$ <0.95 eV. The overlap is important as it governs the transition rate which in turn determines the absorption coefficient of the material. This in turn influences device geometry and dimensions. If the overlap is large, the material optical absorption coefficient is also large. This facilitates normal incidence detectors. In contrast, lower overlaps require longer waveguide detectors.

To obtain the design shown in Figure 5-10, $W_1$ and $W_2$ were independently varied between 1.75 nm and 4 nm. This was repeated for different barriers compositions x varied between 0.2 and 0.49 in steps of 0.01. The optimum design incorporates a 1.75 nm thick $Si_{0.61}Ge_{0.39}$ barrier with 3nm thick Si wells and has a bandedge of detection of 0.926 eV corresponding to a wavelength of 1.34 μm. For this configuration, the wavefunction overlap is 42%. The design approach reveals that the parameter that has the most significant effect on the overlap is the barrier layer thickness. For all composition, the optimum well thickness was between 2.75 nm and

3 nm. The variation of the overlap with barrier thickness for x=0.34, 0.39 and 0.44 is shown in Figure 5-12.

With an increase in barrier thickness, the overlap decreases as expected. For a given thickness, lower Ge-composition in the barriers results in a larger overlap. Again, this is not unexpected as a lower x in the barrier results in a shorter barrier. This comes at the price of a blue-shift in the bandedge of detection. This blue shift arises because the fundamental gap of the heterostructure $E_g$ is also blue-shifted. The bandedge of detection as a function of composition for $W_1$=2 nm, $W_2$=3 nm is shown in Figure 5-13

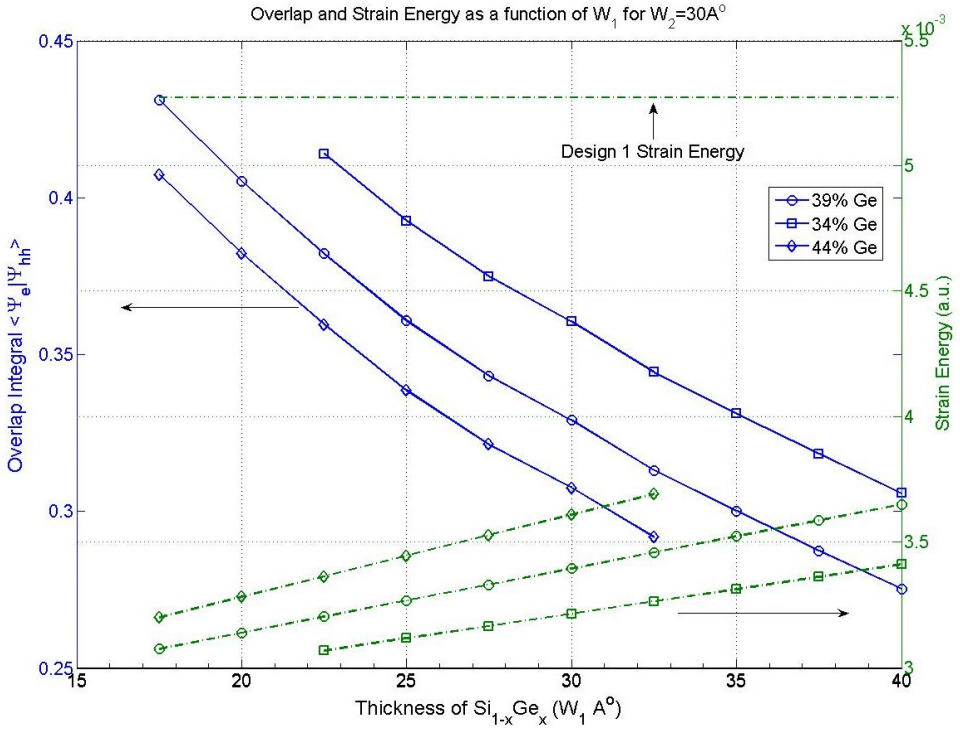


**Figure 5-12:** The overlap and strain energy as a function of the thickness and composition of the central SiGe barrier for fixed Si wells of width 3 nm. Only structures with $E_g$<0.95 eV are shown

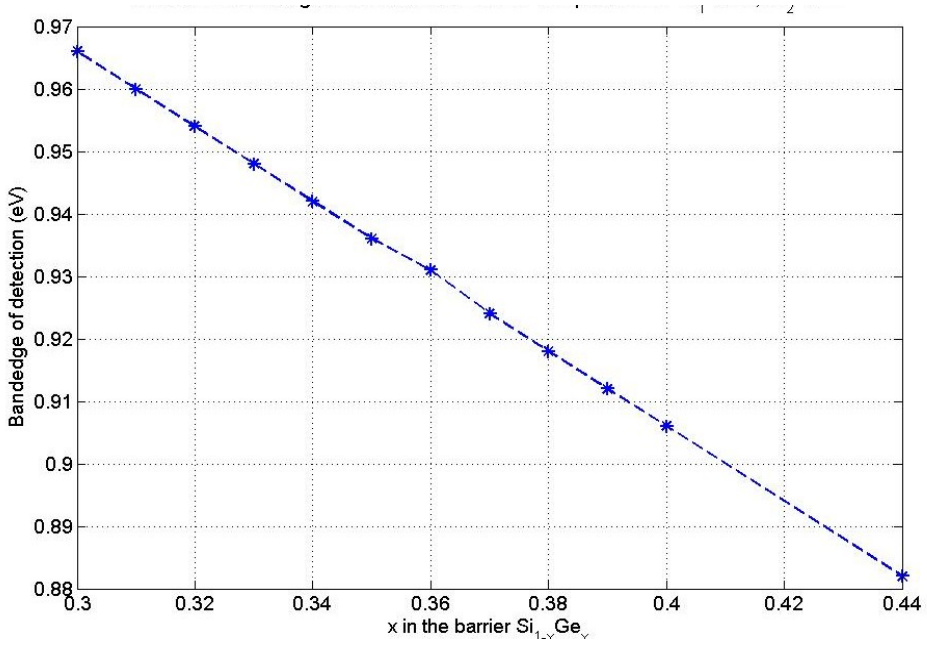


**Figure 5-13:** The variation of detection bandedge as a function of barrier composition for fixed well and barrier widths.

Also shown in Figure 5-12 is the strain energy of this design. This strain energy S is computed using the relation

$$S = \sum_{n-layers} k_i \varepsilon_i^2 t_i \,, \qquad \textbf{(5.2)}$$

on the entire heterostructure including the optical confinement regions. The value of the layer strains $\varepsilon_i$ is obtained as detailed in earlier in this chapter and k is the material stiffness constant. To first order, we can approximate the stiffness constant to be constant and removed from the summation. A decrease in strain by 42% as compared to the original design is noted. As expected, lower Ge-content barrier regions have lower residual strain energies. About 72% of the strain in the W-structure design comes from the optical confinement layer. The reduced strain ensures that this design

is significantly below the limit of the critical thickness, unlike the more conventional p-i-n structure presented as Design 1.To fully explore the design space, three different heterostructures are considered for growth:

i. A heterostructure with 1 W-absorber region sandwiched by two 75 nm-thick $Si_{0.9}Ge_{0.1}$ layers that act as an optical confinement layers.
ii. A heterostructure with 4 W-absorber regions, with a 25 nm-thick $Si_{0.9}Ge_{0.1}$ optical confinement layers separating each of the W absorbers. The total thickness of the $Si_{0.9}Ge_{0.1}$ layers in this sample is 125 nm.
iii. A heterostructure with only 150 nm $Si_{0.9}Ge_{0.1}$ layers (i.e. 0 W-absorbers) to act as a control device.

The full structure grown consists of these absorber regions, p- and n- contact layers. A preliminary structure consisting of the 1 W-absorber heterostructure was grown at NRL for demonstration of optical absorption. This sample is labeled NRL-1W. This 1-W structure, along with the 4 W and 0W – absorber structures were regrown by me at LPS, and are designated LPS-1W, LPS-4W and LPS-0W respectively. Each of these LPS grown heterostructures is further sandwiched between two 500-nm-thick i-Si layers. These layers are included to reduce the effect of free carrier absorption arising from the interaction of the optical mode of the waveguide with the doped contact regions in the NRL-1W sample, as will be demonstrated in the following sections. The full layer structures for each of these structures is shown in Figure 5-14 and Figure 5-15

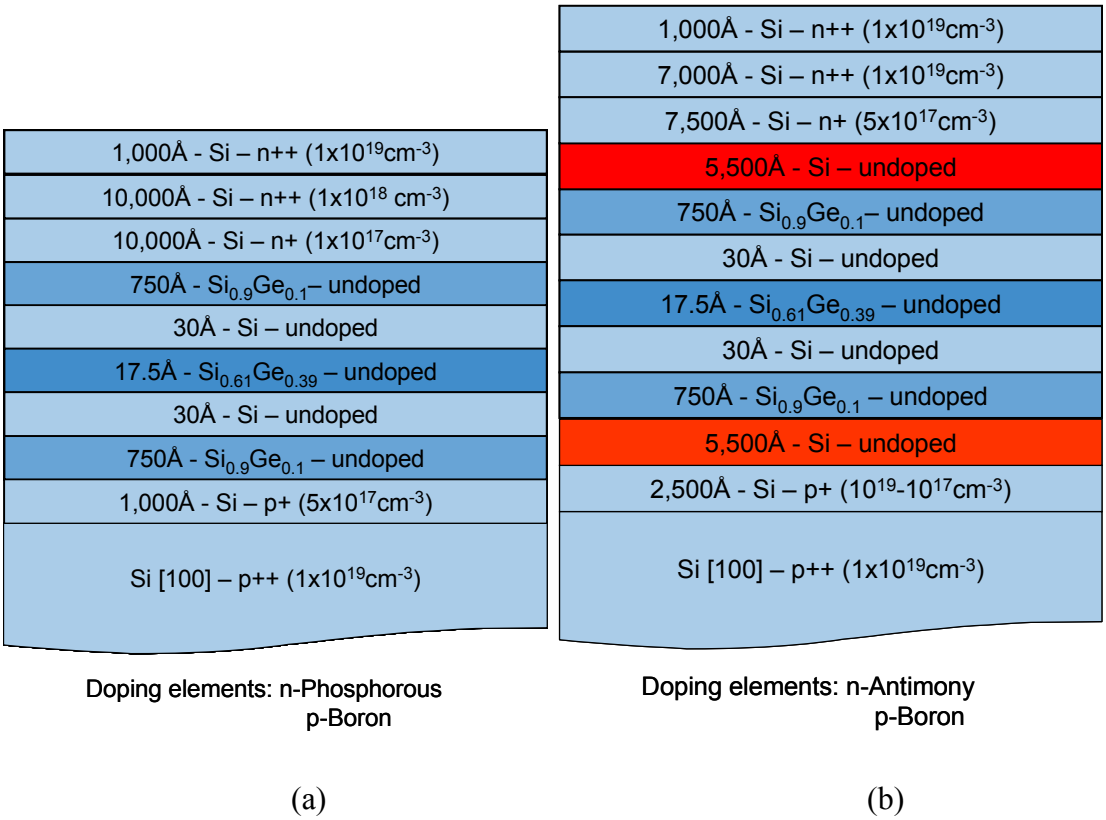


**Figure 5-14:** The full layer structures for samples (a) NRL-1W and (b) LPS-1W. The additional i-Si layers labeled in red to highlight the difference.

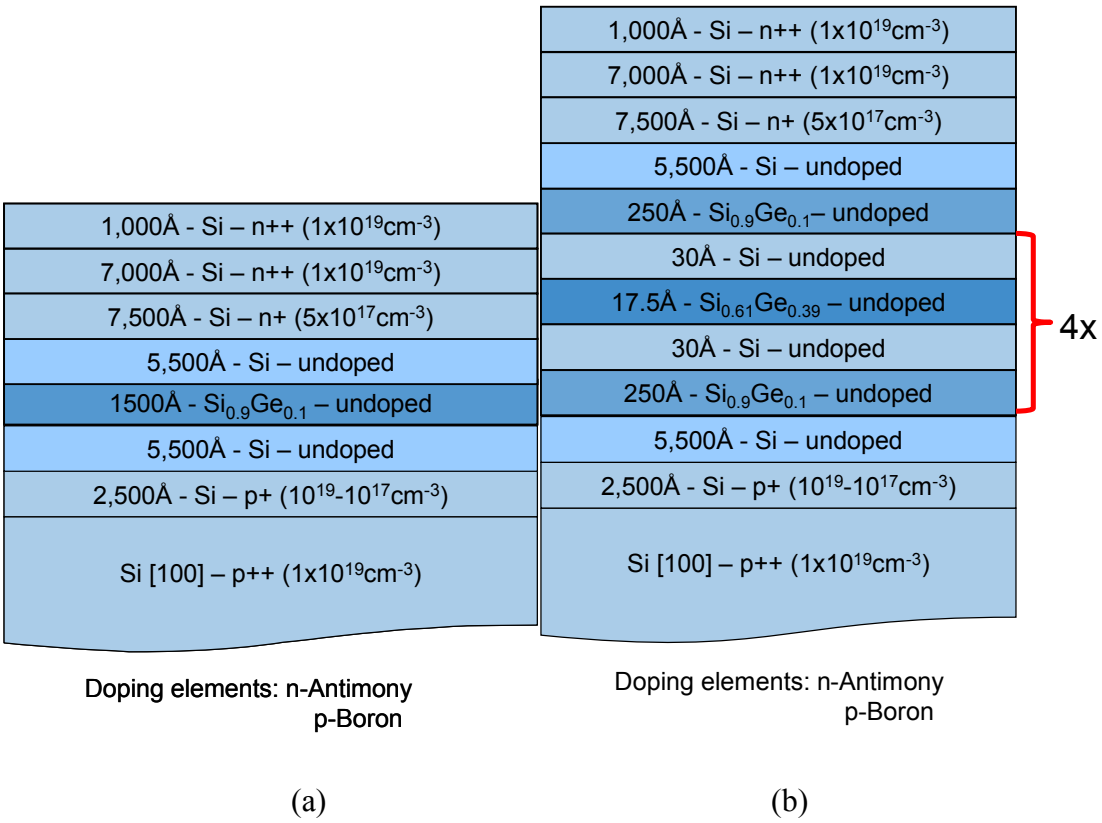


**Figure 5-15:** The full layer structures of samples (a) LPS-0W and (b) LPS-4W

### 5.3 2 Material growth and characterization

As shown in Figure 5-14 and Figure 5-15, all the device structures are grown on p-doped substrates with resistivity 13-15 mΩ-cm. All growths were performed using the AAS flux monitor described in Chapter 3 to control the silicon source. The typical silicon growth rate used was 0.9 Å/s. The exact composition of the W-absorbers in the final design structure cannot be measured using XRD because the layers are too thin to simulate accurately. Instead, their composition and thickness are estimated based on a separate growth of a calibration superlattice. The target for this 10-period calibration superlattice is a 30 nm Si / 7.5 nm $Si_{0.61}Ge_{0.39}$ layer stack.

Shown in Figure 5-16 is the XRD data and the best fit to this data, which is calculated to be is a 29.4 nm Si / 7.5 nm $Si_{0.57}Ge_{0.43}$ superlattice. To accurately achieve the target composition of $Si_{0.61}Ge_{0.39}$ in the W-absorber, the BEP equations Equation 2.14-2.16 from Chapter 2 are used to adjust the cell temperature and the relative growth rate of Ge with respect to that of silicon.

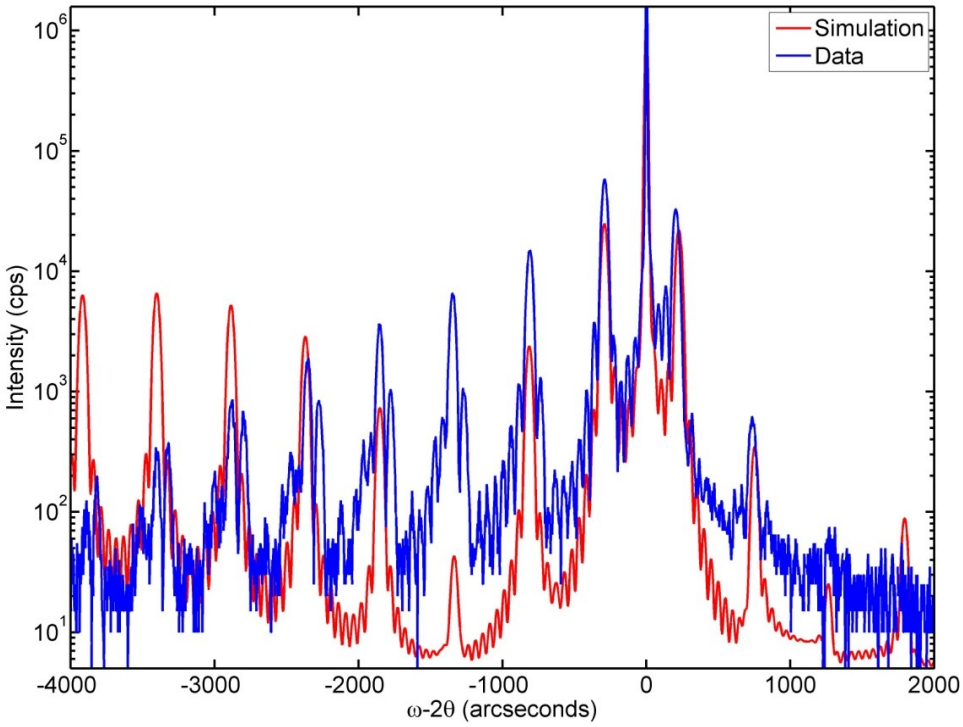


**Figure 5-16:** The ω-2θ XRD scan (blue) and simulation (red) for the calibration superlattice for the W-structure described in the text.

XRD analysis was performed after growth on the samples LPS-0W, LPS-1W and LPS-4W, and the results of which are summarized in Table 5-1 below. As mentioned earlier, the composition of the W-absorbers cannot be determined from this analysis and they are not included in Table 5-1. Analysis of the (004) and (113) reciprocal space maps was also performed to identify if there was any strain

relaxation in the film and it was found that both, LPS-0W and LPS-1W were fully strained, while sample LPS-4W was ~4% relaxed. The XRD data and simulation traces are shown in Figure 5-17, Figure 5-18 and Figure 5-19 and show good fits to the actual structure, with the actual structures grown being close to the target structures. The NRL-1W sample could not be characterized using XRD as the capability to perform these measurements was not available at the time the sample was obtained, and the sample has since been consumed.

| Sample | Target SCH | Actual SCH | % Relaxation |
|---|---|---|---|
| LPS-0W | 150 nm $Si_{0.9}Ge_{0.1}$ | 150 nm $Si_{0.88}Ge_{0.12}$ | 0 |
| LPS-1W | 2x 75 nm $Si_{0.9}Ge_{0.1}$ | 75 nm $Si_{0.86}Ge_{0.14}$ + 75 nm $Si_{0.87}Ge_{0.13}$ | 1 |
| LPS-4W | 5x25 nm $Si_{0.9}Ge_{0.1}$ | 5x25 nm $Si_{0.87}Ge_{0.13}$ | 4 |

**Table 5-1:** A summary of XRD analysis of the W-structure photodetectors.

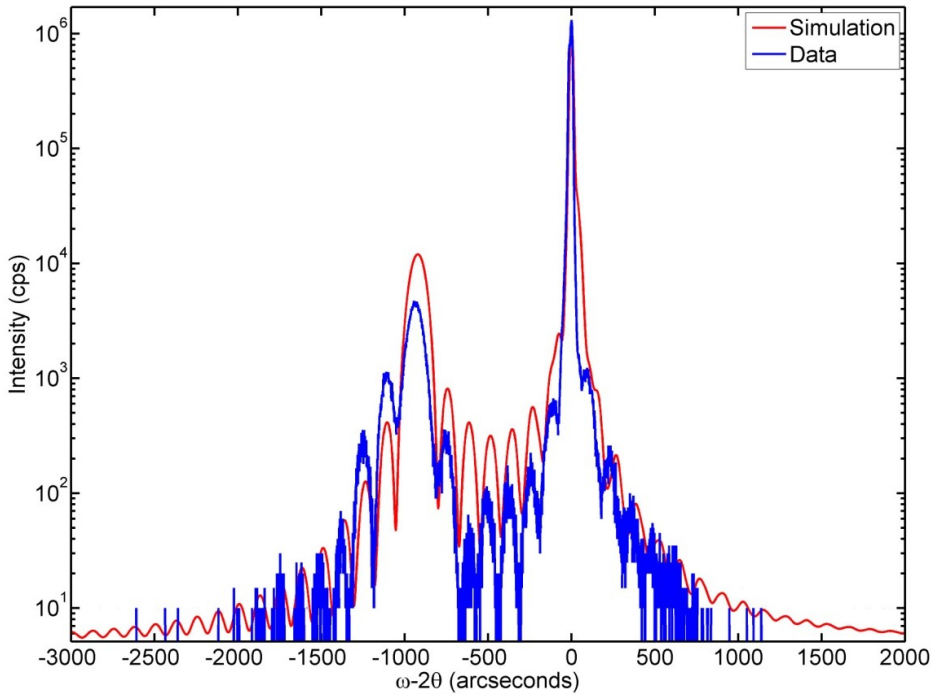


**Figure 5-17:** The ω-2θ XRD scan (blue) and simulation (red) for LPS-0W.

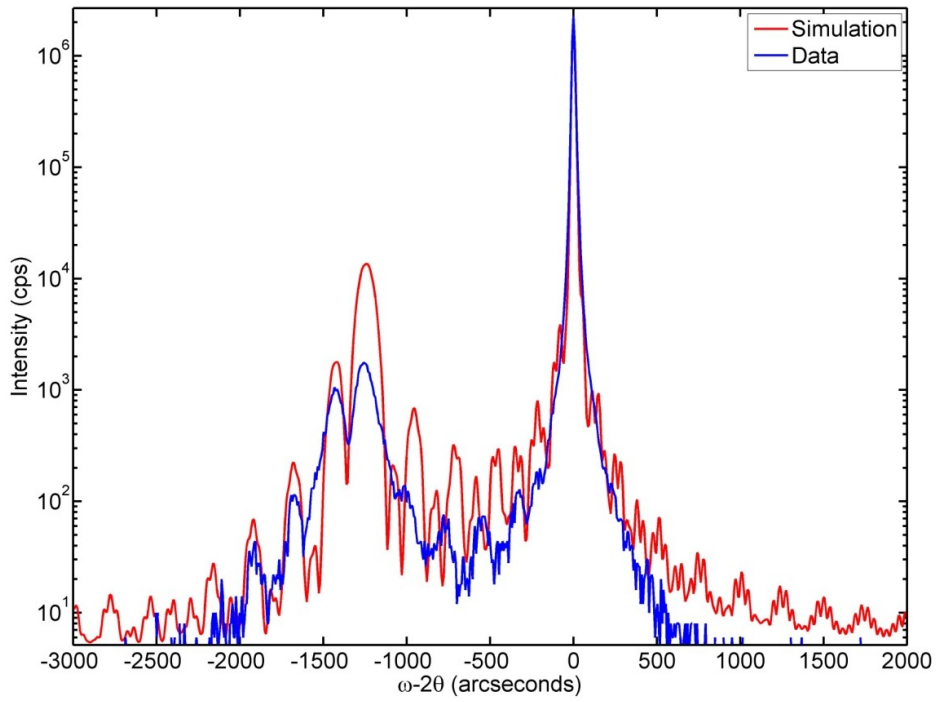


**Figure 5-18:** The ω-2θ XRD scan (blue) and simulation (red) for LPS-1W.

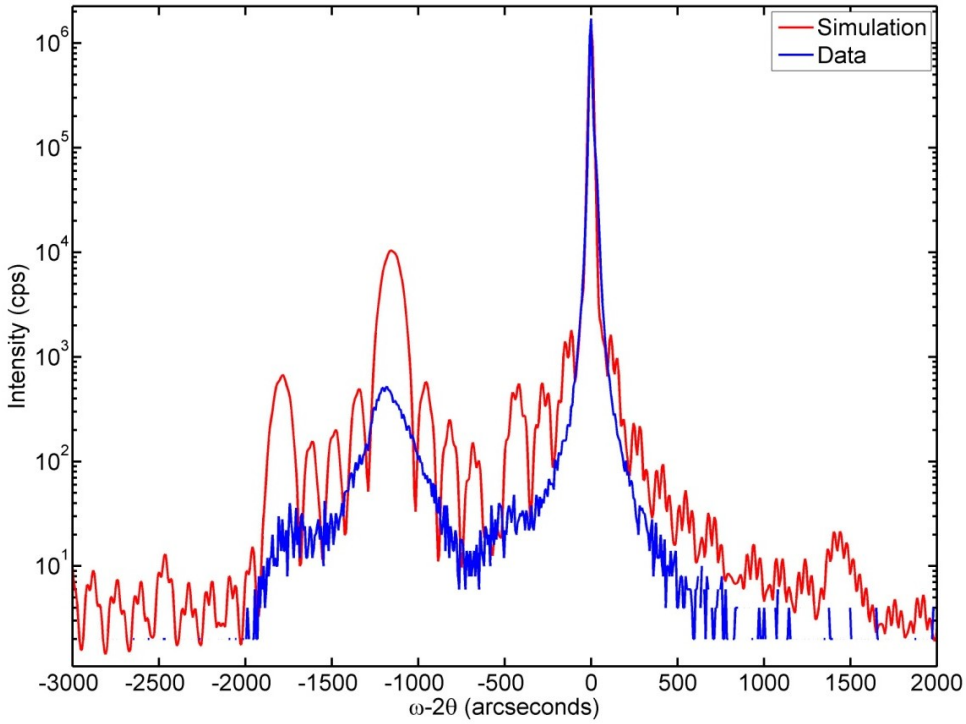


**Figure 5-19:** The ω-2θ XRD scan (blue) and simulation (red) for the LPS-4W sample.

### 5.3.3 Device design and processing

To characterize these 4 materials, two sets of devices are processed. To determine the absorption coefficient at 1.32 μm using the fiber-coupled laser detailed earlier, a series of single mode waveguides (SMWG) of varying lengths are required. The effective index method (EIM) [102] is used to calculate the number of modes for a waveguide of a specified width. The details of the EIM are presented in Appendix C. The results of these calculations for a 2.1 μm high waveguide are shown in Figure 5-20 where we see that for ridges of widths less than 5.6 μm are single mode.

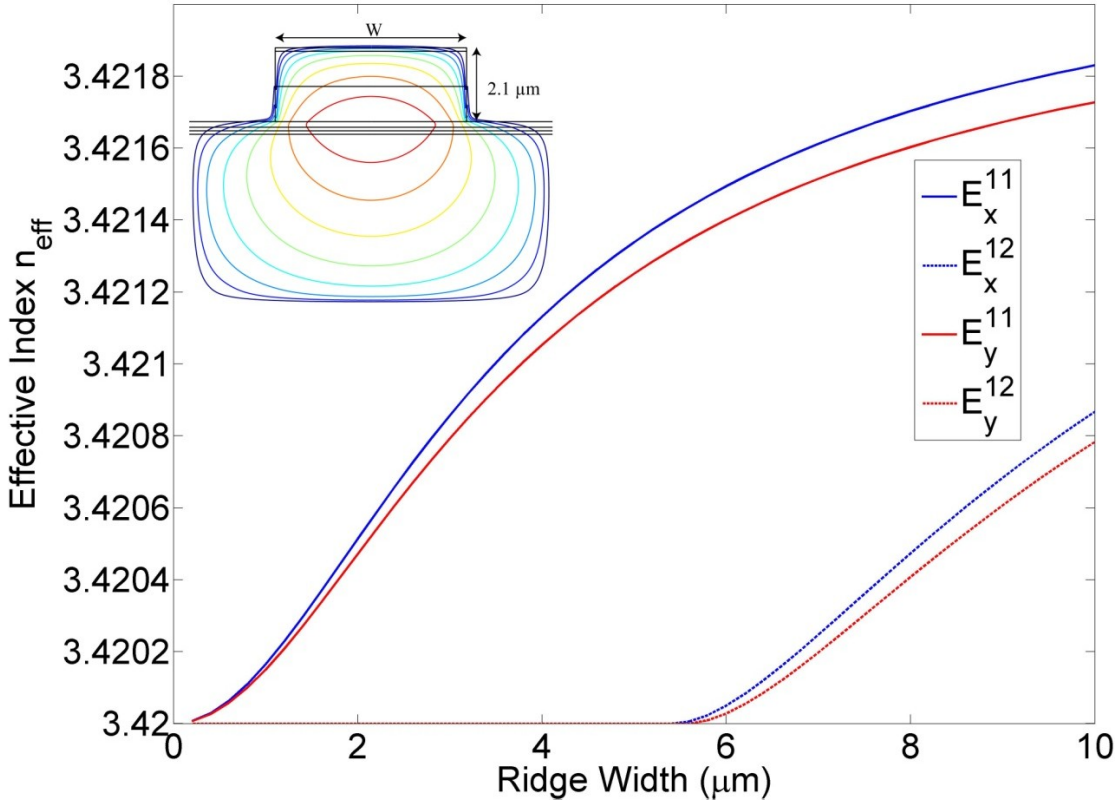


**Figure 5-20:** The effective refractive indices of all modes of the waveguide shown in the insert as a function of waveguide width.

The geometry used in the EIM calculations is shown in the insert in Figure 5-20. It is important to note that the actual geometry of the waveguides differs from the modeled structure in that the wet-etched waveguides have sidewalls that slope at 53º. To account for this, the width of the trace on the photomask needs to be smaller than the target waveguide width at the core by a geometric factor. For 2.1 μm tall waveguides, this factor is calculated as $2\times \cot(53^\circ)\times 2.1\ \mu m = 3.1\ \mu m$. Thus, waveguides with top widths of up to 2.5 μm are expected to be single mode. This is the chosen width for fabrication and testing.

Strip loaded ridge waveguides were aligned along the [110] axis. The waveguide mesas were selectively wet etched using an IPA-saturated 10% aqueous $NH_4OH$ solution at 60°C. This solution is used as the silicon etch so that the top SiGe SCH layer can be used as an etch stop. The resulting 2.1 μm high waveguides had smooth <111> sidewalls with a surface roughness comparable to that of the MMWG devices detailed in section 5.2.2. Benzocyclobutene (BCB) is used to planarize and passivate the sidewalls and Ti/Pt/Au is deposited for both p- and n-ohmic contacts. After metallization, the die was thinned to 100 μm and cleaved to define waveguide facets. A scanning electron micrograph of the device is shown in Figure 5-21, where the SiGe active region can clearly be seen as the lighter gray horizontal line underneath the trapezoidal shaped waveguide ridge. SMWG devices are fabricated from the three growths with W-absorbers i.e. NRL-1W, LPS-1W and LPS-4W.

The second set of devices is MMWG waveguides as detailed in Section 5.2.2. These are fabricated for spectral characterization to allow for easy coupling of

extended light sources (such as tungsten halogen and xenon arc lamps). MMWGs 40 μm wide, 5 μm high and up to 2.2 mm long are fabricated as detailed earlier. These devices are discussed in section 5.3.5.

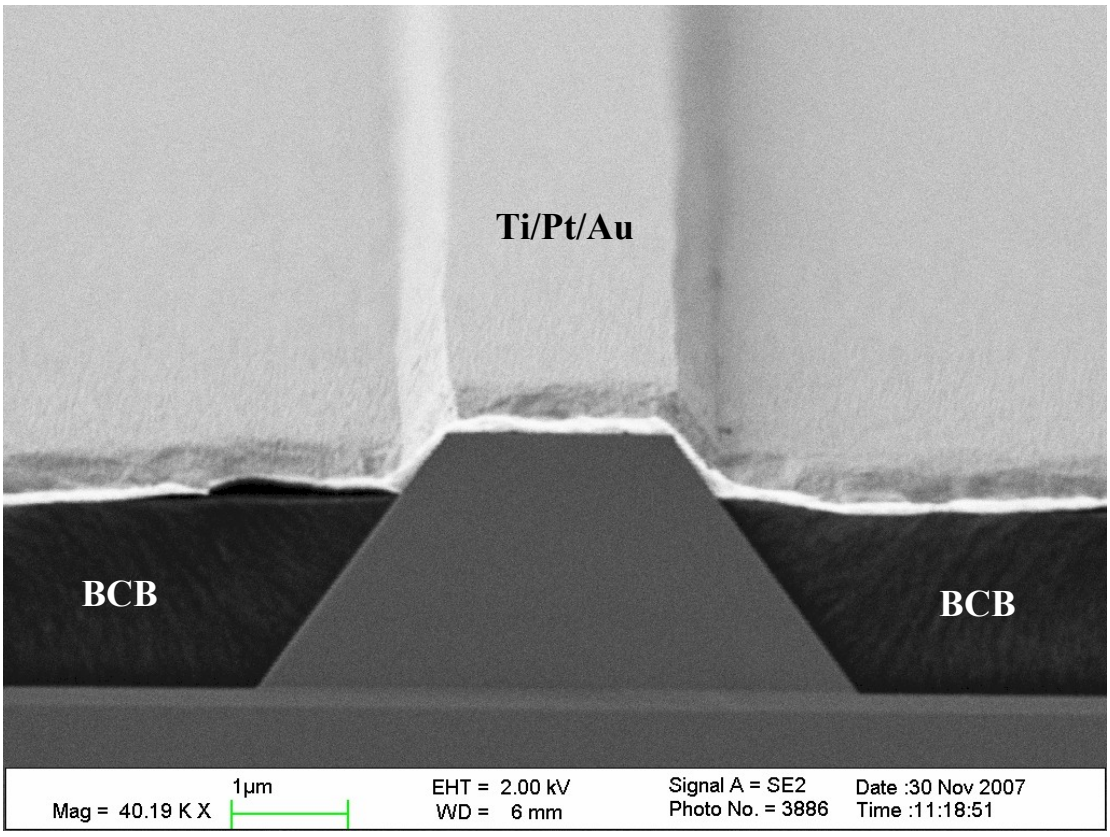


**Figure 5-21:** Scanning electron micrograph of a single-mode waveguide photodetector. The lighter gray SCH and active region is apparent below the trapezoidal waveguide ridge. BCB surrounds the waveguide ridge, upon which an ohmic contact is deposited.

### 5.3.4 Single mode waveguide testing

Fabricated single mode waveguide devices are tested for diode behavior using a HP4156B semiconductor parameter analyzer. All diodes are found to have a turn-on

voltage of 0.8 ± 0.1 V, and 1-mm-long diodes are found to have a forward resistance of 10 – 15 Ω. These are shown in Figure 5-22. The reverse leakage current densities for these devices are significantly lower than those of the QW devices and are measured to be 8.7 μAmm$^{-2}$ for sample LPS-4W, 211 μAmm$^{-2}$ for LPS-1W and 230 μAmm$^{-2}$ for NRL-1W at a bias of -1V.

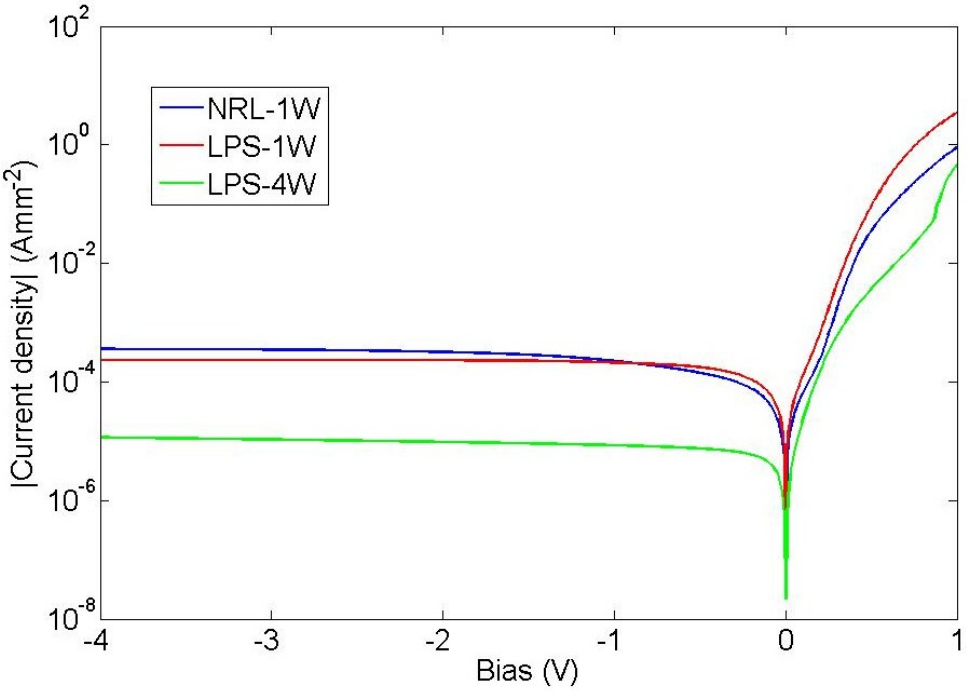


**Figure 5-22:** V-I characteristics of fabricated 1mm-long SMWG diodes

These devices are tested for optical absorption at 1.32 μm using the fiber-coupled solid-state laser described earlier. The output of this laser is coupled into the waveguide using a lensed fiber, and its power is monitored using an Eigenlight 420 power monitor. The photocurrent at different biases is extracted from the V-I characteristics measured using the HP4156B. To verify that each of the devices is operating unsaturated, the photocurrent is measured at different incident powers. This

is shown in Figure 5-23 for a 5-mm-long LPS-1W device and a 4-mm-long NRL-1W device at 0 V bias. The dashed line is a linear fit of the photocurrent as a function of incident power. The close proximity of the data to these lines demonstrates that the devices are operating in the linear, unsaturated regime.

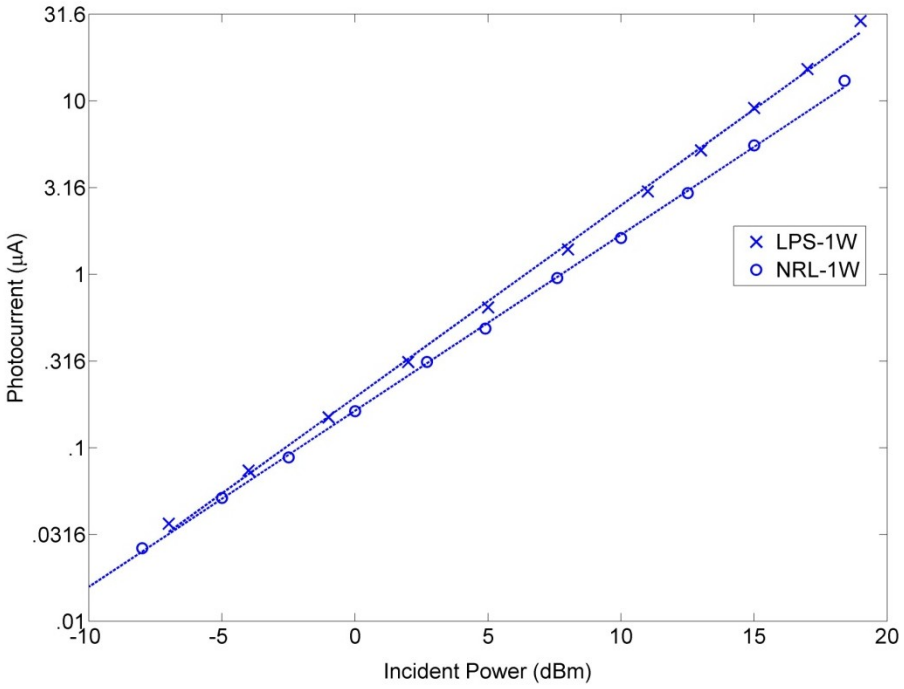


**Figure 5-23:** The photocurrent at different powers for devices from NRL-1W and LPS-1W showing that these devices are operating in the linear, unsaturated regime.

To determine the optical absorption coefficient of the material, the responsivity as a function of waveguide length is studied. The responsivity $R_m(L)$ of a single mode waveguide photodetector as a function of length L is known to be governed by: [103]

$$R_m(L) = \frac{e}{h\nu}(1-R) f \frac{\Gamma\alpha_m}{\Gamma\alpha_m + \alpha_l}\left(1 - e^{-(\Gamma\alpha_m+\alpha_l)L}\right)$$
$$\sim \left(1 - e^{-\alpha_o L}\right) \quad \textbf{(5.3)}$$

Here, e is the electronic charge, hν the photon energy (=0.95 eV), R, the facet reflectivity and f, the fiber to waveguide coupling efficiency. For these devices with uncoated facets, the reflectivity of the optical waveguide mode can be approximated as the Fresnel reflection coefficient for the air-semiconductor interface and is ~29%. f is estimated by computing the overlap integral of the fiber mode and the waveguide mode and is estimated to be 25%.This is done by numerically calculating the electric field distribution of the fundamental mode for the waveguide and computing its inner product with the fundamental Gaussian mode of a single mode fiber. $\alpha_m$ is the optical absorption coefficient of the waveguide core and Γ is the confinement factor of the waveguide i.e. the fraction of the optical mode that is contained within the waveguide core This confinement factor determines the strength of the response and is higher for devices with higher overlaps. , $\alpha_l$ is the waveguide loss coefficient and is comprised of scattering losses from rough sidewalls, free carrier absorption in the waveguide as well as optical absorption in the substrate. The total absorption coefficient $\alpha_o$ of the waveguide is given by ($\Gamma\alpha_m+\alpha_l$), and can be extracted by fitting $R_m(L) \sim(1-\exp(-\alpha_o L)$ ). The responsivity data at 0 V bias and fit for the NRL-1W, LPS-1W and LPS-4W samples are shown in Figure 5-24 (a), (b) and (c). The values of $\alpha_o$ for the different devices are fit as 11.08 ± 4.42 $cm^{-1}$ (NRL-1W), 4.55 ± 1.36 $cm^{-1}$ (LPS-1W) and 6.17 ± 0.76 $cm^{-1}$ (LPS-4W). The error in the estimate of $\alpha_o$ is derived from the 95% confidence bounds of the fit to the data.

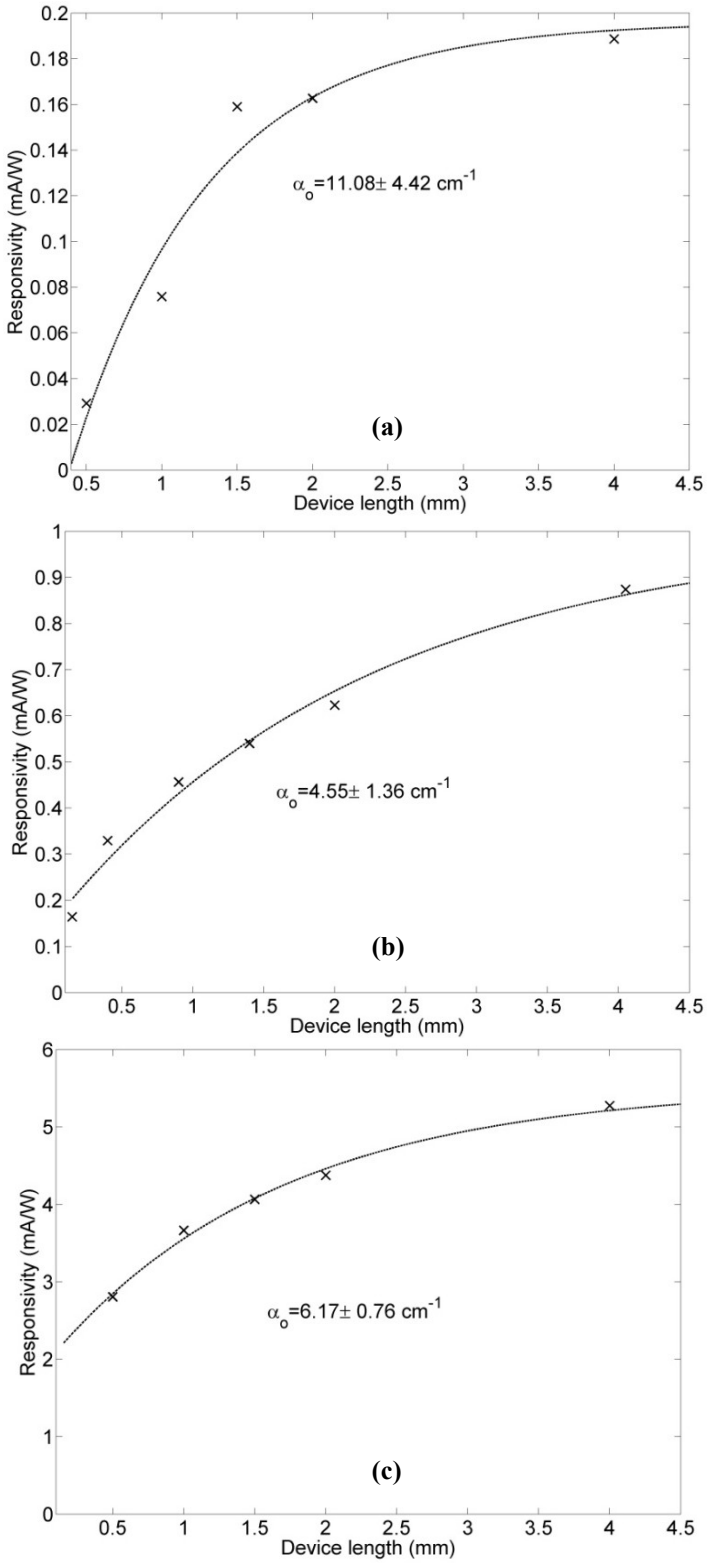


**Figure 5-24:** Responsivity as a function of length at 0V bias for samples (a) NRL-1W, (b) LPS-1W and (c) LPS-4W.

Despite the larger value of $\alpha_o$ for the NRL-1W structure, we note that this device has a lower responsivity when compared to the LPS-1W structure. This can be understood comparing the loss mechanisms in the two devices. From Equation 5.3 above, the internal quantum efficiency $\eta_i$ is $\eta_i(L) = \frac{\Gamma\alpha_m}{\Gamma\alpha_m + \alpha_l}\left(1 - e^{-(\Gamma\alpha_m+\alpha_l)L}\right)$

In the limit of long waveguides ($L \gg \alpha_o^{-1}$), we have

$$\eta_i = \frac{\Gamma\alpha_m}{\Gamma\alpha_m + \alpha_l} \tag{5.4}$$

This demonstrates that all other factors being equal, waveguides with lower losses will have higher internal quantum efficiencies and higher responsivities.

Using Equation 5.4 above, we can compare the responsivities of two different waveguide devices with identical optical confinement and material absorption coefficients but differing loss coefficients as

$$\frac{R_1(L_1)}{R_2(L_2)} = \frac{\alpha_{o2}}{\alpha_{o1}}\frac{1-\exp(\alpha_{o1}L_1)}{1-\exp(\alpha_{o2}L_2)} \tag{5.5}$$

Using the measured responsivities of the 4-mm-long NRL-1W (0.189 $mAW^{-1}$) and the 4.05-mm-long LPS-1W (0.874 $mAW^{-1}$) devices and the extracted values of $\alpha_o$, we have,

$$\frac{R_1(L_1)}{R_2(L_2)} = 0.22; \frac{\alpha_{o2}}{\alpha_{o1}}\frac{1-\exp(\alpha_{o1}L_1)}{1-\exp(\alpha_{o2}L_2)} = 0.4 \pm 0.5$$

This suggests that the difference in responsivities is explained by the differing optical absorption coefficients in the two materials. However, the large error associated with the scatter in the responsivity data makes definitive statements difficult.

The origin of the higher loss in the NRL-1W device can be understood by

inspecting the mode profile for a 5.5-µm-wide ridge waveguide as plotted in Figure 5-25, intensity contours of the fundamental mode are plotted in 5 dB steps. The mode profile is calculated using an optical eigenmode solver for dielectric waveguide. [117] These contours are overlaid on the ridge with the dopant densities of the various layers included. As can be seen, there is a large overlap of the mode with the highly doped substrate, and with the doped contact regions, which gives rise to free carrier absorption (FCA).

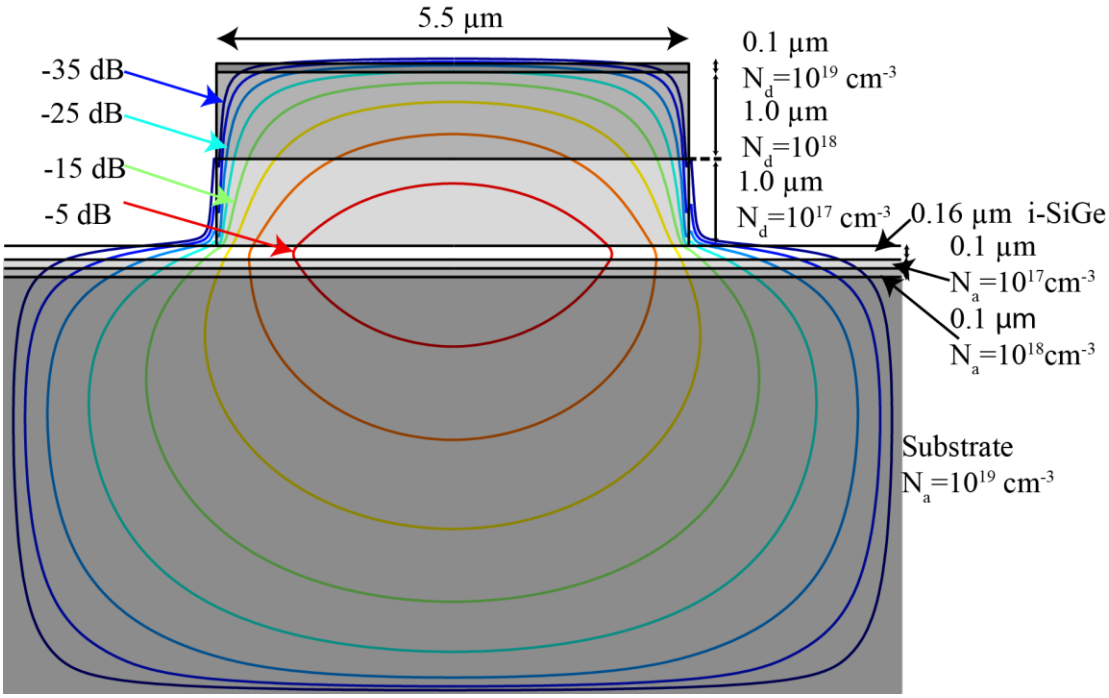


**Figure 5-25:** Intensity contours of the fundamental TE mode of a ridge waveguide overlaid on the ridge with dopant information of sample NRL-1W included. The high overlap of the optical mode with highly doped regions gives rise to high free carrier absorption losses.

FCA is a loss mechanism arising due to intraband scattering of an available carrier by an incident photon, and increases with dopant density. For p-doped silicon,

loss coefficient in $cm^{-1}$is experimentally determined to be [104]

$$\alpha_p(\lambda, p) = 2.7 \times 10^{-18} \lambda^2 p \tag{5.6}$$

In n-doped silicon, this is [105]

$$\alpha_n(\lambda, n) = 5.5 \times 10^{-17} \lambda^2 n \tag{5.7}$$

Based on these equations, the FCA loss coefficients at 1.3 μm at different dopant densities can be estimated as listed in Table 5-2. Also listed are the loss tangents for these dopant densities

| Dopant density ($cm^{-3}$) | $\alpha_p$ ($cm^{-1}$) | $\tan\delta_p$ | $\alpha_n$ ($cm^{-1}$) | $\tan\delta_p$ |
|---|---|---|---|---|
| $10^{17}$ | 0.456 | $1.9 \times 10^{-12}$ | 0.169 | $2.6 \times 10^{-13}$ |
| $10^{18}$ | 4.563 | $1.9 \times 10^{-10}$ | 1.69 | $2.6 \times 10^{-11}$ |
| $10^{19}$ | 45.63 | $1.9 \times 10^{-8}$ | 16.9 | $2.6 \times 10^{-9}$ |

**Table 5-2:** Free carrier absorption loss coefficients at 1.3 μm at different dopant densities in p- and n-doped silicon.

These loss tangents can be used to estimate the total loss in the waveguide using an extended method of the effective index method, mathematical details of which are included in Appendix C. For the structure NRL-1W, the waveguide loss due to FCA $\alpha_{FCA}$ is estimated to be approximately 7.3 $cm^{-1}$ at 1.32 μm. With the change in the doping densities for sample LPS-1W as shown, this is estimated to reduce optical loss due to free carrier absorption to about 0.8 $cm^{-1}$. This difference in $\alpha_{FCA}$ of 6.5 $cm^{-1}$ almost entirely accounts for the difference in optical absorption coefficients between samples LPS-1W and LPS-4W.

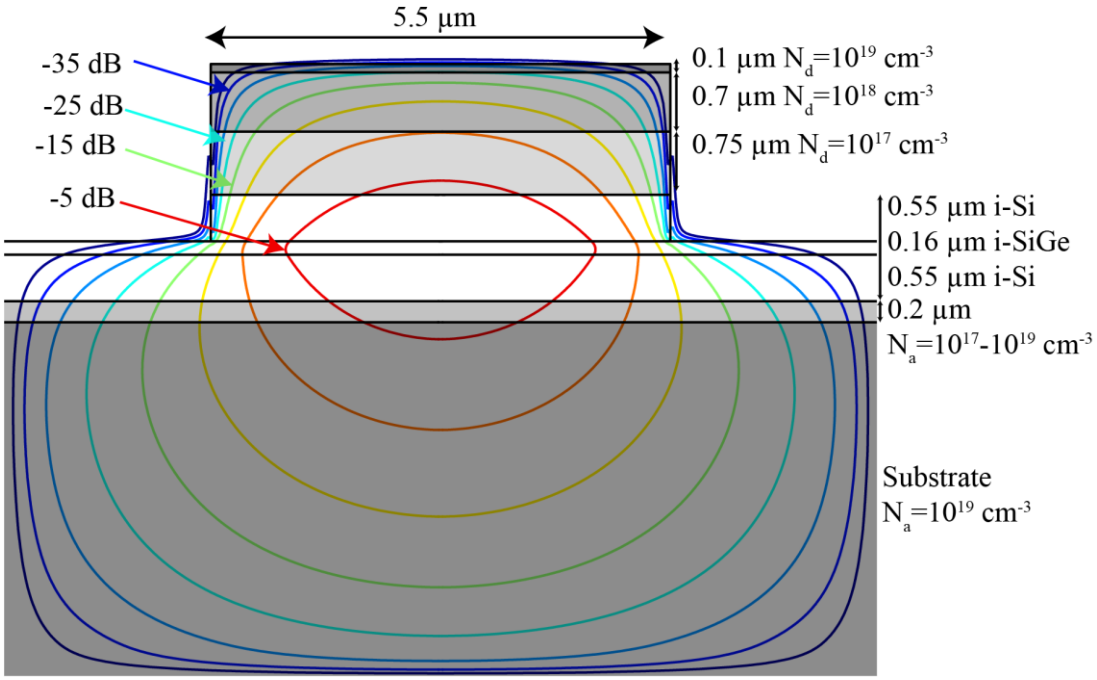


**Figure 5-26:** Intensity contours of the fundamental TE mode of a ridge waveguide overlaid on the ridge with dopant information of sample LPS-1W included. The overlap of the optical mode with highly doped regions is reduced in comparison to that of sample NRL-1W, resulting in lower losses. The mode profile is calculated using a semi-vectorial optical modesolver [106].

The final test performed on the SMWGs is a measurement of the RF performance of these devices. The high-speed performance of a short devices (L<1.0mm) was tested at 4 V reverse bias using a 40 GHz ground-signal-ground (GSG) probe and an Agilent 8565EC 50GHz RF spectrum analyzer. RF modulation was achieved by temperature-tuning two 1.32 µm lasers and co-propagating their output through the fiber to yield an RF tone resulting from their interference. This beat note was tuned from 160 MHz to 7 GHz with a modulation depth of 88%. A schematic of the experimental setup is shown in Figure 5-27.

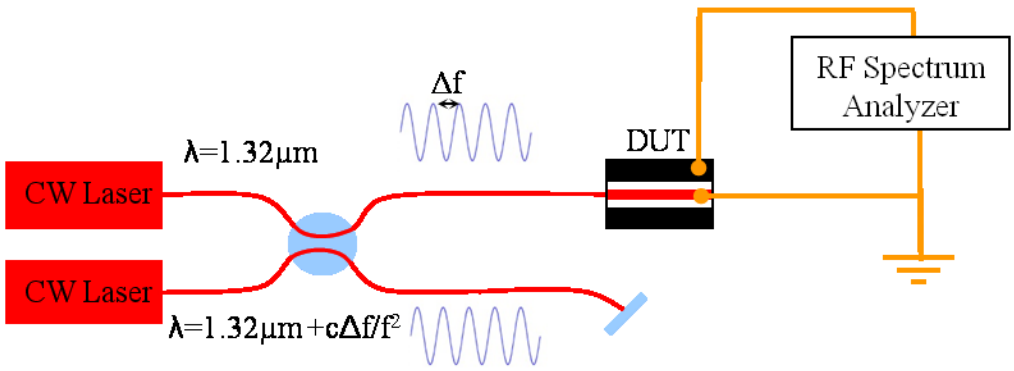


**Figure 5-27:** A schematic of the experimental setup used to measure the high-speed performance of the SMGW photodiodes

For the sample NRL-1W, the 0.5-mm-long device was found to have a 3 dB bandwidth of 1.54 GHz while the 1mm device had a 3 dB bandwidth of 976 MHz. These results are shown in Figure 5-28 with the traces shifted for clarity. The scaling of the cut-off frequency with device length suggests that high-speed performance is limited by the capacitance of the narrow intrinsic region. The devices fabricated from sample LPS-1W were found to have higher 3 dB bandwidths of 2.28 GHz for the 0.5-mm-long devices and 1.2 GHz for the 0.75-mm-long devices. These devices have a thicker intrinsic region and are expected to have a higher bandwidth when compared to NRL-1W  Devices from LPS-4W were measured to have significantly lower bandwidths of 715 MHz for the 0.5 mm devices and 660 MHz for the 0.75- mm-long devices. This reduced bandwidth is attributed to carrier trapping at in the valence band, which has been reported in the literature for similar structures. [107]

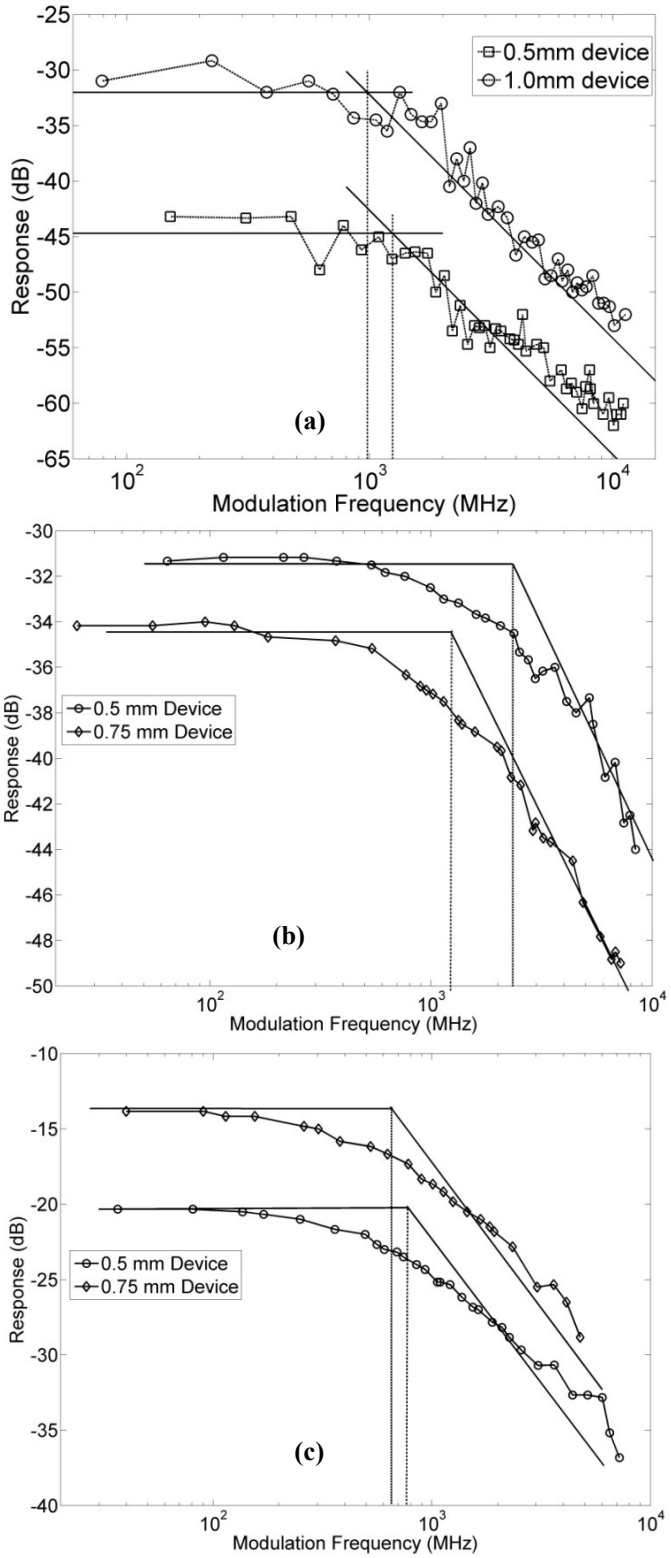


**Figure 5-28:** The measured RF performance of short SMWG photodiodes from samples (a) NRL-1W, (b) LPS-1W and (c) LPS-4W

### 5.3.5 Multimode waveguide testing

While SMWGs allow for accurate measurements of material response at a particular wavelength, their use for spectral measurements pose a number of difficulties:

i. Coupling from an extended source (such as a light bulb) into a waveguide mode is extremely inefficient due to the large mismatch in the geometric extent of the two sources.
ii. Careful corrections will have to be made to obtain the correct values of Γ and f in Equation 5.3 at all wavelengths under test.

Using MMWG for spectral measurements avoids both these difficulties. First, by providing a larger number of possible waveguide modes to couple into, coupling is made easier. Second, due to the large number of modes, a slight increase (or decrease) in the number of modes has a smaller effect on optical power in the waveguide, especially when compared to SMWGs where an increase (or decrease) in the number of modes dramatically affects the couple optical power. To this end, multimode waveguide photodiodes 40 μm wide, 5 μm high and 1.85 mm long from the 3 LPS samples were processed as described in Section 5.2.2. Using EIM calculations, we calculate that there are in excess of 40 modes at 1.3 μm for this structure.

As with the single QW device, photocurrent spectroscopy was used to measure the spectral response of the MMWG devices. The experimental setup was modified to include a 175 W xenon arc lamp and a double-side polished 675 μm-

thick silicon wafer as an order sorting filter. In addition, a shorter 1/8 m monochromator with a 600 groove/mm grating blazed for 1.6 μm and 2.4 mm slits is used to maximize optical throughput. Using the grating equation

$$\Delta\lambda = \frac{\Delta x \cos\beta}{GF} \tag{5.8}$$

where Δx is the slit width, β is the diffraction angle, G is the groove density of the grating and F is the focal length of the monochromator, the resolution of measurement Δλ of this setup is 18 nm (~10 meV at 1.3 μm). The output of the monochromator is then collimated and focused onto the waveguide facet. The spot size is estimated to be 60 μm in diameter i.e. it overfills the device. The experimental setup is shown in Figure 5-29.

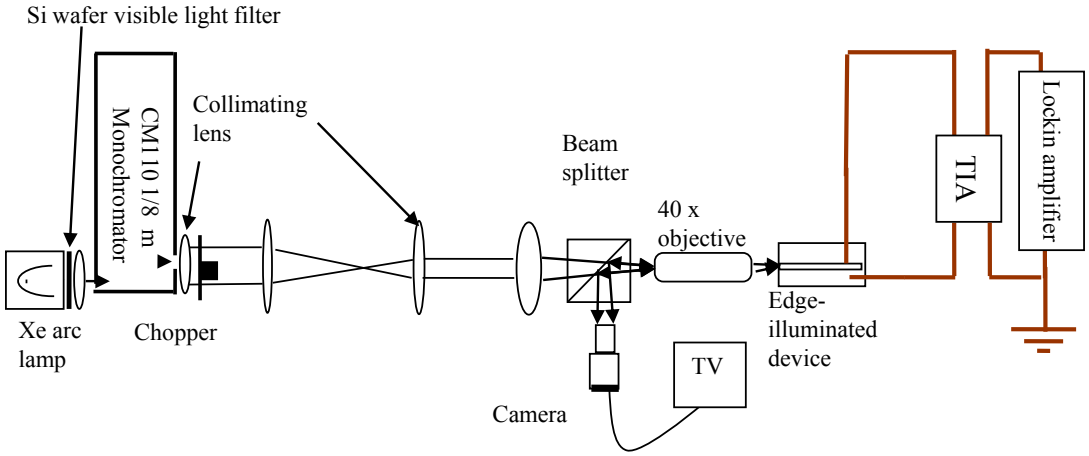


**Figure 5-29:** The experimental setup for the characterization of multimode waveguide devices.

he total spectral power incident is measured by placing a large-area Ge detector at this focal point. An SR570 low-noise transimpedance amplifier is used to bias the MMWG diodes as required as well as to convert the photocurrent into a

voltage signal that is then measured by a lock-in amplifier. This lock-in amplifier output is then divided by the TIA gain and the spectral power to convert it from photocurrent (in units of Amps) to responsivity ($AW^{-1}$).

Photocurrent spectra of samples LPS-0W, LPS-1W and LPS-4W are collected at 0 V bias between 1 μm and 1.5 μm. This is shown in Figure 5-30. It is immediately noted that the sample with no W-absorbers has a higher responsivity than both, LPS-1W and LPS-4W. Furthermore, we note that all devices have a measurable response at a wavelength of 1.5μm (0.82 eV). This corresponds to an energy level smaller than the smallest bandgap in the band diagram shown in Figure 5-10. This suggests that defect-mediated absorption contributes significantly to sub-bandgap absorption.

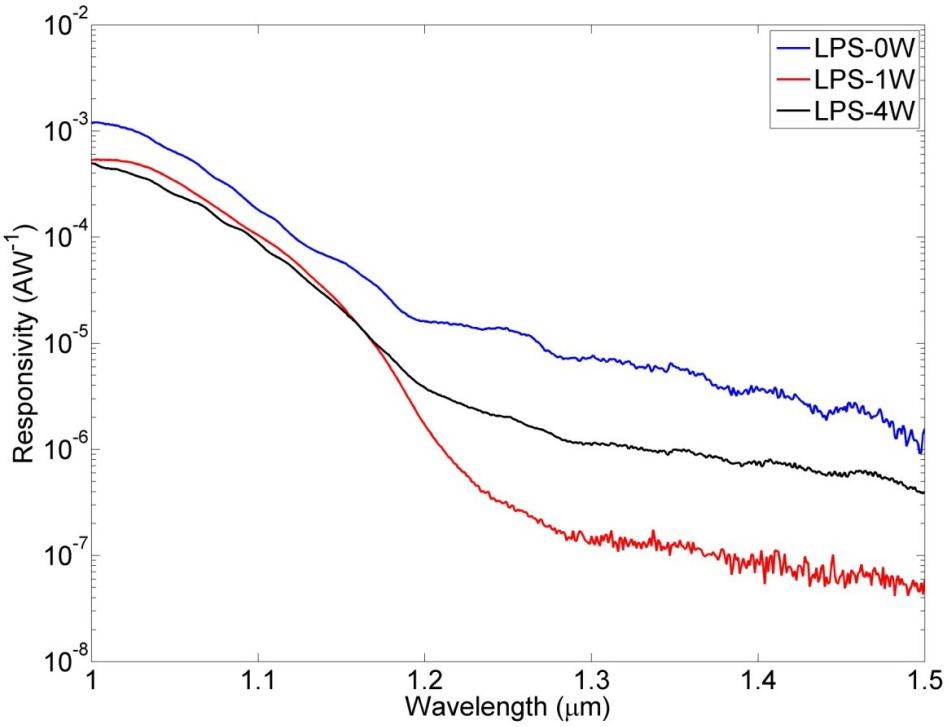


**Figure 5-30:** Collected photocurrent spectra of samples with differing number of W-absorbers.

To understand this result, we decompose the photocurrent data into components corresponding to bulk absorption (in the i-Si and SCH layers), W-absorption and defect-mediated absorption at photon energies smaller than the fundamental bandgap of the device. This is performed by fitting the imaginary component of the complex index of refraction k (= $\lambda\alpha(\lambda)/4\pi$) as a quadratic function of the photon energy E as [108]

$$k(E) = \sum_i A_i \left(E - E_{b_i}\right)^2 U\left(E - E_{b_i}\right) \tag{5.9}$$

where the summation is carried out over i participating bands. $A_i$ is a fitting parameter associated with the strength of the transition, $E_{bi}$ is the bandedge associated with the $i^{th}$ transition and U(x) is the unit step function. To verify accuracy of the technique and fitting procedure, the photocurrent spectrum of a commercially-available large area silicon detector was also collected. The strong responsivity of this detector allowed the use of 0.6 mm slits, yielding better a measurement resolution of 5 nm, or 3 meV. The extracted bandedges for this silicon device are included in Table 5-3, along with the absorption bandedges of silicon measured in a high-resolution (0.5 meV) experimental setup [109]. The data and fit are also shown in Figure 5-31. The correspondence between these measured values and the accepted values taken from the literature validates this fitting technique.

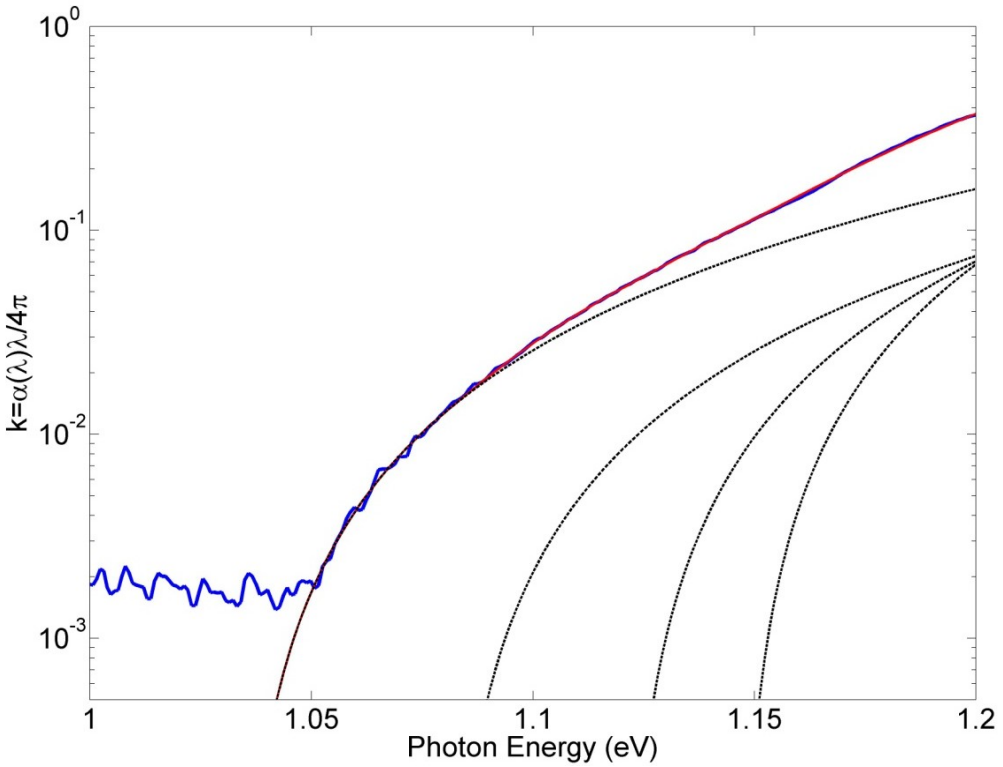


**Figure 5-31:** The data fit to the photocurrent a commercially-available silicon detector that was used to verify the fitting technique. The collected data is shown as 1the thick, blue line, and each of the four dashed black curves correspond to a bandgap specified in Table 5-3, which are added to yield the total response.

For the sample LPS-0W, the entire photocurrent spectrum could be described by 3 absorption bandedges. In contrast, the LPS-1W and LPS-4W samples required 4 absorption bandedges to accurately fit the measured spectra. The results of this decomposition are summarized in Table 5-3, and plots of both, measured and fitted k(E) are shown in Figure 5-32.

| Sample | Photocurrent Bandedges (eV) | | | |
|---|---|---|---|---|
| | $E_{b1}$ | $E_{b2}$ | $E_{b3}$ | $E_{b4}$ |
| Si | 1.034 (1.023) | 1.090 (1.096) | 1.126 (1.132) | 1.143 (1.155) |
| LPS-0W | 0.764 | 1.025 | 1.103 | |
| LPS-1W | 0.644 | 0.956 | 1.030 | 1.099 |
| LPS-4W | 0.649 | 0.946 | 1033 | 1.121 |

**Table 5-3:** The extracted bandedges from the photocurrent spectra of the LPS-0W, -1W and -4W samples, and a NewFocus 2031 large area silicon photodiode. For comparison, the corresponding bandedges for silicon are included in parentheses [108]

As summarized in Table 5-3, all three samples have defect bandgaps deep in the forbidden band. We note that LPS-1W and LPS-4W have nearly identical defect bandedges, while that of LPS-0W is approximately 110 meV higher. The reason for this discrepancy is not clear, and might have to do with the fact that the samples LPS-1W and LPS-4W were grown in sequence, while LPS-0W was grown 8 months later following several maintenance cycles of the MBE chamber which weren't followed by bakeout. While photocurrent spectroscopy can be used to identify the presence of defect states in materials, more involved techniques such as deep level transient spectroscopy (DLTS) and photoinduced current transient spectroscopy (PICTS) are required to fully investigate these defects and characterize them in terms of trap cross-sections and trap lifetimes. It is also noted that these defects are not associated with strain relaxation, as these films are found to be almost fully strained.

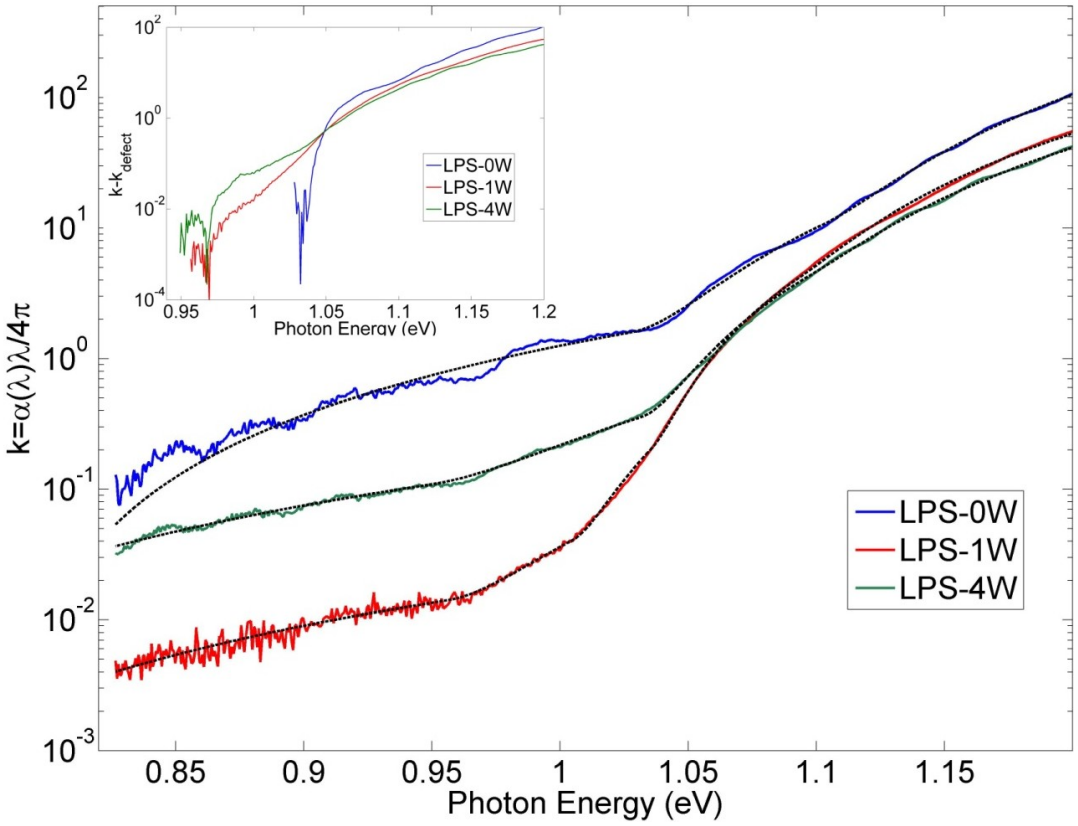


**Figure 5-32:** Data (solid colored curves) and fits (dashed black curves) of the photocurrent spectra for the three W-absorber samples. The insert shows the experimentally collected data with the contribution of the defect tail removed, highlighting the difference in bandedges of the structures.

We note that all the LPS-grown samples have bandedges at approximately 1.03 eV and 1.1 eV. These are ascribed to bulk absorption in the i-Si and i-$Si_{0.9}Ge_{0.1}$ SCH layers. However, only the samples with the W-absorber have bandedges corresponding to the designed bandgap of 0.93 eV. This shows that despite the large contribution to optical absorption from midgap defects, the contribution of W-absorbers can be extracted. This contribution is made clearer in the insert of Figure 5-32 where $k-k_{defect}$ is plotted. With the contribution of the defect band removed from

the experimental data, the difference in bandedges of the structure with the W-absorbers and that of the control structure is more clearly seen. The relative strengths of the defect-mediated absorption and absorption in the W-absorber near the band-edge is given by $k_w / k_d = A_w (E - E_w)^2 / A_d (E - E_d)^2$ where the subscripts w and d correspond to the W-absorber and defect state respectively. Using the fit to the data, a ratio of 0.18 at 0.98 eV is obtained for both, the LPS-1W and LPS-4W samples. This implies that defect-mediated absorption is 5.5 times larger than absorption in the W-absorbers near the bandedge.

## ***5. 4 Conclusions***

In this chapter, two approaches to near-infrared photodection on silicon are tested. The preliminary approach employing the reduced bandgap of a single $Si_{0.6}Ge_{0.4}$ quantum well demonstrated to be limited by threading dislocations in the active region arising due to the relaxation strain. This strain relaxation results in devices with very high reverse leakage currents and make for impractical photodetectors.

A second approach utilizing both the reduced bandgaps of SiGe layers and the type-II band offsets of the SiGe material system to create a W-absorber region was proposed and designed. These designs were grown using MBE. The reduction in strain proved to be crucial in reducing the reverse leakage current densities from 25 $mAmm^{-2}$ to as low as 9 $\mu Amm^{-2}$. Photocurrent spectroscopy was used to characterize processed multimode waveguide devices. Devices with W-absorbers were measured

to have a bandedge at 0.95 eV, close to the designed bandedge of 0.93 eV. Furthermore, this transition was found to be absent in a control structure, proving that the W-absorber is the source of this bandedge. In addition, all devices were found to have deep defect levels corresponding to a bandedge of approximately 0.7 eV that give rise to absorption below the bandedge of the W-absorber. This defect band is responsible for a major proportion of the photocurrent near the bandedge of the W-absorber (82% at 0.98 eV), and is also found in the control structure. These defects are not associated with strain relaxation in the active region and their exact origin is currently unknown. The presence of this defect band necessitates a different approach to SiGe photodetector design that is presented in the following chapter.

# Chapter 6 : Strain-balanced Silicon-Germanium Photodetectors

## *6. 1 Introduction*

Chapter 5 detailed efforts on realizing efficient, strained silicon germanium photodetectors on silicon substrates. It was shown that while heterostructures could be designed with transition bandedges in the near infrared, optical absorption from defect states deep in the forbidden gap dominate the total absorption. To reduce the relative contribution of the defect states, it is necessary to increase the optical absorption in the designed heterostructure. This can be accomplished by increasing the thickness of the absorber region, and by increasing the Ge fraction in these absorbers. This approach, however, is limited by the strain in the films arising from the lattice mismatch of SiGe on Si. It is thus imperative to find a way of reducing the film strain while simultaneously increasing the germanium mole fraction in the active layer. Both these goals are achieved through the design and growth of strain-balanced superlattices on virtual substrates. Strain-free heterostructures also allow for the implementation of large, normal incidence photodiodes which are easier to couple into than smaller, single mode waveguides. In this chapter, this design paradigm will be explored to achieve larger reduction in the detector bandedge than realized in Chapter 5

## *6.2 Stain-balanced structures and virtual substrates*

As mentioned in Chapter 4, the lattice constant of $Si_{1-x}Ge_x$ for all germanium

fractions x is larger than that of silicon, yielding films that are exclusively compressively strained when grown on silicon substrates. This strain can be reduced in two ways. The simplest approach is to reduce x. This however, is incompatible with the requirement to extend the bandgap into the near infrared. The second approach is to reduce this compressive strain by growing a tensile strained layer on top. On silicon substrates, this can be achieved either by inclusion of small amounts of carbon (~5%), or by heavily doping the film with boron, both of which are known to cause the silicon lattice to contract. [41, 110] While it is possible to grow $Si_{1-x-y}Ge_xC_y$ layers that are lattice matched to silicon, the electronic band properties of this material system are quite different from that of silicon,-silicon germanium material system and are not fully modeled. The use of thick silicon layers that are heavily doped to reduce strain is incompatible with p-i-n photodetector. This is because a low dopant density is required in the active region to reduce free carrier absorption. An alternative approach to strain-balanced involves epitaxial growth on so-called virtual substrates, or relaxed buffer layers (RBL), which have a thick, fully relaxed $Si_{1-x}Ge_x$ layer upon which alternating layers of tensile-strained silicon and compressively strained SiGe can be grown.

One method of producing these substrates is by growing thick, gently-graded SiGe buffer layers on a silicon substrate. This buffer layer undergoes relaxation and there is a significant concentration of misfit and threading dislocations. Further epitaxy of a constant-composition results in the formation of a smooth, relatively defect-free overlayer that is suitable for device fabrication. This layer also has a larger lattice constant than that of the underlying silicon substrate and is given by Equation

2.1. A cross-section image of a typical SiGe virtual substrate is shown in Figure 6-1. For a structure with different layers of composition $x_i$ and of thickness $t_i$ grown on a substrate of composition $x_s$, the strain balanced condition is given by

$$\sum_{n-layers} t_i (x_i - x_s) = 0 \tag{6.1}$$

It is important to note, however that each individual layer thickness be less than the critical thickness for the grown film on the substrate used. The strain-balance structures presented in this chapter are grown commercially available $Si_{0.83}Ge_{0.17}$ RBLs

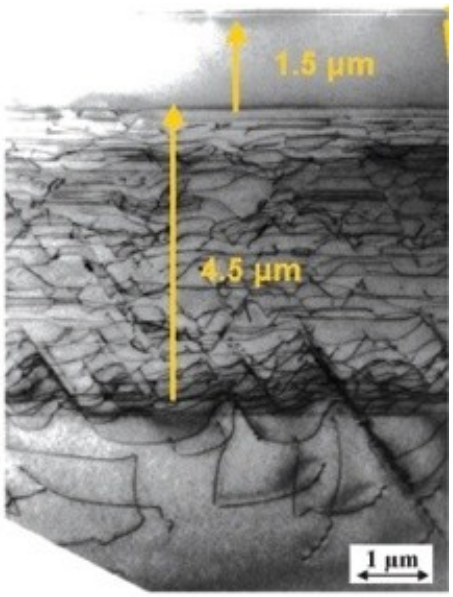


**Figure 6-1:** Cross-section image of a SiGe virtual substrate [111]

## ***6.3 Design approach***

As with the W-absorber regions demonstrated in Chapter 5, both, the reduced bandgaps of SiGe and the type-II band offsets of the material system are exploited to create structures with bandgap lower than that of the constituent alloys. Unlike the

case of strained heterostructures, there is no limit on the total layer thickness. This allows the multiple absorber regions to be included, either in a multiple quantum well (MQW) or superlattice (SL) structure. As shown in Chapter 4, the type-II band offsets result in a significant decrease in the overlap of the electron and hole wavefunctions in QW-type devices due to the strong localization of the electrons and holes in spatially separate regions. This problem mitigated in superlattices due to the fact that the wavefunctions aren't as strongly localized, and this is the design approach chosen.

The design of the strain-balanced superlattice (SBSL) is approached as follows. First, for a given Ge fraction x in $Si_{1-x}Ge_x$, the conduction and valence band potentials are determined as detailed in Chapter 4. Using this model, the potentials of the light hole, heavy hole, $\Delta_2$ and $\Delta_4$ are calculated. Unlike the devices detailed in Chapter 5, where only the HH and $\Delta_4$ bands were considered, these additional bands need to be considered in the SBSL which has layers of alternating tensile and compressive strain. This is due to the fact that in tensile strained silicon, the LH and $\Delta_2$ bands are the most energetically favorable levels in the valence and conduction bands respectively, while in compressively strained SiGe, the HH and $\Delta_4$ are preferred. This is shown in Figure 6-2 for a $Si/Si_{0.4}Ge_{0.6}$ SBSL on $Si_{0.83}Ge_{0.17}$, showing the degenerate bands in the unstrained substrate, and the splitting in the strained layers as described above. Next, for varying silicon thickness $t_{Si}$ between 4 and 20 nm, the thicknesses $t_{SiGe}$ of the $Si_{1-x}Ge_x$ are with the strain-balance constraint for the $Si_{0.83}Ge_{0.17}$ RBLs:

$$0.17 t_{Si} = (x - 0.17) t_{SiGe} \quad \textbf{(6.2)}$$

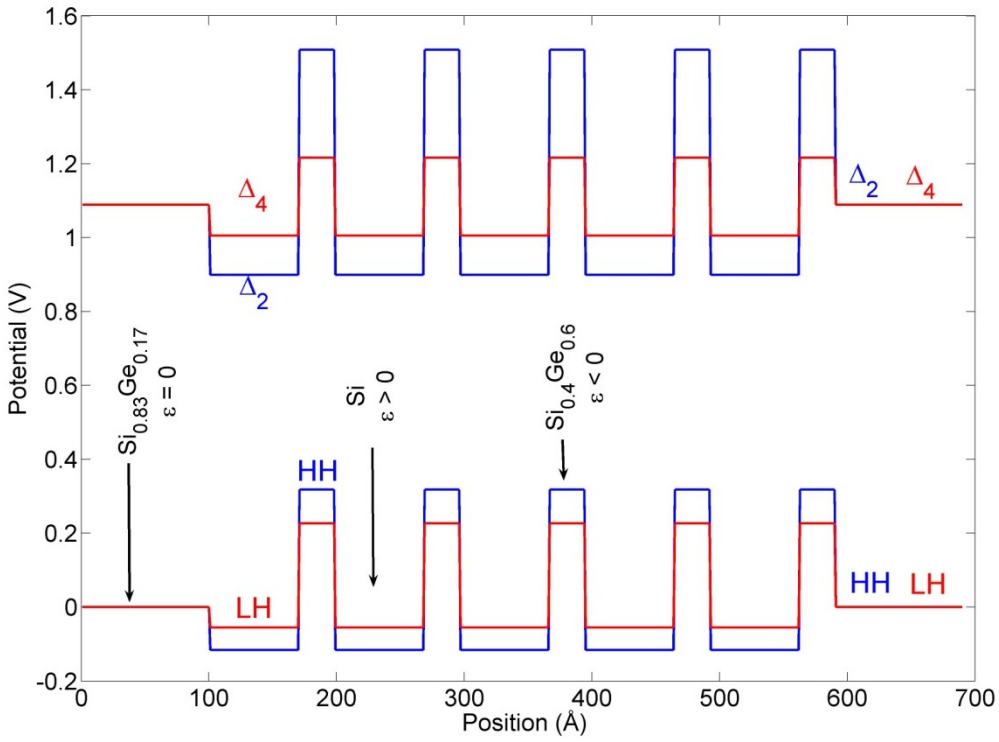


**Figure 6-2:** The band diagram for a 5-period $Si/Si_{0.4}Ge_{0.6}$ SBSL on $Si_{0.83}Ge_{0.17}$, showing the effect of tensile and compressive strain on the degeneracy in the conduction and valence bands

With the band potentials and the layer thicknesses determined, the energy levels of the carriers in each of these four bands are calculated. This is done by approximating the N-period Si/SiGe superlattice (N>30) as an infinitely-periodic superlattice and solving Schrödinger's equation for the carriers in such this structure analytically as detailed in Section 4.6.2. The absorption bandedge is calculated for transitions involving each of the participating bands i.e HH-$\Delta_2$, HH-$\Delta_4$, LH-$\Delta_2$ and LH-$\Delta_2$. In all cases, the fundamental transition is found to be the HH-$\Delta_2$ transition. The variation of this fundamental gap with germanium fraction x and the silicon layer thickness $t_{Si}$ is shown in Figure 6-3. This model for the bandgap of an SBSL does not

take into account the effects of applied bias and the built-in potential from applied bias on the energy levels. Furthermore, the effect of band mixing in the valence band is not included. As a result, this model serves as a guide to the choice of SBSL for investigation rather than accurately model the device characteristics.

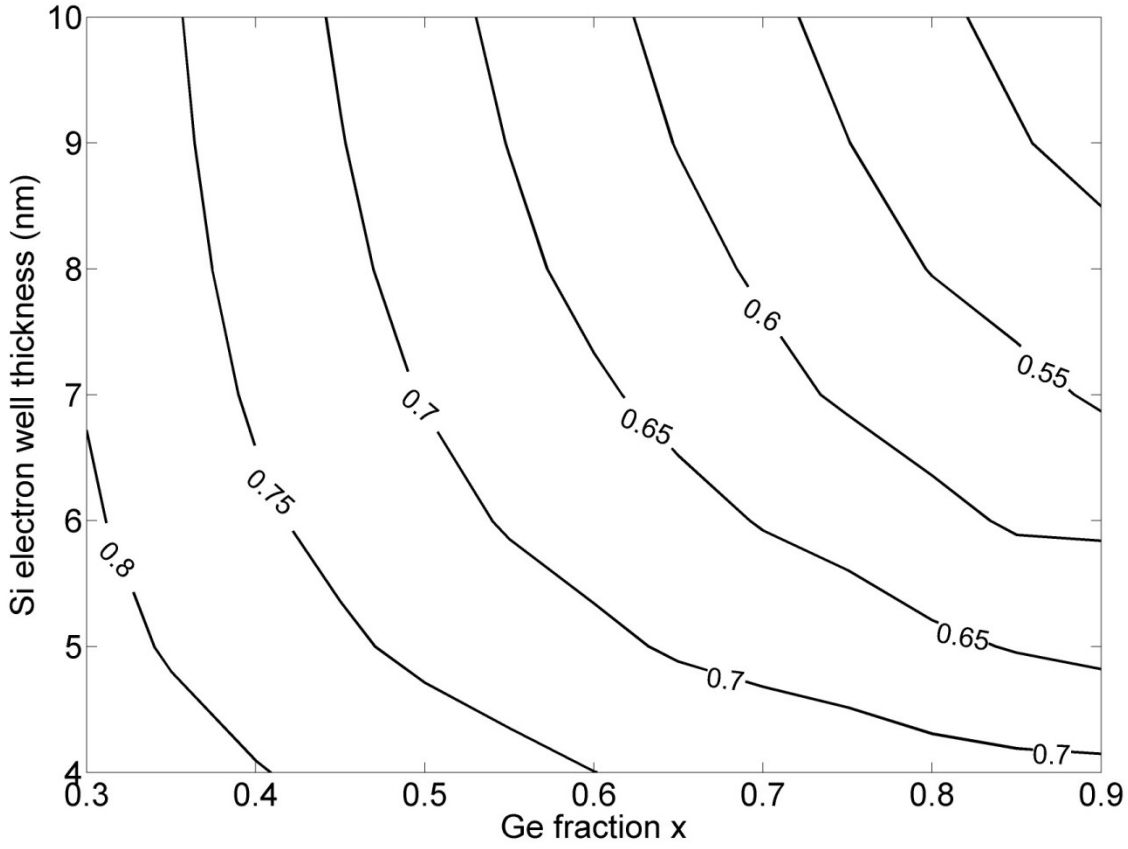


**Figure 6-3:** A contour plot of the fundamental bandgap of a SBSL as a function of Ge fraction x in the hole well and the silicon electron well thickness.

Based on these calculations, three different SBSLs with approximately equal superlattice thicknesses are chosen to explore the design space: 200 Å Si/ 89 Å $Si_{0.45}Ge_{0.55}$, 50-period 70 Å Si/28 Å $Si_{0.4}Ge_{0.6}$ and 50-period 85 Å Si/25 Å $Si_{0.25}Ge_{0.75}$. The bandgaps of these structures are summarized in Table 6-1.

| SBSL | Transition Energy (meV) | | | |
|---|---|---|---|---|
| | HH-$\Delta_2$ | HH-$\Delta_4$ | LH-$\Delta_2$ | LH-$\Delta_4$ |
| 200 Å Si/ 89 Å $Si_{0.45}Ge_{0.55}$ | 645 | 751 | 739 | 831 |
| 70 Å Si/28 Å $Si_{0.4}Ge_{0.6}$ | 706 | 813 | 804 | 902 |
| 85 Å Si/25 Å $Si_{0.25}Ge_{0.75}$ | 607 | 715 | 737 | 828 |

**Table 6-1:** Summary of the modeled bandgaps of the SBSLs chosen for investigation.

## ***6. 4 Growth and fabrication details***

### 6.4.1 Substrate details

The SBSLs designed in the previous section are grown using MBE on 1.75" x 1.75" dies cut from an 8" $Si_{0.83}Ge_{0.17}$ RBL available from IQE [112]. This RBL is capped with a 175 Å thick strained-silicon layer. The full layer structure and the specifics of the process used to grow this substrate are proprietary and no specified. However, XRD and cross-section SEM can be used to sufficiently understand the substrate to allow for post-growth analysis of the superlattice. A cross-section SEM image is shown in Figure 6-4. The different layers are discernible but not uniquely identifiable. The dislocations that are clearly visible in the TEM image Figure 6-1 are not seen here simply because SEM is not as sensitive to these dislocations

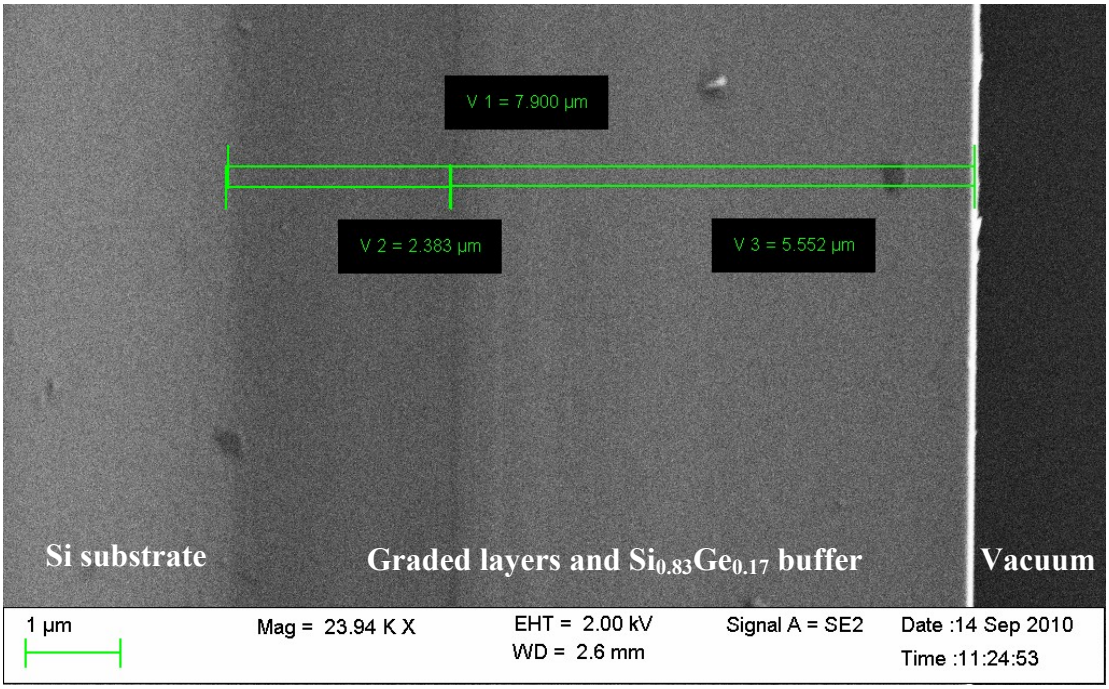


**Figure 6-4:** A cross-section SEM image of the RBL on which the SBSLs are grown, showing the different layers. The caption vacuum refers to the SEM chamber.

Figure 6-5 shows the ω-2θ scan of the bare RBL, and a fit to this data. It is best fit by a fully relaxed 2.2-µm-thick $Si_{1-x}Ge_x$ layer linearly graded in germanium composition from x=0 at the substrate to x=0.17 at the top. On top of this graded layer, a $Si_{0.83}Ge_{0.17}$ layer is grown of arbitrary thickness (the simulation shows a 2.5 µm thick layer), followed by the strained-silicon layer. The contributions of the individual layers are highlighted in the plot.

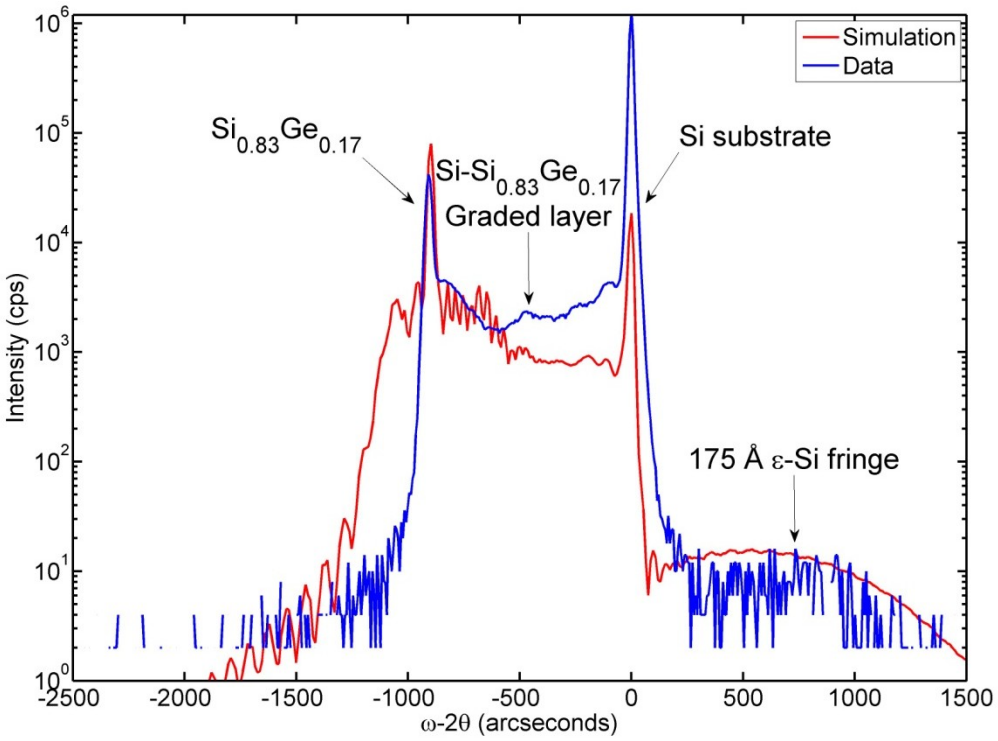


**Figure 6-5:** ω-2θ scans of the $Si_{0.83}Ge_{0.17}$ RBL showing the contributions of the various layers detailed in the text.

### 6.4.2 Material growth

The structures described in Table 6-1 were grown in DepD. The full p-i-n diode structure consists of the superlattice sandwiched by 0.1-μm-thick i- $Si_{0.83}Ge_{0.17}$ regions with a 0.6μm thick bottom p-contact and a 0.4-μm-thick top n-contact. Two attempts were made at growing the 85 Å Si/25 Å $Si_{0.25}Ge_{0.75}$ superlattice, yielding two different device structures. Post-growth XRD analysis was performed on all samples, the results of which are summarized in Table 6-2. The (004) and (113) reciprocal space maps were analyzed and the residual strain in all samples was not found to have resulted in relaxation in the film. This data is also included. The SBSLs are

henceforth described by their germanium fraction per the labels specified in Table 6-2. To simulate these samples, the contributions of the silicon substrate on which the RBL is grown and the linearly graded layer are not included as they obscure peaks close to the RBL peak. Instead, the substrates for these SBSLs are set as $Si_{0.83}Ge_{0.17}$ during simulation with the knowledge that the plateau seen in Figure 6-5 between approximately 0 and -1000 arcseconds and the silicon substrate peak will not be present. The ω-2θ XRD traces for these 4 samples are shown in Figure 6-6, Figure 6-7, Figure 6-8 and Figure 6-9. As expected, sample Ge54 which has the longer period superlattice has much shorter fringe spacing, than the other samples. In addition, for samples Ge54, Ge72 and Ge77, small peaks adjacent to the strong superlattice fringes are observed. These minor fringes show the same periodicity as the strong fringes within measurement error and are attributed to a <5%drift in the silicon flux, which is a known issue with the system.

| SBSL | Target superlattice | Grown superlattice | Residual strain |
|---|---|---|---|
| Ge54 | 30x 200 Å Si/ 89 Å $Si_{0.45}Ge_{0.55}$ | 184 Å Si/ 84 Å $Si_{0.46}Ge_{0.54}$ | 0.063% |
| Ge61 | 50x 70 Å Si/28 Å $Si_{0.4}Ge_{0.6}$ | 66 Å Si/28 Å $Si_{0.39}Ge_{0.61}$ | 0.064% |
| Ge72 | 50x 85 Å Si/25 Å $Si_{0.25}Ge_{0.75}$ | 91 Å Si/24 Å $Si_{0.28}Ge_{0.72}$ | -0.09% |
| Ge77 | 50x 85 Å Si/25 Å $Si_{0.25}Ge_{0.75}$ | 74 Å Si/25 Å $Si_{0.23}Ge_{0.77}$ | 0.14% |

**Table 6-2:** A summary of layer thicknesses and strain in the SBSLs grown.

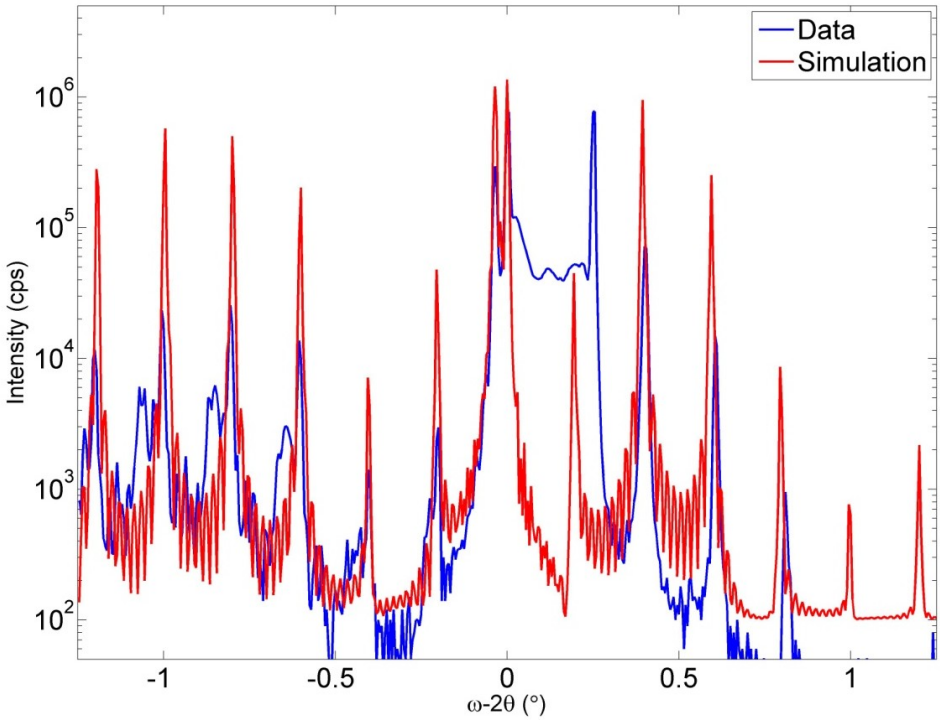


**Figure 6-6:** ω-2θ scans of and fit to sample Ge54

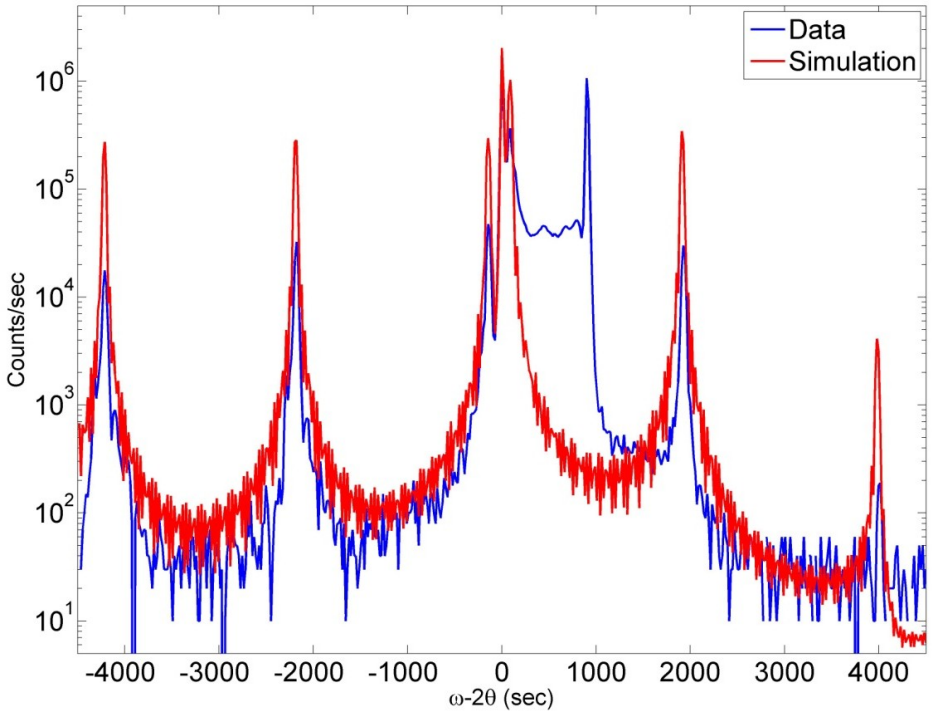


**Figure 6-7:** ω-2θ scans of and fit to sample Ge61

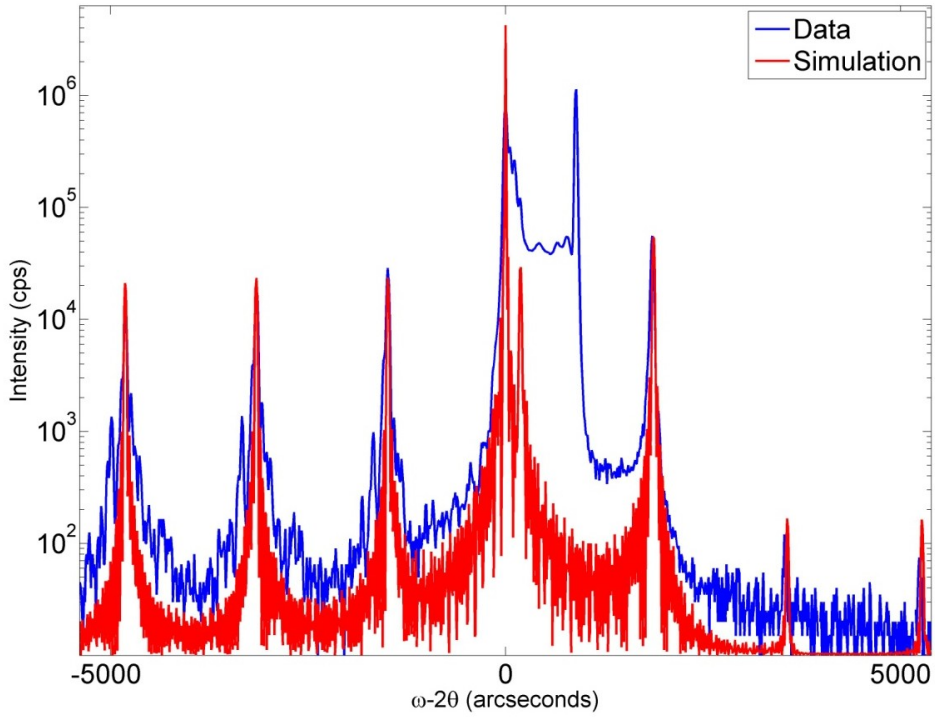


**Figure 6-8:** ω-2θ scans of and fit to sample Ge72

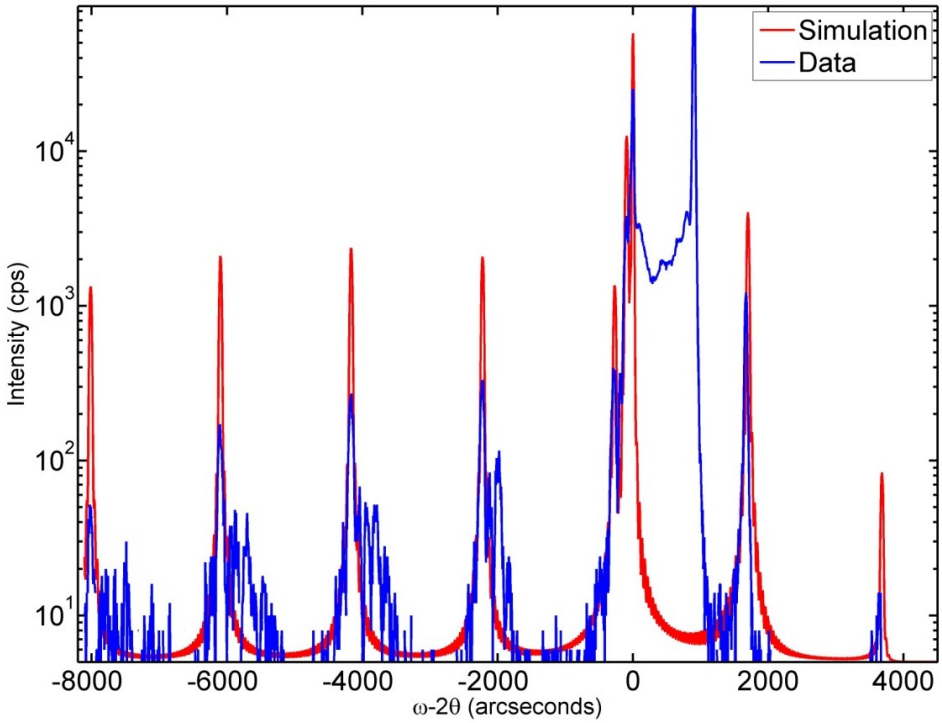


**Figure 6-9:** ω-2θ scans of and fit to sample Ge77

The calculations for the bandedge calculations detailed in section 6.3 were repeated for the actual structures grown. This was done to determine if the difference between the target and actual superlattices would cause a large change in the expected bandedge. This was found not to be the case, with the lowest bandgap (HH-$\Delta_2$) increasing by approximately 10 meV for all structures.

### 6.4.3 Fabrication details

As mentioned earlier, the thick SBSL absorber region allows for the implementation of normal incidence photodetectors. The fabrication steps for these devices are different from that of the waveguide devices in Chapter 5. Most significantly, the wet etch process used to define the waveguides cannot be used to define the mesas. This is because both, KOH and $NH_4OH$ do not etch high germanium containing SiGe layers. [99, 112] While hot KOH is found to etch 0.5-μm-thick $Si_{0.83}Ge_{0.17}$ contact layers, but not the superlattice. Indeed, KOH was also found to etch through the $Si_{0.6}Ge_{0.4}$ layers in the W-absorbers in Chapter 5, but those layers were only 2 nm thick. The reason for the different reactivities of Si and Ge in hot bases is explained by a study of the etching chemistry. Silicon easily reacts with KOH forming a water soluble silicon salt according to

$$Si + 2KOH + H_2O \rightarrow K_2SiO_3 + H_2 \uparrow$$

In contrast, germanium is hydrolyzed in the basic medium forming a pasty oxide that is adsorbed on the wafer surface and acts as an etch stop

$$Ge^{4+} + 4OH^- \rightarrow GeO_2.2H_2O \downarrow$$

Alternatively, the use of a fluorine-based dry etch process allows the simultaneous etching of Si and Ge according to

$$Si + 4F \rightarrow SiF_4 \uparrow$$

$$Ge + 4F \rightarrow GeF_4 \uparrow$$

It was found that for the 8" wafer capable PlasmaTherm Reactive Ion Etcher 790 which was used for all the dry etching steps in this thesis, an etch rate of approximately 0.35 μm/min could be achieved with an $SF_6$ flow rate of 20 sccm, a chamber pressure of 15 mTorr and an RF power of 170 W. The exact etch rate depended on the composition of the layer being etched and was not studied in detail. Figure 6-10 shows an SEM image of the typical sidewall quality obtained using this etch recipe. Due to the near-verticality of the sidewall, could not be characterized using AFM unlike the wet-etched sidewalls of the waveguide devices. Some roughness and texture are clearly visible on these sidewalls. Since these are not waveguide devices, this roughness is not expected to contribute significantly to the loss. This roughness, however, could contribute to surface leakage currents.

Using this etch process and standard clean room processing techniques, devices from these four samples were processed into mesa p-i-n diodes of diameter 0.1, 0.25, 0.5 and 1.0 mm. Standard ultraviolet lithography was used to pattern photoresist, followed by $SF_6$ dry etching to transfer the pattern to mesas. The sidewalls are passivated with a conformal $Si_3N_4$ layer deposited using plasma-enhanced chemical vapor deposition as before, and Ti/Pt/Au was deposited for ohmic contacts. A cross-section schematic and photomicrograph of finished device are shown in Figure 6-11and Figure 6-12.

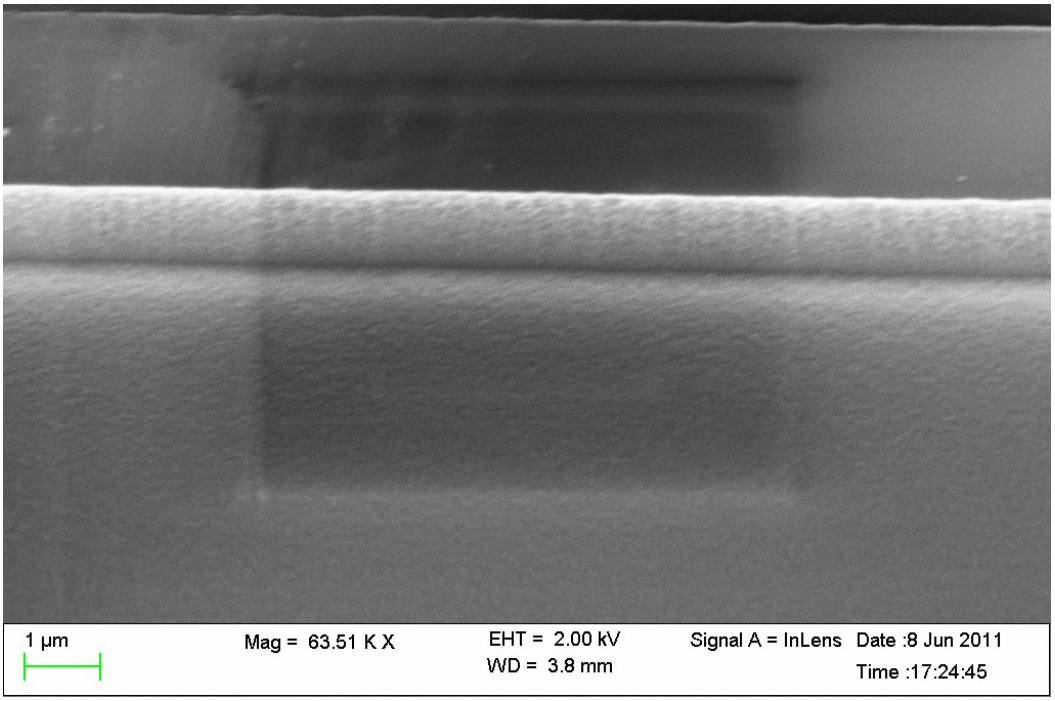


**Figure 6-10:** An SEM micrograph of a the sidewall of a ridge defined by $SF_6$-based dry etch process used.

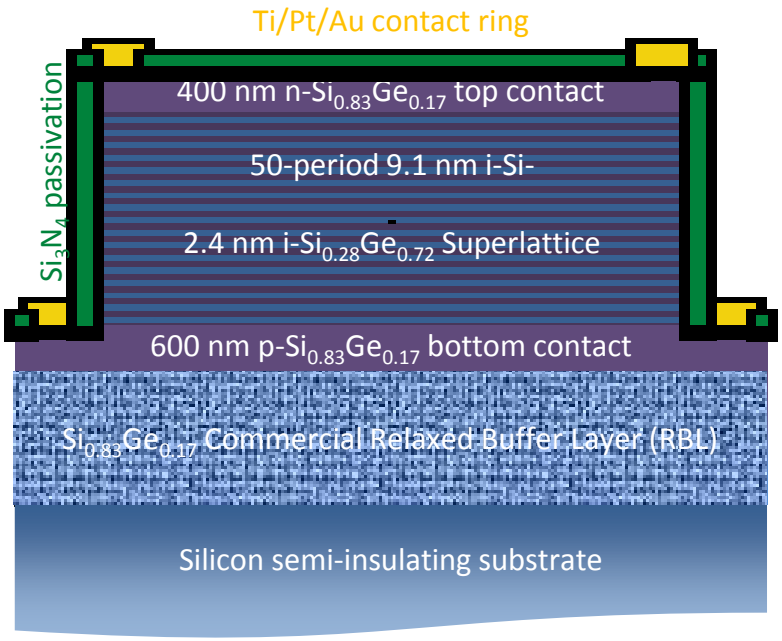


**Figure 6-11:** A cross-section schematic of a typical SiGe SBSL device (Ge72 shown), showing the $Si_3N_4$ passivation and Ti/Pt/Au metal contact layer as well as the MBE-grown superlattice and contact layers.

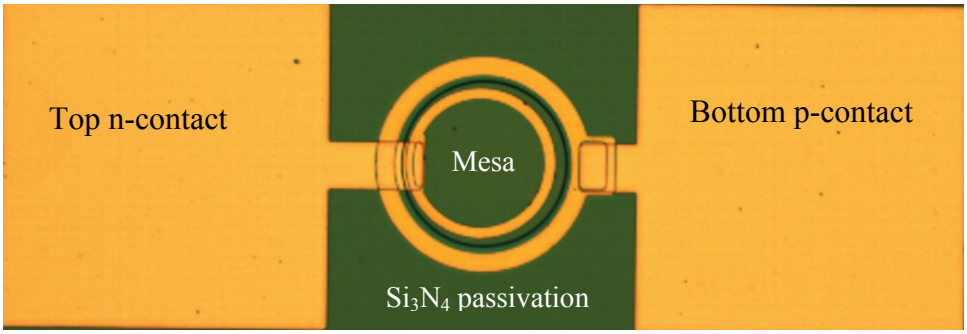


**Figure 6-12:** A plan-view photomicrograph of a finished 100 μm diameter mesa photodiode.

## *6.5 Device characterization*

### 6.5.1 Electrical characterization

V-I characteristics of finished diodes were measured using the HP4156B semiconductor parameter analyzer. The typical V-I characteristics for each of the devices is shown in Figure 6-13. The diodes were found to be well-behaved with typical turn on voltages of 0.5±0.05 V and low forward resistances of 20±5 Ω (except for Ge72, which has a higher resistance of 300 Ω due to a problem with the n-contact layer) for the 1mm diameter mesas. As expected, smaller devices were found to have identical turn on voltages, but higher forward resistances.

A study of the dark current at a reverse bias of 1V for devices with different areas revealed that surface leakage is statistically absent, and that the bulk leakage current scaled only with area. This is shown in Figure 6-14. This bulk leakage current density was found to be different for different SBSLs and uncorrelated with the Ge fraction in the SBSL and is found to be 0.28 $\mu Amm^{-2}$ (LPS54), 3.42±0.07 $\mu Amm^{-2}$ (LPS61), 0.27±0.03 $\mu Amm^{-2}$ (LPS72) and 0.82 $\mu Amm^{-2}$ (LPS77).

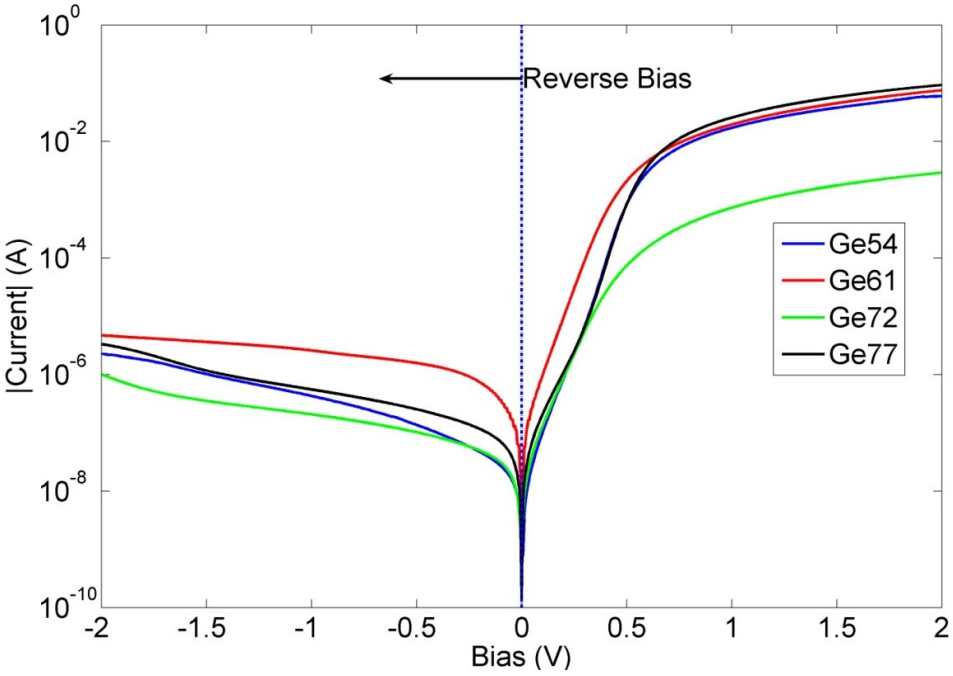


**Figure 6-13:** Typical V-I characteristics for 1 mm diameter mesa diodes fabricated from each of the four epitaxial samples described in the text.

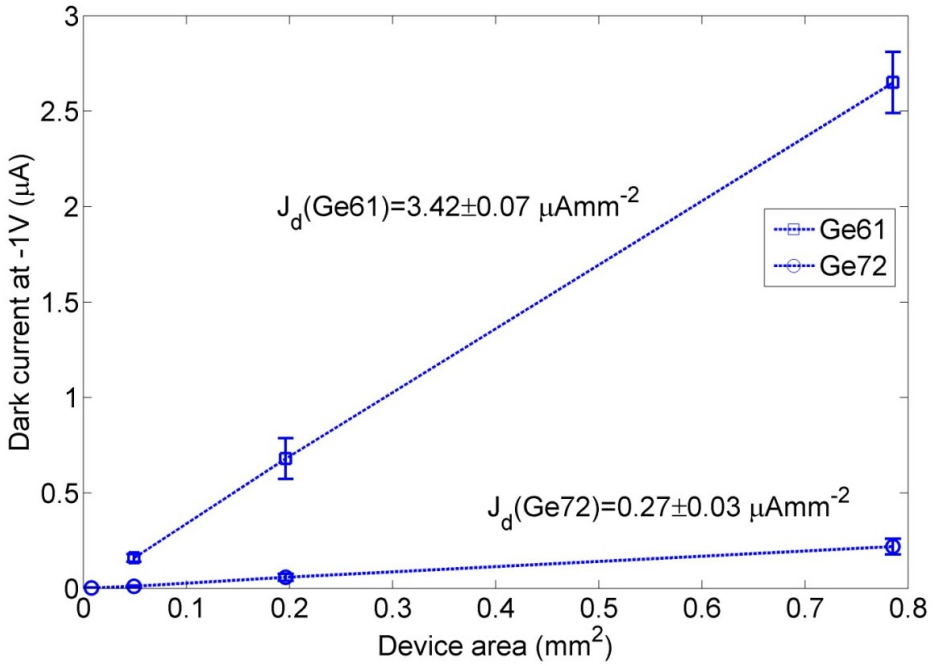


**Figure 6-14:** The scaling of dark current with device area for two SBSLs showing only bulk leakage with no surface leakage.

The lack of a clear trend is ascribed to differing magnitudes of hole trapping at the superlattice-bottom p-contact interface. [106, 114] Secondary ion mass spectroscopy (SIMS) analysis measured the oxygen and carbon concentrations in the intrinsic region are measured as $10^{18}$-$10^{19}$cm$^{-3}$ (oxygen) and $10^{17}$cm$^{-3}$ (carbon). Both elements are known to be deep traps in SiGe and are expected to reduce the photoresponse by enhancing trap-assisted recombination at low biases, as well as contributing differently to bulk leakage.

### 6.5.2 Photocurrent spectroscopy

The effect of composition on the bandedge of detection was studied by photocurrent spectroscopy in the 1.0 μm-1.6 μm wavelength range. A Xe arc lamp for illumination, a ½m monochromator equipped with 3 mm entry and exit slits and a 600 groove/mm ruled grating were used along with focusing optics. An optical chopper is used to implement lock-in detection at 190 Hz with a measurement bandwidth of 1 Hz. As in the characterization of the W-absorber photodetectors in Chapter 5, a double-side polished 675-μm-thick Si wafer was used to suppress higher diffraction orders. The expected resolution of this setup is 10 nm (7 meV at 1.3 μm). The photodector output is collected by a low-noise transimpedance amplifier that is capable of applying bias voltages of ±5V. This data was decomposed into bulk absorption and superlattice absorption components with bandedges $E_{bi}$, i=1, 2, 3, as in Equation 5.9, $k(E) = \sum A_i (E - E_{bi})^2 U(E - E_{bi})$.

Figure 6-15 shows a comparison of the experimentally determined k and fits

employing this model for samples Ge54, Ge61 and Ge77 (Ge=72 is not shown for clarity). The bandedges extracted for all four samples are given in Table 6-3.

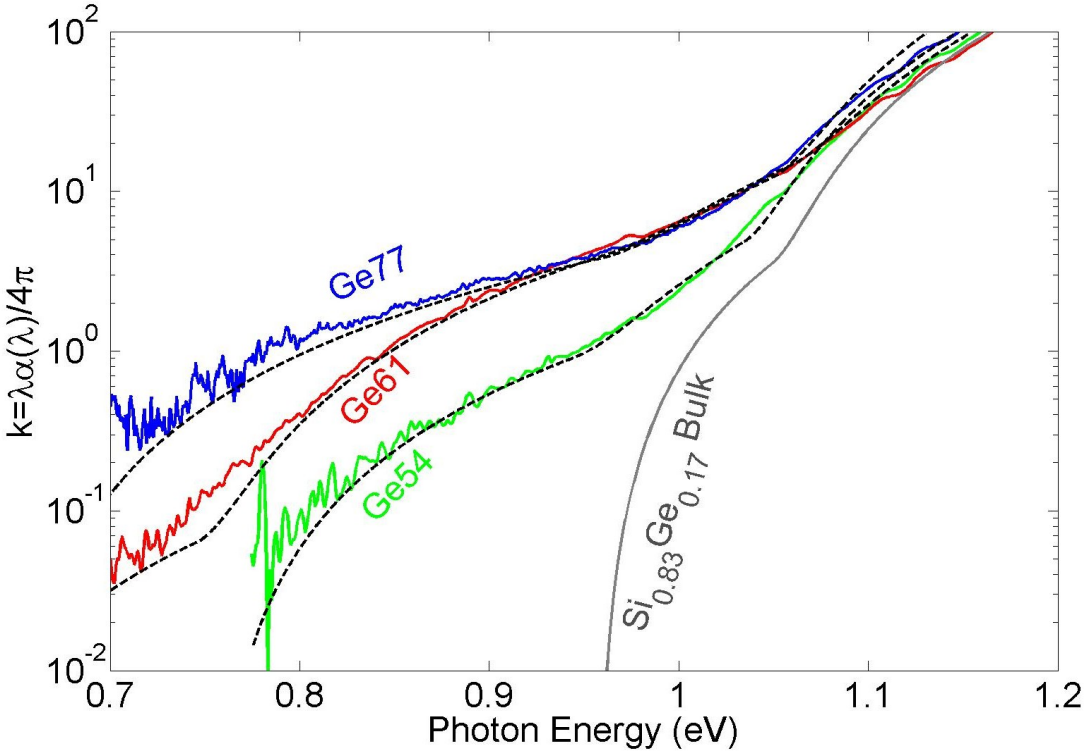


**Figure 6-15:** The experimentally measured photocurrent spectrum and fits to the data for 3 SBSLs (Ge54, Ge61 and Ge77). The extracted value of the bulk absorption is also included, showing the decrease in bandgap of photodetection due to the SBSL.

| Sample | Photocurrent Bandedges (eV) | | |
|---|---|---|---|
| | $E_{b1}$ | $E_{b2}$ | $E_{b3}$ |
| Ge54 | 0.766 | 0.969 | 1.05 |
| Ge61 | 0.735 | 0.970 | 1.04 |
| Ge72 | 0.704 | 0.980 | 1.06 |
| Ge77 | 0.673 | 0.990 | 1.06 |

**Table 6-3:** The bandedges measured by photocurrent spectroscopy of the SBSLs described in the text.

Figure 6-16 compares the experimentally measured bandgaps with the calculated bandgap of a strained $Si_{1-x}Ge_x$ film grown on a $Si_{0.83}Ge_{0.17}$ substrate. We note the significant decrease in the bandedge of photodetection of the SBSL over the strained bandgap of a film with the same Ge composition. In particular, we note that the film with Ge77 has a bandedge slightly *lower* than that of strained Ge on the same RBL. This clearly demonstrates the use of the Type-II band offsets to create a structure with a bandgap lower than any of the bandgaps of the constituent films.

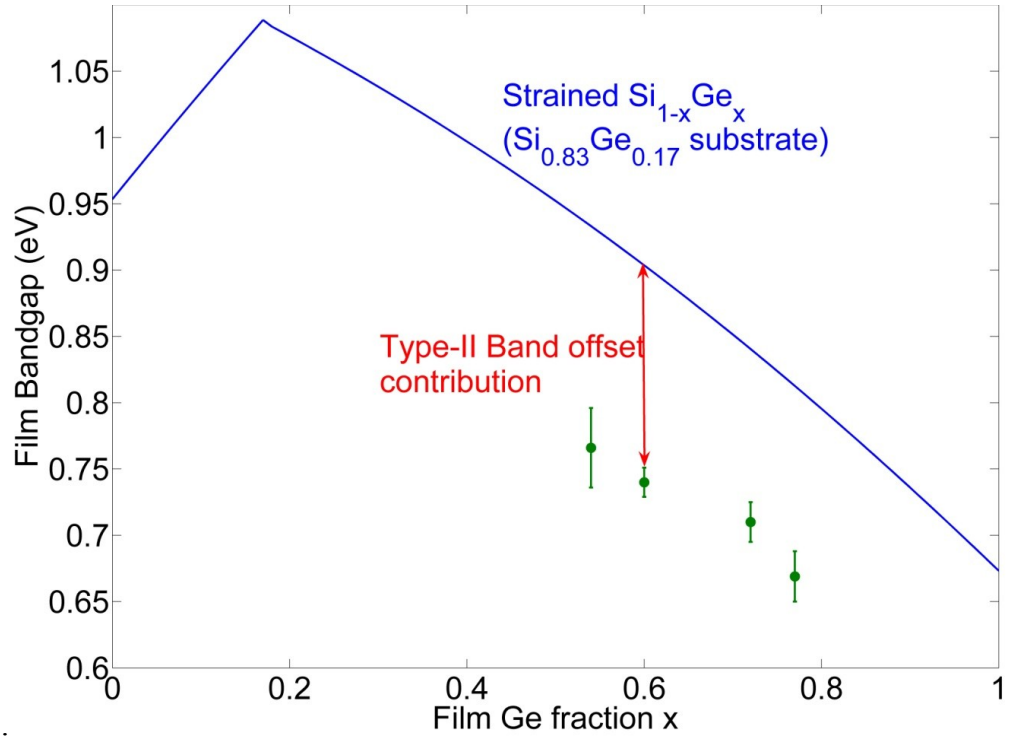


**Figure 6-16:** The measured absorption bandgedges of the four SBSLs described in the text. Reductions over the calculated bandgaps of strained SiGe films on $Si_{0.83}Ge_{0.17}$ relaxed buffer layers (solid line) are observed, demonstrating the significant contribution of the type-II band offsets in reducing the superlattice bandgap.

No bias dependence of this detection bandedge is observed. The bulk contribution to absorption across all samples is fit to a bandgap of 1.02±0.01 eV, which is close to the experimentally determined bandgap of 1.044 eV. [115] This bulk absorption is further decomposed into phonon absorption and emission branches corresponding to a phonon of 40±2 meV, close to the optical phonon energy of SiGe, which is measured as 50 meV. [116]

It should be noted that the measured bandedges plotted in Figure 6-16 are larger than the predicted values in Table 6-1 by 70-100 meV. The origin of this discrepancy is not fully understood. As mentioned in section 6.3, the model for the superlattice is incomplete in that it does not include valence band mixing and the effect of electric fields on the energy levels. It should also be noted that there has been no experimental measurement of the bandgaps of highly strained SiGe films on comparable substrates as a result of which it is possible that the band parameters used haven't been verified. This could also account for this difference.

### 6.5.3 Responsivity measurements

The responsivity of the different films at 1.32 μm was measured by illuminating the mesas with single mode fiber-coupled solid state laser with an output power of 115 mW and measuring the VI characteristics. As with the V-I characteristics in section 6.5.1, we find that at low biases ($\lesssim$2 V), hole trapping affects some of the devices. This is shown in Figure 6-17. At a reverse bias of -4 V, the responsivites of the devices are 155 μA/W (Ge54), 252 μA/W (Ge61), 176 μA/W

(Ge72) and 172 μA/W (Ge77) with an uncertainty of 7% for each. No corrections have been made for the reflection losses from the air-$Si_3N_4$-SiGe interface, which is calculated to be 15%.

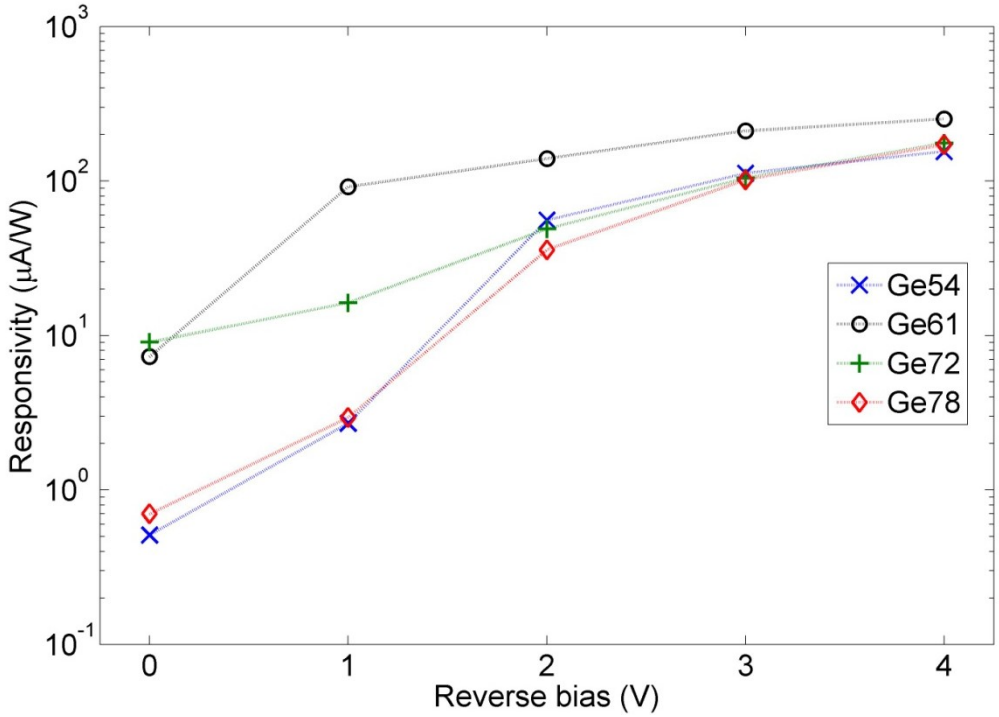


**Figure 6-17:** Responsivity as a function of bias for the four different SBSLs studied

As mentioned in section 6.5.1, hole trapping is known to be a problem in SiGe heterostructures, giving rise to strong variation in the responsivity with small changes in applied bias. The model for SBSLs in section 6.3 can be used to estimate the barrier to hole extraction, which is the difference between the bound HH level in the superlattice and the $Si_{0.83}Ge_{0.17}$ contact layers. This is found to be the smallest in sample LPS61 and is calculated to be 221 meV. As a consequence, it is expected (and verified) that this structure is less strongly affected by hole trapping than the other

structure. For structures LPS54, LPS72 and LPS77, this hole extraction barrier is calculated to be 249 meV, 274 meV and 306 meV. It is then surprising that sample LPS72 has the *highest* responsivity at 0 V bias. This discrepancy can be explained by differing levels of trap-assisted recombination in these three samples. From separate SIMS analysis, samples LPS54, LPS61 and LPS77 are known to have an oxygen concentration of $10^{19}$ $cm^{-3}$. This high oxygen background was due to a vacuum leak in the MBE system, which was identified and fixed after the growth of these three samples. The chamber was then baked out, and the oxygen contamination level was reduced to $10^{18}$ $cm^{-3}$. These oxygen atoms, which are known deep traps, act as recombination centers for the photogenerated electron-hole. The increased responsivity of LPS72 over LPS77 and LPS54 zero bias is almost entirely explained by this trapping mechanism and is argued below.

For the dopant densities used, in the SBSL diodes, the built in potential of the p-i-n diode is calculated using

$$V_{bi} = \frac{k_B T}{q} \ln\left(\frac{N_a N_d}{n_i^2}\right) \tag{6.3}$$

to be 0.7 V, and the resulting electric field in the 0.75 μm thick intrinsic region (0.55 μm thick SBSL + 0.2 μm thick i-$Si_{0.83}Ge_{0.17}$ )is approximately 10 $kVcm^{-1}$. At this electric field, the electron drift velocity $v_{th,e}$ is $5\times10^6$ $cms^{-1}$, and that of holes $v_{th,h}$ is $3\times10^6$ $cms^{-1}$, and the transit times for the carriers through the intrinsic region are 15 psec for electrons and 25 psec for holes.

The oxygen traps are characterized by their density $N_t$ and capture cross-sections (σ), which have been measured to be $10^{-14}$ $cm^{-2}$ for electrons ($\sigma_e$) and $10^{-14}$

$cm^{-2}$ for holes ($\sigma_h$). [117] This capture cross-section yields trap lifetimes given by

$$\tau_e = \left(\sigma_e N_t v_{th,e}\right)^{-1}$$
$$\tau_h = \left(\sigma_h N_t v_{th,h}\right)^{-1} \quad \textbf{(6.4)}$$

For samples LPS54 and LPS77, this is calculated as 2 ps for electrons and 3.3 ps for holes. This implies that it is highly likely that electrons and holes drifting through the intrinsic region will be trapped and will recombine at these traps. In contrast with sample LPS72, the reduced oxygen levels yield longer trap lifetimes of 20 ps for electrons and 33 ps for holes, increasing the probability that the photogenerated carriers being swept out of the intrinsic region and contributing to the photocurrent. This order of magnitude increase in carrier lifetime almost entirely accounts for the ~10x improvement in the responsivity of sample LPS72 over that of LPS54 and LP77 at low bias (0-1 V bias)

### 6.5.4 Noise characterization

All devices are found to operate in the linear, unsaturated regime, and with 1 mm, 0.5mm and 0.25 mm mesa diameter devices having measured responsivities within 9% of each other. This suggests that further reducing the mesa diameter will allow for devices with the same responsivity but lower dark currents and higher noise-equivalent powers. This then allows us to compare our devices directly with recent approaches to near infrared photodetection on silicon.

One approach is the growth of strain-balanced 10 nm-thick Ge quantum wells on a $Si_{0.1}Ge_{0.9}$ RBL. [18] In these devices, strain is used to change the relative

positions of the Γ and L valleys to yield a type-I QW with the direct gap at the Γ point being the most energetically favorable. 15 nm-thick $Si_{0.15}Ge_{0.85}$ layers are grown to balance the strain. This approach is found to yield devices with a dark current density of 2.1 $mAmm^{-2}$, which is 5 orders of magnitude larger than that of Ge72. Optical testing of 12 μm diameter mesa devices yielded typical responsivities of 35 $mAW^{-1}$ at -1 V bias at 1.39 μm and is estimated to be the same at 1.32 μm. This corresponds to a noise equivalent power of 6.6 $\mu WHz^{1/2}$. In contrast, extrapolating the performance of sample Ge72 down to a similar size, and with the same measured responsivity of 16 $\mu A\text{-}W^{-1}$, we have an NEP of 244 $nWHz^{1/2}$ for a 12-μm-diameter mesa device.

Another recently developed approach is that of selective-area-grown germanium on silicon substrate.[17] This approach uses a silicon wafer on which a thick $SiO_2$ layer is grown and subsequently patterned to open windows for germanium growth by CVD. This approach is found to yield epitaxial Ge with threading dislocation densities of $10^7$ $cm^{-2}$, approximately 100× larger than for the SBSLs discussed. Dark current densities of 250 $\mu Amm^{-2}$, which are 4 orders of magnitude than that of Ge72, are achieved. The 1 μm-thick germanium absorber is highly efficient and found to have responsivities of ~0.7 $AW^{-1}$ in the NIR. Based on these reported numbers for a 75 μm mesa diode, an NEP of 4.55 $\mu WHz^{1/2}$ is estimated. For comparison, an equivalently-sized diode fabricated from LPS72 is expected to have an NEP of 9.5 $\mu WHz^{1/2}$.

## ***6.6 Conclusions***

In this chapter, a design approach for strain-balanced superlattices on

commercially available $Si_{0.83}Ge_{0.17}$ relaxed buffer layers was presented. This approach was used to identify heterostructures for growth using MBE with germanium fractions in the superlattice varying from 54% to 77%. Devices fabricated from these materials were found to have dark current densities as low at 272 nA mm-2 at -1 V bias, which is several orders of magnitude smaller than that of competing approaches to near infrared photodetection on silicon.

Photocurrent spectroscopy was used to optically characterize the grown superlattices. In all cases, the superlattice bandgap is found to be lower than that of the constituent alloys of the superlattice, with the 74 Å Si/ 25 Å $Si_{0.23}Ge_{0.77}$ superlattice having a bandgap slightly less than that of strained Ge on the same substrates. Devices were measured to have a responsivity of up to 250 $\mu AW^{-1}$ at a bias of -4 V. In particular, the low dark currents offset the relatively poorer responsivity, yielding devices with noise equivalent powers similar to those of competing devices.

# Chapter 7 : Conclusions and future work

## *7.1 Conclusions*

The primary goal of this thesis was to investigate and develop the use of silicon-germanium as a material system for a near infrared photodetection on CMOS-compatible silicon and strained silicon substrates. This includes the challenges of material modeling, heterostructure design, epitaxial growth by molecular beam epitaxy, device design, device processing and device characterization.

In this work, I demonstrated contributions to the field of silicon molecular beam epitaxy that facilitate this effort. To address the challenges faced with controlling a silicon electron beam source, I designed and fully commissioned an atomic-absorption spectroscopy-based flux monitor and controller. This flux monitor is found to be stable and typically accurate to ± 0.05 Å/s, with no adjustments necessary to account for depletion in the source and with no in-vacuum parts. This is in contrast with the original flux monitor that had a best-case resolution of ±0.1 Å/s, needed frequent and intrusive changes to a calibration constant, and required frequent in-vacuum service.

Material compatibility is a big challenge for MBE, and understanding and developing criteria for acceptable contamination of the epitaxial layers is both, a scientific and an engineering problem. To this end, I proved, for the first time, that despite continued commercial availability, beryllium oxide is an incompatible material for high temperature effusion cells, especially as a crucible liner. I demonstrated that significant co-doping of the grown film with beryllium and oxygen

liberated during the thermal decomposition of the liner occurred. The crystallinity of these films was also shown to be poor. By performing a careful energetic analysis, I demonstrated that this decomposition was not catalyzed by the source charge (boron, in this case), and pyrolytic graphite is a material better suited for use in MBE reactors.

Unlike with silicon substrates, there are no reports of substrate preparation procedures for silicon-germanium relaxed buffer layers that are compatible with solid-source MBE. In this thesis, I have reported on a method involving a wet chemical clean followed by a thermal deoxidation step immediately prior to growth to desorb the residual oxides. To identify the temperature at which this desorption occurs, I used a combination of *in-situ* reflection high energy electron diffraction and *ex-situ* defect selective etching. I found evidence for the two-phase nature of the residual suboxides on a silicon-germanium surface, proving that to obtain an oxygen-free silicon-germanium surface, it is necessary to heat the surface to the same temperature that one would have to heat a similarly prepared silicon surface. These developments in the technique of MBE allowed me to grow a number of strained and strain-free silicon-germanium heterostructures for photodetector applications. I developed a procedure that I used to design strained heterostructures for photodetection at 1.3 μm. These structures were grown using MBE. Photocurrent spectroscopy was used to characterize devices fabricated from these epitaxial growths. By this technique, I validated the design approach by comparing the observed bandgaps of the designed structure to that of a separate control structure. The designed structures were found to have an absorption band at 0.95 eV, which is

absent in the control structure. While the reponsivity in the near infrared of single mode waveguide photodetectors was measured to be up to 6 $mAW^{-1}$ at -4V bias. for 1 mm long devices, photocurrent spectroscopy proved that over 80% of this photoresponse arose from a defect-mediated interband transition and not the designed heterostructure itself.

To reduce the effect of the defect band, and to further extend the detection bandedge deeper into the near infrared, I proposed and designed a number of SiGe/Si strain-balanced superlattices for growth on commercially available silicon-germanium relaxed buffer layers with germanium compositions between 54% and 77%. This strain-free paradigm allows the growth of 0.5 μm thick superlattices and fabrication of normal-incidence photodiodes. I clearly demonstrated that one can use the type-II band-offsets in the silicon-germanium material system to design heterostructures with a bandgap lower than that of any of the constituent alloys. In particular, the 77% Ge superlattice is measured to have a bandgap slightly lower than that of strained germanium on the same substrate. The low defect density yields dark current densities as low as 272 $nA\text{-}mm^{-2}$ at -1V bias, compensating for the lower responsivity (up to 250 $\mu A\ W^{-1}$ at -4V bias) and yielding noise equivalent powers comparable to, and in some cases, better than recent competing approaches to the same problem. The dark current densities at a reverse bias of -1V of all the films in relation to competing approaches is shown below in Figure 7-1, demonstrating high-quality epitaxy that allows these low-noise performance characteristics.

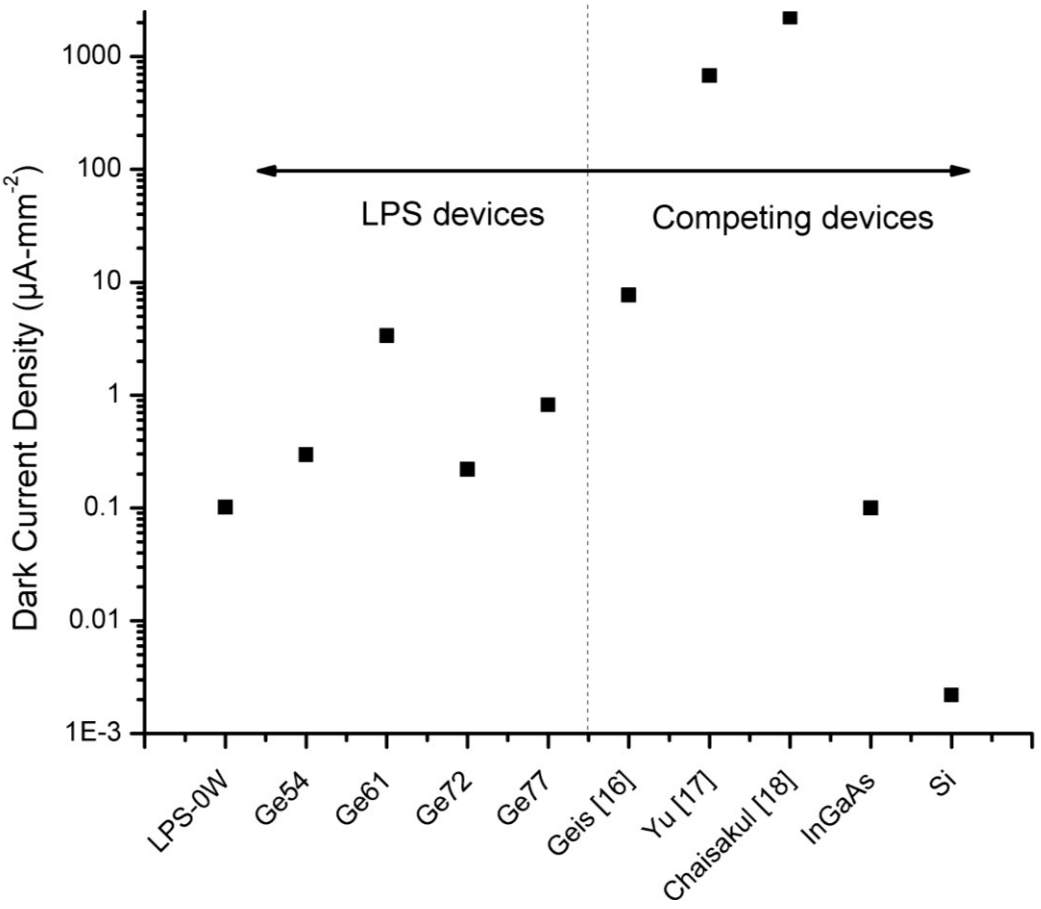


**Figure 7-1:** A survey of the dark current densities of the samples grown by me, and those of competing devices described in the text. Also shown are typical values for silicon and InGaAs diodes.

## *7.2 Future work*

While I have achieved the goals set for this project, I believe that there are still a few open questions that fell out of the scope of this thesis. Here, I present a few of them that I think are particularly interesting, challenging or important.

From the perspective of a material scientist, the results detailed in Chapter 3.4

present interesting avenues for research. As mentioned, the *c* (4×4) reconstruction observed on Si surfaces is not observed on $Si_{0.83}Ge_{0.17}$ and $Si_{0.7}Ge_{0.3}$ surfaces. At this time, there have been no reported *ab initio* calculations to argue against such a reconstruction on SiGe surfaces. RHEED coupled with an MBE chamber offers a way (albeit simple) to study the effect of germanium on the reconstruction of the SiGe surface. By growing a series of $Si_{1-x}Ge_x$ films with small x (x=0.01-0.05), repeating the chemical clean and the RHEED study as presented in Chapter 3, this effect can be experimentally studied. In addition, the experimental verification of the effect of strain on the mobility of dimers on the silicon surface can be studied in detail by repeating this experiment on different relaxed buffer layers capped with strained silicon

As an MBE grower particularly invested in the quality and purity of the grown epilayers, the high levels of oxygen and carbon are issues to be addressed. Based on SIMS analysis, we believe that an improperly designed cooling system for the walls of the mini-chamber (the chamber housing the electron beam source) that allows the walls of the chamber to reach temperatures in excess of 100 ºC is responsible for the oxygen background. This high temperature during operation is detrimental as the chamber walls outgas during epitaxial growth. In addition, the carbon background level in the grown films is found to be correlated with the operation of the electron beam source. We found that epitaxial germanium films have a carbon background of $5x10^{16}$ $cm^{-3}$, which is smaller than that of epitaxial silicon films that have a background of $2x10^{17}$ $cm^{-3}$. Identifying the source of this carbon and suppressing it are of prime importance, especially if high-mobility two-dimensional electron gases

are to be grown in this chamber.

These growth capabilities also allow for the experimental measurement of the bandgaps of strained silicon-germanium alloys on relaxed buffer layers. As I described in Chapter 4, and again in Chapter 6, there has been no systematic report of the bandgaps of these materials, and this information would be exceedingly useful in heterostructure design, and allow for refinements to the bandgap calculations in. [90] These improvements would also help address the discrepancy between the designed and measured values of the superlattice bandgaps specified in Table 6-1and Table 6-3. Improvements to the model for the superlattice will also lend confidence to the design procedure used. Specifically, the effect of band bending due to applied biases and doped layers on the energy levels of the superlattice will result in a more complete model. That can be done by integrating the model with a one-dimensional Poisson's equation solver.

The origin and characteristics of the defect-band giving rise to optical absorption at ~0.7 eV is not understood at all. A technique such as deep level transient spectroscopy or photoinduced current transient spectroscopy can help describe these defects. While it is likely that these defects are related to carbon and oxygen, this is yet to be proven.

The design of structures strain-balanced structures with higher responsivities is a separate challenge. One solution is the growth of thicker superlattices. This option is limited by the relatively low absorption coefficient of the superlattice. Based on the performance of the current devices it is calculated that to reach responsivities of up to 100 mA $W^{-1}$, we would need superlattices 200 μm thick. Such a growth

would be impossible in DepD, which typically can grow films only up to ~15 μm thick per silicon ingot. In addition, with currently achievable growth rates, such a growth would take in excess of 550 hours to grow, an impractical requirement. Alternately, the use of relaxed buffer layers with higher germanium fractions will allow for structures with even smaller bandgaps and higher responsivities than those designed in this thesis. Finally, the use of the refractive index contrast can be used to fabricate strain-balanced superlattice waveguide photodiodes. We estimate that a 2-mm-long multimode waveguide with a 20 μm wide ridge and a 1 μm thick superlattice absorber can have a responsivity of up to 150 $mAW^{-1}$, while retaining low reverse leakage currents of the devices fabricated so far.

# Appendix A: MatLab script to calculate RHEED pattern

Below is the MatLab code used to calculate the positions of the RHEED maxima as shown in Figure 2-11.

---

```
%% Define parameters here
as=5.431;
a1=1*as*[1 1 0]; %Primitive lattice vector #1 and 2. As per convention, a1>a2
a2=1*as*[1 -1 0];
d=as*[0 0 0]; %Basis for crystal
normal=[0 0 1]; %Surface normal vector.
dirs=[1 1 0]; %Directions of incident beam to calculate
V=3e4; %Energy of electrons
ti=2.5*pi/180; %Angle of incidence of e-beam
tdmax=11*pi/180; %Maximum diffraction angle to consider.
colors=['r' 'b' 'g'];


A=dot(a1,cross(a2,normal));
b1=2*pi*cross(a2,normal)/A; %Reciprocal lattice constants #1 and 2
b2=2*pi*cross(a1,normal)/A;
B1=sqrt(dot(b1,b1));
B2=sqrt(dot(b2,b2));
lend=length(d(:,1)); %Number of atoms in the basis
```

```
numdir=length(dirs(:,1));
l=12.3/sqrt(V*(1+1.95e-6*V)); %De Broglie wavelength of the electron including
relativistic correction
K=(2*pi/l); %Absolute value of the electron K vector

%% This is the real calculation where the angle of incidence can be chosen.
%% Calculations are carried out with vectors c1 and c2 representing the
%% periodicity of the reciprocal lattice when viewed from the chosen angle
%% of incidence. c1 is the spacing between planes, in the direction of the
%% incident beam, and c2 is the spacing of rods in the plane of incidence.
%% By definition, c1 and c2 are perpendicular

for num=1:numdir

   clear lmax Beta Theta SF count;
   dir=dirs(num,:)/sqrt(dot(dirs(num,:),dirs(num,:))); %Normalize dir so that it's a true
unit vector
   kp=cross(dir,normal); %This is the unit vector perpendicular to dir

   n1=dot(b1,kp);
   n2=dot(b2,kp);
   if n1==0
      %b1 is perpendicular to the incident beam
```

```
    c1=b1;
    c2=b2;
elseif n2==0
    c1=b2;
    c2=b1;
else
    %First, sort out the rod spacings in the plane of incidence
    [m y]=max(abs([n1/n2 n2/n1]));
    if y==1
        %In this case, n1>n2
        if floor(m)==m
            c2=m*b1 + sign(n1/n2)*b2;
        else
            temp=1;
            while (floor(m)~=m)
                m=m/temp;
                temp=temp+1;
                m=m*temp;
            end
            c2=m*b1 + temp*b2;
        end
    else
        %In this case, n2>n1
```

```
    if floor(m)==m
        c2=sign(n1/n2)*b1 + m*b2;
    else
        temp=1;
        while (floor(m)~=m)
            m=m/temp;
            temp=temp+1;
            m=m*temp;
        end
        c2=temp*b1 + m*b2;
    end
end
%At this point, the rod spacing in the plane of incidence has been
%determined. Next, the rod spacing in the direction of incidence,
%i.e. along the normal to the plane of incidence is to be
%determined. The equation of the plane of incidence in vector form
%is p.dir =0. This plane passes through the origin. The point
%closest to the origin is given by vector b2 (by convention). The
%plane that passes through this point and is parallel to the plane
%of incidence is p.dir = b2.dir and the distance between the planes
%is b2.dir . Thus, the rod spacing in the direction of the incident
%beam is given by a vector of magnitude b2.dir and along the unit
%vector dir.
```

```
    c1=dot(b2,dir)*dir;
  end
  c1;
  c2;

  C1=sqrt(dot(c1,c1));
  C2=sqrt(dot(c2,c2));

  lmax=floor(K*(cos(ti)-cos(tdmax))/C1); %Number of Laue rings within our
observation window

  for L=0:lmax
    cont=1;
    n=0;
    while cont
      Beta(L+1,n+1)=atan(n*C2/((K*cos(ti))-L*C1));
      Kxy=(K*cos(ti)-L*C1)/cos(Beta(L+1,n+1));
      Kz=sqrt(K^2-Kxy^2);
      Theta(L+1,n+1)=atan(Kz/Kxy);
      SF(L+1,n+1)=0;
      S=L*c1+n*c2;
      for k=1:lend
```

```
            SF(L+1,n+1)=SF(L+1,n+1)+exp(1i*dot(S,d(k,:)));
        end
        if ~isreal(Kz)
            Beta(L+1,n+1)=0;
            Theta(L+1,n+1)=0;
            SF(L+1,n+1)=0;
            cont=0;
            count(L+1)=n;
        else
            n=n+1;
        end
    end
end

r=1./(cos(Theta).*cos(Beta));
y=r.*cos(Theta).*sin(Beta);
z=r.*sin(Theta);

ploty=zeros(1,2*sum(count));
plotz=zeros(1,2*sum(count));
sizez=zeros(1,2*sum(count));

ploty(1:2*count(1))=[y(1,1:count(1)) -y(1,1:count(1))];
```

```
    plotz(1:2*count(1))=[-z(1,1:count(1)) -z(1,1:count(1))];
    sizez(1:2*count(1))=[50*abs(SF(1,1:count(1))) 20*abs(SF(1,1:count(1)))];

    %Assemble data to plot
    for L=1:lmax
        ploty(2*sum(count(1:L))+1:2*sum(count(1:L+1)))=[y(L+1,1:count(L+1)) -
y(L+1,1:count(L+1))];
        plotz(2*sum(count(1:L))+1:2*sum(count(1:L+1)))=[-z(L+1,1:count(L+1)) -
z(L+1,1:count(L+1)) ];
        sizez(2*sum(count(1:L))+1:2*sum(count(1:L+1)))=
[20*abs(SF(L+1,1:count(L+1))) 20*abs(SF(L+1,1:count(L+1)))];

    end
   scatter(10.3*ploty,10.3*plotz,colors(num),'o'); %10.3= substrate to screen distance
   hold on;

end
```

# Appendix B: G- matrix used in bandgap computation

Parametrized energy gaps (in eV) of the three lowest conduction bands in (100)-strained $Si_{1-x}Ge_x$/ $Si_{1-y}Ge_y$ alloys in terms of the 3X3 matrix G as defined in Equation 4.15.. The first column gives the band edge to which the gap refers. Each table entry contains the Cartesian components $G_{ij}^{<}$ and $G_{ij}^{>}$, as defined by Eq. 2.5 [90].

| **Gap** |  | $G_{ij}^{<}$ | | | $G_{ij}^{>}$ | | |
|---|---|---|---|---|---|---|---|
| | | 1 | 2 | 3 | 1 | 2 | 3 |
| $\Delta_{\perp}$ | 1 | 1.0779 | 0.052736 | -0.06185 | 1.0781 | 0.047577 | -0.05902 |
| | 2 | 0.80632 | -0.17026 | 0.036626 | 0.25362 | 0.072361 | -0.04306 |
| | 3 | 0.052413 | -0.17056 | 0.058282 | 0.030001 | -0.12063 | 0.056297 |
| $\Delta_{\parallel}$ | 1 | 1.07800 | 0.052405 | -0.0616 | 1.0775 | 0.048883 | -0.05972 |
| | 2 | 0.19598 | -0.27122 | 0.051422 | -0.34601 | -0.04886 | -0.01894 |
| | 3 | 0.02978 | -0.15449 | 0.058774 | 0.001446 | -0.07636 | 0.039134 |
| N | 1 | 2.185300 | -0.6048 | -0.05955 | 2.1832 | -0.60394 | -0.05981 |
| | 2 | -0.016767 | -0.36353 | 0.10632 | -0.64811 | 0.012404 | -0.03869 |
| | 3 | -0.114550 | -0.28617 | 0.13733 | -0.11477 | -0.11609 | 0.06726 |

# Appendix C: The Effective Index Method

## *C.1 Lossless waveguides*

The effective index method is a well-known technique used in the analysis (especially the determination of the modal refractive indices) of rectangular dielectric waveguides. This technique involves the splitting of the two-dimensional waveguide into a combination of one-dimensional guiding structures using the separation of variables. Consider the rectangular waveguide shown in Figure A3-1 Shown are the refractive indices of the various layers, as well as the thicknesses.

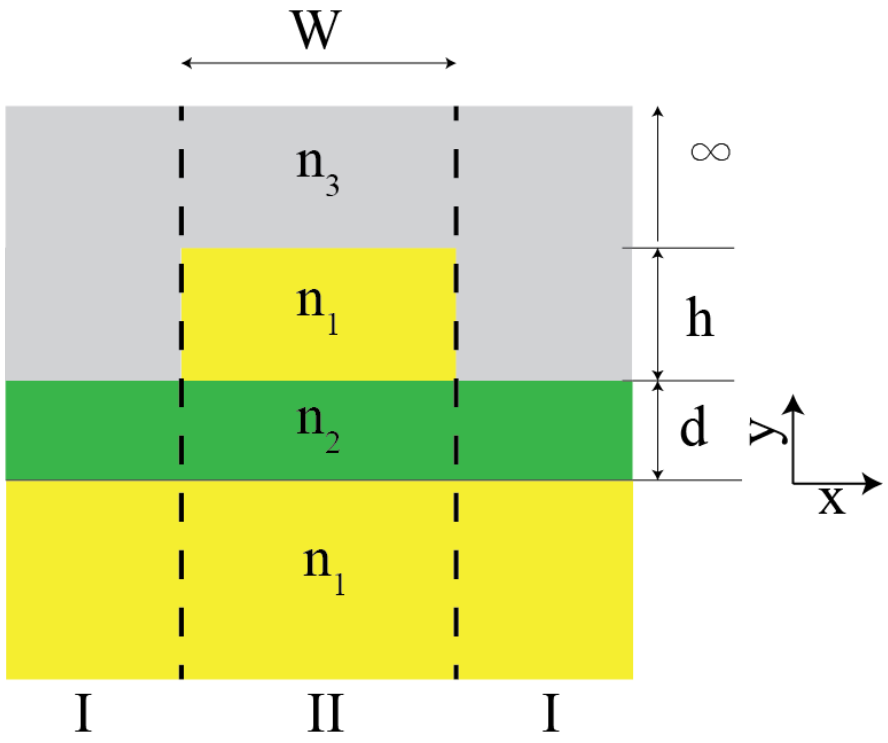


**Figure A3-1:** The refractive index profile of a rectangular waveguide for EIM analysis

The modes of this waveguide are given by the solution to Maxwell's equations with appropriate boundary conditions

$$\nabla \times \overline{E} = -\mu_0 \frac{\partial \overline{H}}{\partial t}$$
$$\nabla \times \overline{H} = \varepsilon_0 n^2 \frac{\partial \overline{E}}{\partial t} \qquad \textbf{(A3.1)}$$

where, for modes propagating in the z-direction (out of the plane of the page)

$$\overline{E}(\bar{r},t) = \overline{E}(x,y)\exp\left(j\left(\varpi t - \beta z\right)\right)$$
$$\overline{H}(\bar{r},t) = \overline{H}(x,y)\exp\left(j\left(\varpi t - \beta z\right)\right)$$

$$\overline{E}(x,y) = \overline{E}_x(x,y)\hat{x} + \overline{E}_y(x,y)\hat{y} + \overline{E}_z(x,y)\hat{z}$$
$$\overline{H}(x,y) = \overline{H}_x(x,y)\hat{x} + \overline{H}_y(x,y)\hat{y} + \overline{H}_z(x,y)\hat{z} \qquad \textbf{(A3.2)}$$

Consider the $E_x^{pq}$ mode, which has $\overline{H}_x = 0$. We can write $\overline{H}_y(x,y) = X(x)Y(y)$, which gives us

$$Y\frac{\partial^2 X}{\partial x^2} + X\frac{\partial^2 Y}{\partial y^2} + \left(k_0^2 n^2(x,y) - \beta^2\right)XY = 0 \qquad \textbf{(A3.3)}$$

where $k_0 = 2\pi/\lambda$ is the free space wave vector. Now, if we add and subtract a term $k_0^2 n_{eff}^2(x)$, where $n_{eff}$ is the effective index in the x-direction, we can separate the equation above into

$$\frac{1}{X}\frac{\partial^2 X}{\partial x^2} + \left(k_0^2 n_{eff}^2(x) - \beta^2\right) = 0$$
$$\frac{1}{Y}\frac{\partial^2 Y}{\partial y^2} + \left(k_0^2 n^2(x,y) - k_0^2 n_{eff}^2(x)\right) = 0 \qquad \textbf{(A3.4)}$$

Now, if we look at the regions labeled I and II in Figure A3-1 individually, there is no x-dependence of the refractive index, and we can determine $n_{eff}(x)$

Consider region II. The fields in the different regions are given by

$$Y(y)=\begin{cases} A\exp(-k_1 y); y<0 \\ B\cos(k_2 y)+C\sin(k_2 y); 0<y<d \\ D\exp(k_1(y+d))+E\exp(k_2(y-d)); d<y<d+h \\ F\exp(-k_3(y-d-h)); y>d+h \end{cases} \quad \textbf{(A3.5)}$$

Here, the propagation constants are given by

$$\begin{aligned} k_1^2 &= k_0^2 n_1^2 - k_0^2 n_{eff}^2 \\ k_2^2 &= k_0^2 n_{eff}^2 - k_0^2 n_2^2 \\ k_3^2 &= k_0^2 n_3^2 - k_0^2 n_{eff}^2 \end{aligned} \quad \textbf{(A3.6)}$$

For the chosen mode, the boundary conditions are the continuity of $H_z$ at y=0,y=d and y=d+h, and $\frac{\partial Y}{\partial x}=0$. This reduces the problem identically to that of the transverse electric mode of a slab waveguide with this index profile. Applying these boundary conditions give the dispersion relation

$$\begin{aligned} \frac{\sin(k_2 d-2\phi)}{\sin(k_2 d)} &= \exp(-2k_1 h)\left(\frac{k_1-k_3}{k_1+k_3}\right) \\ \tan(2\phi) &= \frac{2k_1 k_2}{k_1^2-k_2^2} \end{aligned} \quad \textbf{(A3.7)}$$

These two equations can be solved numerically to yield a value of $n_{eff}$ for layer II. Similarly, a value can be obtained for layer I using the simpler dispersion relation for the 3-layer stack

$$\tan(2k_2 d) = k_2 \frac{k_1+k_3}{k_2^2-k_1 k_3} \quad \textbf{(A3.8)}$$

We now have the effective index of each layer stack, as shown in Figure A3-2

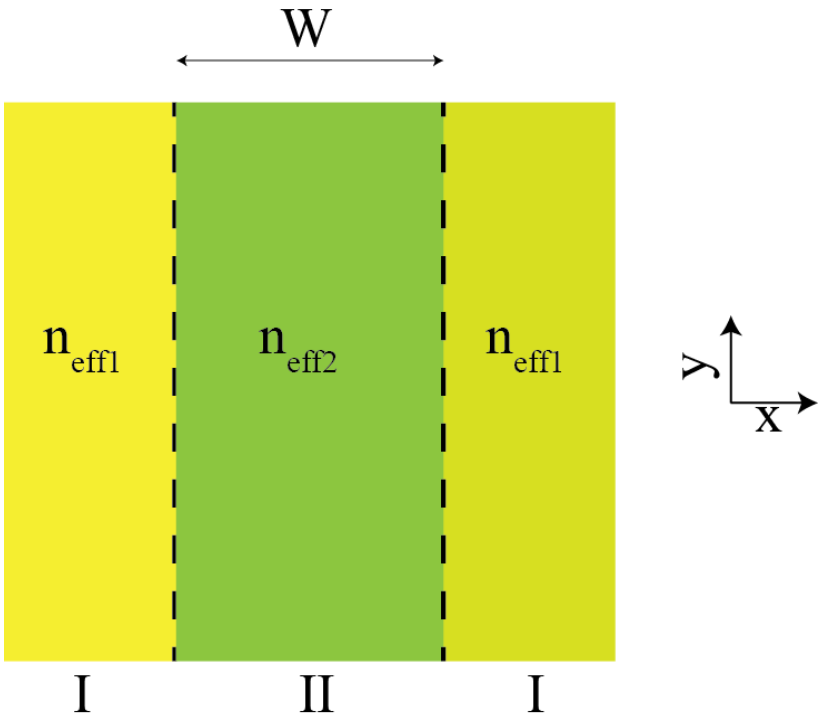


**Figure A3-2:** Simplification of the original index profile by the effective index method

Again, since we are interested in the $E_x^{pq}$ mode with $H_x$=0, the equation

$$\frac{1}{X}\frac{\partial^2 X}{\partial x^2} + \left(k_0^2 n_{eff}^2(x) - \beta^2\right) = 0 \qquad \textbf{(A3.9)}$$

is solved with the condition that $\frac{\partial X}{\partial y} = 0$, which leads to $H_z$=0, $E_y$=0. These are the conditions for the transverse magnetic field in a one-dimensional slab waveguide, and the transcendental equation governing the propagation constant is

$$\tan\left(\frac{k_2' W}{2}\right) = \left(\frac{n_{eff\,2}}{n_{eff\,1}}\right)^2 \frac{k_1'}{k_2'} \qquad \textbf{(A3.10)}$$

where the propagation constants are given by

$$\begin{aligned} k_1'^2 &= k_0^2 n_{eff\,1}^2 - \beta^2 \\ k_2'^2 &= \beta^2 - k_0^2 n_{eff\,2}^2 \end{aligned} \qquad \textbf{(A3.11)}$$

The solution to the $E_y^{pq}$ mode is obtained in a similar fashion, with the finding the effective indices of the TM mode of the layers I and II in Figure A3-1, followed by the determination of the modal refractive index as the solution to the TE mode of the profile in Figure A3-2.

## ***C.2 Lossy waveguides***

While not explicitly designed to handle calculations of waveguide loss, the effective index method has been used in the past to calculate loss coefficients. [118] The loss coefficients of each layer can be specified in terms of its loss tangent

$$\begin{aligned} \varepsilon &= \varepsilon_r\left(1 - j\tan\delta\right) \\ \tan\delta &= \frac{\varepsilon_i}{\varepsilon_r} \end{aligned} \qquad \textbf{(A3.12)}$$

The loss tangents for the different layers can be included in the dispersion equations by rewriting the propagation constants in the equations above as

$$\begin{aligned} K_i^2 &= k_0^2\left(\varepsilon_{ri}\left(1 - j\tan\delta_i\right) - \varepsilon_{eff}\left(1 - j\tan\delta_{eff}\right)\right) \\ &= k_0^2\left(\varepsilon_{ri} - \varepsilon_{eff}\right)\left(1 - j\frac{\varepsilon_{ri}\tan\delta_i - \varepsilon_{eff}\tan\delta_{eff}}{\varepsilon_{ri} - \varepsilon_{eff}}\right) \\ &= k_i^2\left(1 - j\frac{\varepsilon_{ri}\tan\delta_i - \varepsilon_{eff}\tan\delta_{eff}}{\varepsilon_{ri} - \varepsilon_{eff}}\right) \end{aligned} \qquad \textbf{(A3.13)}$$

Since the loss tangents are typically small (~$10^{-8}$ for the cases considered in this thesis), we can use the binomial theorem to approximate

$$K_i = k_i\left(1 - j\frac{\varepsilon_{ri}\tan\delta_i - \varepsilon_{eff}\tan\delta_{eff}}{2\left(\varepsilon_{ri} - \varepsilon_{eff}\right)}\right) \quad \textbf{(A3.14)}$$

Furthermore, the magnitudes of $K_i$ and $k_i$ are assumed to be identical due to the very small loss. These lossy propagation constants can then be substituted into the dispersion relations Equation A3.8. By then equating both sides of the equation and comparing the imaginary parts, the values of $\tan\delta_{eff}$ can be determined graphically for each of the layer stacks I and II. These effective loss tangents can then be used in Equation A3.10 to then determine the loss tangent of the mode of the complete waveguide structure, from which the waveguide loss can be calculated using

$$\varepsilon_{i,eff} = \varepsilon_{r,eff}\tan\delta_{eff}$$
$$\alpha = \frac{4\pi}{\lambda}\sqrt{\varepsilon_{i,eff}} \quad \textbf{(A3.15)}$$

# Bibliography


[1] A. Beling, H.-G. Bach, R. Kunkel, G.G. Mekonnen, and D. Schmidt, "InP-Based 1.55μm High-Speed Photodetectors for 80Gbit/s Systems and Beyond", *Transparent Optical Networks, 2005, Proceedings of 2005 7th International Conference*,Vol.1, pp. 303-308 (2005)

[2] D.J. Paul, "Silicon-Germanium Strained Layer Materials in Microelectronics", *Advanced Materials*, Vol.11, No.3, pp. 191-204 (1999)

[3] John C. Bean, "Silicon-based semiconductor heterostructures: Column IV bandgap engineering", *Proceedings of the IEEE*,Vol. 80, No. 4, pp.571-587, (1992)

[4] D. Choi, E. Kim, P. C. McIntyre, and J. S. Harris, "Molecular-beam epitaxial growth of III–V semiconductors on Ge/Si for metal-oxide-semiconductor device fabrication", *Applied Physics Letters*, Vol. 92, pp.203502 (2008)

[5] S. Verdonckt-Vanderbroek, E.F. Crabbé, B. Meyerson, D.L. Harame, P.J. Restle, J.M.C. Stork, J.B. Johnson, "SiGe-Channel Heteroj unc tion p-MOSFET ' s", *IEEE Transactions on Electron Devices,* Vol.41, No.1, pp. 90-101 (1994)

[6] A.R. Hawkins, W. Wu, P. Abraham, K. Streubel, and J. E. Bowers, "High gain-bandwidth-product silicon heterointerface photodetector", *Applied Physics Letters,* Vol.70, pp. 303-305, (1997)

[7] A. Black, A. R. Hawkins, N. M. Margalit, D. I. Babić, A. L. Holmes, Jr.,Y.-L. Chang, P. Abraham, J. E. Bowers, and E. L. Hu, "Wafer Fusion: Materials

Issues and Device Results", *IEEE Journal of Selected Topics in Quantum Electronics*, Vol. 3, No.3, pp. 943-952, (1997)

[8] Govind P. Agrawal, "Fiber-Optic Communication Systems", Third Edition, John Wiley & Sons Ltd., 2003

[9] Federal Standard 1037C (http://www.its.bldrdoc.gov/fs-1037/fs-1037c.htm)

[10] Y. Chiu, S.B. Fleischer, D. Lasaosa, J.E. Bowers, "Ultrafast (370 GHz bandwidth) p-i-n traveling wave photodetector using low-temperature-grown GaAs", *Applied Physics Letters,*Vol.71, No.17 pp.2508-2510 (1997)

[11] http://www.tf.uni-kiel.de/matwis/amat/semi_en/kap_5/backbone/r5_2_2.html

[12] H. Temkin, A. Antreasyan, N.A. Olsson, T.P.Pearsall, J.C. Bean. "$Ge_{1-x}Si_x$ strained layer superlattice waveguide photodetectors operating near 1.3μm", *Applied Physics Letters,* Vol.48, No.15, pp.963-965 (1986)

[13] T.P. Pearsall, H. Temkin, J.C. Bean, S.Luryi, "Avalanche Gain in $Ge_xSi_{1-x}$/Si Infrared Waveguide Detectors", *IEEE Electron Device Letters,* Vol. EDL-7, No.5, pp.330-332 (1986)

[14] B. Schüppert, J. Schmidtchen, A. Splett, U. Fischer, T. Zinke, R. Moosburger, K. Petermann, "Integrated Optics in Silicon and SiGe-Heterostructures", *IEEE Journal of Lightwave Technology,* Vol.14, No.19, pp. 2311-2323 (1996)

[15] L. Colace, G. Masini, G. Assanto, "Ge-on-Si Approaches to the Detection of Near-Infrared Light", *IEEE Journal of Quantum Electronics,* Vol.35, No.12, pp.1843-1852 (1999)

[16] M.W. Geis, S.J. Spector, M.E. Grein, R.T. Schulein, J.U. Yoon, D.M. Lennon, S. Deneault, F.Gan, F. X. Kaertner, and T. M. Lyszczarz, "CMOS-Compatible

All-Si High-Speed Waveguide Photodiodes With High Responsivity in Near-Infrared Communication Band", *IEEE Photonics Technology Letters*, Vol. 19 No.3 pp. 152-154 (2007)

[17] H.-Y. Yu, S. Ren, W.S. Jung, A. K. Okyay, D. A. B. Miller, and K. C. Saraswat, "High-Efficiency p-i-n Photodetectors on Selective-Area-Grown Ge for Monolithic Integration", *IEEE Electron Device Letters*, Vol. 30, No. 11, pp.1611-1613 (2009)

[18] P. Chaisakul, D. Marris-Morini, G. Isella , D. Chrastina, X. Le Roux, S. Edmond, E. Cassan, J.R. Coudevylle and L. Vivien, "Ge/SiGe multiple quantum well photodiode with 30 GHz bandwidth", *Applied Physics Letters.*, Vol. 98,pp. 131112, (2011)

[19] N.L. Mattey, M. Hopkinson∗, R.F. Houghton, M.G. Dowsett, D.S. McPhail, T.E. Whall, E.H.C. Parker, "P-type delta doping in silicon MBE", *Thin Solid Films*, Vol. 184 No.1-2, pp. 15-19 (1990)

[20] J.W. Shi, C.Y. Wu, S.H. Hsieh, H.C. Hsu, F.H. Suang, P.S. Chen, J.Y. Lu, C.W. Liu, C.K. Sun, " High Responsivity and High Power Performance of Si/SiGe Based Avalanche Photodiode for 10-Gb/s Short-Reach Fiber Communication", *Proceedings of the Conference on Lasers and Electro-Optics, 2005,* CPDA5

[21] M. Gunes, N. Balkan, E. Tiras, S. Ardali, A. O. Ajagunna, E. Iliopoulos, and A. Georgakilas, "Superconductivity in MBE grown InN", *physica status solidi (c)*, Vol. 8, No. 5, 1637–1640 (2011)

[22] H. J. Osten, E. Bugiel, M. Czernohorsky, Z. Elassar, O. Kirfel and A. Fissel,

"Molecular Beam Epitaxy of Rare-Earth Oxides", *Topics in Applied Physics: Rare Earth Oxide Thin Films*, Vol. 106 pp. 101-114

[23] M. Zölfl, M. Brockmann, M. Köhler, S. Kreuzer, T. Schweinböck, S. Miethaner, F. Bensch, G. Bayreuther, "Magneticfilms epitaxially grown on semiconductors", *Journal of Magnetism and Magnetic Materials*, Vol. 175, No. 1-2, pp. 16-22 (1997)

[24] G. A. Prinz and J. J. Krebs, "Molecular beam epitaxial growth of single crystal Fe films on GaAs", *Applied Physics Letters*, Vol. 39 No. 5 pp. 397-399 (1981)

[25] G. G. Jernigan,P. E. Thompson, and C. L. Silvestre, "Ge segregation during the initial stages of $Si_{1-x}Ge_x$ alloy growth", *Applied Physics Letters*, Vol.69, No. 13 pp. 1894-1896 (1996)

[26] R. F. C. Farrow, "Molecular Beam Epitaxy: Applications to Key Materials",(Noyes Publications, 1996)

[27] M. A. Herman and H. Sitter, "Molecular Beam Epitaxy: Fundamentals and Current Status", Second Edition, (Springer-Verlag Berlin Heidelberg, 1996)

[28] S.M. Sze, "Physics of Semiconductor Devices", Second Edition, (Wiley-Interscience, 1981)

[29] "$4^{th}$ Edition MBE Product Guide", Veeco Inc. (2004)

[30] EPI-930 Product Specification Sheet, Veeco Inc.

[31] J. Griesche, "The effect of refraction in reflection high-energy electron diffraction", *Journal of Crystal Growth*, Vol. 149, No. 1-2, pp. 141-142 (1995)

[32] B.A. Joyce, P.J. Dobson, J.H. Neave, K. Woodbridge, J. Zhang, P.K. Larsen, B. Bôlger, "RHEED studies of heterojunction and quantum well formation

during MBE growth — from multiple scattering to band offsets", *Surface Science*, Vol.168, No. 1-3, pp. 423-438 (1986)

[33] P.F. Fewster, "X-Ray Scattering from Semiconductors", Second Edition, (World Scientific Publishing Company, 2003)

[34] R. A. Metzeger and F. G. Allen, "Evaporative antimony growth of silicon during molecular beam epitaxial growth", *Journal of Applied Physics*, Vol. 55, No.4, pp. 931-940 (1984)

[35] J. L. Murray and A. J. McAlister, "The Al-Si (Aluminum-Silicon) System", *Bulletin of Alloy Phase Diagrams*, Vol. 5, No. 1, pp. 74-84 (1984)

[36] B. Volf, M. Belousov, and A. I. Gurary, US Patent# 7452125B2 (2008)

[37] C. Lu and Y. Guan, "Improved method of nonintrusive deposition rate monitoring by atomic absorption spectroscopy for physical vapor deposition processes", *Journal of Vacuum Science & Technology A*, Vol. 13, No. 3, pp1797-1801 (1995)

[38] M. E. Klausmeier-Brown, J. N. Eckstein, I. Bozovic and G. F. Virshup, "Accurate measurement of atomic beam flux by pseudo-double-beam atomic absorption spectroscopy for growth of thin-film oxide superconductors", *Applied Physics Letters*, Vol. 60, pp.657-659 (1992)

[39] C. Lu, M. J. Lightner, and C. A. Gogol, "Rate controlling and composition analysis of alloy deposition processes by electron impact emission spectroscopy (EIES)", *Journal of Vacuum Science & Technology*, Vol. 14, No. 1, pp.103-107 (1977)

[40] D. W. Covington and E. L. Meeks, "Unintentional dopants incorporated in

GaAs layers grown by molecular beam epitaxy", *Journal of Vacuum Science & Technology*, Vol. 16, No. 3, pp.847-850 (1979)

[41] H.-J.Herzog, L. Csepregi and H. Seidel, "X-Ray Investigation of Boron- and Germanium-Doped Silicon Epitaxial Layers", *Journal of the Electrochemical Society*, Vol. 131 No. 12, pp. 2969-2974 (1984)

[42] B. deB. Darwent, "Bond Dissociation Energies in Simple Molecules", (National Bureau of Standards, 1970),

[43] A. Seidl and G. Müller, "Oxygen Solubility in Silicon Melt Measured *In Situ* by an Electrochemical Solid Ionic Sensor", *Journal of the Electrochemical Society*, Vol. 144, No. 9, pp. 3243-3245 (1997)

[44] M. A. Littlejohn and J. B. Robertson, "Piezoresistance and Hole Transport in Beryllium-Doped Silicon", *Journal of Applied Physics*, Vol. 43, No. 7, pp.2986-2992 (1972)

[45] W. Kern, "Handbook of Semiconductor Wafer Cleaning Technology: Science, Technology and Applications", (William Andrew, 1994)

[46] W. Kern, "The Evolution of Silicon Wafer Cleaning Technology", *Journal of the Electrochemical Society*, Vol. 137, No. 6, pp. 1887-1892 (1990)

[47] J. Dabrowski and H.- J. Mussig, "Silicon Surfaces and Formation of Interfaces: Basic Science in the Industrial World", (World Scientific Pub Co Inc, 2000)

[48] Y. Morita and H. Tokomuto, "Atomic scale flattening and hydrogen termination of the Si(001) surface by wet-chemical treatment", *Journal of Vacuum Science & Technology A*, Vol. 16, No. 3 pp. 854-858 (1996)

[49] P. E. Thompson, M. E. Twigg, D. J. Godbey, K. D. Hobart, and D. S. Simons,

"Low-temperature cleaning process for Si molecular beam epitaxy", *Journal of Vacuum Science & Technology B*, Vol. 11, No. 3 pp. 1077-1082 (1993)

[50] A. Ishizaka and Y. Shiraki, "Low Temperature Surface Cleaning of Silicon and Its Application to Silicon MBE", ", *Journal of the Electrochemical Society*, Vol. 133, No. 4, pp. 666-671 (1986)

[51] D. J. Eaglesham, G. S. Higashi, M. Cerullo, "370°C clean for Si molecular beam epitaxy using a HF dip", *Applied Physics Letters*, Vol. 59, No. 6, pp. 685-687 (1991)

[52] K. Choi, H. Harris, S. Gangopadhyay, and H. Temkin, "Cleaning of Si and properties of the $HfO_2$–Si interface", *Journal of Vacuum Science & Technology A*, Vol. 21, No. 3, pp. 718-722 (2003)

[53] T. Takahagi, I. Nagai, A. Ishitani, H. Kuroda, and Y. Nagasawa, "The formation of hydrogen passivated silicon single-crystal surfaces using ultraviolet cleaning and HF etching", *Journal of Applied Physics*, Vol. 64, pp. 3516-3521 (1988)

[54] J. Parsons, R. J. H. Morris, D. R. Leadley, E. H. C. Parker, D. J. F. Fulgoni,and L. J. Nash, "Relaxation of strained silicon on $Si_{0.5}Ge_{0.5}$ virtual substrates", *Applied Physics Letters*, Vol. 93, pp. 072108 (2008)

[55] J. R. Engstrom, M. M. Nelson, and T. Engel, "Thermal decomposition of a silicon-fluoride adlayer: Evidence for spatially inhomogeneous removal of a single monolayer of the silicon substrate", *Physical Review B*, Vol. 37 pp. 6563-6566 (1988)

[56] H. Spjut and D. A. Faux, "Computer simulation of strain-induced diffusion

enhancement of Si adatoms on the Si( 001) surface", *Surface Science*, Vol. 306, pp. 233-239 (1994)

[57] E. Zoethout , O. Gürlü , H.J.W. Zandvliet, B. Poelsema, "The influence of strain on the diffusion of Si dimers on Si(001)", *Surface Science*, Vol. 452, pp. 247-252 (2000)

[58] J. S. Hovis, R. J. Hamers, and C. M. Greenlief, "Preparation of clean and atomically flat germanium(001) surfaces", *Surface Science Letters*, Vol. 440, pp. L815-819 (1999)

[59] N. Tabet, M. Faiz, N.M. Hamdan, and Z. Hussain, "High resolution XPS study of oxide layers grown on Ge substrates", *Surface Science*, Vol. 523, pp. 68-72 (2003)

[60] K. Prabhakaran and T. Ogino, "Oxidation of Ge(100) and Ge(ll 1) surfaces: an UPS and XPS study", *Surface Science*, Vol. 325, pp. 263-273, (1995)

[61] X.-J. Zhang, G. Xue, A. Agarwal, R. Tsu, M.-A. Hasan, J. E. Greene, and A. Rockett, "Thermal desorption of ultraviolet-ozone oxidized Ge(001) for substrate cleaning", *Journal of Vacuum Science & Technology A*, Vol.11, No. 5, pp. 2553-2561 (1993)

[62] A. Mahmood and L.E. Sansores, "Band structure and bulk modulus calculations of germanium carbide", *Journal of Materials Research*, Vol. 20, No. 5, pp.1101- 1106 (2005)

[63] S. Gan, L. Li, T. Nguyen, H. Qi, R.F. Hicks, and M. Yang, "Scanning tunneling microscopy of chemically cleaned germanium (100) surfaces", *Surface Science*, Vol. 3595, pp. 69-74 (1998)

[64] L. H. Chan, E. I. Altman and Y. Liang, "Development of procedures for obtaining clean, low-defect-density Ge (100) surfaces", *Journal of Vacuum Science & Technology A*, Vol. 19, pp. 976-981 (2001)

[65] R. C. Henderson, R. B. Marcus, and W. J. Polito, "Carbide contamination of silicon surfaces", *Journal of Applied Physics*, Vol. 42, pp.1208-1215 (1971)

[66] J. P. Becker, R. G. Long, and J. E. Mahan, "Reflection high-energy electron diffraction patterns of carbide-contaminated silicon surfaces", *Journal of Vacuum Science & Technology A*, Vol. 12, No. 1, pp. 174-178 (1994)

[67] F. Secco d' Aragona, "Dislocation etch for (100) planes in silicon", *Journal of the Electrochemical Society*, Vol.119, pp.948-951 (1972)

[68] M.W. Jenkins, "A new preferential etch for defects in silicon crystals", *Journal of the Electrochemical Society*, Vol.124, pp. 757-762 (1977)

[69] D. G. Schimmel, "Defect etch for <I00> silicon evaluation", *Journal of the Electrochemical Society*, Vol.126, pp. 479-483 (1979)

[70] W.C. Dash, "Copper precipitation on dislocations in silicon", *Journal of Applied Physics*, Vol. 27, pp1193-1195 (1956)

[71] E. A. Fitzgerald, Y.-H. Xie, M. L. Green, D. Brasen, A. R. Kortan, J. Michel, Y.-J Mii, and B. E. Weir, "Totally relaxed $Ge_xSi_{1-x}$ layers with low threading dislocation densities grown on Si substrates", *Applied Physics Letters*, Vol. 59, pp. 811-813 (1991)

[72] R. I. G. Uhrberg, J. E. Northrup, D. K. Biegelsen, R. D. Bringans, and L.-E.Swartz, "Atomic structure of the metastable c(4×4) reconstruction of Si(100)", *Physical Review B*, Vol. 46, pp.10251-10260 (1992)

[73] F.K. Men and J.L. Erskine, "Metastable oxygen-induced ordered structure on the Si(001) surface", *Physical Review B*, Vol. 50, pp.11200-11205 (1994)

[74] S. T. Jemander, H. M. Zhang, R. I. G. Uhrberg, and G. V. Hansson, "STM study of the C-induced Si (100)-c(4×4) reconstruction" *Physical Review B*, Vol. 65, pp115321 (2002)

[75] K. Miki, K. Sakamoto, and T. Sakamoto, "Is the c(4×4) reconstruction of Si (001) associated with the presence of carbon?", *Applied Physics Letters*, Vol. 71, pp. 3266-3268 (1997)

[76] K. E. Johnson, P. K. Wu, M. Sander and T. Engel, "The mesoscopic and microscopic structural consequences from decomposition and desorption of ultrathin oxide layers on Si(100) studied by scanning tunneling microscopy", *Surface Science*, Vol. 290, pp.213-231 (1993)

[77] C. Ebner, J. V. Seiple, and J. P. Pelz, "Simulation of a lattice model for the evolution of Si(001) surfaces exposed to oxygen at elevated temperatures", *Physical Review B*, Vol. 53, pp.16651-16664 (1995)

[78] R. W. Olesinski and G.J. Abbaschian, "The Ge-Si (Germanium-Silicon) System", *Bulletin of Alloy Phase Diagrams*, Vol. 5, pp. 180-183 (1984)

[79] A. Agarwal, J. K. Patterson, J. E. Greene, and A. Rockett, "Ultraviolet ozone induced oxidation of epitaxial $Si_{1-x}Ge_x$ (111)", *Applied Physics Letters*, Vol. 63, pp.518-520 (1993)

[80] L. M. Giovane, H.- C. Luan, A. M. Agarwal, and L. C. Kimerling, "Correlation between leakage current density and threading dislocation density in SiGe p-i-n diodes grown on relaxed graded buffer layers", *Applied Physics Letters*, Vol.

78, pp.541-543 (2001)

[81] J.W. Matthews, A.E. Blakeslee, “Defects in epitaxial multilayers : I. Misfit dislocations”, *Journal of Crystal Growth*, Vol 27, pp.118-125 (1974)

[82] R. People, “Physics and applications of $Ge_xSi_{1-x}$/Si strained layer heterostructures”, *IEEE Journal of Quantum Electronics*, Vol. QE-22, No. 9, pp.1696-1710 (1986)

[83] D. C. Houghton, D. D. Perovic, J.-M. Baribeau, and G. C. Weatherly, “Misfit strain relaxation in $Ge_xSi_{1-x}$/Si heterostructures: The structural stability of buried strained layers and strained-layer superlattices”, *Journal of Applied Physics*, Vol. 67, pp.1850-1862 (1990)

[84] D. C. Houghton, “Strain relaxation kinetics in $Si_{1-x}Ge_x$/Si heterostructures”, *Journal of Applied Physics*, Vol. 70, pp.2136-2151(1991)

[85] Govind P. Agrawal, "Fiber-Optic Communication Systems", Third Edition, (John Wiley & Sons Ltd., 2003)

[86] J. P. Dismukes, L. Ekstrom, E. F. Steigmeier, I. Kudman, and D. S. Beers, “Thermal and Electrical Properties of Heavily Doped Ge-Si Alloys up to 1300°K”, *Journal of Applied Physics*, Vol. 35, pp. 2899-2907 (1964)

[87] A. R. Denton and N. W. Ashcroft, “Vegard’s Law”, *Physical Review A*, Vol. 43, No. 6, pp. 3161-3164 (1991)

[88] F. Schaffler in “Properties of Advanced SemiconductorMaterials GaN, AlN, InN, BN, SiC, SiGe”, Eds. Levinshtein M.E., Rumyantsev S.L., Shur M.S., (John Wiley & Sons, Inc., New York, 2001) pp. 149-188.

[89] L. Yang, J. R. Watling, R. C. W. Wilkins, M. Boric, J. R. Barker, A. Asenov

and S. Roy, “Si/SiGe heterostructure parameters for device simulations”, *Semiconductor Science and Technology*, Vol. 19, pp. 1174-1182 (2004)

[90] M.M. Rieger and P. Vogl, “Electronic-band parameters in strained $Si_{1-x}Ge_x$ alloys on $Si_{1-y}Ge_y$ substrates”, *Physical Review B,* Vol.48, No.19, pp.14276-14287 (1993), “Erratum: Electronic-band parameters in strained $Si_{1-x}Ge_x$ alloys on $Si_{1-y}Ge_y$ substrates” , *Physical Review B*, Vol. 50, No. 11, p. 8138 (1994)

[91] D. J. Paul, “Si/SiGe heterostructures: from material and physics to devices and circuits”, *Semiconductor Science and Technology*, Vol. 19, pp. R75-R108 (2004)

[92] C. G. Van de Walle, “Band lineups and deformation potentials in the model-solid theory”, *Physical Review B*, Vol. 39, pp.1871-1883 (1989)

[93] F. Schaffler, “High mobility Si and Ge structures”, *Semiconductor Science and Technology*, Vol. 12, pp. 151-1549 (1997)

[94] S. L. Chuang, “Physics of Optoelectronic Devices”, (Wiley-Interscience, 1995)

[95] P. Harrison, “Quantum Wells, Wires and Dots: Theoretical and Computational Physics of Semiconductor Nanostructures”, Second edition, (Wiley-Interscience, 2004)

[96] G. Bastard, “Wave Mechanics Applied to Semiconductor Heterostructures”, (Wiley-Interscience, 1991)

[97] Larry A. Coldren and Scott W. Corzine, “Diode Lasers and Photonic Integrated Circuits”, (John Wiley & Sons Inc., 1995)

[98] P.E. Thompson, T.L. Kreifels, M. Gregg, R.L. Hengehold, Y.K. Yeo, D.S Simons, M.E. Twigg, M. Fatemi, K. Hobart, “The growth and characterization

of $Si_{1-x}Ge_x$ multiple quantum wells on Si(110) and Si(111)" , *Journal of Crystal Growth*, Vol. 157, pp. 21-26 (1995)

[99] F. Wang, Y. Shi, J. Liu, Y. Lu, S. Gu, Y. Zheng, "Highly Selective Chemical Etching of Si vs. $Si_{1-x}Ge_x$ Using $NH_4OH$ Solution", *Journal of the Electrochemical Society,* Vol.144, No.3 pp.L37-L39 (1997)

[100] S.A. Campbell, K. Cooper, L. Dixon, R. Earwaker, S.N. Port, D.J. Schiffrin, "Inhibition of pyramid formation in the etching of Si <100> in aqueous potassium hydroxide-isopropanol", *Journal of Micromechanics and Microengineering,* Vol.5 pp.209-218, (1995)

[101] C. L. Canedy, W. W. Bewley, J. R. Lindle, I. Vurgaftman, C. S. Kim, M. Kim, J. R. Meyer "High-power continuous-wave midinfrared type-II "W" diode lasers", *Applied Physics Letters,* Vol.86, pp.211105-211107 (2005)

[102] K. S. Chiang, "Effective-index method for the analysis of optical waveguide couplers and arrays: an asymptotic theory", *IEEE Journal of Lightwave Technology*, Vol. 9, pp. 62-72 (1991)

[103] K. Bernhard-Hofer, A. Zrenner, J. Brunner, G. Abstreiter, F. Wittmann, I. Eisele, "Growth and characterization of strained $Si_{1-x}Ge_x$ multi-quantum well waveguide photodetectors on (110) Si for 1.3 and 1.55 μm", *Physica E*, Vol. 2, pp. 753-757 (1998)

[104] D. K. Schroeder, R. N. Thomas, J. C. Schwartz, "Free carrier absorption in silicon", *IEEE Journal of Solid State Circuits*, Vol. SC-13, pp. 180-187 (1978)

[105] W. Spitzer and H. Y. Fan, "Infrared absorption in n-type silicon", *Physical Review*, Vol. 108, pp. 268-271 (1957)

[106] A. B. Fallahkhair, K. S. Li and T. E. Murphy, "Vector Finite Difference Modesolver for Anisotropic Dielectric Waveguides", *IEEE Journal of Lightwave Technology,* Vol.26, No.11, pp. 1423-1431 (2008)

[107] A. Splett, T. Zinke, K. Petermann, E. Kasper, H. Kibbel, H.-J. Herzog and H. Presting, "Integration of waveguides and photodetectors in SiGe for 1.3 μm operation", *IEEE Photonics Technology. Letters* , Vol. 6, pp. 59-61 (1994)

[108] D. V. Lang, R. People, J. C. Bean, and A. M. Sergent, "Measurement of the bandgap of $Ge_{1-x}Si_x$/Si strained layer heterostructures", *Applied Physics Letters*, Vol. 47, pp. 1333-1335 (1985)

[109] G. G. MacFarlane, T. P. McLean, J. E. Quarrington, V. Roberts, "Fine structure in the absorption-edge spectrum of Si", *Physical Review*, Vol. 111, pp. 1245-1254, (1958)

[110] J. A. Baker, T. N. Tucker, N. E. Moyer, and R. C. Buschert, "Effect of Carbon on the Lattice Parameter of Silicon", *Journal of Applied Physics*, Vo. 39, pp. 4365-4368 (1968)

[111] J. Ramm and H. von Kaenel, "Low Energy Plasma Processing (LEPP): a new Approach for Pre-Epi Wafer Clean and Epitaxial Growth" *Future Fab Intl.,* Vol.15 http://www.future-fab.com/documents.asp?d_ID=1905#

[112] IQE Strained Silicon Substrate (http://www.iqesilicon.com/capabilities/ssi17.pdf)

[113] H.-U. Schreiber, "High-speed double mesa SiGe/Si heterojunction bipolar transistor fabricated by selfalignment technology", *Electronics Letters*, Vol. 28, pp. 485-487 (1992)

[114] H. Temkin, T. P. Pearsall, J. C. Bean, R. A. Logan, and S. Luryi, "$Ge_{1-x}Si_x$ strained layer superlattice waveguide photodetectors operating near 1.3μm" *Applied Physics Letters*, Vol. 48, pp. 963-965 (1985)

[115] J. Weber and M. I. Alonso, "Near bandgap photoluminescence of Si-Ge alloys", *Physical Review B*, Vol. 40, pp.5683-5693 (1989)

[116] M. I. Alonso and K. Winer, "Raman spectra of c-$Si_{1-x}Ge_x$ alloys", *Physical Review B*, **39**, 10056 (1989)

[117] J. A. J. Tejada, A. Godoy, J. E. Carceller, and J. A. L. Villanueva, "Effects of oxygen related defects on the electrical and thermal behavior of a $n^+$- p junction", *Journal of Applied Physics*, Vol. 95, pp. 561-570 (2004)

[118] P. R. Young and R. J. Collier, " Extension of the effective-index method to include the calculation of losses in dielectric waveguides", *Electronics Letters*, Vol 33, pp. 1551-1552 (1997)